Università degli Studi di Genova

Dipartimento di Neuroscienze, Riabilitazione, Oftalmologia, Genetica e Scienze Materno-Infantili (DINOGMI)

PhD School
Clinical and Experimental Neurosciences
XXXIV cycle

Candidate
ENRICO PEIRA

Advances and perspectives in amyloid PET quantitative interpretation

3RD MAY 2022

Supervisor: Dott. A. Chincarini
Supervisor: Dott. M. Pardini

Referee: Prof. D. Cecchin
Referee: Prof. M.L. Calcagni

Introduction

My PhD focused on amyloid imaging: in this manuscript are described the activities carried out in this field.

Amyloid imaging refers to a diagnostic examination that allows for the in-vivo detection of amyloid aggregation, which is considered a crucial step in the development of Alzheimer's disease. Specifically, the technique of choice for amyloid imaging is the positron emission tomography (PET) with appropriate radioligands. The amyloid PET was developed in the framework of research and diagnosis of Alzheimer disease and it is considered a key tool in the management of this pathology.

Alzheimer's disease is currently the most common and well known cause of neurodegenerative dementia in elderly people accounting for 60 to 80% of all cases. It is currently estimated that over 55 million people live with dementia worldwide: this staggering figure is made more striking as it is foreseen to reach 78 million by 2030. In the 2021 World Alzheimer Report of the Alzheimer's Disease International (ADI) it is estimated that globally 75% of people with dementia are not diagnosed and this percentage rises to 90% in some low- and middle-income countries. Due to the non-straightforward relationship between its presentation and the underlying molecular pathology, the diagnosis of Alzheimer's disease on purely clinical manifestation is a non-trivial task. There is great interest in metodologies for the assessment of in-vivo biomarkers (such as the amyloid aggregation) that can be used to complement the clinical evaluation and provide direct evidence of the core features of the pathology. Moreover, in June 2021, the U.S. Food and Drug Administration (FDA) has approved the first anti-amyloid drug for Alzheimer's disease on the grounds that it significantly lowers the amyloid PET signal and assuming that this reduction is likely to be of benefit. Despite the great controversies over the clinical efficacy of this therapy, the approval might pave the way for a new age of molecular targeted treatment in this field, which could possibly lead to a surge in the use of amyloid PET. For example, identification of potential targets for this drug will require increased access to amyloid PET and other biomarkers, and might even boost the biomarker-supported early diagnosis of Alzheimer's disease.

As one can easily imagine, these developments make the challenges of improving the analysis and interpretation of amyloid PET even more pressing. For example, it is becoming of common wisdom that the dichotomous classification - classically used in clinical practice - based solely on visual analysis is inadequate, as it does not provide information on the level of positivity and is used to describe a phenomenon that is gradual and can last up to 15 years. Quantitative approaches that provide numerical estimates of the physiological processes of interest may help by giving the opportunity of ranking brain amyloidosis to find out, for example, patients who would benefit from a threatment. These approaches are constantly evolving and there is currently no consensus on which is the best way to perform a quantitative analysis of amyloid PET images or which is the most feasible in clinical setting. Other relevant issues are related to the

differences between radiotracers and to image quality factors that that can affect the interpretation of the scan even for expert readers even when supported by quantification. Another poorly understood aspect is the potential information that is lost in amyloid PET images using current analysis pipelines. Up to now, the amyloid imaging data have mainly been used for the definition of global amyloid profile. Recent studies have shown that this imaging modality can provide much more detailed information when assessed at regional level.

In this context, I looked at two of the main aspects of amyloid PET assessment. The first is related to technical issues that can arise in the evaluation of the scans, such as the application of an appropriate analysis method to different radiotracer, the comparison of multiple-reader visual evaluations and the effect of image quality. A novel quantitative approach has also been developed, validated and compared to both standard and hihgly sohpisticated techniques. The second aspect is more clinical-related and has to do with the possible interpretation of regional amyloid burden and the assessment of the relationship between the regional load, the cognitive decline and the regional tau (the other major biomarker in Alzheimer's disease).

The activities to which I contributed during my PhD allowed me to collaborate on studies that highlight the role of neuroimaging biomarkers for neurodegenerative diseases. A list of related publications and scientific contributions is provided in Appendix A.

Table of Contents

Chapter 1

Amyloid

1.1 Aβ production, forms and toxicity

Amyloidosis is a family of protein misfolding disorders characterized by deposits of amyloid fibrils in different organs. These aggregates are characterised by a fibrillar morphology of a few nanometers in diameters and a β-sheet structure.

The amyloid beta peptide derives from proteolysis of a transmembrane glycoprotein expressed in many tissues and concentrated in the synapses of neurons, called amyloid precursor protein (APP). This precursor is synthesized in the endoplasmic reticulum and transported to the Golgi complex, where it completes maturation and is finally transported to the plasma membrane where its cleavage occurs. The APP is processed via two alternative pathways: a non-amyloidogenic and an amyloidogenic. In the first case, the APP is cleaved by a α-secretase to generate sAPPα. In the latter, the APP is cleaved by a β-secretase generating the sAPPβ. The sAPPα and the sAPPβ are soluble fragments released into the extracellular environment. Following cleavage by β-secretase, additional cleavage by γ-secretase detaches the intracellular domain from the cytofacial leaflet and releases two additional fragments: the p3 peptide, that corresponds to the region 17-40/42 of the Aβ sequence; and the a Aβ fragment consisting of 40/42 amino acids, that comes from the amyloidogenic pathway and has fibrillogenic characteristics (see figure 1.1).

The most common forms of Aβ peptides are those with 40 or 42 amino acids in their chains (Aβ_{1-40} Aβ_{1-42}), distinguishable for the different carboxylic group. The longest peptide (Aβ_{1-42}) is equipped with additional hydrophobic groups that makes the Aβ_{1-42} the most amyloidogenic form of peptides. Two main mechanisms of Aβ_{1-42} clearance have been identified:

- The active transport of Aβ_{1-42} across the blood brain barrier (BBB) into the circulation [298]. This mechanism is mediated by the LRP-1, which is a low-density lipoprotein receptor-related protein that mediates transport of Aβ_{1-42} outside the brain.

- The degradation of Aβ_{1-42} and the toxic soluble oligomers that are not effectively cleared by active transport, by means of degrading enzymes in the brain parenchyma [102] such as NEP (neutral endopeptidase) and IDE (insulin degrading enzyme).

The Aβ_{1-42} peptide aggregate into various types of assemblies as monomers, dimers and oligomers of high molecular weight. The oligomers gradually generate protofibrils
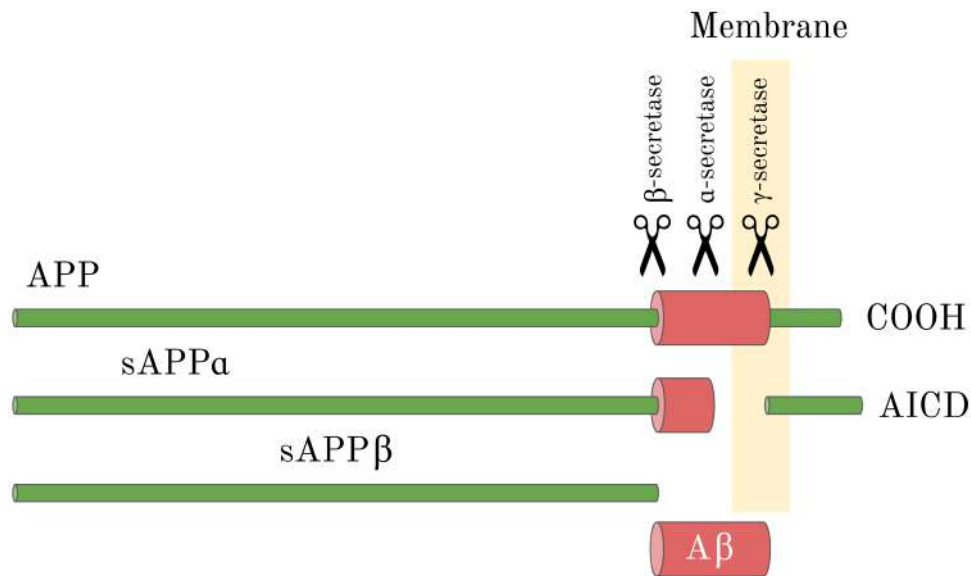
Figure 1.1: Formation of the Aβ peptide. The APP protein (695 amino acids) is processed via two alternative pathways, resulting in cleavage by α-secretase to generate sAPPα or β secretase to generate sAPPβ. The cleavage by β secretase, and the additional cleavage by γ secretase releases the Aβ peptide and the intracellular domain (AICD) detaches from the cytofacial leaflet.

and amyloid fibrils. The fibrils are larger and insoluble, and they can further assemble into amyloid plaques, while amyloid oligomers are soluble and may spread throughout the brain [71, 141]. In figure 1.2, a schematic representation of the aggregation states of β_{1-42}. Hereinafter the Aβ_{1-42} is referred to as Aβ.
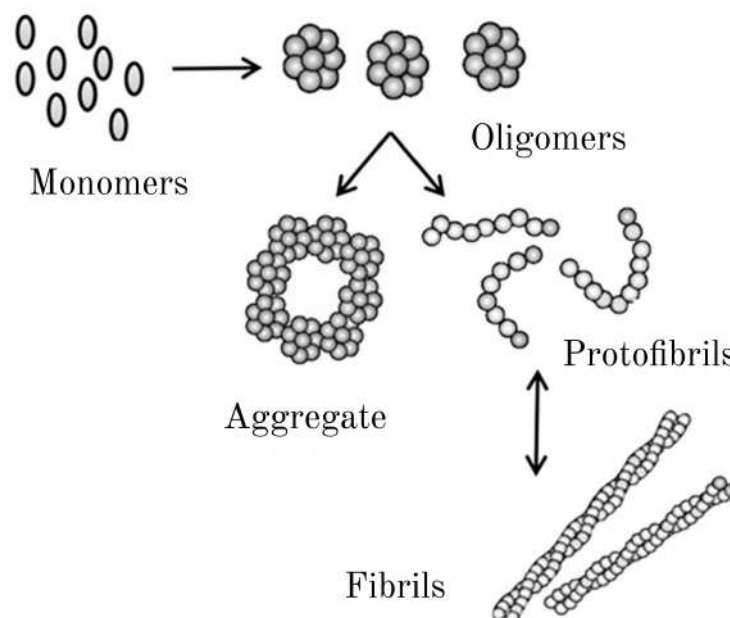
Figure 1.2: Overview of the Aβ aggregation.

Studies suggested the existence of a dynamic compartmentalization of the different types of Aβ between plaques and soluble Aβ, and that these forms may contribute to neurodegeneration at different stages of the disease [115, 157]. Aβ is known to promote depolarization of the synaptic membrane, excessive calcium influx and mitochondrial

damage, thus altering the ability of cells to conduct their normal physiological activities [174].

In addition, the Aβ aggregation produces free radicals such as the reactive oxygen species that generate toxic oxidized proteins and peroxidized lipids by reacting with proteins or lipids [71]. Oxidized proteins put the membrane integrity at risk and alter the sensitivity to oxidative modifications of enzymes that are critical to neuronal function such as glutamine synthetase and creatine kinase [2, 293]. Peroxidized lipids generate many toxic products that cause multiple harmful alterations to cellular activity by drifting to different parts of neurons. The harmful functions connected with neuronal death include the inhibition of ion-motive ATPases and Na^+-dependent glutamate transport of the glial cell, loss of Ca^{2+} homoeostasis, and disruption of signaling pathways [269, 67]. The oxidative stress induced by Aβ aggregation has also been reported to cause oxidation and damage to DNA [71].

Continuous aggregation and persistent high Aβ level also promote a chronic response of the innate immune system by activating microglia, leading to neuronal loss through direct phagocytosis [197]. The Aβ aggregation also initiates a toxic inflammatory response with the subsequent release of inflammation-related mediators (i.e.: eicosanoids, chemokines, proinflammatory cytokines and complement factors) which increase neuronal demise, the loss of neuronal synapses and impair the clearance of Aβ and of the neuronal debris mediated by microglia [71]. When the APP precursor accumulates in mitochondrial membrane, the translocation of mitochondrial metabolism and protein is stopped up, leading to mitochondrial dysfunction, which in turn increase the Aβ generation resulting in a toxic feed-forward loop [6, 293].

During the Aβ accumulating process, tau protein hyperphosphorylation occurs in response to kinase/phosphatase activity changes mediated by Aβ aggregation, leading to the formation of neurofibrillary tangles (NFTs), neuronal and eventual synaptic dysfunction, and finally Alzheimer's disease [71]. These aggregation process occurs on neuron membranes generating a toxic aldehyde called 4-hydroxynonenal and leads to lipid peroxidation, which can damage the function of ion-motive ATPases, glucose transporters and glutamate transporters leading to cell demise [71].

1.2   Aβ related pathology

Cerebral Aβ deposition is a distinguishing feature of different pathological conditions. Together with neurofibrillary tangles (NFTs), the β-amyloid plaques are the major hallmark of Alzheimer's disease.

Aβ can also be observed in cerebral and leptomeningeal blood vessels affected by cerebral amyloid angiopathy (CAA) [291], as soluble, dispersible Aβ in extra- or intracellular fluid, and as membrane-associated Aβ aggregates [38, 291]. In adults with Down syndrome (DS), the overexpression of APP is triplicated on chromosome 21 resulting in an excess deposition of Aβ, that occurs as early as the teenage years [108, 287]. Moreover, a faster rate of grey matter loss in patients with Lewy body dementia (DLB) has been associated with high amyloid-β deposition [240].

Amyloid accumulation can occur in the body too – for example it has been recently proposed to be involved in ischemic heart disease and in ischemia-reperfusion injury [86]. Moreover, recent studies suggested that Aβ and its precursor might be implicated in cancer. Plasma levels of Aβ were significantly higher in hepatic cancer patients than in

normal controls [135], and APP expression increased in human breast cancer [160].

1.3   Alzheimer's disease

Alzheimer disease (AD) is an progressive neurodegenerative disease that represents the most common cause of dementia. According to the annual report of the Alzheimer Association it is estimated that 6.2 million people in the U.S. are living with AD; this number is expected to increase to 13.8 by mid century [88]. Because of this plague, only in 2019 more than 16 million U.S. family members and other volunteer caregivers provided an estimated 18.6 billion hours of care to people with AD. This care is valued at nearly $ 244 billion, but its costs do not take into account family caregivers' increased risk for emotional distress and negative mental and physical health outcomes [88].

Dementia is described as an individual pattern of decline in memory and impairment in, at least, two cognitive domains [180]. Dementia due to AD is associated with the onset of significant and progressive impairment of daily life functions throughout the disease course leading to death in 15-24 years [271].

Clinical and preclinical disease

The majority of AD cases occur after age 65 (late-onset AD or sporadic), while cases occurring earlier are rarer (less than 5% of all cases) and named early-onset AD [88]. The latter cases are linked to mutations in three different genes (APP, PSEN1 and PSEN2) which respectively encode the precursor protein APP and the APP-processing enzymes presenilin 1 and 2. These genes alter the amyloidogenic processing of the protein APP affecting the levels of $A\beta_{1-42}$ production. Moreover, specific allelic combinations of the APOE gene have been identified as a risk factor for the AD [230]. The APOE $\epsilon4$ genotype is the major susceptibility gene identified in the human genome for both early-onset and sporadic AD [52]. Other risk factors include: lifestyle, history of psychiatric conditions and education, possibly modulated by systemic comorbidities such as diabetes and vascular diseases.

In a rarer proportion of patients (1%–2% of all cases), AD is inherited in an autosomal dominant fashion: dementia, in this patient is developed very early (in their 30s to 60s) depending on the specific gene mutation, and progresses much faster than sporadic AD [13].

Typical early impairment in memory and learning, followed by impairments in complex attention, executive function, language, visuospatial function, praxis, gnosis, and behavior and/or social comportment characterize the most frequent amnestic cases [180]. Some cases also report early impairment in non-memory domains. Early deficits in visuospatial function, praxis, and gnosis are coupled with posterior cortical atrophy [257]. Other atypical clinical presentations of AD are the logopenic/phonological variant [95], and the behavioral/dysexecutive variant presenting with early executive dysfunction or behavioral impairment (apathy, hyperorality, and perseveration) [201].

The dementia severity is typically graded with standardized instruments such as the Clinical Dementia Rating (CDR) [189]. This scale grades the dementia severity with a composite score that takes into account dysfunction in domains of memory, judgement, orientation, problem solving, involvement in community affairs, function in home and hobbies, and self-care.

Several longitudinal studies of biomarker changes have identified a preclinical phase of the disease preceding onset of clinical symptoms by 10-20 years. In this preclinical phase deposition of $A\beta$ in the precuneus and other cortical regions comprising the default mode network has been observed followed by: I) accumulation of NFTs, II) cortical hypometabolism, III) hippocampal volume loss and atrophy and IV) onset of symptomatic cognitive impairment [271, 13, 69, 68, 93, 94, 104, 281].

In figure 1.3 a representation of the timing of major AD pathophysiological events in relation to clinical course.
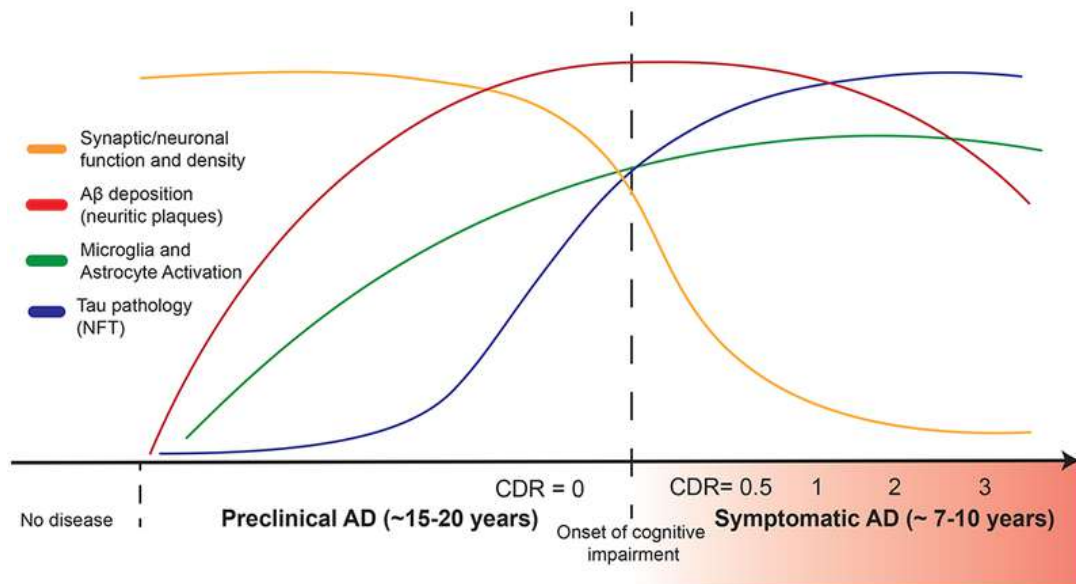
Figure 1.3: Timing of major AD pathophysiological events in relation to clinical staged by use of the CDR scale. A protracted preclinical phase of disease is characterized by the early onset of amyloid deposition. This is detected by a reduction in cerebro-spinal fluid and plasma levels of $A\beta_{1-42}$ or increased global signal on amyloid imaging. Concurrently, there are early neuroinflammatory changes (such as microglial activation) followed by the spread of NFTs tau pathology from the medial temporal lobes into neocortex. Increased signal on tau imaging and increased cerebro-spinal phospho-tau levels mark this change in patients. Synaptic dysfunction, synapse loss and neurodegeneration accumulates with pathologic spread of tau aggregates. Imaging analysis of hippocampal and cortical volumes allows for longitudinal tracking of neurodegenerative changes. Onset and progression of cognitive impairment correlates with accumulation of tau and hippocampal volume loss but not amyloid deposition. On the x-axis, the CDR scale: a score of 0 indicates normal cognition and scores of 0.5, 1, 2 and 3 indicate questionable, mild, moderate and severe dementia, respectively. Courtesy of Long and Holtzman [162].

Clinical and research diagnostic criteria

In the years, the assessment of brain amyloidosis has gained a pivotal role in the in-vivo diagnosis of AD. The first criteria for clinical diagnosis of AD were introduced in 1984 by the National Institute of Neurological and Communicative Disorders and Stroke's - Alzheimer's Disease and Related Disorders Association (ADRDA-NINCDS). These criteria were focused on the clinical presentation of the AD requiring a confirmation with an autopsy and the presence of significant functional disability [179].

In 2007 these guidelines were revisited linking the AD diagnosis to the presence of biological markers (such as the presence $A\beta$ in brain): the diagnosis started the trans-

ition from a clinical-pathological entity to a clinical-biological one [61]. According to these revised criteria, the AD is recognised in vivo and regardless of the dementia symptoms if the presence of at least two essential factors can be objectively measured. The first is clinical evidence of significant memory impairment associated with a progressive worsening of the performance. The second, is the objective evidence of alteration in one or more of the following biomarkers:

- Presence of atrophy of the medial temporal lobe (MTL) measured with structural imaging such as the magnetic resonance imaging (MRI).

- Anomalous concentration of $A\beta$ in the cerebro-spinal fluid (CSF).

- Impaired glucose metabolism assessed with an FDG positron emission tomography.

Although still not mandatory for clinical diagnosis, the introduction of biomarkers as a support feature was a major innovation introduced by these criteria that allow for the identification of the prodromal AD: a condition at risk of AD where at least one biomarker shows alteration.

Dubois and colleagues, of the International Work Group (IWG), in 2010 redefined the lexicon of AD that now represents a life-long, a continuum whose range spans from an (asymptomatic) pre-clinical stage, to mild cognitive impairment and to dementia [60].

Another step towards the definition of Alzheimer disease as it now stands was taken one year later by the experts of the National Institute of Aging (NIA) along with those of the Alzheimer's Association (AA). In their recommendations it was recognized that the AD starts before symptoms occur and patients with only evidence of amyloid accumulation were identified as asymptomatic AD. For the stages of pre-dementia and dementia three levels of probability were recognized (high, intermediate or unlikely) that the disease is due to AD based on the information of biomarkers, which now increase the confidence level of diagnosis and are no longer a criterion of diagnosis by themselves [180].

In the last IWG criteria advances to the diagnostic algorithm were proposed requiring in-vivo evidence of Alzheimer's-like pathology to be demonstrated by positivity of at least one biomarker between the reduction of the concentration of $A\beta_{1-42}$ in the CSF together with increased concentration of phosphorylated tau (alternatively these two biomarker can be assessed with amyloid or tau imaging) [62].

According to these criteria, the presence of pathological $A\beta$ load is not sufficient for a diagnosis of AD, but the absence of amyloid in a patient who is having symptoms of either mild cognitive impairment or early dementia excludes AD as the basis of that dementia. The most recent criteria were proposed by NIA-AA in 2018. With the reinforced idea that certain biomarkers are valid proxies for neuropathologic changes of AD, the proposed research framework primarily aims to define and stage the disease across its entire spectrum reserving the term AD to the concomitant amyloid and tau pathology thus defining the Alzheimer's disease as a biologic construct identified by biomarkers [125]. Since this framework needs to be thoroughly examined and tested before being adopted into general clinical practice, the authors suggest following these recommendations in a research context solely. In these guidelines, an unbiased biomarker classification system (the A/T/N [126]), was proposed to complete the previous scheme. In this system, each biomarker category is binarized as positive or negative. "A" represents the $A\beta$ deposition detected by amyloid imaging or CSF $A\beta_{1-42}$. "T" represents the tau biomarkers assessed with CSF p-tau or tau imaging. Finally, "N" represents neurodegeneration biomarkers using CSF p-tau, structural MRI or FDG positron emission tomography. The

aim of this classification is to categorize multidomain biomarker finding at individual level in a format that can be easy to adopt and interpret. A patient with the only evidence of Aβ accumulation but normal tau biomarker is labeled as "Alzheimer's pathologic change", while the term "Alzheimer's disease" is assigned if biomarker evidence of both Aβ and pathologic tau is present. These two labels are applied independently from clinical symptoms and not regarded as separate entities but earlier and later phases of the "Alzheimer's Disease continuum". In figure 1.4 the possible biomarker profiles and respective categories are summarized.

AT(N) profiles	Biomarker category	
A-T-(N)-	Normal AD biomarkers	
A+T-(N)-	Alzheimer's pathologic change	Alzheimer's continuum
A+T+(N)-	Alzheimer's disease	
A+T+(N)+	Alzheimer's disease	
A+T-(N)+	Alzheimer's and concomitant suspected non Alzheimer's pathologic change	
A-T+(N)-	Non-AD pathologic change	
A-T-(N)+	Non-AD pathologic change	
A-T+(N)+	Non-AD pathologic change	

Figure 1.4: Possible biomarker profiles and categories according to the last NIA-AA framework. Binarizing the three A/T/N biomarker types leads to eight different profiles. Every individual can be placed into one of the three categories based on biomarker profiles: those with normal AD biomarkers (no color), those with non-AD pathologic change (dark grey), and those who are in the Alzheimer's continuum which is an umbrella term that denotes either Alzheimer's pathologic change or AD (light grey). Courtesy of Jack and colleagues [125].

Amyloid cascade hypothesis and therapeutic development

Although mutations in APP, PSEN1 and PSEN2 occur only in familial AD, similar neuropathological changes in Aβ and tau were observed also in sporadic AD [224, 245] leading to the formulation of the amyloid cascade hypothesis [107]. This hypothesis posits Aβ triggers the formation of NFTs, neuronal cell loss, vascular damage, and AD dementia. It has evolved over the years to an integrative model that also includes other disease mechanisms such as microgliosis, immunoreactivity, oxidative stress, proteostasis [246].

To date, this picture is still supported by numerous genetic, biomarker, and genome-wide association studies in both familial and sporadic AD [261]. The amyloid cascade

hypothesis has also guided most drug discovery efforts that have focused on the removal of various forms of cerebral Aβ. A number of Aβ-targeted therapies tested in phase III clinical trials could effectively reduce amyloid in the brains of patients with mild cognitive impairment (MCI) or AD dementia (such as bapineuzumab [239], gantenerumab [204], solanezumab [113], lanabecestat [284], atabecestat [109] and verubecestat [65]). However, they have not successfully slowed cognitive decline in those patients.

Two phase III trials (named ENGAGE and EMERGE) of an anti-amyloid agent named aducanumab, were prematurely stopped after a futility analysis predicted that the two studies would unlikely meet their primary endpoint [191]. Subsequent analyses showed that a subset of participants receiving sufficiently high doses of aducanumab demonstrated benefits in both trials. Despite the generated debate, this agent received the first FDA [1] approval for the treatment of Alzheimer disease [234, 146, 261].

The lack of success in most of these trials may be due to the timing of the interventions (the studies involved patients in clinically advanced stages of AD) [218], insufficient dosing, or the wrong Aβ species being targeted [193, 181]. Conversely, this might indicate that removing Aβ from the brain does not stop (nor slow down) cognitive decline because tau-mediated neurodegeneration in AD can be triggered by independent factors.

---

[1]FDA: The Food and Drug Administration is a federal agency of the Department of Health and Human Services. It is responsible for protecting and promoting public health through the control and supervision of food safety, tobacco products, dietary supplements, prescription and over-the-counter pharmaceutical drugs, vaccines, blood transfusions, medical devices, electromagnetic radiation emitting devices, cosmetics, animal foods and veterinary products.

Chapter 2

Positron emission tomography

The positron emission tomography (PET), is a minimally-invasive imaging procedure that allows for visualization and measurements of in-vivo biological and physiological processes. This relatively new technique exploits the distribution of radioactive labeled substances injected into the patient body to provide a three-dimensional image of a target process in the examined anatomical district. The PET methodology has become a cornerstone both in oncological imaging (tumor grading, assessing treatment efficacy during or after treatment, radiotherapy planning) and neurological imaging (differential diagnosis, monitoring of pathophysiologic changes, treatment effects monitoring) [110, 33].

2.1 Principles and detection

PET is a nuclear medicine technique that uses the decay of radioactive isotopes to generate the signals that are reconstructed and converted into images. The radioactive isotopes are used to mark molecules (or tracers) that are compounds engineered to trace the path of a specific biological process related to the pathology under consideration. The radioisotopes in these compounds decay $\beta+$: a proton is converted to a neutron creating a positron e^+ and a neutrino ν_e. The patient is injected with tracer and placed in the scanner for the acquisition, to reveal the distribution of the tracer in the anatomical district of interest. The radionuclide emits a positron that has a mean free path of $\sim 1-2$ mm in organic tissues. Then, the positron annihilates with an electron and two collinear photons of 511 keV are emitted. In figure 2.1 a pictorial representation of this process is provided.

The local PET signal comes from the simultaneous detection of the photons: a ring of scintillators detect the signal only when two collinear events are detected within a certain time window (10-20 ns). To avoid counting photons not due to an annihilation event, there is also an energy based selection of the events: the photon energy should range between 350 and 650 keV [236]. The scintillators convert high energy photons to the range of visible photons; these photons hit the photomultiplier coupled with the scintillators producing the electrical signal. In figure 2.2 a representation of a typical PET detector is depicted: the patient lies on a support that slides within the ring while signals from equally spaced planes are acquired.

An appropriate post processing allows reconstructing, from each acquired plane, a 2-D image. By neatly arranging the sequence of 2-D images, the final 3-D image is obtained. In this volume, the signal intensity in any image voxel (analogous to the pixel in a two-dimensional image) is proportional to the amount of radionuclide and, hence, to
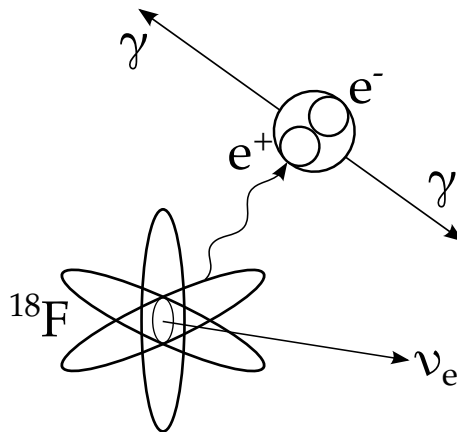
Figure 2.1: ^{18}F β-decay and annihilation of the resulting positron with a nearby electron. Two photons γ are emitted with an angle π.

the amount of tracer to which it is bound in a specific portion of tissues.

Among the others, the most common radioisotopes in PET are ^{18}F and ^{11}C due to their rather short half-life (~ 110 min and ~ 20 min respectively) and the relatively easy simple production in cyclotrons.

The spatial resolution of PET images is generally 2-3 mm and depends on many factors: the structure of the detector, the size and shape of the scintillators, their efficiency and the electrical signal filtering and amplification system [58].

2.1.1   Detection issues

Before the annihilation, the positron emitted during β decay interacts with the atoms of the surrounding tissues losing its kinetic energy. Depending on the parent nucleus, the emitted positron has different initial energies and can travel for different distances (for ^{18}F the typical distance is 2.4 mm [110]). If kinetic energy of the positron is still present at the time of annihilation, then this energy excess is manifested as an imperfect alignment of the two emitted photons. This non-collinearity is in the order of some fraction of a degree which can lead to an error in the annihilation coordinates of 2-3 mm.

After the annihilation, the travelling photons interact with patient tissues resulting in an attenuation of their intensity. This phenomenon can be so relevant that it is necessary to know the magnitude of the attenuation to get the real distribution of the tracer in the target anatomical district. Thus, PET is often combined with computerized tomography (CT), which is a structural imaging modality, into PET/CT scanner. The co-acquired CT is converted into an attenuation map and used to correct the intensities in the image [58, 163].

More recently, the PET has also been coupled with MRI into PET/MRI solutions. The MRI has a superior definition of anatomical structures and provides a wide range of investigating solutions with sequences for both functional and physiologic imaging. However, the attenuation correction is still a methodological challenge in this hybrid solution [35].

Another issue possibly affects the detection. Ideally, only the events associated with the annihilation of positrons should be recorded (true coincidence). However, spurious events that met the coincidence criteria can be recorded as well causing loss of spatial resolution and noise. The possible coincidence events (depicted in figure 2.3) can be
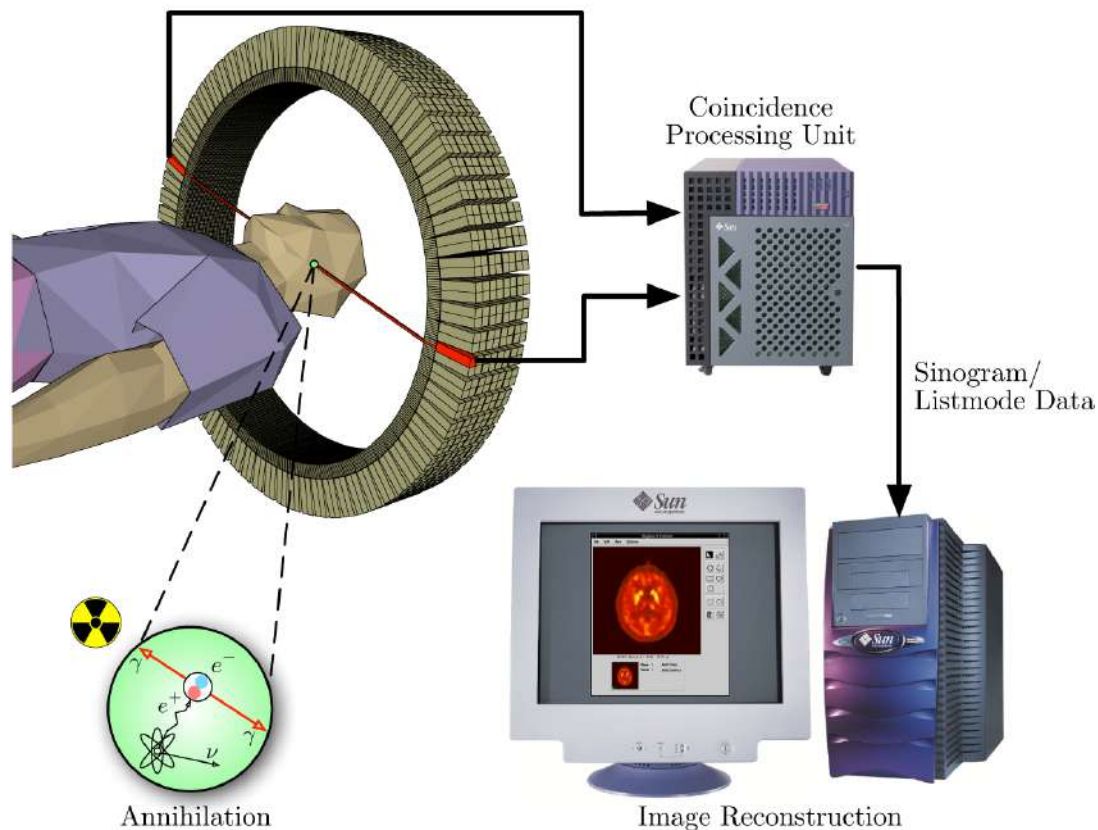
Figure 2.2: Pictorial representation of a typical PET detector. The two annihilation photons γ are detected by two opposite detector elements. The detector consist of a ring of scintillators coupled to photomultipliers and a processing unit to retrieve the emitter position. The detected signals are then processed and reconstructed into images.

summarized as follows:

- *True coincidence*: associated with the detection of a pair of photons emitted by the annihilation event. The two photons, with a certain energy, are revealed within the temporal and spatial coincidence window, that is, between an opposed pair of scintillators.

- *Scattered coincidence*: occurs when one or both photons undergo Compton scattering that causes both energy loss and change of direction. This results in an incorrect location of annihilation, and ultimately in image degradation and a reduction in contrast.

- *Random coincidence*: when photons associated with two distinct annihilations are detected by the system as coming from a common annihilation event. Random coincidences are sources of noise and are generally proportional to the square of the activity in the field of view (FOV), and to the time and energy window.

Also the presence of high counts rate can cause degraded PET acquisitions. This effect is corrected with the coincidence cancellation method. It consists of a random event evaluation performed with a delay of the temporal window that avoids any real coincidences. The ratio between delayed and non-delayed coincidences provides the proportion of real and random coincidences [58, 236]. Significant improvements have been made

over the years in detectors and electronics. Some of these achievements, including the development and incorporation of new scintillators crystals and detector configurations for higher spatial and temporal resolution, allowed the time-of-flight (TOF) technology to be included into the PET imaging [138]. The TOF is used to approximately define the position of the annihilation events along the line of response (LOR). The LOR is the line of coincidence between two detectors that record the same event.

The position of each event is estimated by measuring the difference in arrival times of the photons (Δt): for an annihilation event placed at a distance Δx from the FOV center, the delay between the two detection will be:

$$\Delta t = 2\frac{\Delta x}{c} \tag{2.1}$$

Since c is approximately the speed of light, the Δt, the time-of-flight resolution of the system, is really tiny ranging from 500 to 600 ps.

The TOF information considerably improves image quality, contrast and signal-to-noise ratio [268].
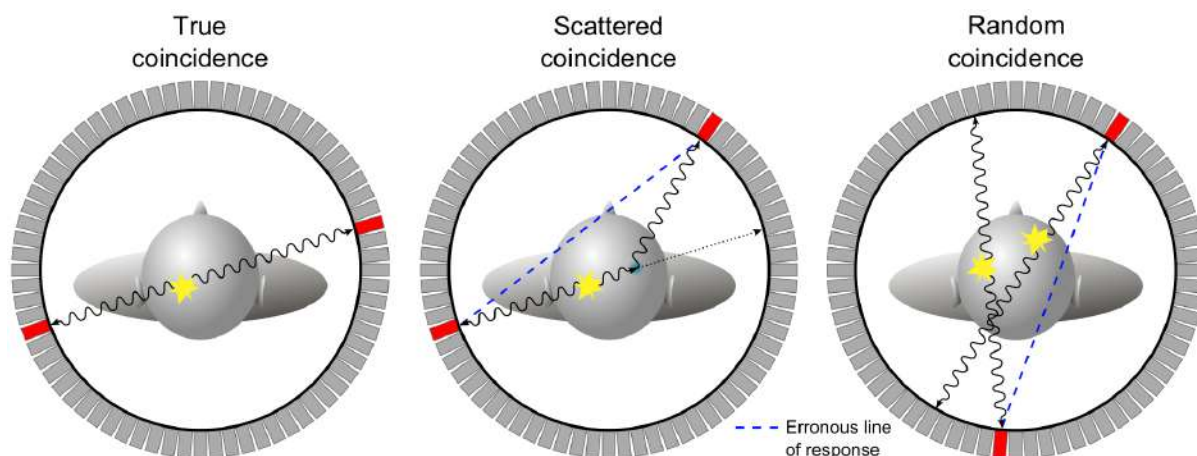
Figure 2.3: True, scattered and random coincidences. Courtesy of Häggström and colleagues [118].

2.2   Image reconstruction

The number of events detected along a LOR is proportional to the integral of the activity along that line. During the PET acquisition, a huge number of events along different LOR are collected, processed and stored as a sinogram file. The sinogram is a two-dimensional array representing all the possible LORs of an acquisition and composed of many overlapping sine waves. Each LOR is identifiable by its distance with the center of the FOV (r) and its angle (Θ). The image reconstruction is the mathematical process that is used to reconstruct the image from the sinogram: in PET data it recovers the tracer distribution delivering a matrix whose coordinates and values respectively represent appropriate anatomical position and radiopharmaceutical uptake. In figure 2.4 a pictorial representation of a sinogram and its acquisition is provided.

Two main families of reconstruction algorithms exist: the analytical approaches (such as the filtered back projection, FBP) which the mathematical model is analytically inverted, and the iterative algorithms (such as the Ordered Subset Expectation Maximization,

PET camera (image)   Sinogram
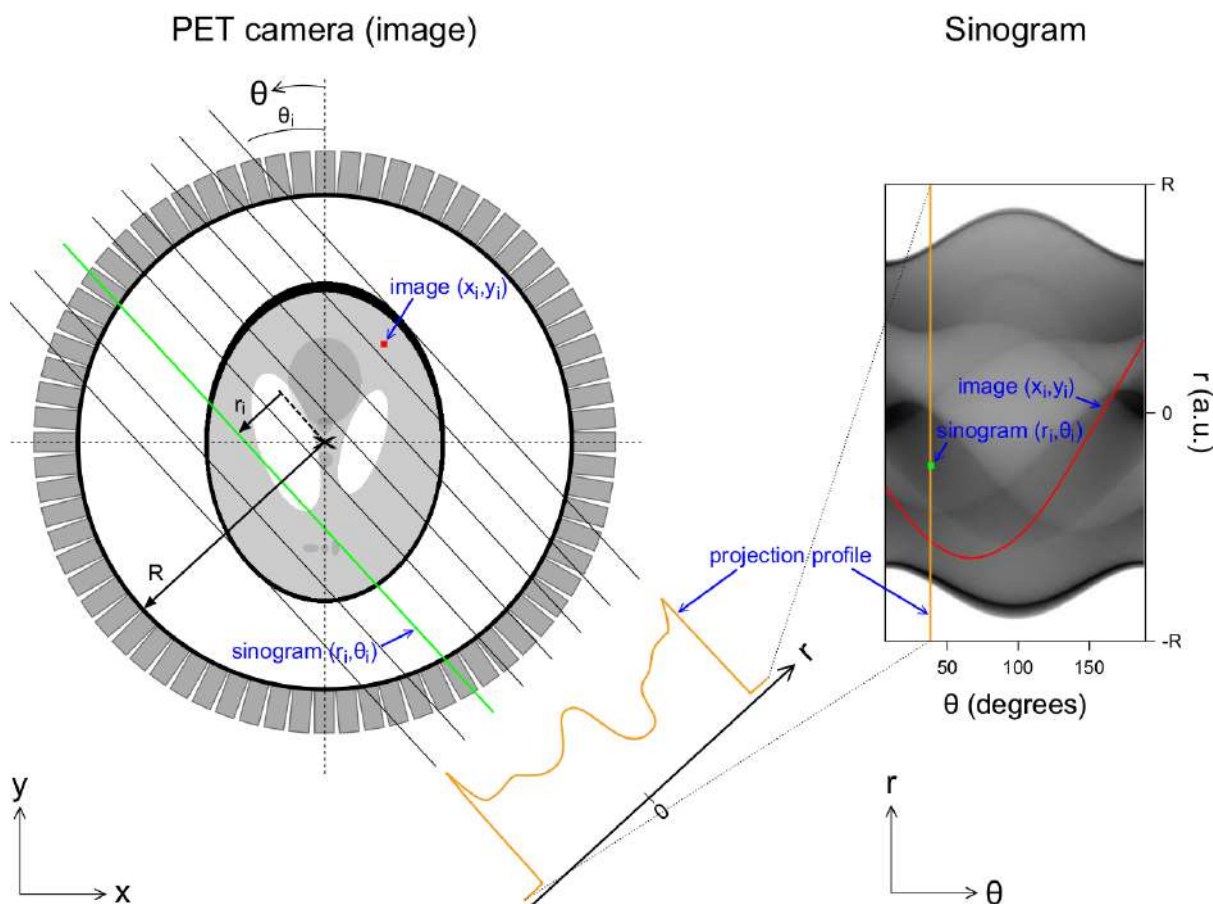
Figure 2.4: A phantom in image (camera) space (xy) and the corresponding sinogram in sinogram space ($r\Theta$). A set of LORs constitutes a projection profile, corresponding to a column in the sinogram. A point in image space will trace out a curve in the sinogram space, and a point in sinogram space is a line (specifically, a LOR) in image space. Courtesy of Häggström and colleagues [118].

OSEM) in which the tomographic image is reconstructed using iterative statistical methods [58, 116].

While analytic reconstruction methods are faster and easier to implement, the reconstruction accuracy is limited by two main factors: these methods cannot model the degrading agents in a PET scanner and they take no account of the stochastic variability in photon detection [262].

Although more computationally expensive (particularly for 3-D PET data and its added dimensionality in both the image and the projection domains), the iterative approach allows for a more accurate modeling of the data acquisition by accounting for statistical fluctuations associated with noise [262, 58]. Due to the superiority of the iterative algorithms, in this paragraph only a brief introduction of these methods is provided. An iterative method initially estimates the object uptake distribution, then it calculates its projection by forward projecting this initial estimation. The initial estimation is then compared with measured projection and refined until a satisfying convergence is reached [58, 118]. The iterative approaches are based on the following elements:

- An image model, which consists in the discretization of the space domain in N pixel or voxel.

- A system model that links the estimated image with the projections.

- A statistical model, which describes the relationship linking the measurements to their expected values. Since photon detections are Poisson distributed, most methods adopt a Poisson model.

- A metric, that is the measure used to define how well the image estimate fits the data.

Different choices in these components have resulted in a variety of iterative reconstruction methods [158, 262, 154]. Two of the most representative methods are the MLEM and the OSEM.

The maximum-likelihood expectation maximization method (MLEM) adopts the maximum likelihood as optimization criterion and the expectation maximization algorithm to find the optimal solution. The MLEM algorithm has a consistent convergence behaviour, but provides noisy images due to the ill-conditioning nature of the problem [262]. To mitigate this effect several strategies have been proposed: one can apply smoothing filters or sieves to the reconstructed image for noise suppression or can stop the algorithm before convergence [262]. Moreover, the convergence rate of the MLEM is quite slow, requiring from 50 to 100 iterations to reach an acceptable solution with PET data.

The OSEM [116] has been developed to address the issue of slow convergence: it splits the projection data into a number of mutually exclusive subsets (for instance by dividing the projections into sets with different views, or azimuthal angles) and uses only a subset for each iteration. The number of subsets determines the degree of acceleration with respect to the MLEM. Approximately, the OSEM converges a number of times equal to the number of subsets faster than MLEM and is currently the most widely used reconstruction method [262].

It is possible to improve the performance of the reconstruction methods by exploiting the anatomical information and by modeling the physics of the imaging process. Compared to structural imaging (MRI or CT), PET imaging has lower resolution. The PET/CT systems offer the advantage to complement the PET image reconstruction with anatomical information provided by CT data. This improves the estimated models enhancing the spatial resolution, refining the noise regularization and improving the image signal-to-noise ratio [262, 50, 20]. The greatest challenge for this technique is that the CT must be segmented first to provide anatomical bounds and this is a non-trivial task. Moreover, it assumes an accurate alignment between PET and CT, which is not always valid when physiologic motions occur (e.g., cardiac and respiratory motions) that can cause artifacts in the fused image [262, 223].

Point Spread Function

One important component of the physics modeling is the point spread function (PSF) which describes the response of an imaging system to a point source. In PET, the PSF is frequently described by the width at half of the maximum value (FWHM) of a Gaussian shaped function fitted to the PSF. The PSF of the system can be derived analytically [252], with experimental measurements or with Monte Carlo simulations [3]. Including the PSF model in reconstruction has proven to increase the spatial resolution and the contrast [262]. On the other hand, the PSF correction can introduce Gibbs ringing artifacts in the reconstructed image [3].

Partial Volume Effect

Besides the effect of the positron mean free path, another important phenomenon can limit the spatial resolution and the accuracy of PET imaging: the partial volume effect (PVE). The PVE is linked to the PSF concept, it occurs when multiple sources contribute to the intensity of a single element of the image (pixel or voxel). The mixture of signals is a combination of two factors.

The first is represented by the limited spatial resolution of PET imaging due to the detector design (i.e. the pitch of the crystal) and to the reconstruction process. Because of the finite spatial resolution and of the PSF, the signal coming from a point source is detected not only in one voxel, but it spills-out and is also recorded outside the actual source. Mathematically, the effect of the finite resolution is described by a 3-D convolution operation of the actual source with the three dimensional PSF of the imaging system [251] (see figure 2.5).
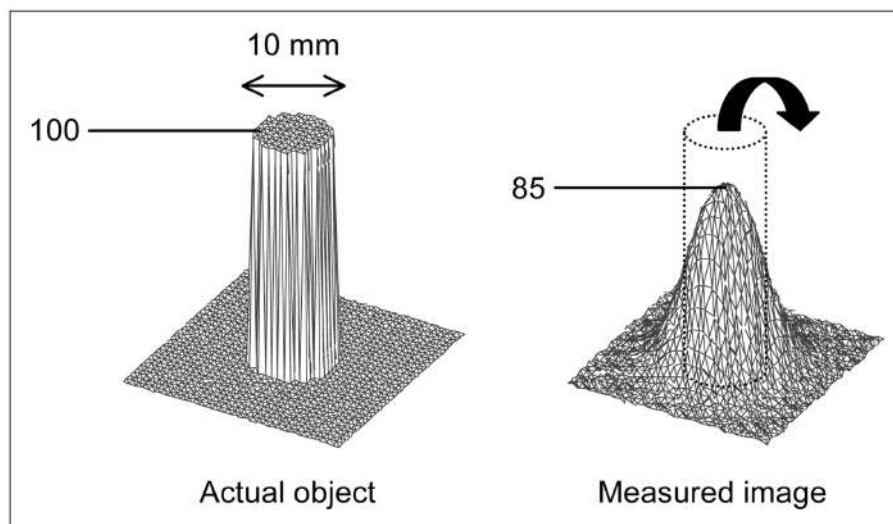
Figure 2.5: A representation of the blurring and the spillover between regions due to PVE. A circular source (diameter of 10 mm) of uniform activity (100 arbitrary units) in nonradioactive background yields measured image in which part of signal emanating from source is seen outside actual source. Maximum activity in measured image is reduced to 85. Courtesy of Soret and colleagues [251].

The second phenomenon causing the PVE is the image sampling. The radiotracer distribution is sampled on a voxel grid, which does not match the actual contours of the tracer distribution. Hence, a voxel can include different tissues and its intensity is the mean of the signal intensities of underlying tissues included in that voxel [251]. Figure 2.6 illustrates this effect in 2 dimensions.

This combined effect results in a blurring of tissue boundaries that can lead to underestimation of the activity concentration and thus to misinterpretation of the reconstructed image. Thus, when considering a functional region of interest (ROI), part of the activity from the ROI will thus also be detected outside (an effect that is called spill-out). Conversely, activity from regions close to the ROI will spill-in to the structure of interest. As one might expect, the PVE is a major source of quantitative biases (particularly for brain imaging) that can be corrected with different methods [173, 251].

Actual object with pixel grid overlapped   Measured image   Spill-out
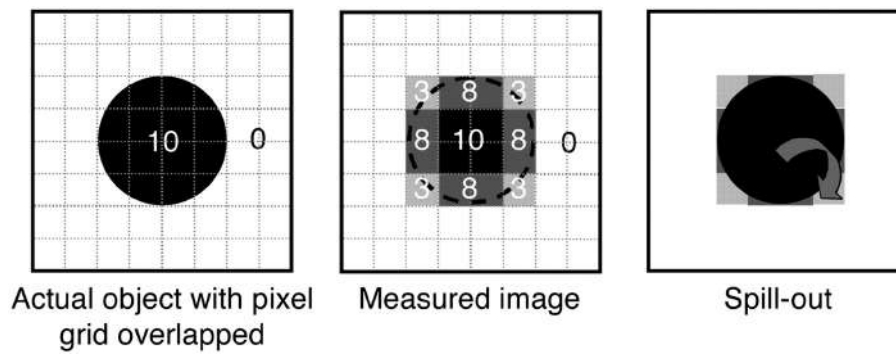
Figure 2.6: Influence of image sampling on PVE. Pixels on edges of source include both source and background tissues. Signal intensity in these pixels is mean of signal intensities of underlying tissues. Part of signal emanating from source is seen outside actual object and therefore is described as spilling out. Courtesy of Soret and colleagues [251].

Chapter 3

Amyloid PET

Amyloid PET (amyPET) allows for the in-vivo detection of amyloid-β plaques, hallmarks of Alzheimer's disease. Over the years, the amyPET has shown a very high negative predictive power and a milder positive power that relies on the age and on the pre-test probability of having AD [48]. Indeed, in cognitively unimpaired elderly people the prevalence of amyloid positivity increased from 10% to 44% in the age group from 50 to 90 years [134].

AmyPET has also proven to detect the amyloid pathology in the clinically atypical variants of AD such as posterior cortical atrophy, logopenic variant or frontal executive variant [17, 57]. Since 2004, many amyloid-specific PET ligands have been developed. The first human study was proposed by Klunk and colleagues: the molecule involved was a ^{11}C marked compound named Pittsburgh Compound B (PiB) [142]. PiB retention was marked in cortical areas known for the amyloid deposition in AD patients, whereas equivalent uptake was observed in AD and controls in regions known to be relatively unaffected.

The validity of PiB imaging as a method for in vivo evaluation of Aβ plaque burden was also confirmed with post-mortem examinations [121]. Since then, the PiB has been comprehensively studied at many institutions around the world to assess the amount of amyloid-β in the brain. Specifically, the amyloid imaging was widely used to follow amyloid-positive patients over time to verify whether the typical patterns of AD were observed or not.

Based on the results of the PiB, a great interest arose in the development of new amyloid ligands that were developed and approved since 2012. It first began with the ^{18}F-Florbetapir [48], sold under the brand name Amyvid. That was followed by the ^{18}F-Flutemetamol [238] (brand name Vizamyl) and the ^{18}F-Florbetaben [235] (trade name Neuraceq).

These three fluorinated tracers have proven to be essentially equivalent in clinical practice [147, 275]. Moreover, to allow for direct comparison of quantitative assessment standardization approaches have been proposed [143].

Due to the growing clinical interest in amyloid imaging, the Society of Nuclear Medicine and Molecular Imaging (SNMMI) and the AA have jointly developed appropriate use criteria to better define and properly context I) the potential clinical utility of this imaging modality and II) the circumstances in which amyPET imaging would be inappropriate [136]. This framework is being widely studied. In 2019, a large prospective multicentre trial, including more that 16000 participants, named Imaging Dementia-Evidence for Amyloid Scanning (IDEAS) showed that the appropriate use of amyPET

resulted in change in management in a relevant proportion of cases (61%). Further analyses are determining whether those changes improved the clinical outcomes or not [225].

Similarly, another ongoing multicenter study, called Amyloid Imaging to Prevent Alzheimer's Disease (AMYPAD), is collecting data from thousands of patients with the aim of providing answers regarding the diagnostic confidence, change in diagnosis, and alterations between planned and actual patient management plans after the amyloid-β imaging [84].

3.1 Radiotracers

Radiotracers are administered so as to not perturb normal physiology, but allows in vivo studies under physiological conditions. The compounds can be substrates of physiological pathways of interest or they have high affinity for particular targets because of specific binding interactions.

The potential tracers for amyPET belong to the second group and, to be taken into consideration, they should meet certain requirements: they must be non-toxic, small molecule with a high affinity binding, specificity and selectivity for Aβ. They have to be neutral and lipophilic to cross the BBB. However, it should not be too lipophilic to avoid binding in sites that do not contain Aβ, hence causing nonspecific uptake in the image.

Among the other desirable characteristics, the amyloid-specific tracer should have a good in vivo stability and be amenable to kinetic modelling. In addition, no radio-labelled metabolites that bind to the brain should be formed.

Of central importance, the compound must have a suitable site for labelling with radioisotopes with a rapid time of decaying by positron emission. Two common radioisotopes for PET are the carbon 11 (^{11}C) and the fluorine 18 (^{18}F). The ^{11}C is a radioactive isotope of carbon with a half-life of about 20 minutes. With a long half life of approximately 110 minutes and the lowest positron energy (which contributes to a better image resolution), the ^{18}F is the most frequent isotope.

PiB is the first developed amyloid tracer: it is a Thioflavin-T (ThT) derivative labeled with ^{11}C [142]. The ThT is a fluorescent probe commonly used to monitor the in vitro formation of amyloid fibril [171]. The PiB chemical formula is $C_{14}H_{12}N_2OS$. Being the first compound capable of crossing the BBB, of binding to amyloid with high affinity, and of rapidly clearing from normal gray matter; the PiB is one of the most studied. However, the short half-life of its radioactive isotope limits its practical use to imaging centers that have access to a cyclotron.

This drawback has encouraged the development of ^{18}F labeled molecules whose longer half-life allowed more extensive clinical and research use. The first fluorinated compound that received the FDA approval as a diagnostic tool for Alzheimer's disease (2012) derived from polietilen glicole stilbene. It is named ^{18}F-Florbetapir and its chemical formula is $C_{20}H_{25}^{18}FN_2O_3$ [48]. An analogous of the PiB, based on the chemical structure of the ThT dye received the FDA approval in 2013. It is called ^{18}F-Flutemetamol [238] and its chemical formula is $C_{14}H_{11}^{18}FN_2OS$. The last radiotracer to receive the FDA approval (2014) derived from stilbene as well. It's name is ^{18}F-Florbetaben and its chemical formula is $C_{21}H_{26}FNO_3S$ [235]. In figure 3.1 the chemical structures of the fluorinated radioligands.

To receive the FDA approval, the three fluorinated agents demonstrated high affinity
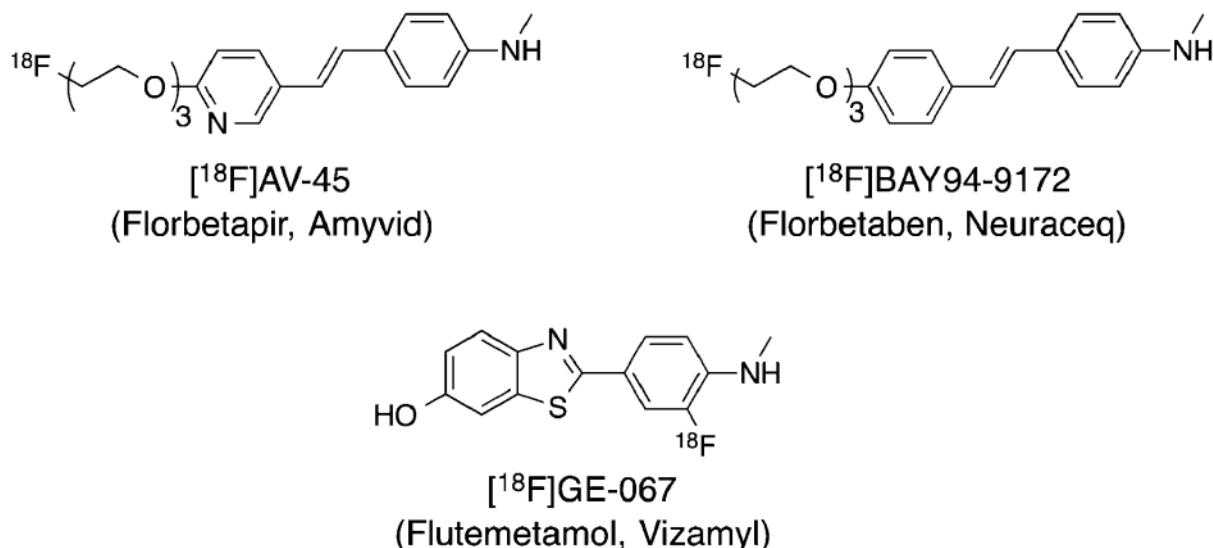
Figure 3.1: Chemical structures of the three FDA-approved ^{18}F-labeled amyloid-binding radio-pharmaceuticals.

binding to cortical β-amyloid plaques in living human subjects and high correlation with postmortem disease [32, 267, 136, 238, 235].

All these tracers rapidly enter the brain through passive diffusion of the BBB. They all reach the site at a very high rate that, however, is heavily dependent on the regional blood flow. The different chemical structures and properties of these agents cause an important source of variability in the extent of the amyloid load stained by the different tracers. Specifically, these differences affect the time that the agents spend in the white matter and the absorption in the gray matter. This means that while the high affinity binding to amyloid fibrils results in a much slower clearance from the amyloid plaques in the gray substance, clearance from the white substance depends on the degree to which non-specific low-affinity links occur.

The differences in chemical structures of tracers agents necessitate specific acquisition protocols and reader training [66, 90, 219]. Figure 3.4 summarizes the injection parameters of the fluorinated tracers recommended by the respective vendors.

Radiotracer	Recommended Dose/Activity	Uptake Time (min)	Acquisition Time (min)	Image Display	Number of Regions for Positive Scan
^{18}F-florbetapir	370 MBq (10 mCi)	30–50	10	Gray scale or inverse gray scale	Two, or only one if gray matter uptake exceeds white matter uptake
^{18}F-flutemetamol	185 MBq (5 mCi)	60–120	10–20	Rainbow color scale	One
^{18}F-florbetaben	300 MBq (8.1 mCi)	45–130	15–20	Gray scale or inverse gray scale	One

Figure 3.2: Guidelines for Performing Imaging and Interpreting Results for the three FDA-approved Radiopharmaceuticals for amyPET. Courtesy of Lundeen and colleagues [167].

3.2   Appropriate Use Criteria

Although the amyloid imaging represented one significant advance enabling clinicians and researchers to visualize in vivo deposition linked to AD, some major concerns about this methodology arose over years. Specifically it was reported: declining specificity in elderly [14] ethical concerns about the lack of disease-modifying therapies available for cognitively uninpaired patients, and concerns about possible overdiagnosis and lack of demonstrated cost-effectiveness [64].

To cope with these concerns, the Alzheimer's Association Amyloid Imaging Task Force and the SNMMI rallied up imaging and dementia specialists to establish the so called Appropriate Use Criteria (AUCr) to define for which patients and in which clinical scenarios in the amyloid PET is appropriate [136]. The AUCr were based on peer-reviewed, published literature to ascertain available evidence relevant. A brief review of these current guidelines is provided in this section. However, as dementia care, amyloid imaging and biomarker framework are in active development, to date, there is still debate on the appropriateness of these AUCr which are subject to periodic revisions [184, 100], critical reviews [7, 5] and appraisals [56, 225].

According to the AUCr, the amyPET is appropriate when the following conditions are met:

- A cognitive complaint with objectively confirmed impairment is present.

- Alzheimer's disease as a possible diagnosis, but when the diagnosis is uncertain after a comprehensive evaluation by a dementia expert.

- Knowledge of the presence or absence of amyloid-beta pathology is expected to increase diagnostic certainty and alter management.

According to the clinical indications for an appropriate diagnostic use of amyloid PET imaging, this examination is suggested for patients:

- With progressive or persistent unexplained mild cognitive impairment.

- Satisfying core clinical criteria for possible Alzheimer's disease because of unclear clinical presentation, either atypical clinical course or etiologically mixed presentation.

- With progressive dementia and atypically early age of onset (usually defined as 65 years or less in age).

Contrariwise, amyloid imaging is inappropriate:

- With patients with core clinical criteria for probable Alzheimer's disease with typical age of onset.

- To determine dementia severity.

- Solely based on a positive family history of dementia or presence of the apolipoprotein E gene (APOE4).

- With patients with a cognitive complaint that is unconfirmed on clinical examination.

- In lieu of genotyping for suspected autosomal mutation carriers.

- In asymptomatic individuals.

- For non-medical usage (e.g.: legal, insurance coverage, or employment screening).

3.3   Scan interpretation: the visual assessment

According to the AUCr, the administration of the tracer and the imaging procedure should be performed by qualified personnel that apply the FDA and EMA[1] recommendation for each agent. The clinical evaluation of the amyloid PET is performed with a visual inspection that can be complemented by quantitative analyses. The visual assessment provides a binary classification (i.e.: negative or positive) of the scan which is the current standard in both clinical and research settings. It assesses the contrast between the signal originated from white matter and the signal originated from the gray matter tissue.

The correct procedure for the visual assessment of an amyloid PET is described in the product labels of all the registered radiotracers [66, 90, 219]. According to the manufacturer's recommendations, the amyPET should be displayed in grayscale (or inverse grayscale) for ^{18}F-Florbetapir and ^{18}F-Florbetaben, and in rainbow color scale for ^{18}F-Flutemetamol.

Also an appropriate intensity reference should be used to facilitate the contrast assessment (for instance, for ^{18}F-Flutemetamol it is recommended to set the scale intensity at 80-90% in the pons region). Due to the off-target binding of the radiotracer in the white matter, in both positive and negative patients high uptake is present in correspondence of this tissue. Healthy control patients are characterized by relatively low levels of amyloid deposit in cortical gray matter. Thus, a typical negative scan presents high uptake only in correspondence of the white matter, and maintains high white / gray contrast in the whole brain. Conversely, the typical positive test exhibits areas of reduced contrast between the cortical gray matter uptake and that of the white matter.

Since the cerebellum does not accumulate amyloid until very late stages of the pathology [232], the contrast between white matter and gray matter is generally unaltered and kept as a reference.

The assessment is carried out on all lobes (temporal, occipital, frontal and parietal) generally by reviewing the axial images from inferior to superior with the cerebellum first to get a clear picture of the base contrast in the reference region. Coronal and sagittal sections are used to confirm the axial assessment and to carefully examine typical sites of accumulation in AD (i.e.: precuneus, cingulate posterior, lateral temporal, parietal and caudate nuclei). A scan with preservation of gray-white matter differentiation is labelled as Aβ negative. In contrast, a scan is evaluated as positive in the presence of a number of regions with an evident loss of contrast between white and gray matter. In figure 3.3 a real example of a positive and a negative scan.

As reported in figure 3.4, the number of affected cortical regions that define a positive scan differs among the radiotracers. Various imaging signs for each brain region are commonly used to distinguish between negative and positive scans. Most of these signs are applicable across the different radiotracers. A systematic integration of these

---

[1]EMA: The European Medicines Agency is an agency of the European Union in charge of the evaluation and supervision of medicinal products.
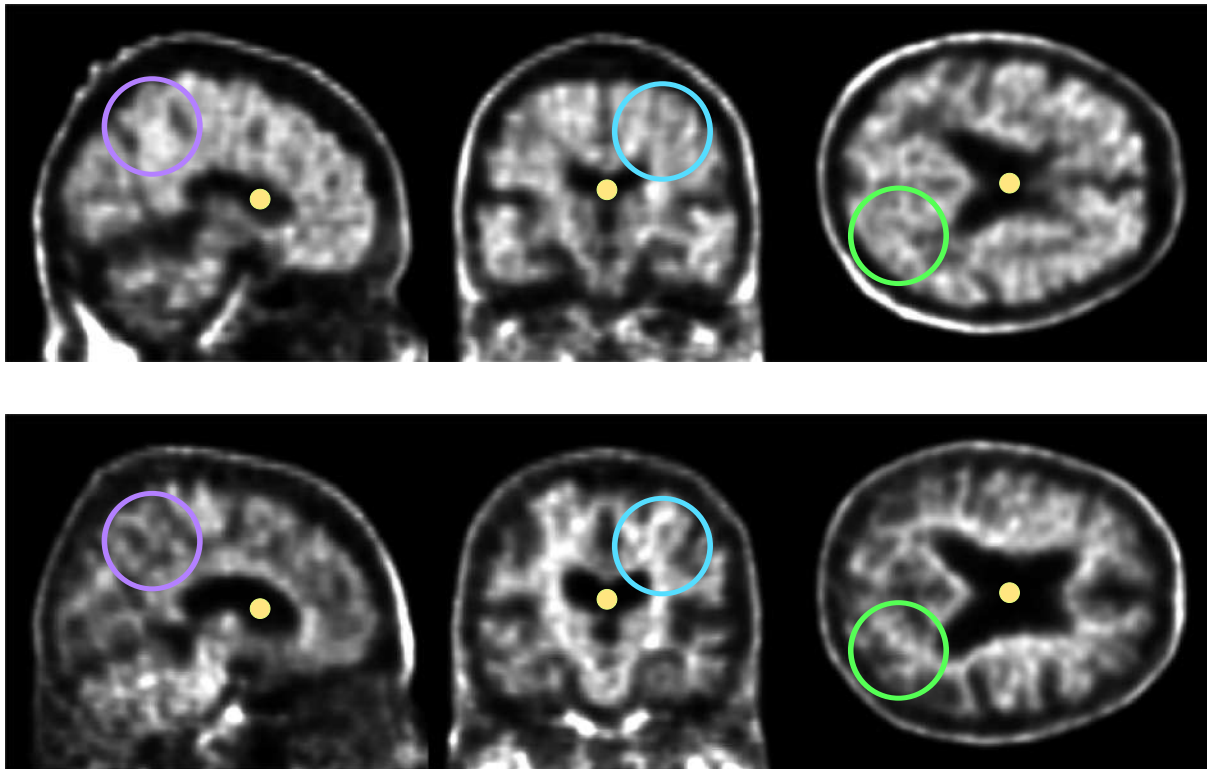
Figure 3.3: A positive (top) and a negative (bottom) scan. The encircled areas can help focusing on the contrast differences between white and gray matter signal in the two cases. In addition, different ventricular dilation can be pointed out (yellow dots). Orthogonal planes examination show the precuneus (purple), fronto-orbital (azure) and occipital (green) regions.

imaging signs during regional evaluation of amyloid PET scans facilitate scan interpretation [167].

In the temporal-occipital region of a negative scan, the white matter tracts create a "ridge" that can be observed on the axial view. Conversely, in a typical positive scan, the tracer binding in the gray matter on both sides of the white matter ridge smooths the edges resulting in a "plain" of tracer activity. Moreover, in a typical negative scan, the gray matter lining the medial aspects of the occipital lobes demonstrates absence of activity. Conversely, in the amyloid-positive brain, uptake of the gray matter permeates the midline, forming the so-called "kissing hemispheres" sign [167].

In the frontal lobe of a typical amyloid-negative scan, the radiotracer bind only to the frontal white matter resulting in the configuration of a "cartoon hand" on the axial view and of a "bare tree" on the coronal view. Moreover, in these scans the gray matter lining the medial aspects of the frontal lobes demonstrates absence of activity and configure a diamond shape that can be observed on the axial view. Contrarily, the addition of activity in the gray matter of an amyloid-positive brain fills in the space between the "fingers" of the "cartoon hand" making this sign disappear. Similarly, on the coronal view, the empty spaces between the "branches" is gradually filled up making the "bare tree" look like a "luxuriant tree" [167]. It should be highlighted that the appearance of these signs depends not only on the amyloid status, but also on the position of the section through the frontal or coronal region.

In the parietal region of a negative subject, the radiotracers binding to the white matter of the centrum semiovale creates a "double convex lens" sign on the axial view.

The effect of the amyloid deposition on this sign is a loss of the "double convex lens" that is replaced with a "kissing hemispheres" sign. A similar phenomenon occurs in the precuneus, where amyloid deposition seems to fill the interhemispheric fissure creating another "kissing hemispheres" sign. This effect is particularly relevant since the precuneus is one of the regions where the Aβ accumulation preferentially starts [271, 13, 69, 68, 93, 94, 104, 281]. Moreover, due to its thin dimension and location it is suggested to observe the precuneus in all three planes [167].

The last sign has been observed with the ^{18}F-Flutemetamol, which has frequently demonstrates striatal binding on positive scans. On the three views of a negative scan, lack of uptake in the striatum creates a "striatal gap" that is filled in positive scans ("striatal bridge") [167].

Figure 3.3 provides an overview of the most used signs organized by region.

3.3.1   Pitfalls and artifacts

Cortical atrophy is the most common confounding factor in amyloid PET. Due to the PVE, that averages the activity from thinned cortices and wider sulci, grey matter volume loss can be mistaken for lack of uptake in amyloid positive scans [244]. Thus, for a correct assessment of an amyloid PET, structural imaging (CT or MRI) is highly recommended to complement the visual reading with morphological information. This combined information is very useful also in patients whose brain anatomy is altered (i.e.: those with traumas, past neurosurgery, excessive ventricles dilatation or vascular complications) and the correct estimation of the signal is much more complicated.

In populations with cognitive disorders, motion artifacts can typically occur for many reasons such as lack of attention and concomitant movement disorders. These artifacts can reduce the accuracy by causing image blurring, misregistration between PET and structural imaging or errors in the attenuation correction [263]. In any case, technologists should check for possible artifacts and repeat the acquisition if necessary.

Finally, slight differences exist between the radiotracers in the non specific uptake of the white matter and in the clearance [244]. So, the clinicians should attend specific courses on radioligands they have to use.

Although visual reading and its dichotomic output is a fast and relatively simple procedure, there is a relevant fraction of cases where this qualitative approach is not trivial (from 10 to 30%, depending on the inclusion criteria) and results inadequate for a thorough interpretation [100].
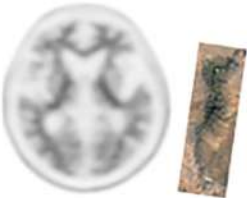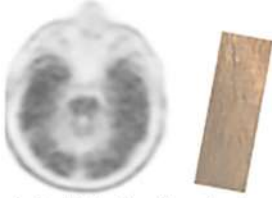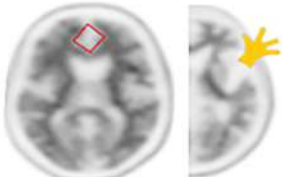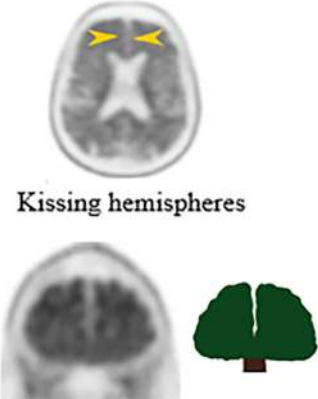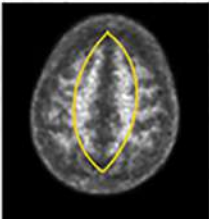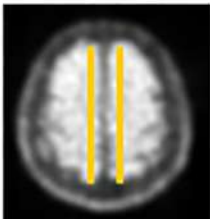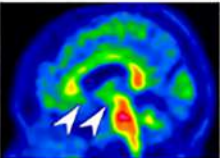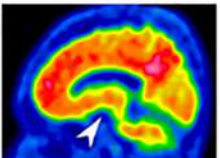
Cortical Region	Amyloid-negative	Amyloid-positive
Temporal/Occipital	Temporal Ridge	Occipital kissing hemispheres and temporal plain
Frontal	Diamond clear space and cartoon hand Tree in winter	Kissing hemispheres Tree in summer
Parietal	Double convex lens	Kissing hemispheres
Striatum	Striatal gap	Striatal bridge

Figure 3.4: Atlas of regional amyloid PET signs. Courtesy of Lundeen and colleagues [167].

3.4   Sex differences in amyloid PET

This section is based on Chapter 5 of the book published in 2021 *"Sex and Gender Differences in Alzheimer's Disease: The Women's Brain Project"* [76].

In this book a critical overview of the evidence documenting sex and gender differences in Alzheimer's disease neurobiology, biomarkers, clinical presentation, treatment, clinical trials and their outcomes, and socioeconomic impact on both patients and caregivers is provided.

Specifically, Chapter 5 offers a description of different imaging techniques used to assess sex-related brain differences, both in the healthy and in pathological aging: structural and functional MRI, perfusion SPECT (single-photon emission computed tomography), DAT-SPECT (dopamine transporter scan-SPECT), FDG PET, amyloid PET and tau PET. The aim is to provide the reader with an overview of the most recent findings coming from different studies, highlight the implications of these findings, and the limitation that need to be overcome in future neuroimaging studies. This chapter was co-authored with F. Massa, D. Arnaldi, M. Balma, M. Bauckneht, A. Chincarini, P. M. Ferraro, M. Grazzini, C. Lapucci, R. Meli, S. Morbelli, M. Pardini, S. Raffa, L. Roccatagliata and F.M. Nobili.

Gender differences in AD biomarkers have been suggested and investigated rather recently and they are starting to be explored systematically thanks to large, international initiatives [79]. However, sex differences in Aβ burden findings are controversial, and very few review studies are available to allow a comprehensive overview of the possible relationship between sex and the in-vivo measurement of amyloid load [75]. Sex-related differences are often found in literature as marginal analyses and there are comparatively few studies using in-vivo positron emission tomography (PET) analyses on AD subjects, whose target is the assessment of sex-dependent relationship with amyloid burden as specific factor.

To date, the main results that most studies report is that the prevalence of amyloid positivity is the same for men and women. Minimal, if any, sex differences have been found cross-sectionally in levels of global Aβ burden in clinically normal older adults [190, 4, 183, 24].

In clinically normal elderly individuals some studies have indicated no sex differences at all [129, 131], one study has demonstrated slightly higher uptake of PiB in men than women (males showing higher PiB uptake than females in the temporal and occipital lobes) [242], but two other reports have indicated higher PiB uptake in women than men [96, 270].

In MCI patients, no clear sex differences in Aβ burden have been reported. A meta-analysis of PET studies revealed no sex differences in amyloid positivity among individuals with subjective cognitive impairment (SCI), amnestic or non amestic MCI [134]. A similar meta-analysis to investigate patients with AD is currently lacking, however, post-mortem studies of AD subjects suggests that there is no sex difference in the occurrence or distribution of Aβ plaques [11].

Similarly, sex seems to have no impact on CSF concentrations of Aβ in living patients with AD dementia, people with prodromal AD or cognitively normal individuals [176, 112].

Some authors suggest that sex differences may be more likely to appear downstream after the onset of Aβ accumulation [111, 272]. This hypothesis has found some traction

in a study comparing age, sex, and APOE ϵ4 effects on memory, brain structure, and amyloid PET (PiB radiotracer) in cognitively normal individuals aged 30 to 95 years old [129].

One of the few studies directly tackling the gender difference in AD using imaging biomarkers found significantly higher accumulation of in vivo brain amyloid load in the anterior cingulate cortex in men than in women [36]. In this study, in spite of equal levels of global intact cognition and after controlling for age, educational level, and clinical comorbidities, men compared with women showed more pronounced amyloid load, neurodegeneration, and reduced functional connectivity in the default mode network. These findings suggest that men may have higher brain resilience to pathophysiological processes of AD than women.

On the same line of reasoning, Pike and colleagues [217] concludes that while there are no known sex-dependent physicochemical/biological differences in the human brain that would explain why women seem more prone to get AD, women have more notable cognitive impairment than men with a smaller amyloid burden, suggesting that they might be more susceptible to suffer the other or more downstream events of AD pathophysiology. This also implies that other factors than the brain amyloid load alone can have pivotal roles in an individual's clinical outcome.

This subtle evidence favoring elderly men in having comparatively lower impairment with a similar Aβ burden than women could be linked to the menopausal stage [190] and parental family history [280].

Conversely, in one of the few studies focused on the examination of the relative contribution of various factors and the effect of their interactions on the accumulation of regional cortical amyloid, it was found that the effect of gender was marginally significant (p=.03) with women showing higher SUVrs (which is a quantitative approach for the PET scans anaylsis, see Section 4.2) than men [192]. On the same line, other findings suggest that - while sex differences in amyloid PET were not significant - women trended toward greater β-amyloid beyond age 70 years [129], and the same trend toward slightly higher median Aβ values in elderly women was observed by Oveisgharan et al [206] and in a similar 2019 study [25].

In spite of the lack of a clear significant sex differences in PET at any age - both for amyloid-negative and amyloid-positive subjects - differences were present in memory (beginning at age 40 years) well before abnormal amyloid PET first appeared in the population. One study found that there was a trend for a gender × amyloid burden interaction (p = .062) with episodic memory, and a significant gender × amyloid burden interaction with visuo-spatial functions [217].

Interestingly, no study found association between sex and APOE genotype, a result independently found by Jack et al. [129] and Jansen and colleagues [134], and later confirmed by Cavedo et al. [36].

The lack of consensus and of significant effects might suggest that sex does not moderate the effect of amyloid on the volumetric, metabolic, and functional imaging marker of AD, and thus the effect of sex seems independent on the amyloid status. Other explanations of the discrepancies between publications could be the result of differences in study designs, sample sizes and ages of individuals included in the study. Indeed, the findings of modest interaction effect of amyloid burden with cognitive performance might help in clarifying the discrepancies, suggesting that sample composition - particularly gender, cognitive level and the number of positive cases - may determine whether a relationship between amyloid burden and sex is found.

While conclusive evidence on gender difference in concentrations of Aβ is still lacking, this might also be due to a comparatively lesser number of studies specifically investigating this difference. In most studies of biomarkers, results are adjusted for age and sex, thereby hindering examination of sex differences.

Chapter 4

Quantitative assessment

Visual interpretation is the de facto standard assessment in clinical practice. However, due to its subjective nature, this approach suffers from many limitations including inter- and intra-observer variability.

Quantitative approaches have been developed to extract numerical estimates of the parameters linked to the physiological processes of interest, and therefore of the quantity of radioligand bound to target tissues. After the injection, the radiotracer can be detected in several bound states in proportions that depend on the pharmacokinetics. At any time of the acquisition, the PET intensity is a mix of overlapping signals: mathematical models of the tracer kinetic are needed to isolate the desired signal component (in amyloid PET, it is the tracer bound to the aggregates of $A\beta$).

In these mathematical representations, each component is modeled by a compartment. The quantification (or absolute quantification) derived with compartmental models represents the ideal method for the in vivo measurement of the specific binding of a PET tracer and is the current gold standard for quantitative approaches.

Simplified approaches have been developed for the PET analysis: these so-called semi-quantitative methods represent leaner, but less accurate, alternatives that can be easily integrated into clinical practice. Current clinical PET guidelines are pushing for the usage of semi-quantitative metrics. Although simple and practical for use in the clinic, semi-quantitative metrics are subject to a number of approximations implicit in the use of uptake ratios that may also lead to variability and bias. As such, their use for robust disease monitoring and assessment of treatment response as well as in clinical trials requires standardization of PET quantification techniques to enable pooling data across different facilities or scanners using different data acquisition and reconstruction protocols.

The correct use of quantitative approaches for the assessment of amyloid PET assumes an ethical value particularly in view of the possible near introduction of anti-amyloid drugs to reduce the number of patients in trials, radiation exposure, to identify the patients who would benefit from the intervention and for therapy monitoring [261, 146].

4.1   Compartimental modeling

The compartmental models are used to describe systems that vary in time but not in space. Applied to PET imaging, these models provide a quantitative description of the uptake and of the clearance of tracers in tissues [122, 283].

According to the well-mixed assumption, in these models no spatial concentration gradients are assumed within the sampled area (e,g.: a voxel in a 3-D image such as the amyloid PET). In this area it is assumed that every radioactive species that contributes to the resulting signal is in uniform concentration and characterized as a single state. Each state is modeled as a compartment described by an ordinary differential equation. Overall, these compartments model the pharmacokinetic of the tracer. The input of this system is the radioactivity concentration in blood-plasma in an artery measured over time: the arterial input function (AIF). The AIF can be derived with invasive continuous (or discrete) arterial sampling [70], with population-based AIF or with an image-derived AIF [194, 256].

These models require a dynamic scan acquired as a time-series of 3-D images starting from the tracer injection until the concentration reaches an equilibrium. A typical dynamic scan contains the few minutes that occur after the injection where the PET signal is dominated by the blood flow. The subsequent frames represent the transition from a non-equilibrium situation, during which the specific tracer binding approaches a plateau, to an equilibrium state. The time required to achieve equilibrium depends on the tracer kinetic, the regional blood flow and the target physiological process. A dynamic acquisition allows to measure the time-activity curve, that is the trend of the radioactivity signal in every point [244]. By knowing the activity concentration in the blood and its temporal trend it is possible to solve the system of differential equations which characterizes the flow among the compartments.

In a typical compartmental model three states are represented: a free compartment, in which the tracer has passed the BBB, but is not yet bound, a compartment, in which the tracer is stick to the amyloid aggregates and a compartment in which the tracer is bound, but not to the desired target (non specific binding). Each compartment is characterized by the concentration of the tracer as a function of time. In figure 4.1 a representation of possible time-activity curves in modeled compartments.
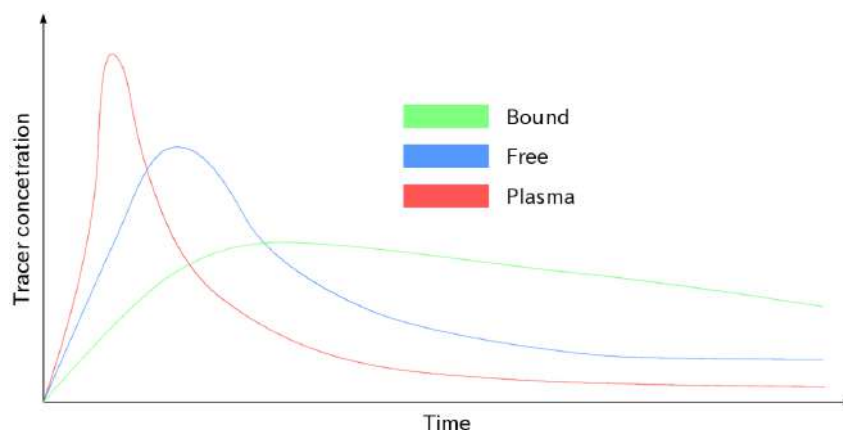
Figure 4.1: Qualitative representation of the time-activity curves in three compartments representing: the bound, the plasma concentration (used in the AIF) and the non-specific binding.

Among different compartments the tracer molecules are free to move with rates that are described by constants that describe, per unit of time, the fraction of molecules moving from one compartment to another. Thus, it is possible to connect concentrations from a compartment to each other by ordinary differential equations that express the balance between the tracer mass entering and leaving each compartment. By solving these equations it is possible to determine the quantities of interest. Radioactive decay is generally

neglected in these models. In figure 4.2 a typical representation of a compartmental model is provided.
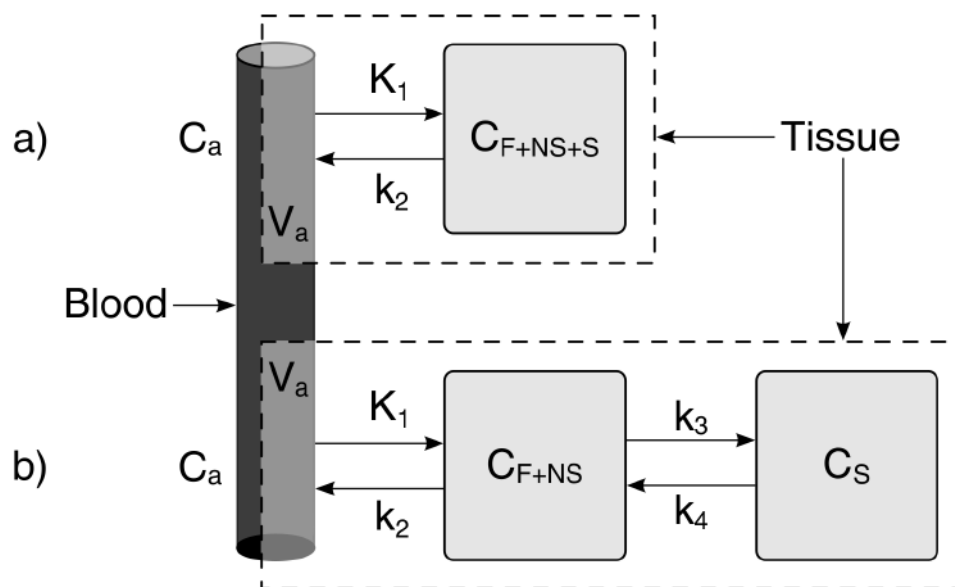
Figure 4.2: Examples of comparmental models: a one-tissue model (a) and a two-tissue model (b). The two models comprise the time course of tracer concentration in arterial blood plasma (C_a), free and non-specific tracer in tissue (C_{F+NS}), specific-bounded tracer in tissue (C_S), and the fraction of arterial blood in the tissue (V_a). K_1, k_2, k_3 and k_4 are the rate constants describing the rate of tracer exchange between contiguous comparments. Courtesy of Häggström and colleagues [118].

Since the compartment model best describes the states of the radiotracer, from the site of administration to the molecular target, the quantification (or absolute quantification) provided is considered the ideal method for the in vivo measurement of the specific binding of a PET tracer to the molecular target.

4.1.1 Limitations

Obtaining arterial blood samples is difficult and invasive. Moreover, the complex imaging and analysis protocol requires longer acquisitions (from 60 to 90 minutes long, depending on the tracer) which increase the patient discomfort and the possibility of motion artifacts. Considering all these points, the absolute quantification in clinical routine is rather impractical and may be impossible for specific patient groups. Other difficulties come from the modelization of the compartments, which requires a full characterization of the in vivo pharmacokinetic profile of the radiotracer.

Consequently, simplified methods have been proposed in the hope that accurate quantitative results can be obtained with no need for arterial sampling or complex mathematical modeling. These approaches involve the reduction of the PET acquisition duration and the use of the input function obtained from region delineated on the PET images, in the internal carotid artery making the arterial sampling superfluous. However, these simplified approaches must be validated against the full compartmental models to confirm their accuracy taking into account the biases introduced by each simplification [1, 119].

4.2   Semi-quantitative approaches

Alternative approaches to absolute quantification have been developed to estimate the activity of tissues in a PET acquisition with no need of arterial input or complex mathematical models: the semi-quantitative methods. These simplified approaches are typically based on a static scan that is a single acquisition lasting about 20 minutes that starts after a relatively long time after the injection. This delay depends on the tracer, and generally it lasts more than 40 minutes. Static scans are easier to acquire, less expensive and minimizes the amount of time that the patient needs to lie still into the scanner, thus reducing the discomfort and the possibility of motion artifacts.

The Standardized Uptake Value (SUV) is a widespread simple image-based method defined as:

$$SUV = \frac{C_{ROI}}{A/W} \tag{4.1}$$

It represents the tracer uptake in a region of interest measured by a calibrated PET scanner (C_{ROI}) normalized to the injected dose (A, expressed in MBq) and to a measure of the volume of distribution (W, usually total body weight) [118]. When computing the SUV, the average or the maximum activity in the region of interest are the most conventional choices.

Many physiologic and technical factors affect the outcome of the SUV. The most common are: the scanner calibration, the effective administered dose, the acquisition time, the presence of artifacts, the image reconstruction parameters, the ROI definition and placement and other inconsistencies [19]. Besides undermining the reliability of the results, these factors can lead to substantial differences in SUV outcomes among sites, therefore, strict standardization of the procedure is of utmost importance [19].

This dimensionless ratio was historically used in oncology by nuclear medicine professionals to assess lesion malignancy in a ^{18}F-FDG PET examination [19, 166].

SUVr definition

The ratio between two SUVs is called Standardized Uptake Value ratio (SUVr) and is used to compare the activity of a target region with respect to a reference region. It is simply:

$$SUVr = \frac{SUV_{target}}{SUV_{reference}} \tag{4.2}$$

The target region is the one that exhibits the physiological or biochemical process of interest (e.g.: an area expected to accumulate amyloid, a tumor). Conversely, the reference region is usually selected among those that do not exhibit specific tracer binding, and so it can be considered as not affected by the pathology under scrutiny.

The SUVr is the most extensively semi-quantitative approach in the assessment of the cerebral amyloid load [143, 48, 57, 17, 289, 265, 260]. In figure 4.3 an example of target and reference ROIs drawn on a typical positive and negatve amyloid PET.

Target region

In amyloid PET, according to the clinical evaluation guidelines, the target ROIs are commonly placed in cortical areas showing the greatest tracer retention and consistently

31
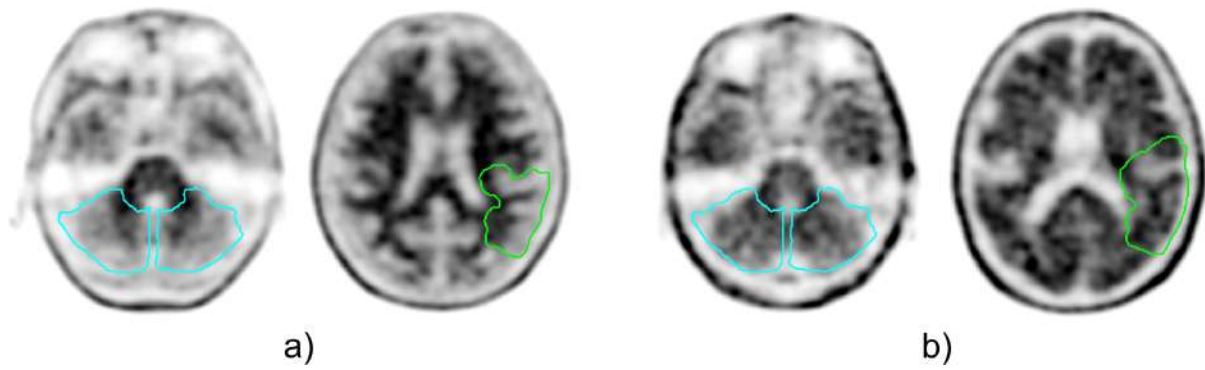
Figure 4.3: Axial sections of two typical amyloid PET: a negative (a) and a positive (b) scan. Cyan lines enclose the reference region for the SUVr calculation (cerebellum). The target region are bounded by green lines.

with pathologic studies of amyloid accumulation [297, 22, 259]. These regions typically include: cortical frontal, lateral temporal and parietal, anterior and posterior cingulate, precuneus. A composite simplified measure is often calculated by averaging the uptake of these regions. Occipital cortex can be also included [228]. Moreover, as anti-amyloid clinical trials move to the early stages of the pathology, some regions has been taken into consideration as they may provide a sensitive marker of early deposition [220, 101, 27]. Methods to correct for atrophy and white matter spillover may play a role as they reduce the portion of target anatomic region [292]. Thus, selecting the most appropriate brain region highly depends on the hypotheses being tested and on the methods to reduce the influence of confounding factors.

Reference region

The choice of the most appropriate reference region is still a matter of debate [244, 28, 45]. It represents one of the most critical factors affecting the quantitative assessment of β-amyloid since it can lead to an overestimation or an underestimation of the SUVr of each region considered in the analysis of a scan. In longitudinal studies, where modest changes in amyloid load is plausible, aslo small variations induced by the reference tissue choice can generate significant variability in the SUVr values, and therefore an inaccurate understanding of the pathology progression [28, 18]. A suitable reference region should be Aβ free and have the same non-displaceable activity as the target area. Several regions fulfill these requirements, but the selection depends on many considerations including the used tracer, the reliability in region delineation, the presence of artifacts and the analysis protocol in case of comparison with other sites. The cerebellar cortex was the first reference region in studies with PiB because of its presumed lack of Aβ plaques [142]. However, the cerebellum (particularly its gray matter) is highly vulnerable to fluctuations due to its proximity to the edge of the scanner FOV where noise and truncation are more likely to occur [149]. Moreover, imaging studies confirmed that the cerebellum may also accumulate Aβ in late-stages of the disease and in some types of familial AD [34, 144]. By including the white matter one may have less susceptibility to noise including tissue less vulnerable to edge and truncation effects [244]. Thus, the whole cerebellum is considered a more stable reference region. Indeed, it was used for the Centiloid project, which is, to date, the most convincing standardization effort for amyloid PET semi-quantification [143]. A possible alternative to the cerebellum is rep-

resented by the pons. This region displays high uptake due to non-specific binding and amyloid depositions occur in the very late stages of the pathology [259]. Due to its placement, the pons is less vulnerable to edge noise and truncation. However, its small volume makes it particularly sensitive to head motion and to delineation error [244]. The subcortical white matter has been proposed since it does not accumulate amyloid. Compared to the cerebellum, It showed more stability (particularly in longitudinal studies), it is a larger region over which to average the signal, potentially leading to less noise and it is potentially located in the same plane as cortical target regions and making the results less susceptible to differences in scatter correction across planes [244, 149, 40, 165]. However, there is no consensus on which region should be considered and how it should be delineated in order to mitigate the effect of the cortical signal spillover. Since the whole cerebellum is less prone to segmentation error than the selection of cerebellum gray matter or pons alone [244], in this study the SUVr was calculated by using the whole cerebellum as a reference region (see figure 4.3).

4.2.1   Strengths and weaknesses

Despite its simplifications that make it feasible for clinical use, the SUVr in amyloid PET shows a general good agreement with both tracer kinetic models [289, 91] and histopathological features of β-amyloid deposits [155, 120]. Moreover, many studies have shown high agreement of SUVr with cerebrospinal fluid assessment [213], and the image assessment stemming from a thresholded SUVr has proven to be comparable with visual assessment [260]. However, the SUVr dichotomization is strictly related to the chosen cutoff, which in turn heavily depends on the tracer, on the image acquisition, on the analysis protocol, on the population discrimination approach [244]. Different thresholds have been proposed based on the comparison with histopathological findings [47], on class separation between diagnostic groups [188] or by defining amyloid negative standards using healthy individuals in their early adulthood [81].

The comparison across sites of SUVr results has been an important issue since the very beginning. Its heterogeneity is due to many factors, including differences in binding properties of tracers, acquisition time duration, image reconstruction protocol, method of analysis, target and reference regions employed and partial volume correction (of lack thereof). All these factors have a significant impact on the actual calculated values [244].

The unique physical and chemical characteristics of each tracer affect the gray versus white matter uptake and tracer retention. Thus, these characteristics affect the SUVr results (even when using the same reference ROI) and may compromise the comparability particularly at regional level [148, 151]. In this study we have proposed a model to map the SUVr results from a fluorinated tracers onto another (see Chapter 6).

The use of PVE to correct the spillover of high uptake white matter in the cortical region represents another source of variability. In absence of corrections, this effect leads to overestimation of SUVr values, especially in those subjects with low amyloid load and significant atrophy [244].

Among the other, the acquisition timing is an important parameter in the SUVr measurement. The acquisition should be performed when the balance between uptake and clearance of the tracer in target tissues has been reached. This timing depends on the characteristics of the tracer which is typically about 40 minutes after the administration. Studies suggest that delayed measurements result in significant variances of SUVr that can be overestimated [196, 265]. This aspect is particularly critical in multicentric

studies in case of unshared acquisition protocol.

The most considerable attempt for standardisation of amyloid PET SUVr was the already mentioned Centiloid project [143]. This project aims to derive a standardised quantitative amyloid imaging measurement scale. This scale ranges beyond an "anchor-point" set to 0, representing young healthy controls, and 100, representing the amyloid burden present in average mild to moderate severity dementia due to AD. To let the center map their own results onto the same scale, Klunk and colleagues have made the dataset used for defining the Centiloid scale publicly available. Further studies are required to assess the comparability of Centiloid values derived from different analysis pipelines and different acquisition settings and what impact will the Centiloid have on both cross-sectional and longitudinal studies [255]. However, this harmonized method has great potential to produce cohesive and comparable results from clinics across the world.

Some remarks regard the accurate image registration and segmentation of the cortical and reference ROIs and the use of SUVr in longitudinal studies. Registering or aligning images is, in general, a necessary step for the SUVr calculation. Spatial normalization is calculated to map the reference atlas to each individual image allowing using the same region of interest for each scan under evaluation. Although many tools and libraries have been developed for image mapping [140, 168, 9], the registration can fail. Thus, visual inspection is often a recommended step to verify the correct alignment.

The ROI placement and segmentation can be a non-trivial task due to the possible template choice, the image quality and reconstruction parameters, and the transformation used to implement the registration. Analyses are prone to errors due to the PVE when using pre-defined ROIs, particularly on the small cortical regions.

Longitudinal amyloid PET studies suggest that the SUVr is impaired by multiple factors. In these studies, where changes in amyloid burden was expected to be modest due to the relatively short time window, the variability of the signal in the reference region generated significant shifts in SUVr value [244, 265]. Moreover, variability in regional blood flow causes considerable uncertainty and underestimation in the SUVr values and significant decrease in amyloid load in patients undergoing no therapy [265]. Indeed, the uptake and clearance of the tracer are strictly related to the blood flow that depends not only on the type of tissue, but also on the advanced neurodegeneration [296]. These issues are so relevant that some authors suggest avoiding longitudinal analysis with SUVr [274].

4.3   SUVr-independent approaches

To overcome some of the limitations of the SUVr and its constraints (such as the need for accurate image registration or predefined ROIs), several SUVr-independent semi-quantification approaches have been developed exploiting different features of the acquisition. Some methods exploit geometric features [43] or texture features [30] to provide quantitative global indices of Aβ deposition with no need of a reference region. Another innovative approach uses deep learning networks to remove the non-specific uptake map from the Aβ load measurement substantially improving amyloid PET accuracy [161]. Similarly, a novel global index of the amyloid burden is obtained by regressing the SUVr of a static scan for the non-specific binding image and a carrying capacity canonic image [285]. Up to now, the most sophisticated semi-quantitative approach that takes

into account the widest spectrum of confounding factors (including correction for atrophy, spillover and blood flow) was developed by Cecchin and colleagues [37]. It requires a dual time point PET/MRI acquisition, full cortical segmentation and the creation of a patient-specific brain atlas.

Since the variability in regional blood flow causes considerable uncertainty in the SUVr, we have developed and validated a semi-quantitative approach, called Time Delayed ratio (TDr) that allows for a blood flux correction (see Chapter 7).

4.3.1 The ELBA method

In the studies described in the Chapters 6, 7, 8 and 9 a SUVr-independent semi-quantitative method named Evaluation of Brain Amyloidosis (ELBA) [43] has been extensively used for both global and regional analyses. Thus, in this section a brief description of this method is provided.

The score provided by ELBA showed excellent agreement with SUVr, clinical evaluation and cerebro-spinal fluid measurement. Moreover, it has ranking characteristics proven both on cross-sectional and longitudinal analyses [43].

It was developed and tested on scans from the ADNI[1] database acquired with ^{18}F-Florbetapir. The intent of ELBA is to capture intensity distribution patterns rather than actual counts in a target ROIs. Considering the brain as a whole, the geometrical appearances of iso-intensity surfaces are rather characteristic in typical negative and positive subjects, the latter showing a sparser and more convoluted appearance than the former. Moreover, intensity distributions appear to be skewed towards higher intensities in positive subjects. In figure 4.4, a graphical representation of the ELBA method.

To capture and quantify these characteristics two features were developed by Chincarini and colleagues: one that gauges the iso-intensity surface complexity and another that assesses the histogram propensity towards higher values. These features, named geometric and intensity feature, represent global properties of the brain and do not require a reference region, they are combined in a single score.

In each study described in the Chapters 6, 7, 8 and 9 the ELBA method has been automated and applied to amyloid PET that were first mapped onto the MNI space[2]. The analysis procedure developed does not need any human supervision save for an optional check after the spatial registration process, to ensure that the processed image is consistent and has acceptable characteristics.

Geometric feature

The selected target brain volume is divided into a number of iso-intensity levels (n_L = 48) $0 < l_j < 1$, j = 1..n_L. These levels are taken at equal quantile distances of the whole intensity distribution (i.e.: n_L quantiles in the interval [1 - $1/n_L$ n_L]). To ensure adequate sampling of the intensity distribution the number of levels was set to 10 is of little importance, as long as it is ≥ 10.

Partitions consist of s_j surfaces and V_j enveloped volumes defined as:

---

[1]ADNI: Alzheimer's Disease Neuroimaging Initiative is a multisite study that aims to improve clinical trials for the prevention and treatment of Alzheimer's disease; its cohort is one of the largest public clinical dataset of AD data. It comprises clinical information about each subject including recruitment, demographics, physical examinations, and cognitive assessment data.

[2]MNI space: Is a 3-D coordinate system used to map the location of brain structures or activity in a standardized space, it was developed by the Montreal Neurological Institute.
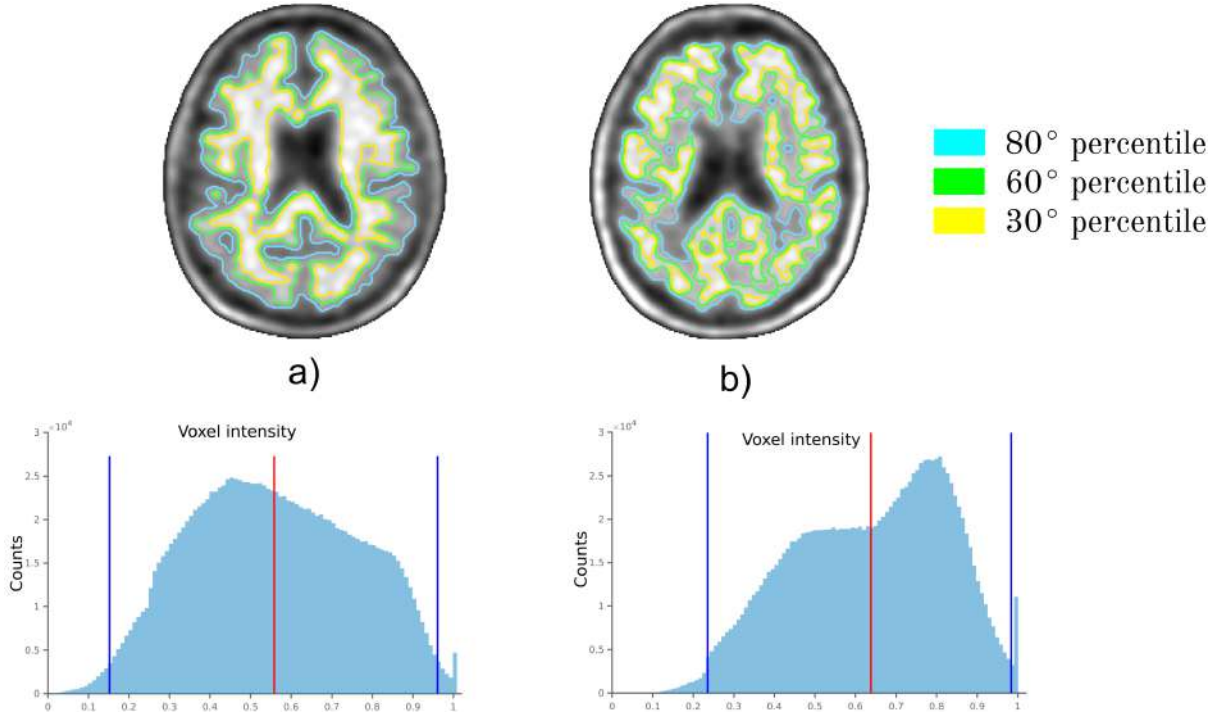
Figure 4.4: Iso-intensity curves in axial projection of a typical negative (a) and positive (b) case. The Curves are related to three percentile values of intensity counts within the brain: 0.2 (cyan), 0.4 (green) and 0.7 (yellow). Each histogram describes the brain intensity distribution in each amyloid PET.

$$V_j = \{number\ of\ voxels\ \in\ volume\ of\ interest,\ voxel\ intensity \geq l_j\} s_j = 1 \qquad (4.3)$$

$$s_j = \sum_{\partial V_j} 1 \qquad (4.4)$$

Where the ∂ symbol represents the boundary, that is s_j counts the number of voxels of the perimeter. The s_j and the enveloped volumes V_j are not required to be a connected set. Each partition is characterized by two numbers: one representing the radius $r_j{}^s$ of an equivalent sphere having the same surface extent as s_j, and another is the radius $r_j{}^v$ of the equivalent sphere of volume V_j, that is:

$$r_j{}^s = \left(\frac{s_j}{4\pi}\right)^{\frac{1}{2}} \qquad (4.5)$$

and

$$r_j{}^v = \left(\frac{3V_j}{4\pi}\right)^{\frac{1}{3}} \qquad (4.6)$$

If $r_j{}^v$ and $r_j{}^s$ are plotted for all j = 1, .., n_L on a cartesian plane ther result is a characteristic curve inferiorly bounded by the bisector line $r^v = r^s$, which is the limit for all s_j being actual spheres. The characteristic curve distances itself from the bisector line the most when the s_j is rough and notched.

By subtracting the bisector line, typically positive scans show a higher surface-to-volume ratio on the higher intensity levels (low r^v) with respect to the lower intensity levels (high r^v). The characteristic curve is integrated without the bisector area on the

lower and higher half of its domain D (i.e.: the range of r^v) to deliver the geometric feature G_i:

$$G_i = \frac{\int_{D_1}(r^s(r) - r)dr}{\int_{D_2}(r^s(r) - r)dr} \qquad (4.7)$$

Where $D_1 = [\min(r^v) \; r^v/2]$ and $D_2 = [r^v/2 \; \min(r^v)]$.

Intensity feature

This feature determines the intensity and contrast values in the volume of interest and divides them into clusters thanks to the k-means clustering method (two classes: High and Low). The k-means uses an iterative algorithm starting form a random sample, to ensure reproducibility and robustness it was repeted for 10 times. then the one with minimum within-cluster sums of point-to-centroid distances was chosen.

In each class the number of elements K_{High} and K_{Low} and the class median intensity value I_{High}, I_{Low} were computed. The intensity histogram is linearly scaled so that the values corresponding to the 1% and the 99% percentiles are mapped onto the interval [0 1]. Then the intensity feature C_i is defined as:

$$C_i = ln(\frac{K_{High}}{K_{Low}} \frac{I_{High}}{I_{Low}}) \qquad (4.8)$$

The intensity feature modulates the relative number of elements in the classes with their contrast. As in the geometric feature, this formulation is expressed as a ratio too, so that both features are internally (intra-subject) normalized.

ELBA score

The two features G_i and C_i were used to fit a quadratic polynomial. Each point of this quadratic model can be projected onto the curve providing new coordinates: a curvilinear abscissa x_c (arc lenght) and a curvilinear ordinate y_c (see figure 4.5).

The ELBA score is x_c after a linear scaling and a shift to conveniently place the origin at the cut-off between negative and positive scans. It was merely a way to combine information on the geometrical distribution of PET counts in the brain and information on the contrast between the brightest and darkest intensity components.

The ELBA score is blind to the subject age or clinical status.

ELBA validation

ELBA was tested on 504 scans from the ADNI cohort. It provided excellent agreement with visual assessment (AUC = 0.99, accuracy = 0.97) and strong correlation with cortico-cerebellar SUVr ($\rho = 0.86$, p $< 10^{-4}$). To provide a more robust validation, ELBA was also compared with CSF Aβ. Concordance between ELBA score and CSF score classification was observed in 90.6% of istances and the accuracy was comparable (ELBA = 0.91, CSF = 0.9). In longitudinal data, ELBA showed higher sensitivity with respect of SUVr to amyloid deposition even in a relatively short time span (48 months).
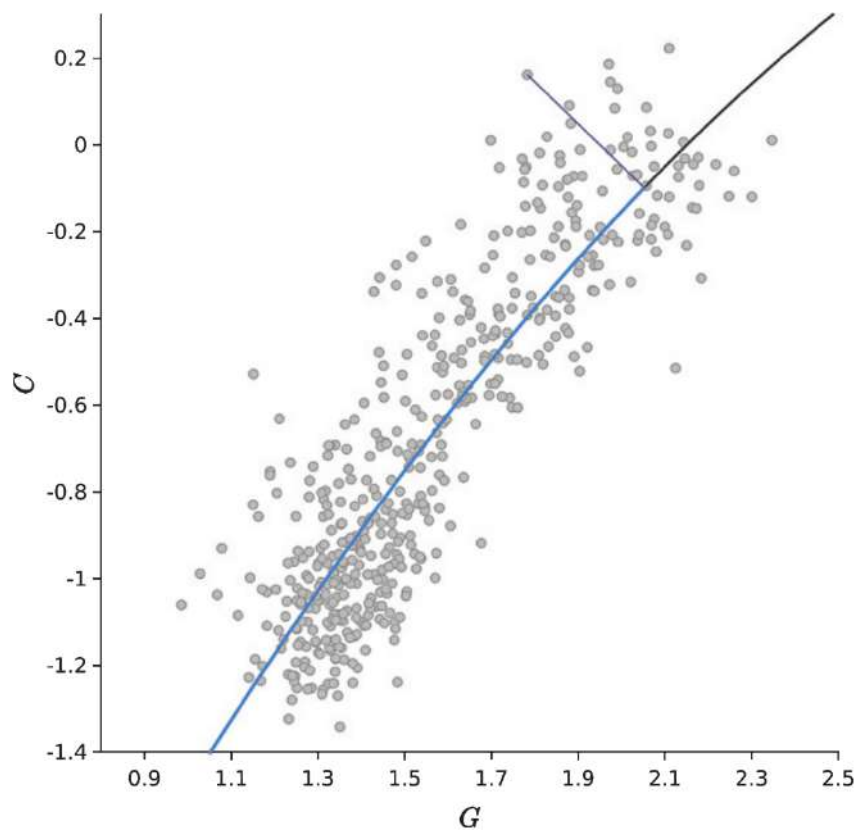
Figure 4.5: Intensity feature C vs. geometric feature G. The black line is the quadratic model. For each scan (dots) the blue part of the line represents the curvilinear abscissa x_c (arc length), and the perpendicular line is the curvilinear ordinate y_c. Courtesy of Chincarini and colleagues [43].

Chapter 5

Activities overview

This chapter summarises the studies carried out in the framework of amyloid PET semi-quantification: from the investigation of technical and clinical aspects, to the development and the comparison of advanced approaches.

5.1 Study I: semi-quantification and grading

Chapter 6 is based on the paper published in Neuroimage: Clinical in 2019 titled *"Semi-quantification and grading of amyloid PET: A project of the European Alzheimer Disease Consortium (EADC)"* [42]. This paper was co-authored with A. Chincarini, S. Morbelli, M. Pardini, M. Bauckneht, J. Arbizu, M. Castelo-Branco, K.A. Büsing, A. de Mendonça, M. Didic, M. Dottorini, S. Engelborghs, C. Ferrarese, G.B. Frisoni, V. Garibotto, E. Guedj, L. Hausner, J. Hugon, J. Verhaeghe, P. Mecocci, M. Musarra, M. Queneau, M. Riverol, I. Santana, U.P. Guerra and F.M. Nobili.

The study stems from the EADC project EAPP2[1]. The EADC (European Alzheimer's Disease Consortium) is a network of over 50 European clinical and research sites of excellence working in the field of AD and related dementias. The primary goal of this consortium is to develop and maintain an organisational structure capable of rapidly carrying outrivals of interventions designed to prevent, slow or ameliorate the primary and secondary symptoms of Alzheimer's disease and to increase the basic scientific understanding of this pathology. This will be done by facilitating large pan-European multidisciplinary wide research studies. Funding for the original realisation of this network was received from the European Commission which supported work towards standardisation of diagnostic criteria, assessment tools and data collection methods, with a view to this being followed by a trial period involving the testing and practical application of the tools agreed.

In this context, the EAPP2 is aimed at joining together amyloid PET scans with corresponding clinical and neuropsychological data from subjects attending a memory clinic of one of the EADC centers. This will help establish frameworks for investigating the amyPET use in clinics in the diagnostic of AD, looking at two main aspects. The first is related to technical issues that can arise in the use of amyPET in clinical routine, such as the choice of an appropriate semi-quantification method, its application to dif-

---

[1]EADC-PET 2.0: Further information about this project is available on the institutional website http://www.eadc.info.

ferent radiotracers, the dichotomous outcome of the visual assesment, the comparison of multiple-reader visual evaluations and scans quality issues. The second aspect is more clinical-related and has to do with the investigation of the relationship between cognition and amyloid burden; especially the prognostic aspects. The aim is to clarify the amount of Aβ and the brain regions that are more meaningful or apt to predict the clinical outcome.

In this study we tried to answer to some of the most technical aspects. In clinical routine, as reported in Section 3.3, the amyloid PET reading is being implemented as a binary assessment although the clinical experience has shown that the number of borderline cases is non negligible not only in epidemiological studies of asymptomatic subjects but also in naturalistic groups of symptomatic patients attending memory clinics. Data from 175 patients acquired with three fluorinated tracers were retrospectively enrolled. The scans were visually classified (with both a binary and a 5-step grading) and the semi-quantified with SUVr and ELBA. The readers accord and inconsistencies in the visual assessment were measuerd, and a model to compare and integrate visual reading with SUVr and ELBA was developed in order to obrain a tracer-independent multi-parametric evaluation. It was possible to map the quantification results across different tracers without resorting to ad-hoc acquired cases. Moreover cut-offs and transition regions were delivered and resulted largely independent from the population. Finally, all fluorinated tracers appeared to have the same contrast and discrimination ability with respect to the negative-to-positive grading; this is an interesting result as there is not much literature comparing all fluorinated tracers by the same set of readers and quantifiers. All these findings together validated the integration of both visual reading and different quantifiers in a more robust framework thus bridging the gap between a binary and a user-independent continuous scale.

5.2   Study II: the Time Delayed ratio

Chapter 7 is based on the paper published in the European Journal of Nuclear Medicine and Molecular Imaging in 2020 titled *"A kinetics-based approach to amyloid PET semi-quantification"* [41]. This paper was co-authored with A. Chincarini, M. Corosu, S. Morbelli, M. Bauckneht, S. Capitanio, M. Pardini, D. Arnaldi, C. Vellani, D. D'Ambrosio, V. Garibotto, F. Assal, B. Paghera, G. Savelli, A. Stefanelli, U.P. Guerra and F.M. Nobili.

Regional blood flow variability has been shown to cause considerable uncertainty and underestimation of Aβ load with common semi-quantitative approaches [265, 274]. Specifically, the uptake and the clearance, which are closely linked to the blood flow, does not depends only on tissue type, but also on atrophy and AD progression [296]. This issue is so relevant that many authors suggest avoiding longitudinal analysis with common approach such as the SUVr [265, 274].

A solution to this problem could come from absolute quantification of amyloid tracers using full kinetic analysis. However, only a limited number of studies, have examined the absolute quantification of amyloid tracers using this approach [173, 16]. On the one hand, the full kinetic modeling, relying on fewer assumptions, is more accurate than a typical semi-quantitative methods. For example, it is not affected by rCBF or tracer clearance. On the other hand, these models are complex, require an arterial sample and a long acquisition protocol with additional discomfort for the patients. These requirements

make, to date, absolute quantification in clinical routine unfeasible. Recently, research is shifting towards the development of quantitative and semi-quantitative approaches that exploit a dual time frame window to integrate the missing tracer kinetic information, thus correcting for changes in rCBF and for radiotracer clearance [37, 26].

To try to overcome some of the limitation of the traditional semi-quantitative techniques, in this paper a semi-quantification method called Time-Delayed ratio (TDr) has been proposed and applied to amyloid PET scans. This approach takes the kinetic behaviour of the tracer into consideration to reduce the blood flow-dependent component in estimates of the $A\beta$ load. The information for this correction comes from an early acquisition in which the signal is dominated by the blood flux. Unlike other methods that extract similar information from the time-activity curve, the TDr relies on a very lean processing, as do the approaches currently used in the clinic.

Thus, the TDr method requires two static scans per subject: one early (~0-10 min after the injection) and one late (typically 50-70 min or 90-100 min after the injection, depending on the tracer). High-perfusion regions are delineated on the early scan and applied onto the late scan. A SUVr-like ratio is calculated between the average intensities in the high-perfusion regions and the late-scan hotspot.

TDr was applied to a naturalistic multicenter dataset of 143 subjects acquired with ^{18}F-Florbetapir. TDr values were compared to visual evaluation, cortical-cerebellar SUVr and to the geometrical semi-quantification method ELBA (see Section 4.3.1). All three methods are gauged versus the heterogeneity of the dataset.

In this study, the TDr shows excellent agreement with respect to the binary visual assessment and significantly correlates with both validated semi-quantification methods. This approach is an alternative to previously validated methods (SUVr and ELBA): it requires minimal image processing, it is independent on predefined regions of interest (ROIs are tailored onto the patient, and different from patient to patient) and does not require MR registration. Besides, it takes advantage on the availability of early scans which are becoming common practice while imposing a negligible added patient discomfort.

Our observations suggested that TDr, ELBA and SUVr are independent approaches to measuring the same biological process. From a mathematical point of view, combining a set of independent measures (with uncertainties in the same order of magnitude) is the best way to provide a more robust score. Thus, an appropriate combination of the three quantifiers would improve the estimation of $A\beta$ load and represent a step forward in the use of semi-quantification methods that could also be open to other techniques.

5.3   Study III: regional assessment

Chapter 8 is based on the paper published in the Journal of Alzheimer's Disease in 2020 titled *"Probing the Role of a Regional Quantitative Assessment of Amyloid PET"* [215]. This paper was co-authored with M. Grazzini, M. Bauckneht, F. Sensi, P. Bosco, D. Arnaldi, S. Morbelli, A. Chincarini, M. Pardini and F.M. Nobili.

The amyloid PET is still used purely for differential diagnosis and evaluated at whole-brain level. However, this approach may not properly exploit the full amount of information. Already in 2002 post-mortem pathologic studies showed that amyloid deposition follows a specific pattern of spread [259]. According to this study, the deposition

starts in the neocortex and limbic area, then extends down into subcortical structures, brainstem and cerebellum. Several studies have shown that abnormal striatal Aβ accumulation predicts late Braak neurofibrillary tangle stage [22] and is associated to greater prevalence of AD pathology [14, 258]. Also other brain region may contribute [212, 177].

Other brain regions might have several implications giving pathophysiological insights into where Aβ fibril accumulation is likely to start in AD [212, 177]. Regional Aβ burden has been associated with cognitive decline in amyloid-negative cognitively unimpaired elderly adults [101] suggesting a role for local amyloid load in cognitive ageing.

This study represents an attempt to deepen the role of regional amyloid burden and its implication on clinical-neuropsychological features. AmyPET and a complete neuropsychological assessment were available in 109 patients with clinical suspicion of AD. By averaging the cortico-cerebellar SUVr and ELBA (see Section 4.2 and 4.3.1), a set of regional quantification scores was calculated for each scan. Patients were grouped according to their overall amyloid load and correlation maps, based on regional quantification, were calculated and compared. To assess whether regional Aβ burden is associated with cognitive decline a regression analysis between neuropsychological assessment and the regional quantification score was carried out.

Significant differences were observed between the correlation maps of patients at increasing levels of Aβ and the overall dataset. The Aβ uptake of the subcortical gray matter was not related to other brain regions independently of the global Aβ level. As stated by staging works based on anatomopathological and imaging findings, the Aβ spreading proceeds differently between cortical and subcortical regions as well as between patients. Our results confirmed the different susceptibility to Aβ accumulation among brain regions.

The regression analysis showed no association of the neuropsychological tests with both whole brain and regional Aβ load. However, a significant association of semantic verbal fluency - which is known to be affected early in AD [241, 29] - was observed with ratios of cortical and subcortical distribution of Aβ which represent a coarse measure of differences in regional distribution of Aβ.

The association between cognition and Aβ distribution deserves further investigations: it is possibly due to a direct local effect or it represents a proxy marker of a more aggressive disease subtype. Interestingly, Cook's distance analysis showed that negative and mild negative subjects drove the asssociation. This is in line with studies that pointed out a possible biological role of Aβ in individual with sub-threshold levels [39, 279, 123, 150, 73].

All these results together suggest that regional Aβ assessment represents an available resource on amy-PET scan with possibly clinical and prognostic implications: future image assessment may benefit from an element of regional evaluation using quantitative or semi-quantitative PET imaging approaches.

5.4   Study IV: comparison of advanced approaches

Chapter 9 is based on the manuscript submitted in the European Journal of Nuclear Medicine and Molecular Imaging in 2022 titled *"A comparison of advanced semi-quantitative amyloid PET analysis methods"*. This paper was co-authored with D. Poggiali, M. Pardini, H. Barthel, O. Sabri, S. Morbelli, A. Cagnin, A. Chincarini and D. Cecchin.

As discussed in Chapter 4, there is currently no consensus on which is the best way (and the most feasible in clinical practice) to perform a quantitative analysis of amyloid PET. Absolute quantification is considered essential to accurately monitor the response to Aβ-modifying treatments for AD and for longitudinal studies.

However, semi-quantitative approaches, that can rely on different sources of information and on increasing sophistication, represents a good compromise between practicality and accuracy in the clinical context. Although the full kinetic modeling is the optimal solution, simpler yet advanced semi-quantitative approaches might be used under the assumption of accepting a larger error. Besides the SUVr, other analysis relies on the late acquisition alone [43, 285] or on tracer kinetic information adding an early acquisition [41]. Other methods takes into consideration also atrophy and spillover by including structural imaging [37].

In this study, we compare, at both global and regional level, five semi-quantitative approaches with increasing refinement level designed to capture specific characteristics of the image: SUVr [139], ELBA [43], TDr [41], WMR [37] and SI [37].

A single-center dataset (from University Hospital of Leipzig, Germany) was used consisting in 85 patients who PET/MRI examination with an early and a late scan acquired after the injection of ~300 MBq of ^{18}F-florbetaben. The scans were classified as amyloid-negative or positive by two independent nuclear medicine experts.

Due to the lack of an absolute quantification the SI, being the most comprehensive and complete approach, was used as the reference measure for the amyloid burden. The choice of a robust measure as a reference allowed us to assess the efficacy of the other quantifiers. We evaluated the correlation of the approaches with the reference and quantified the dispersion with a Bland-Altman analysis. Then, the we computed the discriminating power of each semi-quantification approaches with respect to the visual assessment. Finally, the possible association between each quantifier, age and cortical thickness in amyloid-negative patients was assessed. With the idea that SUVr, ELBA, TDr and WMR are proxy measures of the true amyloid load, we linearly combine them to provide more robust indices and we compare these combinations with SI.

We observed that the different approaches, although there are some regional differences due to the characteristics of individual methods, tend to the reference measure SI both regional and global level. Versus the consensus binary visual assessment all the quantifiers showed excellent results. Moreover, the linear combinations of the quantifiers provided scores that are always closer to the reference, therefore encouraging efforts towards multi-classifiers systems to measure surrogate endpoints for therapy evaluation. Interestingly at a global and regional level, the TDr, the WMR and the SI (that are the methods including information on the tracer kinetic) were significantly associated with age in qualitatively assessed amyloid-negative patients.

This latter result suggest that the TDr could be accurate (deriving information from dual time points) and easier (no structural imaging needed) to implement as compared to SI (accepting some inaccuracy in deep structures).

Possible results of the present study could be of outermost importance in view of the accelerated approval for aducanumab [191] in patients with AD. In fact, while on one hand, one could argue that if amyloid plaque load, as measured by amy-PET with a standard late acquisition, could be considered a valid surrogate endpoint for a drug approval and could demonstrate a clinical benefit in AD, on the other hand it is important to notice that advanced semi-quantitative methods including also a blood flow analysis (using early acquisition) could pick not only amyloid load [87] but also neurodegenera-

tion, therefore constituting a more robust end point to measure diseases modifying drugs targeting amyloid load deposition.

5.5   Study V: amyloid and tau regional relationship

Failure, in recent years, of AD trials on anti-amyloid treatments gave a boost to the development of approaches that involve also other therapeutic targets such as inflammation, oxidative stress or tau aggregation (as a complement to anti-amyloid medications or independently). As posited by the amyloid cascade hypothesis (see Section 1.3), the Aβ accumulation has been considered the initiating toxic event in AD and its relationships with neurodegeneration and cognitive decline are not straightforward. On the other hand, the distribution and burden of NFTs showed clear association with neurodegeneration and clinical status. The most commonly accepted approach is to consider the aggregation of amyloid and tau in parallel, thus biologically defining Alzheimer's disease on the basis of the coexistence of amyloid and tau aggregates in the brain [125]. The introduction of radiotracers that binds to NFTs provided a new tool to in-vivo evaluate the pathology progression [276]. This assessment showed a strong association of regional tau burden with clinical and anatomical heterogeneity in AD patients [203, 220]. Although the use of these imaging modalities is becoming increasingly popular in research, many questions still remain. For example, it is not clear whether amyloid is a driver or trigger for Alzheimer's disease, nor the fundamental relationship between tau and amyloid levels in the brain.

Recent studies showed that the cortical tau retention in AD patients almost only occurs in amyloid-positive individuals [128, 202]. These observations were also verified on a longitudinal study including normal adults with repeated PET measures [104]: Aβ accumulation was associated to successive tau accumulation that mediates the association of baseline amyloid with cognitive decline. These multimodal investigations allowed an in-vivo exploration of the link between β and tau at the whole brain level. However, at the regional level, this relationship is still rather unexplored.

Therefore, the preliminary study described in Chapter 10 aims to investigate the amyloid/tau relationship at the regional level. To do this, we used data from 153 patients with cognitve complains recruited at th Geneva Memory Clinic and acquired with both amyloid and tau PET. Both amyloid and tau PET were semi-quantified with regional SUVr on a common space. A simplified model was developed to fit the possible trajectories of regional accumulation of amyloid and tau and thus, to assess their relationship at regional level. The model essentially assumes that the dynamics of amyloid and tau can be coarsely described by a single curve, and that amyloid and tau increase solely.

The model output provided a regional description of possible amyloid/tau trajectories. These trajectories were verified in terms of: I) internal consistency and agreement with the literature, II) relationship with cognitive decline.

The preliminary results showed some consistency of regional characteristics of amyloid and tau tracers, with the results in the literature. Furthermore, a significant relationship was observed, in the AD subgroup, between marker of neurodegeneration and the model output. Nevertheless, additional confirmatory analyses are mandatory to verify the consistency of the model and validate the estimated regional trajectories with the actual trajectories from longitudinal data.

At the time of this writing, preliminary results and planned confirmatory tests are being collected in a manuscript co-authored by F. Ribaldi, S.E. Tomczyk, R. Gianeri, F. Sensi, V. Garibotto, M. Pardini, A. Chincarini and G.B. Frisoni.

Chapter 6

Semi-quantification and grading of amyloid PET: A project of the European Alzheimer's Disease Consortium (EADC)

6.1 Introduction

Assessment of brain Aβ amyloidosis has gained a pivotal role in the diagnosis of Alzheimer's disease (AD) in vivo, according to the last National Institute of Aging - Alzheimer Association (NIA-AA) [180] and the International Working Group-2 (IWG-2) criteria [62]. Moreover, the 2018 research framework identifies a stage of Alzheimer pathology for isolated brain amyloidosis while the term AD is reserved to the concomitant amyloid and tau pathology [125].

The concordance between CSF Aβ_{1-42} levels and amyloid load on PET is good (over 80%; [106]) although data shows that CSF Aβ levels changes may precede brain amyloid deposition and thus it should be considered as an earlier phenomenon [211]. Instead, brain amyloid load on PET still continues to increase even after the onset of cognitive symptoms [74]. Moreover, the availability of Aβ assays has shown that a non-trivial part of patients are high or low beta-amyloid producers so that the A$\beta_{42/40}$ ratio better reflects the real amyloidosis status of a subject and allows better correlation with amyloid load on PET [198].

The amyloid PET reading has been classically implemented as a binary lecture, i.e., negative or positive for amyloidosis, however the current clinical experience has shown that the number of borderline cases is not trivial not only in epidemiological studies in asymptomatic subjects but also in naturalistic groups of symptomatic patients attending a memory clinic to receive a diagnosis [214]. This behaviour actually mirrors what happens with CSF Aβ assay showing a non-negligible borderzone around the cut-off value identifying positive and negative subjects [185].

The APOE genotype (presence of at least one ϵ-4 allele) is a major determinant of the degree of amyloidosis [59] but other, less known factors may play a role [282].

In any case, the binary lecture is poorly adequate to address the clinical reality and complexity and, even within the two extreme classes - i.e. negative or positive - there is inhomogeneity because there are subjects that are more or less positive and those who are more or less negative [80].

Taking together all this information, brain amyloidosis across subjects attending a memory clinics appears more as a continuum rather than a clusterized, binomial distribution. Therefore, the issue arises on how to quantify and grade such a continuum, whether the continuum with a specific fluorinated radiopharmaceutical is similar to the one obtained with the other two available fluorinated radiopharmaceuticals, and how to share this information among labs.

The so-called "centiloid project" has tried to give an answer to this issue and is certainly of value but it requires that each center builds-up its own cohort of normal subjects in different age ranges [143]. Moreover, it is based on SUVr computation that certainly has advantages but also disadvantages, such as the uncertainty about the reference region and on how to draw the cortical ROIs.

In the present study and in the frame of the PET study group of the European Alzheimer Disease Consortium (EADC) we aim at: (a) propose and validate a method to compare semi-quantification values among tracers regardless of the semi-quantification approach (SUVr-based or SUVr-independent); (b) define transition regions and cut-off values which are (largely) independent from the cohorts; (c) test a more complex visual evaluation scale common across different tracers and assess its performance.

6.2 Methods

6.2.1 Subject selection

The amyloid PET project of the EADC is aimed at joining together amyloid PET scans with corresponding clinical and neuropsychological data from subjects attending a memory clinic of one of the EADC centers. To the purpose of this project, both subjects with a positive or negative amyloid PET scan according to visual dichotomic evaluation, as established by the local nuclear medicine physician, were enrolled.

We identified the fluorinated tracer with the lowest number of scans available (i.e., ^{18}F-Florbetaben, 53 subjects) and then a similar number of subjects with the other two fluorinated tracers (^{18}FFlutemetamol, 62 subjects; ^{18}F-Florbetapir, 60 subjects). Only with the ^{18}F-Florbetapir we randomly sampled the database in order to maintain the highest possible number of centers overlapping with the other two tracers, and to maintain an approximate balance in number of cases per center. These subjects constitute three cohorts, one per each tracer.

The selection was done from some of those EADC centers participating to the PET 2.0 project, namely: Genoa (GEN), Brescia (BRE), Geneva (HUG), Antwerp (ANT), Paris (PAR), and Mannheim (MAN) according to scan availability on the tracer of choice. Subjects main demographics and clinical characteristics are summarized in table 6.1.

Subjects received a diagnosis after the first diagnostic work-up, including the result of amyloid PET scan, and were followed-up clinically for an average time of 30.1 [6-143] months. We considered the diagnosis as clinically confirmed at the last available visit. The selected subjects were diagnosed as affected by mild cognitive impairment (MCI) due to AD (MCIAD), probable (prob) or possible (poss) AD dementia, frontotemporal dementia (FTD), dementia with Lewy bodies (DLB), or vascular dementia (VaD) according to current criteria [180].

Moreover, those subjects who did not received a definite pathogenetic diagnosis were still labeled as affected by amnestic (aMCI) or non-amnestic (naMCI) MCI. The population also included some subjects with the so called "pseudodementia" (pseudoDD, that

Table 6.1: Demographics.

	flutemetamol			florbetaben			florbetapir			
provenance	GEN	PAR	HUG	GEN	MAN	HUG	GEN	BRE	ANT	HUG
sample size	15	33	14	15	30	8	15	15	6	24
scanner	Siemens BioGraph HiRes 1080	GE Discovery 690	Siemens Biograph 128 mCT	Siemens BioGraph HiRes 1080	Siemens BioGraph 40 mCT	Siemens BioGraph 128 mCT	Siemens BioGraph HiRes 1080	Siemens BioGraph 40 mCT	Siemens BioGraph 64 mCT	Siemens BioGraph 128 mCT
age [y]	69.7 [54 79]	62.3 [42 78]	60.3 [45 70]	72.6 [55 82]	66.2 [48 84]	69.2 [51 71]]	72.5 [59 80]	72.0 [60 84]	77.5 [68 85]	71.0 [59 83]
sex (M %)	46.7	40.0	49.1	60.0	56.7	30.0	51.9	45.0	16.7	45.8
MMSE score	26.7 [18 30]	27.9 [24 30]	28.2 [25 30]	27.7 [24 30]	24.6 [14 30]	27.1 [20 30]	26.1 [15 30]	22.1 [13 28]	25.1 [15 30]	27.6 [13 30]
MCIAD (%)		24.1			41.5			23.1		
possAD (%)		1.6						3.4		
probAD (%)		4.8			18.8			15.0		
probFTD (%)		1.6			3.8			3.2		
possFTD (%)		4.8						3.4		
possDLB (%)		1.6								
probVaD (%)								1.5		
PseudoDD (%)		1.6			13.2			10.0		
aMCI (%)		14.6			3.8			8.2		
naMCI (%)		32.2			9.4			6.5		
SCI (%)		13.0			9.4			25.7		

is, psychiatric conditions that can mimic dementia), or with subjective cognitive complaints but without evidence of deficit on neuropsychological tests (SCI). The study was approved by the local Ethics Committees and all the recruited subjects provided an informed consent.

6.2.2 PET acquisition

Amyloid PET acquisition followed the recommendations of tracer manufacturers and the joint guidelines of the European Association of Nuclear Medicine and the Society of Nuclear Medicine [184]. The equipment used was a PET-CT tomograph and is listed in table 6.1 for each center.

Three-dimensional static scan acquisition was performed in all centers, and attenuation correction was based on CT. Image reconstruction was made with Ordered Subset-Expectation Maximization algorithm following the standard brain protocols embedded in each equipment. Each center was responsible for sending good-quality data but a further quality check was performed by the core center in Genoa. In order to reproduce the clinical situation in the real world, only unreadable scans were rejected while all other scans were submitted to further analysis.

6.2.3 CT subset

A subset of all cohorts - 50% in total: 39 subjects with ^{18}F-Flutemetamol, 29 with ^{18}F-Florbetaben and 20 with ^{18}F-Florbetapir - came with the companion CT scans. While all PET scans were read without CT, the subset with the CT underwent a separate, further evaluation following the same rules detailed in Section 6.2.4. The intent is to use this subset to validate the statistics of evaluation and accord among readers even when the assessment was conducted without the CT.

6.2.4   Visual evaluation

The 175 scans were independently presented to five readers, including three expert (UPG, FN and VG) and two intermediate-expert readers (AC and MB). The three experts passed the training qualification of the three vendors and are used to report several scans monthly since the time of availability on the market of the radiopharmaceuticals, always with the agreement of at least another expert and with the assistance of semi-quantification based on both SUVr and SUVr-independent tools [43]. The two intermediate-expert readers share the same characteristics as the experts but are reading scans for a shorter time.

The anonymized scans were presented in the native space, randomized, and the reader was blind to the clinical information and the reading of the other experts. No MRI or CT scans were provided together with PET scans (see also CT subset comparison). Readers were asked three questions as follows:

1. *Quality flag:* a dichotomous response on sub-optimal scans. There is no formal or shared definition on scan quality. This flag was raised according to each reader own's experience. Typically though sub-optimal quality involves image acquisition flaws like field of view cuts or poor count rate; it can also be related to image reconstruction issues like excess smooth, artefacts, etc.

2. *Binary evaluation:* negative/positive according to the approved indications of each manufacturer.

3. *5-step evaluation:* visual grading into classes: negative, mild negative, borderline, mild positive, positive according to Paghera and colleagues [209] (see below).

Readers were presented with 3 batches (one for each tracer) and they were informed of the tracers used. The evaluation of each batch was completed sequentially, with at least 2 weeks time between one batch and the next. After the three evaluation batches, the CT subset was sent to the readers to get a new independent evaluation with the help of the companion CT.

6.2.5   Semi-quantification methods

The visual assessment of the amyloid PET scan is a non-trivial task that is often complemented by measures derived from semi-quantification methods (hereafter named quantifiers). These measures are intended to be proxies of the brain amyloid load. Among quantifiers, the Standardized Uptake Value ratio (SUVr) [139] is the most widely used and validated, compared to the binary reading. This approach calculates the ratio of PET counts between a target region of interest (ROI) versus a reference one.

In this study the SUVr was estimated using the whole cerebellum as reference region. As reported in the literature [244], this choice makes the measure less prone to segmentation errors than the selection of the cerebellum gray matter or the brain stem. The SUVr score was calculated as the average cortico-cerebellar SUVr on all scans. Similarly to what accomplished in [143], the target cortical ROI included the medial frontal gyrus, the lateral frontal cortex (middle frontal gyrus), the lateral temporal cortex (middle temporal gyrus), the lateral parietal cortex (inferior parietal lobule), the insula, the caudate nucleus, and the precuneus-posterior cingulate region.

The other quantifier used in this study is named ELBA [43]. It is a SUVr-independent approach that is designed to capture intensity distribution patterns rather than actual counts in predefined ROIs. These patterns are global properties of the whole brain and do not require a reference ROI. ELBA showed good performance versus the visual classification, highly significant correlation with the result of CSF Aβ_{1-42} assay, and has ranking characteristics proven both on cross-sectional and longitudinal analyses [43].

Similarly to the procedure described in [43], quantifiers were applied onto the spatially normalized image. Briefly, the procedure mapped the PET onto the T1-weighted MRI template in MNI space (with isotropic spacing and voxel dimension of $1 \times 1 \times 1$ mm) with a registration consististing in: global intensity re-scaling, rigid registration, affine registration. Then, a pre-segmented atlas which included cortical and cerebellar ROIs was mapped from the MNI space to the affine-transformed PET with a deformable registration. We used the ANTs registration software [9] with the mutual information metric.

Both quantifiers were implemented in an automatic analysis procedure that did not require any human supervision with the exception of an visual check after the spatial normalization process onto the MNI space.

6.2.6   Analysis

Sample homogeneity and data model

Direct comparison of semi-quantification values over different tracers is possible in principle, if one is in possess of a set of subjects who have been acquired with two or more tracers over a reasonably short time frame (i.e. with respect to the typical physiological change in amyloid deposition). Alternatively, one could use statistically equivalent reference cohorts. This latter approach is the one followed by the centiloid method, where the ad-hoc acquisition of a group of young healthy controls and a group of confirmed AD subjects - both analyzed with the quantification method of choice - constitutes the centiloid scale references. Unfortunately our three cohorts are not statistically equivalent (both in sample size, center distribution and clinical evaluation) and neither can they be considered scale extremes, so that direct comparison among semi-quantification values cannot be applied.

Given that visual reading is the de-facto gold standard in assessing positivity in a clinical setting, we can exploit it as a cross-tracer comparison method. A model is therefore necessary to link the visual assessment to the semi-quantification. The binary reading is though too coarse to provide a meaningful relationship, we therefore resort to the grading.

Positivity grades have been conventionally declined into numbers ranging from 1 to 5 (negative, mild negative, borderline, mild positive, positive). Basic considerations on the transition continuity and on the floor / ceiling effect on negative / positive evaluations suggest that a possible model of the grading versus semi-quantification is a sigmoid function (S), which we write in the following form:

$$g = p - \frac{p - n}{1 + \exp(-s(q - o))} = S(q, s, o) \qquad (6.1)$$

Where g is the grading, p and n are the numerical equivalent of the positive and negative gradings, q is the quantification value, s is the slope and o is the offset. For each tracer, the sigmoid function of our model has only two free parameters: the slope

s and the offset o. All other parameters are set by the limit grading values (negative for quant. score $\rightarrow -\infty$, positive for quant. score $\rightarrow \infty$). This ensures that the models are (largely) independent from the sample characteristics because of the few degrees of freedom versus the sample size (~60 scans in each cohort). Models are used in synergy with visual grading to provide a mapping between tracers.

Readers concordance

Readers evaluated all scans independently. We can therefore assume that their errors are uncorrelated and that their mean is a good estimator of the "true" evaluation. While this holds true for a large number of measures, we need to ensure that the error on the mean is relatively small even when employing 5 readers only. This assumption is acceptable if the accord among readers is sufficiently high.

To assess reader concordance we compute the intra-class correlation coefficient (ICC, two way random-effect model, mean of k raters) for the whole dataset and on the single cohorts (one per tracer, table 6.2).

Table 6.2: ICC Two way random-effect model, mean of k raters (absolute agreement).

tracer	ICC [95% CL]
flutemetamol	0.952 [0.93 - 0.969]
florbetaben	0.987 [0.98 - 0.992]
florbetapir	0.959 [0.94 - 0.974]
all tracers	0.967 [0.96 - 0.975]

Between each reader we also compute the Cohen k. For each tracer and for each reader we compute the grades statistics, i.e. the number scans in each grade (table 6.3). The between tracer distribution is also visually shown with a heatmap (number of scans per each grade pair) and the Bland-Altmann plot (figure 6.7 in supplementary materials).

Table 6.3: Evaluation fraction by grade.

	Reader	neg (%)	mild neg (%)	borderline (%)	mild pos (%)	pos (%)
	UPG	23	14	5	22	36
	FN	25	10	9	17	39
all tracers	AC	17	18	21	19	26
	VG	11	22	9	19	38
	MB	22	21	10	14	33
	all	19.6	17	10.8	18.2	34.4
	UPG	15	23	8	32	23
	FN	23	10	15	19	34
flutemetamol	AC	8	16	35	18	23
	VG	6	24	13	24	32
	MB	23	26	11	18	23
	all	15	19.8	16.4	22.2	27
	UPG	25	9	2	13	51
	FN	23	13	2	11	51
florbetaben	AC	21	11	6	17	45
	VG	19	15	4	17	45
	MB	23	15	8	13	42
	all	22.2	12.6	4.4	14.2	46.8
	UPG	30	10	5	18	37
	FN	30	7	8	20	35
florbetapir	AC	22	25	18	23	12
	VG	10	27	8	17	38
	MB	20	22	10	12	37
	all	22.4	18.2	9.8	18	31.8

Visual assessment and semi-quantification

The relationship between visual grading and quantification is found by fitting the sigmoid model onto the data. Model parameters are fit both onto z-score quantifier values (direct model, grading vs. quantifiers) and on the raw quantifiers data (inverse model, quantifiers vs. grading). In the direct model, each scan is identified by the z-scored value of the quantifier (either ELBA or SUVr) and by its average grading. Z-scores are computed on each cohort separately.

With the z-scores model we can easily visualize relationships with the two quantifiers on the same plot and we can evaluate potential significant differences, both between quantifiers and among tracers. We use the fitted models to define a transition region (from mild-negative to mild-positive) and the cut-off on all tracers. These quantities are found at the intersection of the models with the mild-negative, borderline and mild-positive coordinates on the y-axis (figure 6.1). Both the transition region and the cut-off values depend on the data only through the model, so they can be considered a proxy of cohort-independent definitions.

Given their good correlation (see figure 6.2), the two z-scored quantifiers can be further summarized into a single value, that is the score on the first PCA axis (PCA1).

This allows us to abstract the quantification (potentially including more than two quantifiers) and focus on the relationship with the gradings. While the direct model
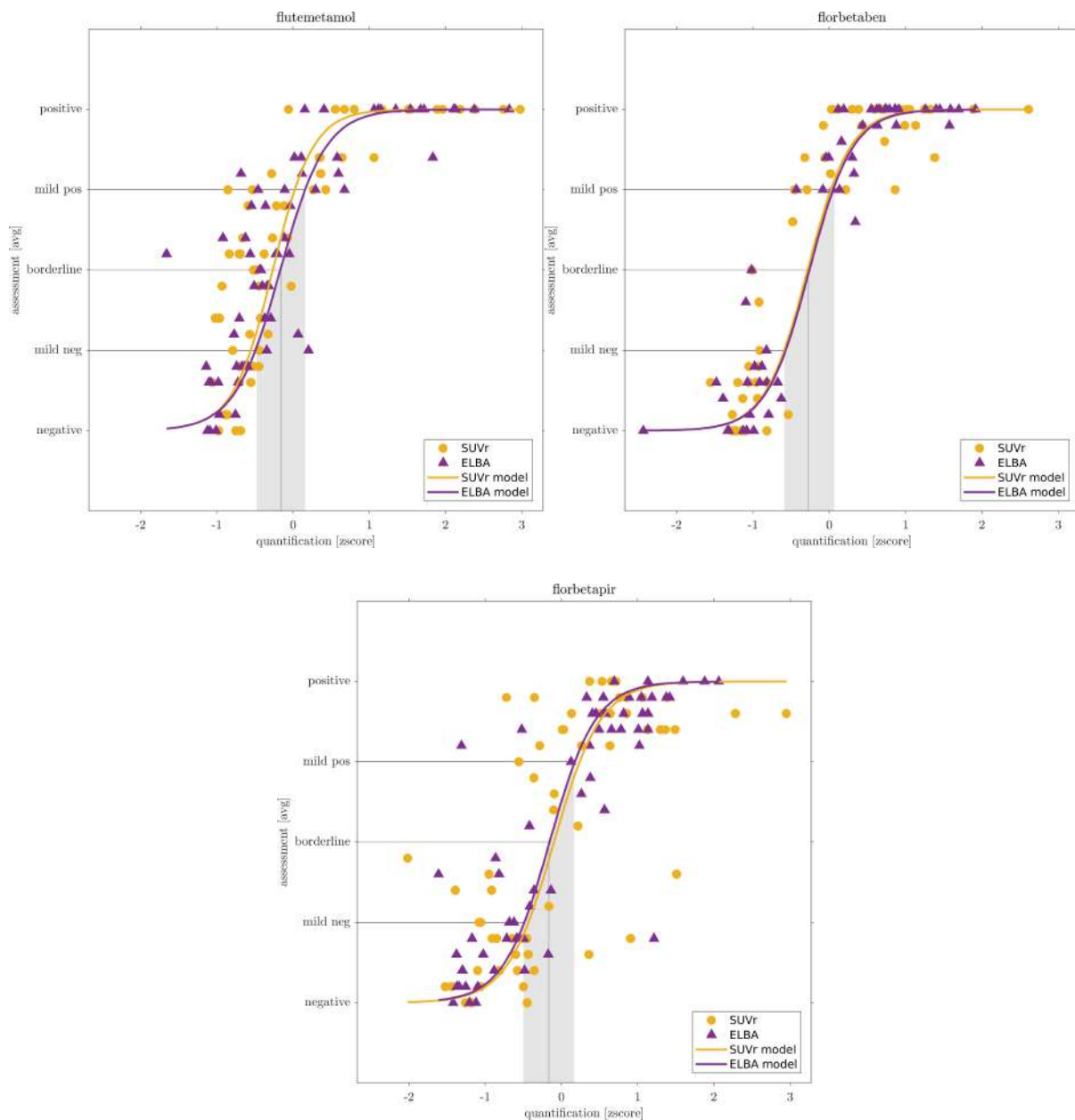
Figure 6.1: Quantification-visual assessment relationship for the 3 fluorinated tracers. On the x- axis: z-score of the two quantifiers; on the y-axis the average visual grading. Dots represent scans, continuous line are the sigmoid model. Intersection of the model with mild and borderline evaluations is projected onto the scores to define a transition region (gray area) and the cutoff (gray line).

is useful for comparison and visualization, the inverse model is used to estimate the between-tracers mapping.
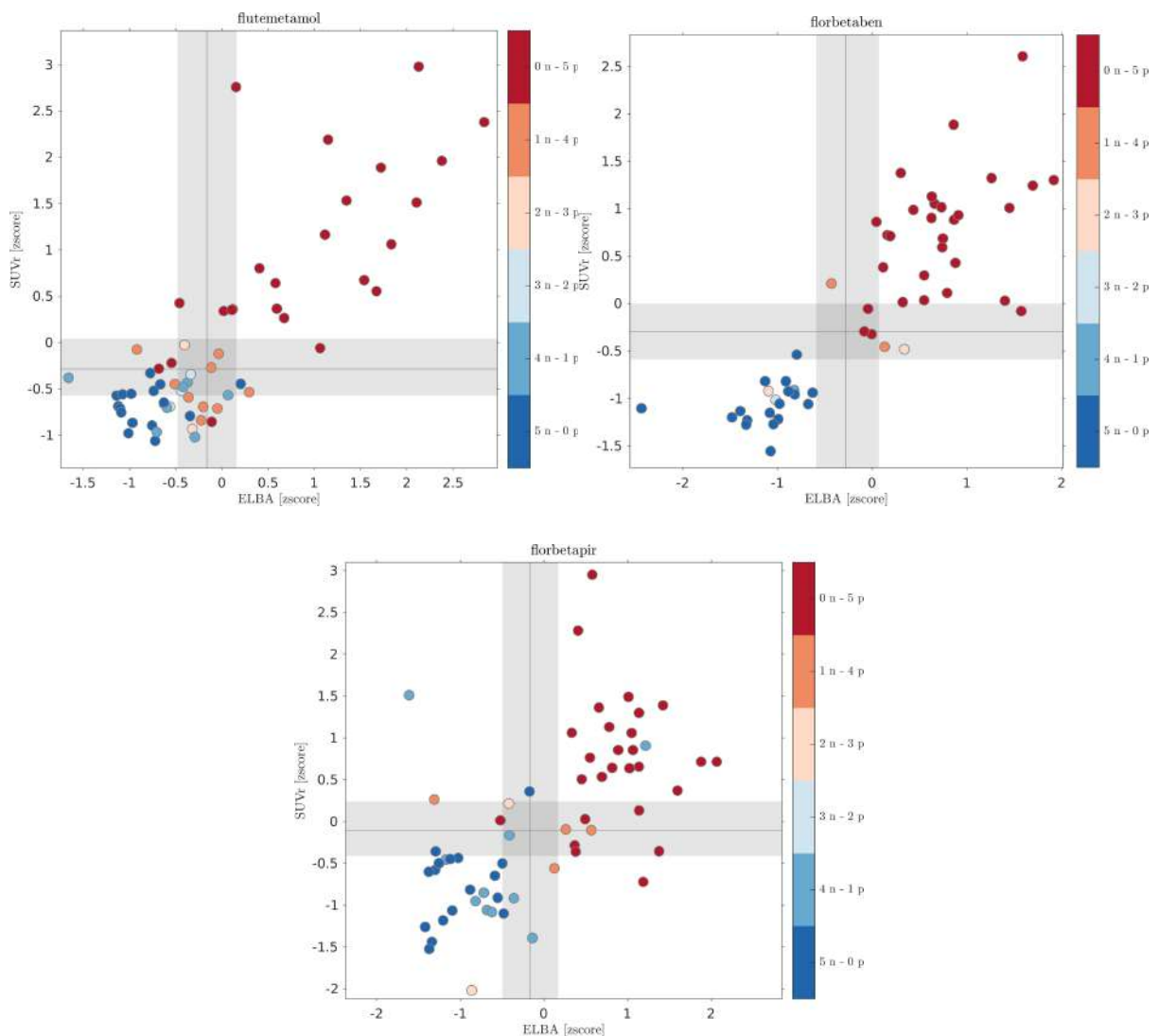
Figure 6.2: ELBA-SUVr scatter-plot with binary visual assessment. Dots represent scans, colors are according to the combination of negative and positive evaluations given by the 5 readers.

Evaluation latitude

We grouped scans according to similar average grading. Groups may contain one or more scans. Each group is assigned a quantification value, which is the average score of its members onto the PCA1. Each group is also assigned an "evaluation latitude"; with this term we intend the overall scope of gradings, that is, the largest span of evaluations given by all readers on a scan or group of scans. The group evaluation latitude is therefore a range, spanning the lowest to highest grading received on any of the group's members. The relationship between group's score and latitude provides further information on the reading discrepancies as function of the quantification (figure 6.3).
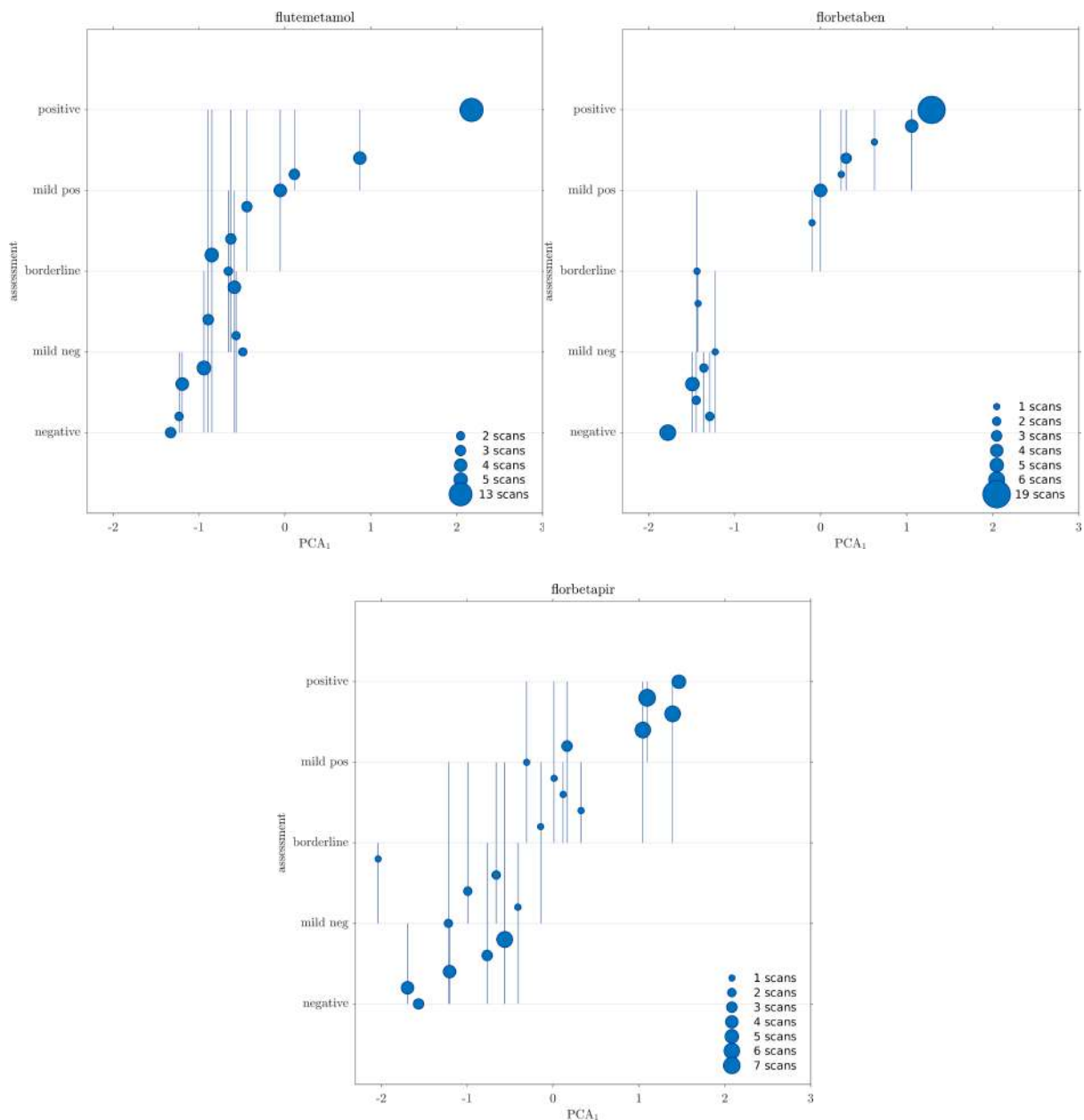
Figure 6.3: Relationship between quantification score and evaluation latitude. Each circle represents a group of scans sharing the same average grading. The group position on the x-axis is the average score of its members on the first PCA axis (PCA computed on the z-score quantifiers). The group position in the y-axis is the average grading. Vertical lines show the group evaluation latitude, that is, the lowest to highest grading received on any of the group's members.

Binary assessment

Each reader assigned a binary visual assessment - negative (n) / positive (p) - to the scan, according to each tracer's standard evaluation rules. With 5 independent readers we have therefore 6 possible classes: 5n-0p, 4n-1p ... 0n-5p. We explored the distribution of the binary reading on a scatter-plot which also shows the relationship between the quantifiers. We used the cut-off and the transition regions derived from the model (see Paragraph "Visual assessment and semi-quantification") to compute accuracies for both quantifiers.

In this latter analysis we considered negative scans as belonging to classes 5n-0p, 4n-1p, 3n-2p and positive scans as belonging to classes 2n-3p, 1n-4p, 0n-5p (figure 6.2). The reader accord on the binary assessment is shown with the Cohen k, to be compared to the grading (table 6.8 and table 6.5).

Table 6.4: Agreement between pairs of readers all tracers with respect to the grading evaluation using accuracy and Cohen k (within brackets).

	UPG	FN	AC	VG	MB
UPG		0.61 (0.48)	0.55 (0.44)	0.59 (0.46)	0.61 (0.49)
FN	0.61 (0.48)		0.60 (0.49)	0.62 (0.49)	0.62 (0.50)
AC	0.55 (0.44)	0.60 (0.49)		0.58 (0.46)	0.55 (0.43)
VG	0.59 (0.46)	0.62 (0.49)	0.58 (0.46)		0.53 (0.39)
MB	0.61 (0.49)	0.62 (0.50)	0.55 (0.43)	0.53 (0.39)	

Table 6.5: Agreement between pairs of readers on all tracers with respect to the binary evaluation using accuracy and Cohen k (within brackets).

	UPG	FN	AC	VG	MB
UPG		0.90 (0.80)	0.91 (0.81)	0.89 (0.76)	0.86 (0.71)
FN	0.90 (0.80)		0.91 (0.82)	0.93 (0.84)	0.86 (0.72)
AC	0.91 (0.81)	0.91 (0.82)		0.90 (0.79)	0.86 (0.71)
VG	0.89 (0.76)	0.93 (0.84)	0.90 (0.79)		0.87 (0.74)
MB	0.86 (0.71)	0.86 (0.72)	0.86 (0.71)	0.87 (0.74)	

Then, we looked at possible relationships between the binary reading and the discrepancies on the grading (latitude). For each scan we assigned the binary class (among the 6 possible choices) and we computed the latitude (i.e.: the maximum grading difference among those received). We then counted how many scans are there per class and latitude (figure 6.4).
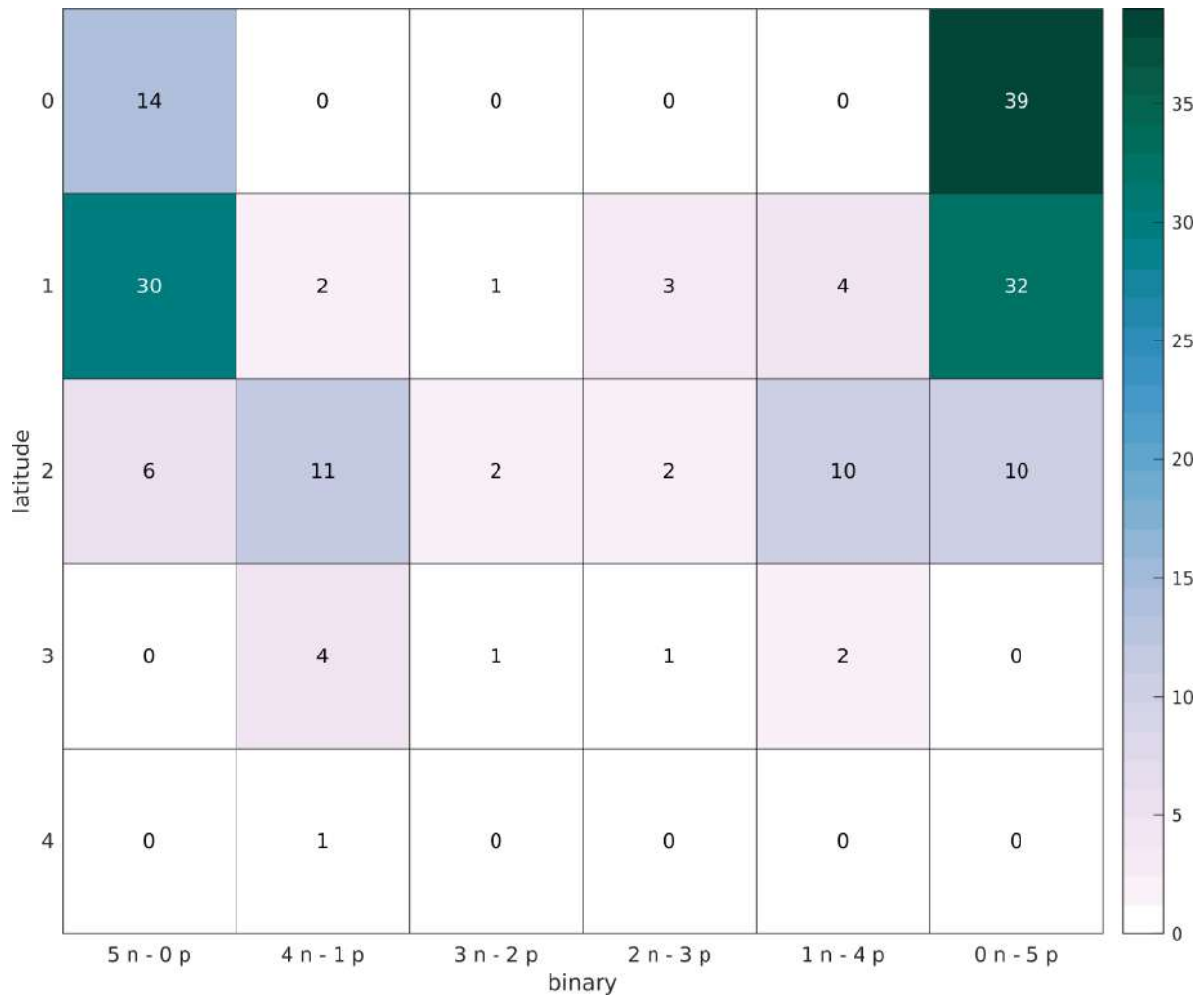
Figure 6.4: Relationship between the binary evaluation and the latitude. Each box shows the number of scans grouped by binary class and maximum grading difference received in the 5-step visual assessment.

Scan quality effect

The third type of visual assessment is the scan quality. This is simply a flag indicating whether acquisition nuisance and/or reconstruction procedures would result in a sub-optimal image, according to each reader's own experience. We study whether scan quality has any relationship with quantification and evaluation latitude. First we plot the number of quality flags versus the second PCA components (PCA2). The PCA1 encodes the quantification (negative to positive), while the PCA2 mainly encodes discrepancies between the quantifiers (approximately off-diagonal distances in the ELBA-SUVr scatter plots, figure 6.2). We then look at biases in the quality distribution. Then, we compute the matrix of the number of quality flags for each scan grouped by the latitude (i.e. the grading range).

CT subset comparison

Finally we compare evaluations on the subset with companion CT. Comparison between evaluations with/without CT is carried out by testing χ^2 statistics on the 5-step grading and binary distribution, and by comparing the intra-rater ICC and Cohen's k.

Mapping

We now have all the tools to map quantifications on one tracer into another. While the direct model S maps z-scored quantifier values into gradings, the inverse model S^{-1} maps the gradings into the raw quantification values. If we keep the visual gradings as constants across tracers, we can bind two models together (model mapping). Mathematically, this means that for each tracer pair $i - j$ we have a set of two equations for the inverse model S^{-1}, with model parameters s (slope) and o (offset, see table 6.6):

$$q_i = S^{-1}(g, s_i, o_i) \tag{6.2}$$

$$q_j = S^{-1}(g, s_i, o_i) \tag{6.3}$$

Table 6.6: Model parameters.

tracer	quantifier	slope	offset
		Raw values (inverse model, quantifier vs. grading)	
flutemetamol	SUVr	-10.05 [-10.84 -9.26]	1.11 [1.04 1.18]
	ELBA	-13.41 [-14.54 -12.28]	0.76 [0.72 0.79]
florbetaben	SUVr	-7.71 [-8.01 -7.41]	1.23 [1.17 1.29]
	ELBA	-9.65 [-10.06 -9.24]	0.85 [0.82 0.89]
florbetapir	SUVr	-16.97 [-18.70 -15.24]	1.16 [1.11 1.21]
	ELBA	-11.40 [-12.00 -10.80]	0.87 [0.84 0.90]
		Z-score values (direct model, grading vs. quantifier)	
flutemetamol	SUVr	3.80 [2.91 4.70]	-0.27 [-0.53 -0.00]
	ELBA	3.37 [2.57 4.17]	-0.17 [-0.51 0.17]
florbetaben	SUVr	3.60 [3.01 4.19]	-0.29 [-0.54 -0.03]
	ELBA	3.54 [3.01 4.07]	-0.26 [-0.50 -0.02]
florbetapir	SUVr	3.27 [2.39 4.15]	-0.10 [-0.40 0.21]
	ELBA	3.32 [2.79 3.84]	-0.16 [-0.40 0.09]

These represent the expected (i.e. modeled) quantifier value q of the i-th and j-th tracer calculated in the grading coordinate g. As g ranges in [1..5], we therefore have a vector of 5 quantifier coordinates $[q_i, q_j]$. These coordinates are linearly regressed to find the mapping functions listed in table 6.7.

Table 6.7: Conversion parameters between tracers (model mapping).

ELBA			
from / to	flutemetamol	florbetaben	florbetapir
flutemetamol		$1.39x - 0.20$	$1.18x - 0.02$
florbetaben	$0.72x + 0.15$		$0.85x + 0.15$
florbetapir	$0.85x + 0.02$	$1.18x - 0.17$	
SUVr			
from / to	flutemetamol	florbetaben	florbetapir
flutemetamol		$1.30x - 0.22$	$0.59x + 0.51$
florbetaben	$0.77x + 0.17$		$0.45x + 0.61$
florbetapir	$1.69x - 0.86$	$2.20x - 1.33$	

Another possible and distinct approach is to consider visual grading ranges as containers, in order to group subjects into comparable sets; that is, we might consider as equivalent two sets from different tracer cohorts, whose subjects received a mean average grading between - say - negative and mild negative. Container classes would therefore be 4: negative to mild negative, mild negative to borderline, borderline to mild positive, mild positive to positive. This latter approach is similar to the centiloid one, as it aims at constructing a series of comparable groups across tracers cohorts, thus avoiding the need for a model.

In principle, albeit with a much higher number of scans, we could detect deviations of the mapping from a linear dependence, a possibility that is lacking in the centiloid method. The linear regression over container cohorts is done on the average quantifier values and takes into account standard deviations on both quantifiers according to [295]. While we are plagued by the relatively small number of subjects in some of the intermediate container classes, we still use this approach to cross-check the model mapping. We therefore require that the model mapping be compatible with the (linear) regression computed on container classes.

Validation

Last analysis is a validation of the mapping model. We run a Monte Carlo simulation to construct populations sharing the same grading distribution. For instance, we first select a reference cohort A - say the florbetaben scans - and another test cohort B - say the flutemetamol scans. The visual grading distributions of cohorts A and B are typically statistically different (Kolmogorov-Smirnov test p-value < 0.05).

We now resample cohort B with appropriate weights (and with repetition), in order to create a new cohort B* whose grading distribution is statistically equivalent to the cohort A. If we look at the distribution of quantification values of the two cohorts A and B* (either with ELBA or with SUVr) we still find these distributions statistically different because of the different tracers (i.e. quantifiers values are expressed in their own tracer units). We show that when we apply the model mapping we can nullify the statistical differences between A and B*.

In essence, population resampling plus model mapping give statistically equivalent results as if we had a single population that underwent multiple-tracers acquisitions.

6.3   Results

6.3.1   Readers concordance

The statistics on the grading evaluations is summarized in table 6.3. The general overall assessment of accord among readers on the grading is measured by the ICC (two way random-effect model, mean of k raters, absolute agreement, table 6.2). The agreement is very good (>95%) both on the whole dataset and on the single cohorts. ICC on Florbetaben is higher due to the relative lack of borderline cases in the graded evaluation (higher rate of AD-like diagnosis, table 6.1).

The Cohen k for agreement between pairs of reviewers ranged from 0.39 to 0.49 (fair agreement, table 6.8).

Table 6.8: Agreement between pairs of readers all tracers with respect to the grading evaluation using accuracy and Cohen k (within brackets).

	UPG	FN	AC	VG	MB
UPG		0.61 (0.48)	0.55 (0.44)	0.59 (0.46)	0.61 (0.49)
FN	0.61 (0.48)		0.60 (0.49)	0.62 (0.49)	0.62 (0.50)
AC	0.55 (0.44)	0.60 (0.49)		0.58 (0.46)	0.55 (0.43)
VG	0.59 (0.46)	0.62 (0.49)	0.58 (0.46)		0.53 (0.39)
MB	0.61 (0.49)	0.62 (0.50)	0.55 (0.43)	0.53 (0.39)	

Overall, the borderline scans were 10.8% (a non-trivial amount) whereas in the 35.2% of cases the readers defined the scan "mildly" positive or negative. A more detailed comparison among raters is shown in figure 6.7 (supplementary materials): this plot summarizes statistics and between readers agreement grouped by the 5 gradings. The heatmap representation (where color intensity is proportional to the number of scans) shows where discrepancies are more likely to occur. Besides the transition region, which is an obvious candidate, severe deviations from the diagonal (i.e. Δ grade >2) can occur on all grades, albeit on very few scans. Finally, we show the number of discrepancies grouped by severity in table 6.9.

Table 6.9: Number of scans with minor (Δ grade $\pm$ 1), mild (Δ grade $\pm$ 2) and severe discrepancies (Δ grade >2).

tracer	no discrepancy	minor	mild	severe
flutemetamol	19	21	16	6
florbetaben	26	22	5	0
florbetapir	8	29	20	3
all tracers	53	72	41	9

6.3.2   Visual assessment and semi-quantification

The model-mediated relationship between the grading and the quantifiers is shown in figure 6.1. There is no significant difference among models (z-score), both with respect to quantifiers and with respect to tracers (direct model, table 6.6). The transition region

width is very similar among tracers, showing that there is no substantial difference in assessing the negative/positive contrast both with different tracers and with different quantifiers. For instance, the ELBA transition region width (in z-score units) is 0.64, 0.66 and 0.67 for ^{18}F-Flutemetamol, ^{18}F-Florbetaben and ^{18}F-Florbetapir respectively. These numbers are all compatible when we consider the parameters uncertainty.

6.3.3 Evaluation latitude

We now group subjects by average evaluation and we plot them versus their mean quantification value (here the score on the PCA1). We can graphically represent the group's latitude by means of a line that spans the lowest and highest evaluation received by any member of the group (figure 6.3). We can glance at the latitude distribution and see that it tends to cluster in the mild negative to borderline region.

6.3.4 Binary assessment

Reader agreement is ranked according to Cohen k (table 6.5) and values ranges from 0.71 to 0.84 (substantial agreement). Accuracies based on binary semi-quantification (i.e. above/below cutoff) are reported in table 6.10.

The distribution of the binary reading is shown on the quantifier scatter-plot in figure 6.2. We see that pure classes {5n-0p, 0n-5p} nicely cluster in the lower-left and upper right quadrant respectively, whereas intermediate classes (particularly {2n-3p, 3n-2p}) tend to aggregate near both transition regions. Gray areas and gray lines are the transition regions and cut-off values derived from the intersection of the models with the mild-negative / borderline / mild-positive coordinates.

Table 6.10: Quantifiers accuracies.

tracer	SUVr	ELBA
flutemetamol	0.85	0.80
florbetaben	0.92	0.96
florbetapir	0.85	0.90
weighted average	0.87	0.89

6.3.5 Scan quality effect

The distribution of quality flags is shown on all tracers together versus the two PCA components computed on the quantifiers (figure 6.5 left). There is a marked bias towards negative-to-borderline scans while there seems to be no relation with respect to quantifiers discrepancy (PCA2 axis). Comparing quality to latitude, one would expect a positive trend linking the number of quality flags and the assessment discrepancies. Results shows that the latitude is substantially independent on the quality, hinting to a solid performance and coping ability of the trained eye (figure 6.5 right).
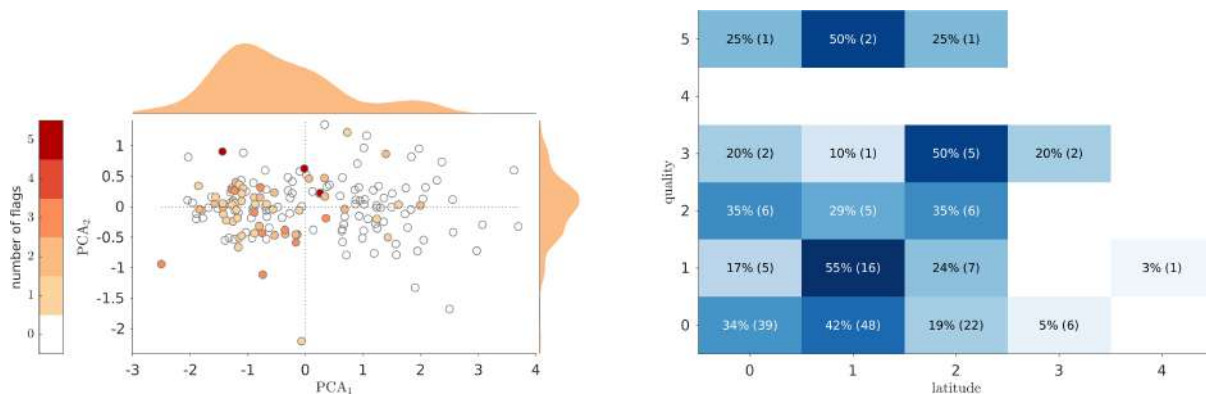
Figure 6.5: Left: distribution of the quality flags in the PCA plane; dots represent all scans, color is proportional to the number of quality issues raised by the 5 readers; marginal distribution shows the kernel density estimation. Right: heatmap of quality and latitude, showing the fraction of scans normalized on the quality and the actual number of scans sharing the same quality interpretation and evaluation latitude (within brackets).

6.3.6   CT subset comparison

We compute the intra-rater statistics on the assessments with and without the CT (88 scans, ~50% of the whole dataset). χ^2 statistics was calculated on all tracers and for each reader on both the grading and the binary frequencies. No significant difference was found on the grading (for all readers, $\chi^2 < 4.72$, p-value > 0.35) and on the binary evaluation ($\chi^2 < 0.75$, p-value > 0.38). The ICC on the grading, for all raters and on the whole CT dataset, is 0.982 [0.980 - 0.987].

The Cohen's k, computed on the grading and per rater, is: k = 0.65, 0.84, 0.76, 0.78, 0.85 for UPG, FN, AC, VG, and MB respectively. We conclude therefore that there is no significant difference in the evaluation statistics when the CT is present.

6.3.7   Mapping and validation

The complete set mapping functions between one tracer to another is shown in figure 6.6. The mapping function looks linear because of the substantial equivalence between model parameters (see table 6.6). We can then easily convert any value from one tracer's own units into another (in particular the cut-off and the transition region), as detailed in table 6.7.

Similarly we can use cohort containers (i.e. grouping subjects by average visual assessment lying between two adjacent gradings) to fit a linear regression. The cohort container regression does not require the sigmoid model and relies on the visual assessment only modestly, as we are fitting the average container values. Results show that the model fitting is well within the container regression error (see table 6.11 in the supplementary materials).
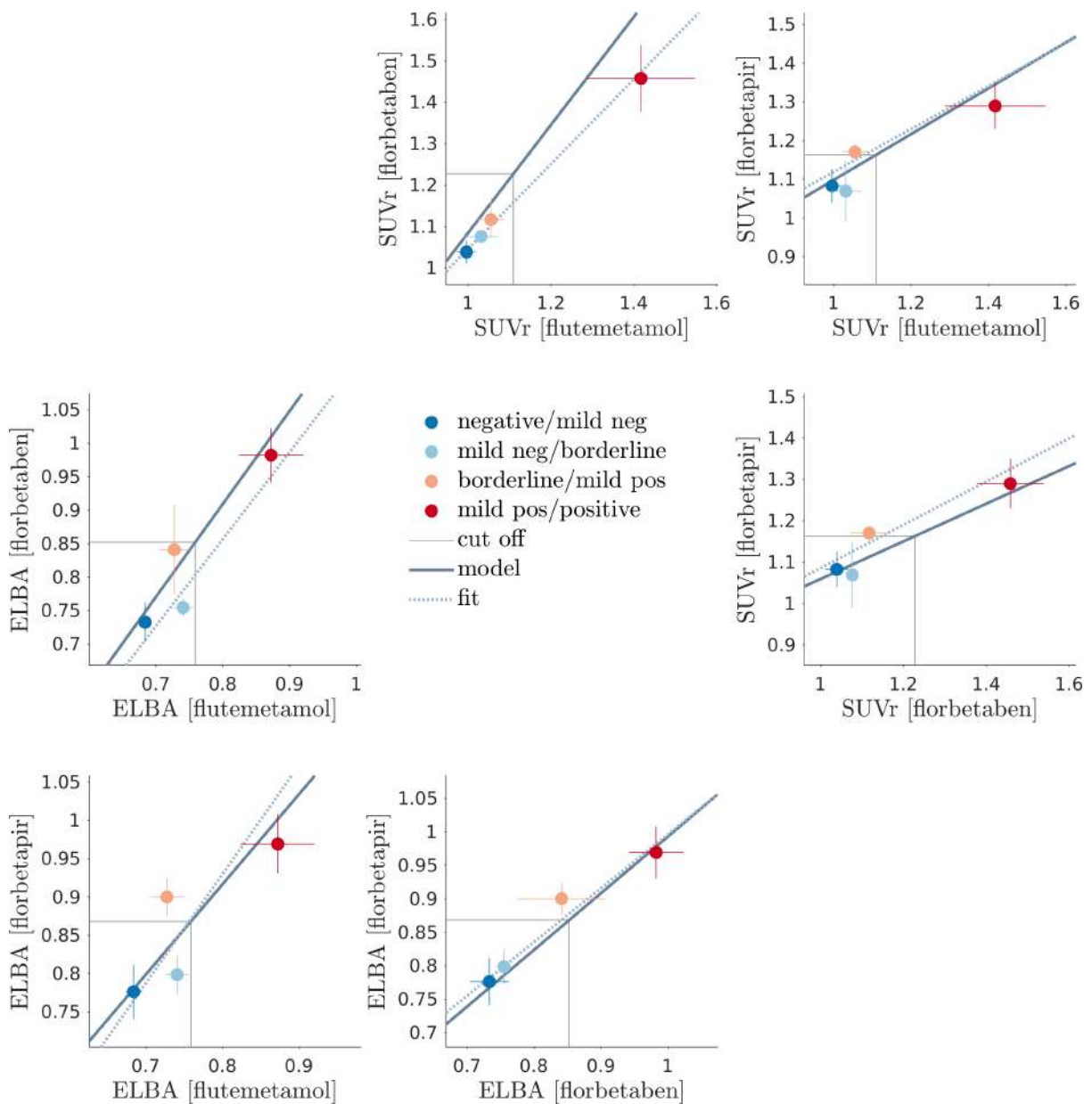
Figure 6.6: Matrix plot of all between-tracers models and container-cohort fits. Dots represent the average quantification on the cohort containers, lines crossing the dots are the standard deviations. The thick line is the model mapping, the dashed thin line is the linear regression based on the average quantification values (container mapping). Cut-offs are based on the model mapping.

6.4   Discussion

We have shown that it is possible to construct a map between different tracers and different quantification methods without resorting to ad-hoc acquired cases, as required in the centiloid approach or in studies where the same subjects are injected with more tracers. In doing this we, used a 5-level visual scale, to define cut-offs and transition regions on tracers in a way largely independent from the population.

The link between the graded visual scale and semi-quantification is the sigmoid model. The use of the sigmoid function simply derives from the considerations that the amyloid load is a biologically continuous process with two boundaries (i.e. satura-

tion at both the decidedly negative and positive range), which naturally translates in a smooth (i.e. infinitely derivable) function with finite limits and a near-linear response in the transition. Obviously, other functional models could do, and possibly with more data one could appreciate the asymmetry already partially visible in these data when transitioning from negative-to-borderline with respect to the borderline-to-positive.

The integration of model and grading allows to compare semi-quantification values regardless of the approach (either SUVr-based or SUVr-independent) and employed tracer. This combination (a) defines transition regions and cut-off values; (b) indirectly confirms the appropriateness of a visual evaluation scale which is more apt to recognize transitions (similarly to several other clinical and visual scales [243]).

As models have only two free parameters, derived quantities (cut-off, transition region) are more robust with respect to the sample size and can be easily generalized. The width of the transition region and the substantial similarity of the sigmoid models show that no tracer is the winner here, all are equivalently discriminating (i.e. no slope difference implies equivalent contrast). While to our knowledge there is no literature on tracers comparison within the same dataset and with the evaluation from the same set of readers, we can compare this result to Curtis et. al. [53], where the accuracy of all three fluorinated tracers in the phase-3 study is compared and similar conclusions are drawn. Importantly, the determination of a threshold for abnormality common across tracers is one of the required validation steps for the use of amyloid PET in AD following a recently proposed roadmap for biomarkers for an early diagnosis [85, 44].

As a by-product of the work, we have studied the relationship between concordance and discordance of readers according to some indicators such as the degree of negativity / positivity, the quality of the scan and the binary evaluation. On the reader concordance, first we notice a very good agreement among readers in binary lectures, accuracy ranging from 86% to 94%, meaning that in routine clinical practice only about one out of ten scans might be read with opposite conclusions. If on the one hand the present experimental setting does not fully reproduce the clinical reality where a doubtful scan is usually evaluated together by more than one reader and sometimes with the aid of semi-quantification tools (while here the raters were blind), on the other hand our raters were high to intermediate experts thus likely more skilled than the average of the real world. However, this figure is in keeping with other studies [49, 195]- if not higher - and points to the need of semi-quantification tools in assisting the nuclear medicine physician in the binary interpretation of scans. In more detail, when we look at the grading we see that while the overall observed ICC was very good, the discrepancies in the mild-negative / borderline regions (latitude) are rather significant. That is, despite the differences in expertise among readers and the multi-centre nature of the study, the learning curve for visual amyloid PET readings is not steep after a moderate degree of expertise has been acquired; on the other hand, evaluation errors are not evenly distributed across the positivity spectrum. Considering the three tracers altogether we observed a "U"-shape distribution with higher percentage at the two extremes and progressively lower percentages toward the borderline cases (see table 6.7 in supplementary materials). With individual tracers this pattern was less evident with flutemetamol disclosing a higher percentage in mild negative than in negative subjects while it was stronger with florbetaben. This mismatch could be due to the higher prevalence of subjects with AD and with non-AD conditions as compared to the flutemetamol cohort (table 6.1). As remark on the evaluations with and without the CT information, we first remind that readers have been trained to read amyloid PET scans as taken alone, leaving the use of

CT/MRI only in doubtful cases, as per approved courses administered by pharmaceutical companies on the respective products; second, readers are all rather experienced; third, evaluation results with and without CT scans are not identical but simply statistically equivalent. This latter statement means that there were indeed patients whose evaluation was changed because of the CT information, but the cohort statistical distribution was not significantly altered. We have to say we used data collected during clinical routine from sparse European centers and thus carrying inhomogeneity in scan quality and characteristics of patients. If this may have generated high variability among scans, it is however the reality collected in naturalistic cohorts and thus closer to the real world with respect to the setting of clinical trials. Inhomogeneities are also evident when looking at latitude scans, where the apparent different relationship with the tracers can be ascribed to the diversity of cohort provenance and statistics. Interestingly, however, we failed to find a correlation between scan quality and latitude (i.e., degree of differences among readers). This may mean that the intrinsic subjectivity in the human eye when reading an amyloid PET scan is higher than quality inhomogeneity among scans. This represents a distinct source of disagreement among readers that adds to the one possibly deriving from low quality [244].

Coming to the not-clearly positive/negative scans, we observed that almost half (i.e., 46%) of scans were visually rated either as borderline (10.8%) or mildly negative/positive (35.2%). Thus, the amount of transitional patients is considerable even in the clinical setting facing symptomatic patients and not only in the studies in the general population dealing with asymptomatic subjects. Apolipoprotein E ϵ-4 genotype is a major determinant of amyloid load but we miss this data in most patients so we cannot evaluate its influence on our population but it is likely other variables can act on amyloid deposition rate [97]. Moreover, differences in disease severity may also be reflected by differences in amyloid load among subjects with MCI [278].

This work, moreover, is timely regarding its possible clinical applications. Firstly, it could be used to indirectly compare anti-amyloid compounds in clinical trials based on different tracers to evaluate drug-specific differences in target engagement and efficacy in brain amyloid clearance, thus allowing a better understanding of their mode of action. Moreover, if and when an anti-amyloid agent will be approved for clinical use, availability of an approach to directly compare PET fluorinated tracers will probably allow to streamline the eligibility criteria evaluation and thus the treatment access. A further possible by-product of the availability of validated, tracer-independent cut-off and transition values that differentiate positive and negative scans is represented by their use during resident training to challenge the new readers with progressively difficult cases.

6.4.1 Study limitations

We have evaluated average tracer uptake in a volumetric ROI distributed in the whole brain without further analyzing regional differences. Some authors have reported that amyloid brain deposition in specific regions has higher predictive value toward transition to dementia or better correlate with cognitive impairment [46, 98].

This exploration was beyond the aim of the present study although the resolution of this issue might have been relevant to rate especially borderline cases. We plan to further explore this issue in the future with a more homogeneous patient sample.

Another limitation is that we lacked coregistered CT in a number of cases (50%), as only PET scans were transferred and for the oldest ones recovery of CT was unfeasible.

Indeed, it has been shown that reading amyloid PET with coregistered CT improves correct classification compared to PET scan alone [53]. However, we did not observe significant differences in classification intra- and inter-observer in the subset of patients (>50% of the whole sample) with CT available.

Finally, APOE information was available in less than 10% of all cases only. It is therefore omitted in the demographic table and it was not used in this study. However, we did not investigate the reason for positivity nor the interplay with demographic variables. The semi-quantification ranking, the visual grading and their relationship should therefore be independent from the APOE information.

6.5   Supplementary materials
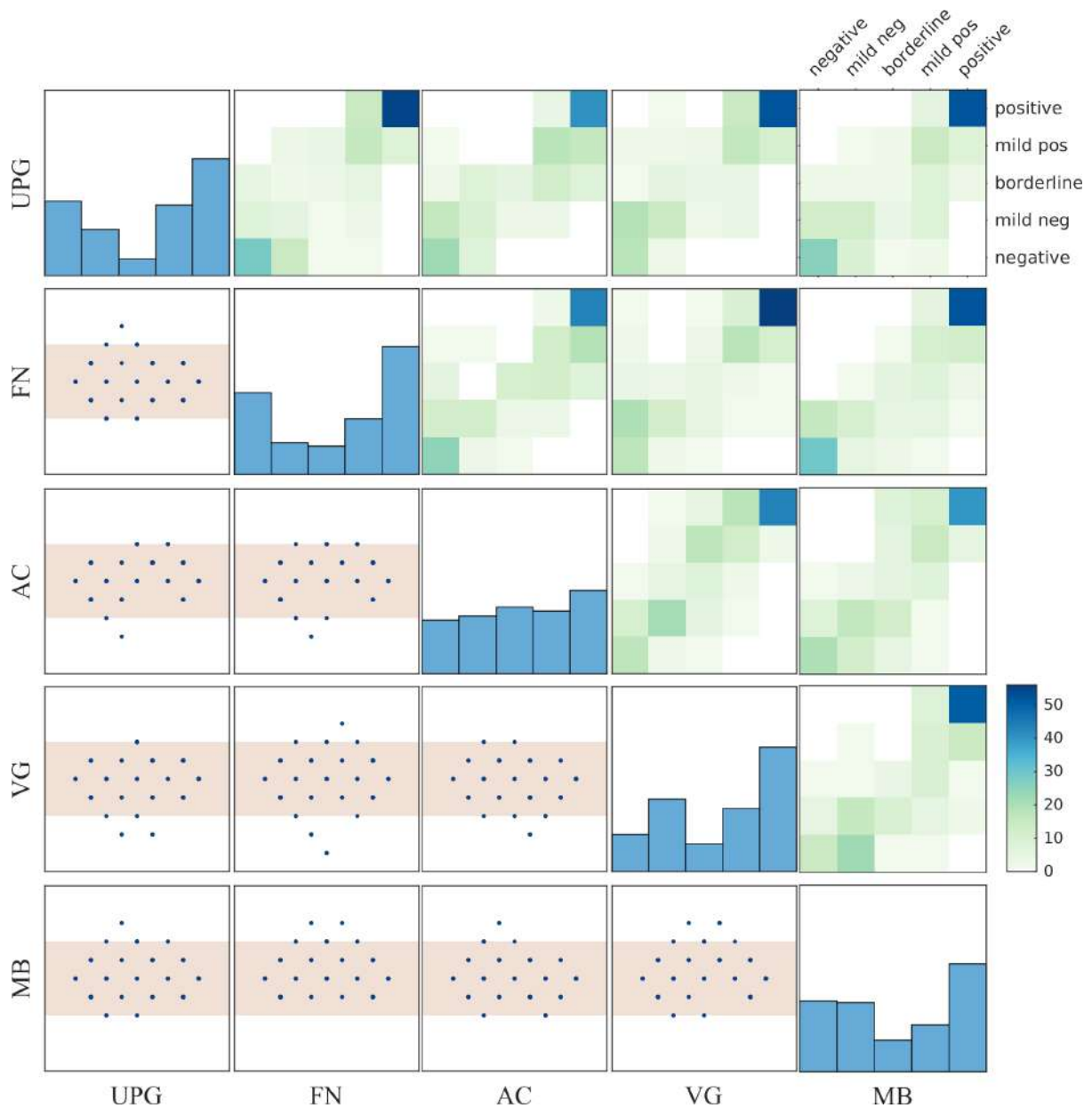
Figure 6.7: Reader concordance plot matrix (all 3 tracers combined). Labels: reader identifier. Diagonal plots: grades statistics for each reader. Upper triangular plots: between-readers heatmaps (number of scans per each grade pair); colors are proportional to the number of scans; white = no scans. Lower triangular plots: between readers Bland-Altmann plots; red band Δ grade = $\pm$ 2 (mild discrepancies).

Table 6.11: Conversion parameters between tracers (container cohort regression).

	ELBA	
from / to	florbetaben	florbetapir
flutemetamol	$1.30x$ [0.50 2.10] -0.18 [-0.77 0.40]	$1.42x$ [0.40 2.45] -0.21 [-0.96 0.54]
florbetaben		$0.80x$ [0.34 1.27] + 0.19 [-0.18 0.56]
	SUVr	
from / to	florbetaben	florbetapir
flutemetamol	$1.02x$ [0.27 1.78] + 0.02 [-0.76 0.80]	$0.55x$ [-0.01 1.12] + 0.57 [-0.04 1.17]
florbetaben		$0.52x$ [0.10 0.95] + 0.56 [0.08 1.05]

Chapter 7

A kinetics-based approach to amyloid PET semi-quantification

7.1 Introduction

The recent NIA-AA diagnostic framework [125] considers the direct (i.e., through PET imaging) or indirect (i.e., through cerebrospinal fluid, CSF, assay) evidence of abnormal brain beta-amyloid deposition as the characteristic signature to define the Alzheimer's spectrum in vivo. This position is shared nowadays by most researchers and clinicians and had been previously proposed by the International Working Group-II research criteria in 2014 [62]. In the past few years, thanks to a number of commercial fluorinated radiotracers, amyloid-PET has indeed emerged as a validated and effective proxy of brain amyloidosis [121, 277, 48, 258], becoming a major tool in the diagnostic process in order to confirm or, even more robustly, rule out Alzheimer's disease (AD) [125, 62], and for improving patient selection for clinical trials [288]. Currently, amyloid-PET assessment consists of a visual evaluation by trained nuclear medicine physicians complemented by the (still optional to date) support of a semi-quantification technique. The outcome is usually a binary evaluation (negative/positive) of the scan, at least in the clinical setting.

In the set of semi-quantification techniques, the Standardized Uptake Value ratio (SUVr) is the most widely used [139]. SUVr values represent the ratio of PET counts between one or more target regions of interest (ROI) versus a reference region. SUVr-based measures of amyloid-tracers uptake show good agreement both with histopathological measures of the density of neuritic plaques [48, 260] and with the binary classification obtained by CSF analysis [175] and visual assessment [260]. However there are several possible choices both in drawing target ROIs and in identifying reference ROIs for the purpose of amyloid status evaluation, and especially on the latter an agreement is still lacking [133]. In addition, SUVr values can be impaired by several factors, such as number of ROI, ROI drawing criteria [143, 264], partial volume effect (PVE) [254, 244], and regional cerebral blood flow (rCBF) fluctuations (particularly for longitudinal studies) [244].

In recent years, such variabilities have paved the way to explore alternative, SUVr-independent approaches, such as ELBA [43] - a ROI-independent method designed to capture intensity distribution patterns rather than actual counts - and the more sophisticated combined method SLOPE [37] which corrects for atrophy, spillover and blood flow using a PET/MRI acquisition and sophisticated post-processing steps.

Many of the SUVr noisances are due to methodological issues, such as differences

in ROI selection and placement [151]. In summary, the main issues that researchers are trying to overcome derive from i) instability or inconsistency of cortical ROIs (MRI-guided versus atlas-guided, hand-drawn versus automatic), ii) effect of rCBF changes between patients and intra-patient, possibly affecting tracer delivery to the cortex, iii) PVE, iv) lack of a standard in the choice of a reference region.

As a possible solution to address these issues, we propose an approach based on a dual-time point acquisition, whose ROI are adapted to the individual patient anatomic and pathophysiological characteristics. This approach does not need any template- or MRI- registration and may be suitable for longitudinal evaluations. We take into account the surrogate rCBF information extracted by an early ("*E*") PET static acquisition: high rCBF regions are concentrated in the cortical gray matter (GM) and are used to delineate the uptake ROIs. The reference ROI, instead, is defined on the standard static acquisition - late ("*L*") PET.

The ratio between the average intensities in the uptake ROIs (from the early scan *E*) and the reference ROI (from the late scan *L*) is named "time-delayed ratio" (TDr). The name underlines the fact that the uptake ROI is defined at an early time point in the acquisition (E) but it is used at a later time point (it is mapped onto the late scan L). TDr is therefore based on tracer kinetics, and the ROI are uniquely adapted to each individual by using two static acquisitions at the opposite ends of the time frame for a lipophilic tracer.

7.2 Material and methods

7.2.1 PET scans and subject selection

A set of 143 subjects consisting of 107 subjects from naturalistic populations (aged 54-87) and 36 elderly normal aging (NA) subjects - undergoing a comprehensive evaluation in the frame of previous studies - were acquired in four clinical centers with ^{18}F-Florbetapir PET.

The participating institutions were: Nuclear Medicine Unit, Department of Health Sciences (DISSAL), University and IRCCS Ospedale Policlinico S. Martino, Genoa, Italy (HSM-GE, 29 subjects acquired with a Siemens BioGraph HiRes 1080); Department of Nuclear Medicine, Fondazione Poliambulanza, Brescia, Italy (FPA-BS, 55 subjects acquired with a Siemens BioGraph 40 mCT); University Hospitals and University of Geneva, Geneva, Switzerland (HUG-GE, 40 subjects acquired with a Siemens BioGraph 128 mCT) and Nuclear Medicine Unit, IRCCS Istituti Clinici Scientifici Maugeri, Pavia, Italy (ICSM-PV, 19 subjects acquired with GE Discovery 690 VCT). Demographics and final diagnostic hypotheses are provided in table 7.1 and table 7.2. A further refinement taking visual assessment into account is shown in the supplementary materials (table 7.6).

Symptomatic outpatients underwent amyloid PET because of a clinical suspicion of AD which could not be confirmed (or ruled out) on the basis of standard clinical-neuropsychological assessment and morphological neuroimaging (usually MRI); a number of patients also had previously undergone brain ^{18}F-Fluorodeoxyglucose PET. Patients were enrolled according to the local clinical practice and in keeping with the international appropriate use criteria for amyloid PET [136]. No other selection criteria was set. Injected dose for HSM-GE, FPA-BS and ICSM-PV had an average of ~442 MBq (min 370 MBq, max 536 MBq), in compliance to the minimum dosage suggested by the

tracer manufacturer. Due to local regulations, HUG-GE injected dose ranged between [180, 220] MBq with an average of ~200 MBq.

Acquisition protocol was as follows: the patient was positioned into the scanner, injected with the tracer and acquired for 5-7 minutes (E). Then he/she was let out of the scanner and left resting for ~40 minutes (i.e. 50 min after the injection). Lastly, the patient was positioned again into the scanner for the L static acquisition (10 minutes) according to the tracer manufacturer indications. E and L were therefore acquired with patient repositioning and hence each scan needed its own CT for attenuation correction.

Table 7.1: Demographics.

Center	# subjects	Gender M/F	Age [95% CI]	Visual assessment Neg / Pos
FPA-BS	55	24/31	71 [69 72]	29/26
HUG-GE	40	19/21	72 [69 74]	24/16
ICSM-PV	19	9/10	76 [73 79]	7/12
HSM-GE	29	15/14	75 [72 78]	10/19

Table 7.2: Post-test diagnosis.

Center	NA	Diagnosis MCI / Dem.	Subtype MCI / MCI-AD / AD dem.	Subtype FTD / VCI / CBS / MSA
FPA-BS	9	12 / 34	12 / 0 / 19	6 / 6 / 2 / 1
HUG-GE	13	19 / 8	13 / 6 / 6	2 / 0 / 0 / 0
ICSM-PV	5	4 / 10	4 / 0 / 9	1 / 0 / 0 / 0
HSM-GE	9	6 / 14	4 / 2 / 14	0 / 0 / 0 / 0

Legend: NA, Normal Aging; MCI, Mild Cognitive Impairment; MCI-AD, MCI due to Alzheimer's Disease; AD dem, dementia due to Alzheimer's Disease; FTD, Frontotemporal Dementia; VCI, Vascular Cognitive Impairment; CBS, Cortico-basal Syndrome; MSA, Multisystem atrophy; Dem, Dementia.

7.2.2   Kinetics

The TDr is a semi-quantification method that is inspired by the absolute quantification approach. Initially, the tracer flows into the blood vessels and then migrates to the tissues. Thus, in the first 5-8 minutes the signal is dominated by the uptake in brain structures as a function of rCBF, so that E can be taken as a proxy of brain perfusion [289, 221, 51, 182]. Then, from E it is possible to select highly-perfused tissues and this selection is restricted to the broad cortical areas. Several studies compared rCBF in both gray matter (GM) and white matter (WM): MRI-based arterial spin labeling (ASL) studies reported that WM blood flow is 1.6 to 4.6-times lower then GM flow [266, 227, 8, 294], while PET perfusion studies showed 0.15 to 0.18 ml/g/min for WM [153, 186, 208] and 1.05 ml/g/min for GM [153] resulting in a GM/WM ratio of 5.8/1 to 7.0/1. A high rCFB in a tissue ensures that the tracer is properly delivered. If $A\beta$ is present in this tissue, the tracer will bind to it; otherwise, it will be quickly washed

out (good clearance). Therefore the selection of the relatively higher rCBF tissue in the brain - which largely coincides with the GM - is the best place to look for good contrast in the tracer uptake.

7.2.3   TDr computation

We denote by D_E the highest perfusion domain delineated on E and D_L is the highest uptake domain identified on L. These two domains are a collection of voxels defined on E and L as follows:

$$D_E = (v \in E | I_v \geq I_E^0) \tag{7.1}$$

$$D_L = (v \in L | I_v \geq I_L^0) \tag{7.2}$$

Where v represents the voxels, I_v is the intensity (counts) in v. I_E^0 and I_L^0 are thresholds applied on E and L respectively (typical values are I_E^0 = 0.85 percentile and I_L^0 = 0.99 percentile on the respective intensity distributions). In words, D_E and D_L are collections of voxels whose intensities are greater than a specified value (see figure 7.1). The TDr is then defined as:

$$TDr = \frac{<I^L>|_{D_E}}{<I^L>|_{D_L}} \tag{7.3}$$

The numerator of the TDr formula is the mean intensity in L ($<I^L>$), averaged on the voxels with high perfusion defined in E (D_E, equation 7.1). Clearly, a high value of $I^L|_{D_E}$ corresponds to a high uptake and vice-versa. As the absolute value of this intensity can vary among subjects for a number of reasons (injected activity, rCBF, physiological characteristics, etc.), this intensity must be normalized.

There are several choices for the reference ROIs according to the semi-quantification approaches that require normalization: the pons [155], the cerebellar GM or the whole cerebellum [48, 143, 148]. In recent years, concern has been raised about these reference regions: the small size of the pons or the peripheral position of the cerebellum in the field of view may introduce artifacts, and thus noise and variability in longitudinal measurements [40, 149]. These works, in agreement with other longitudinal studies [253, 82, 23], highlighted the potential advantages of a WM-based ROI as reference: reduction of the variability in longitudinal measurement, improvement of semi-quantification to track the increases of Aβ deposition and stability of SUVr at single subject level.

Since the delineation of the most appropriate WM region has not yet been standardized, it was decided to use the highest uptake domain (D_L), otherwise known as the "hot spot", which is typically located in the WM (a-specific uptake). The denominator of the TDr formula (equation 7.3) is therefore the mean intensity in L ($<I^L>$), averaged on the voxels with highest uptake (D_L).
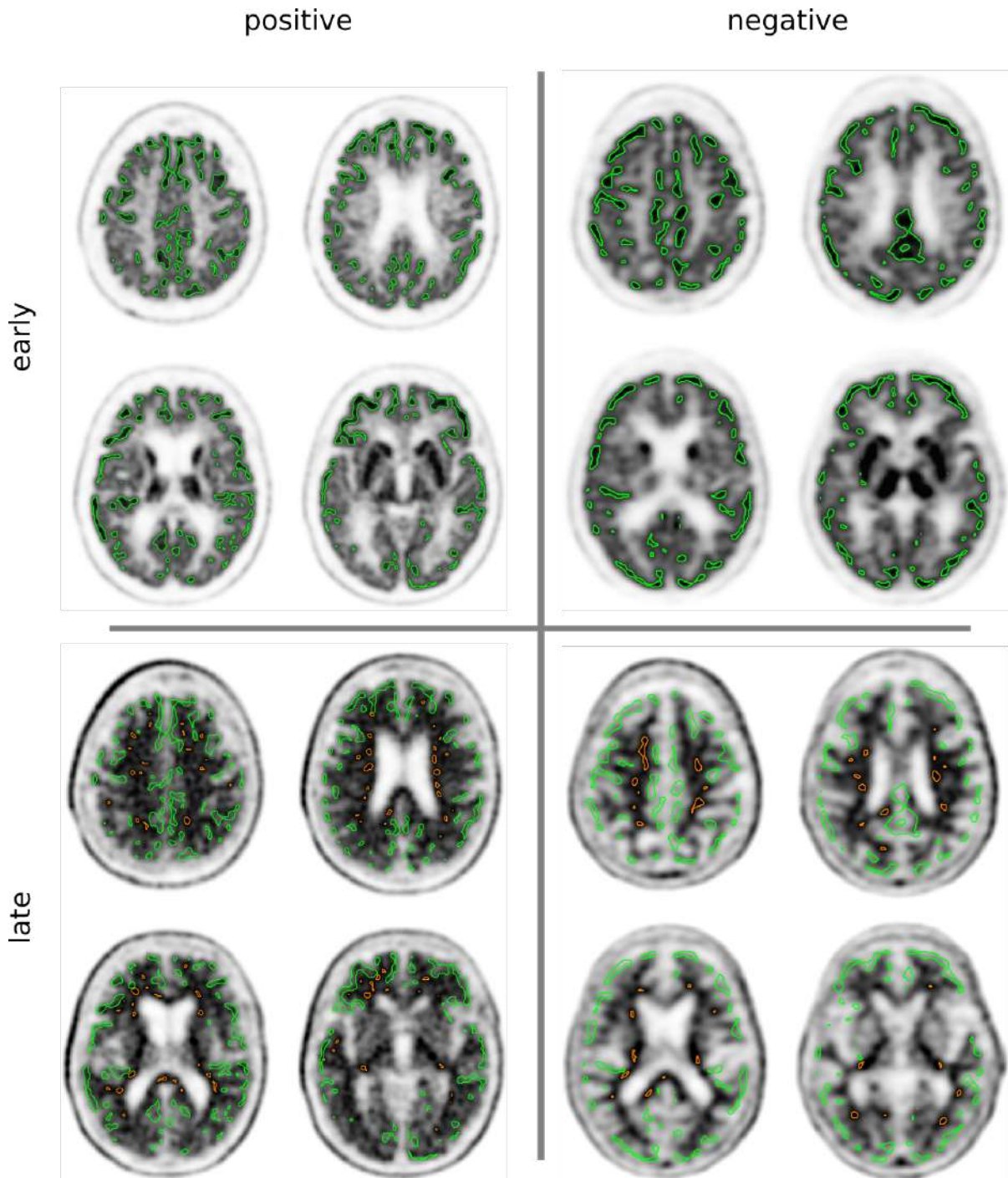
Figure 7.1: The early (E) and the late (L) scans of a positive and negative subject. On the E scans the highest flow domain (D_E) are outlined in green. On the L scans the highest uptake domains (D_L) are also outlined (in orange).

7.2.4   Threshold definition

MRI-based measurements of the cerebral cortical GM showed its thickness ranging from 2.5 ± 0.7 mm up to 3.74 ± 0.32 mm [78, 137, 117, 156]. As we look for amyloid presence in the cortex it is reasonable to select an intensity threshold I_E^0 that outlines a domain D_E whose thickness is comparable to the cortical GM thickness taking into account the spatial resolution and the point spread function. The threshold $I_E^0 = 0.85$

is defined as a quantile on the E intensity distribution: it is practically independent of the single subject scan and it can be defined once and for all. To show this we computed the threshold statistics on each patient finding the quantile corresponding to an average thickness $\mu = 3.0 \pm 0.16$ mm. It turns out that the quantiles cluster along the mean ($\mu = 0.847 \pm 0.036$). Moreover, small variations within these limits do not affect the TDr overall results.

Similarly, if D_L indicates the hot spot in the image, we choose the threshold $I_L^0 = 0.99$ percentile on the L scan intensity distribution. This value was chosen so that D_L is a non-negligible volume ($\mu = 13.47 \pm 1.2$ ml) and therefore less susceptible to intensity fluctuations. Further information on the threshold computation are in Appendix A, supplementary materials.

7.2.5   Image processing

TDr implementation is rather straightforward. It only needs a spatial registration of E onto L, so that D_E voxels can be mapped onto the late scan. This is done with a 6-parameters linear transformation, with the L scan as fixed image.

TDr can be implemented as an automatic procedure which does not require any supervision (save an image registration check after mapping the early scan onto the late scan).

In order to compare TDr with other semi-quantification methods (SUVr and ELBA) we spatially normalized all scans to the MNI space as an additional step. This procedure is identical to the one used in [43] and allowed us to take advantage of predefined MNI segmentations to provide the confidential volume C. The confidential volume was used to compute SUVr and ELBA values and therefore we now use it to constrain the domains D_E and D_L, so that TDr is compared to other semi-quantification methods using information coming from the same brain volume. The confidential volume C comes from the MNI lobe atlas and is defined as the whole brain parenchyma minus some specific regions: cerebellum, ventricles, brainstem and basal ganglia (figure 7.4 in supplementary materials).

The average cortico-cerebellar SUVr was computed following the approach described in [143], whereas the ELBA score was computed according to [43].

7.2.6   Validation

TDr values were compared to a) the binary visual assessment; b) two validated semi-quantification methods (SUVr and ELBA).

The 143 PET scans were assessed by two expert readers (one nuclear medicine physician - MB - and one neurologist with certified reader training for ^{18}F-Florbetapir and with 5-y experience in evaluation - FN) who reached consensus on the visual evaluation (i.e. negative or positive) on all scans. The discriminating power of the TDr was measured by the area under the receiver operating characteristic curve (AUC) for negative versus positive labeled scans. To get an estimate of the generalized performances of the TDr versus visual assessment we used a bootstrap procedure combined with a leave-10-out cross-validation. For each bootstrap step, 10 subjects were omitted (testing group), a cut-off value maximizing the accuracy was calculated with the remaining subjects (training group) and applied to the testing group. The whole process was repeated until all subjects were labeled: then the accuracy, sensitivity and specificity were calcu-

lated. The cut-off value was calculated as the mean of the cut-offs applied to the testing groups. This procedure was iterated 500 times.

TDr was compared to SUVr and ELBA, and performance measured by Pearson correlation. Finally, we looked at possible TDr-specific center effects with respect to SUVr and ELBA. In the last analysis, we looked at residuals in the linear models TDr-SUVr and TDr-ELBA in order to rule out non-linear relationships and to verify that TDr is indeed an independent measure of amyloid load. Residual analysis involved the Lilliefors normality test and the estimation of the Pearson correlation coefficient between the model residuals and the predictors.

7.3   Results

TDr performance versus the consensus binary visual assessment is summarized in table 7.3, together with SUVr and ELBA values. TDr shows excellent results both on the whole dataset and on single center cohorts.

Table 7.3: Performance (AUC) of TDr, SUVr and ELBA versus visual assessment.

Site	TDr	SUVr	ELBA
FPA-BS	1.00	0.99	1.00
HUG-GE	1.00	0.95	1.00
ICSM-PV	1.00	0.94	0.98
HSM-GE	0.99	0.92	0.99
Whole set	0.99	0.95	0.99

The bootstrapped, cross-validation results are summarized in table 7.4. Within the same procedure we computed the cut-off values: c_{TDr}= 0.611 [0.610 - 0.620] (95% CI). Similarly, c_{ELBA}= 0.956 [0.944 - 0.958] and c_{SUVr}= 1.133 [1.113 - 1.149].

Table 7.4: Bootstrap estimation of accuracy, specificity and sensitivity versus visual assessment calculated on the entire dataset.

	Accuracy	Specificity	Sensitivity
	[95% CI]		
TDr	0.945 [0.937 0.951]	0.933 [0.931 0.934]	0.957 [0.928 0.970]
SUVr	0.863 [0.846 0.881]	0.842 [0.831 0.859]	0.888 [0.854 0.908]
ELBA	0.955 [0.944 0.958]	0.958 [0.958 0.959]	0.953 [0.930 0.957]

Figure 7.2 shows the direct comparison of the quantifier values together with the visual evaluation (negative / positive label). c_{SUVr}, c_{ELBA} and c_{TDr} are also reported in figure. Correlation results are summarized in table 5. TDr significantly correlates with both SUVr and ELBA although it relates better with ELBA, as evidenced by the correlation coefficients on the negative and positive classes separately.
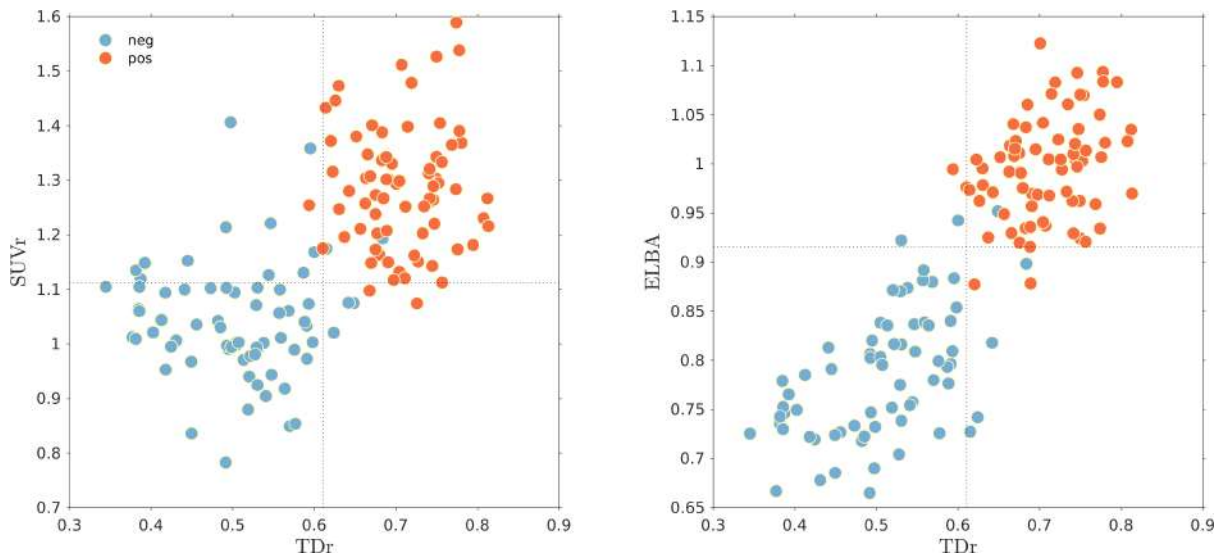
Figure 7.2: Scatter plot of all three semi-quantification methods versus the visual assessment. Dotted horizontal and vertical lines show the cut-off ($c_{SUVr} = 1.133$, $c_{ELBA} = 0.956$, $c_{TDr} = 0.611$).

The impact of scan provenance is shown in figure 7.3. Negative and positive scans are grouped by center and plotted on the same scale for all quantifier methods; the common scale being the z-score values computed on the whole dataset (figure 7.3 left). For comparison, figure 7.3 (right) shows the distribution of the whole dataset grouped by binary evaluation.
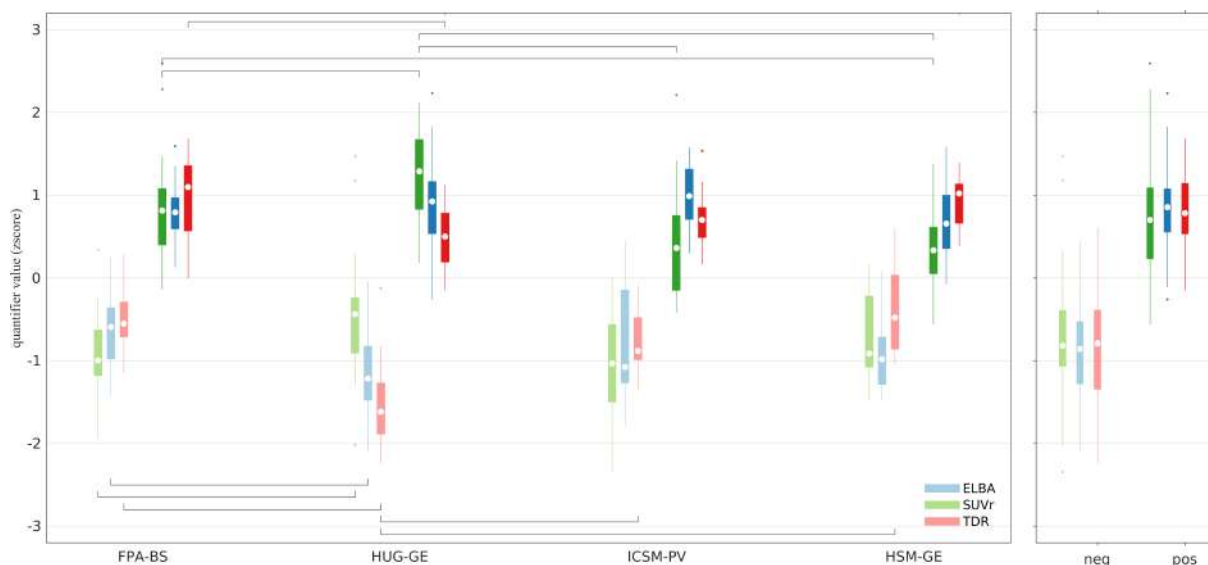
Figure 7.3: Boxplot of ELBA, SUVr and TDr (z-score) versus center and visual assessment (left). The whole dataset distribution (z-score) (right). Between cohorts (same method) significant differences are marked with brackets (t-test p-value < 0.05); a summary is also shown in table 7.5. Negative scans are represented with lighter hues, positive with darker hues. White dots inside the colored boxes are the medians.

For each method and for each visual class we computed t-test statistics among centers to look for possible bias in centers and/or methods. Significant differences are shown in figure 7.3 (left) and summarized in table 7.5. There is no clear pattern related to a specific center and/or method, rather, each method shows significant differences between cohorts

that seem unrelated to other methods.

Finally, we assessed whether TDr is an independent measure. We took a linear model in the form TDr = k_1 (ELBA) + k_2 and found k_1 = 0.849 [0.765 - 0.934] and k_2 = -0.149 [-0.226 - -0.073]. Similarly for TDr vs. SUVr, k_1 = 0.464 [0.370 - 0.559] and k_2 = 0.068 [-0.042 - 0.179].

Residual analysis showed no significant deviations from normality (Lilliefors test, p-value < 10^{-3}) in both models. Moreover, the residuals and the predictor were found to be uncorrelated and the linear regression of the residuals versus ELBA was found to be compatible with the null model. The same analysis was carried on by switching the dependent variable, and with TDr vs. SUVr; all yielded no significant relations. Graphical representations for this latter analysis are shown in figure 7.5 (left), figure 7.5 (right), figure 7.6 (left) and figure 7.6 (right) (supplementary materials).

Table 7.5: Significant differences among cohorts in each visual class and by quantifier method (t-test). Upper triangular slots refer to negative subjects (light hues), lower triangular slots refer to positive subjects (darker hues).

	FPA-BS	HUG-GE	ICSM-PV	HSM-GE
FPA-BS		X X X		
HUG-GE	X X		X	X
ICSM-PV		X		
HSM-GE	X	X		

X = ELBA; X = SUVr; X = TDr.

7.4 Discussion

This work describes a semi-quantification method to be applied to amyloid-PET scans. It is based on the typical properties of a non-receptorial tracer kinetics, that is, the radioligand exhibits a perfusion-like trait if acquired for a short time after the injection.

As ^{18}F-Florbetapir and the other radiopharmaceuticals to image brain amyloidosis are lipophilic, they cross the blood-brain barrier and distribute to the brain as a function of rCBF, with a ratio of about 0.8 (at least for ^{11}C PiB) [221]. It may be assumed that these early scans are a rCBF surrogate since a very good correlation has been demonstrated with ^{18}F-FDG PET data [54] according to the well known rCBF-metabolism coupling.

Clearly, a highly perfused region has the capability of good imaging contrast because it holds the highest probability of ligand binding (if amyloid is present) and high washout rate (when there is no amyloid). The drawback to exploit this information is that we need an ad-hoc acquisition consisting of two separate scans per subject.

We should underline though that the term "high-perfusion regions" does not signify a selection of the most perfused GM volumes. We identify the cortex areas by exploiting the differential flux between the WM and GM so that the "high perfusion regions" are indeed the "only" perfused regions. That is, the GM is in general more perfused than the WM.

When we select the 85% percentile on the global WM+GM brain ROI we actually select the only (relatively) more perfused part: the GM (plus some spill-over onto the WM).

Therefore, even when we consider a lesser perfusion of the GM due to aging, pharmacological treatment or atrophy, the GM will still be selected as the relatively more perfused part in the GM + WM volume. In other words, we don't select the highest perfusion ROIs within the GM, but rather we select the whole GM (be it normal or relatively preserved), which is identified in the same space and with the same resolution as the late PET image.

Some notable exceptions exist however, such as focal loss of perfusion due, for instance, to seizures, strokes or advanced atrophy. In these cases the D_E domain (i.e. the selected GM in the early scan) would not include these areas but we would not expect to evaluate them either.

Early image acquisition can provide insights regarding rCBF (which is coupled with metabolism and thus indirectly, with synaptic function/dysfunction) and at the same time can be exploited to help in the quantification of the late scan. Indeed, the introduction of early scans is becoming more and more popular for it is investigated to be a proxy even of ^{18}F-FDG PET [54, 205, 231, 40]. Besides, the acquisition of an early scan poses little inconvenience on the patient and on the scanner management.

We have therefore hope that more data will be available with two scans per subject, that we shall use to consolidate the validation procedure.

Methodologically, TDr relies on a (crude) estimation of high perfusion volumes, which are closely related to the cortical thickness. Works in literature show a rather large spectrum of values, depending also on the used techniques. These however should not be taken at face value as we must take into consideration the peculiarity of the estimation technique and its meaning and equivalent for PET. For instance, ASL-based perfusion values may be affected by partial volume effect and blurring that can lead to underestimation of GM and overestimation of WM perfusion amplitude. Anyway, we showed that the estimation of perfusion volume - defined by imposing a threshold on the intensity statistics of the early scan - is not overly critical, so that a mean value can be effectively used for the sake of robustness.

A particular, potential useful characteristic of TDr is that its computation depends on the definition of regions with the high rCBF and thus should be less affected by the issue of reduced tracer delivery because of focal hypoperfusion. This characteristic may be especially relevant not only in cross-sectional but even more in longitudinal studies because it is known that in AD as well as in other neurodegenerative diseases both atrophy increases and rCBF decreases with time as a function of hypometabolism. Using TDr should ensure that the cortical ROI are always positioned in regions with sufficient rCBF and not in severely atrophic or hypoperfused ones. Whether TDr could improve semi-quantification in longitudinal studies remains to be tested although preliminary analyses (to be published) seem to confirm this hypothesis.

Concerning overall performance, the TDr is an independent measure with very good accuracy and on par - if not better - with previously validated methods.

As TDr is mathematically similar to SUVr (a ratio between two uptakes, averaged over some ROIs), one would expect a closer relationship with it. Instead, we find TDr to be more related to ELBA, both as correlation on the whole population and on the separate negative and positive subjects. This could be ascribed to the inherent SUVr variability due to the fact that uptake and reference ROIs are pre-defined in size and positioning, which can lead to larger errors on the single subject. This variability underlines the need to use the subject's MRI when positioning ROIs, a step that was lacking in the SUVr computation of this study.

The intra-class correlation between TDr and ELBA impacts not only the TDr validation, but it also has pathophysiological implications: it confirms that the transition between the negative and positive state is neither abrupt nor untraceable and that the concept of borderline scans is actually not a mere technical nuisance.

Results grouped by center show some uneven behavior. The discrepancies can depend on several factors: on the one hand there is heterogeneity in patient selection, scanner and the image reconstruction protocol; on the other hand, each semi-quantification method may respond differently to scan type, quality and reconstruction parameters.

We argue that the latter hypothesis is indeed the most likely, as we do not see a consistent response of all methods on a particular center; rather, differences are scattered in methods, centers and visual assessment. It is therefore likely that significant cohort differences can be attributed to the sensitivity each quantifier has with respect to the hardware and reconstruction parameters, that is due to the specific methodological approach. For instance, the peculiar response for HUG-GE could be explained by the larger number of NA subjects and by the difference in acquisition protocol (lowest injected dose paired with the newest scanner model).

Among the technical heterogeneities we could mention the variability on the acquisition time of the early scan, which might be of concern since it captures a significant transient in the kinetics. The early scan timings defined in this work (5-8 min) has been agreed upon by our Nuclear Medicine physicians to be a reasonable range that takes into consideration the variability due to patient handling and possible nuisances in the positioning in the scanner. In practice though, all participating centers followed the stricter acquisition interval [0 min - 1 min] as the starting time, to [5 min - 7 min] as the end time. As a concluding remark, one might observe from table 7.5 that ELBA is different among centers in just one case while SUVr is different in 4 cases and TDr in 5 cases. Indeed, the lack of uptake and reference regions that characterizes the ELBA method is a strong point in favour of this approach and might explain the better robustness with respect to data provenance. However ELBA is not immune to the nuisances typical of multicenter studies, such as the signal-to-noise ratio and severe differences in the image reconstruction methods (as also discussed in [42]). Hence, we believe there is no single winner in the semi-quantification race, but all methods must be considered and - possibly - integrated in order to deliver more reliable results. On this note, and taking into consideration the residuals independence, we argue that a suitable weighted average of all three methods would be a more robust estimate of the brain amyloid burden.

7.4.1 Study limitations

The main limitation of this study is the lack of histopathological validation. While this is true for most semi-quantification works, this study also lacks the cerebrospinal fluid (CSF) assays. In our dataset we only have a handful of patients with CSF-$A\beta_{1-42}$ and tau assays and these were collected from different centers (3 from HSM-GE and 6 from HUG-GE); a plot summarizing these data is provided in the supplementary materials (figure 7.7). While we believe that a further validation of TDr should entail the comparison with $A\beta_{1-42}$ CSF levels, we can point out that ELBA was successfully compared with CSF on a much larger number of subjects and that the strong correlation of TDr with ELBA suggest that TDr would perform equally well.

Another limitation of this study is the lack of data with other fluorinated tracers. This is an unfortunate consequence caused by the need of the supplementary early acquisi-

tion, which is usually not available in larger, public dataset such as the ADNI. However, we refer to Chincarini et al. [42] for a thorough validation of ELBA and SUVr on a naturalistic population using all three fluorinated tracers. The substantial equivalent of all tracers both for negative/positive contrast and between quantification methods, together with the similar non-receptorial characteristics, suggest that the TDr should perform similarly on the other tracers (florbetaben and flutemetamol).

7.5 Compliance with ethical standards

The scans were acquired in the clinical setting for diagnostic purposes. All subjects (or their legal representative, if demented) were informed that their scans would have been used for research purposes and gave their written consent. All procedures performed were in accordance with the ethical standards of each local institutional Ethics Committee and with the 1964 Helsinki declaration and its later amendments or comparable ethical standards. The supervising ethics committee for this study is the CER (Comitato Etico della Regione Liguria), based in Genoa, Italy. Ethics Committees approvals included the transfer of imaging data, all anonymized brain amyloid-PET were collected from the centers in DICOM format.

Quality of images was checked by an experienced Nuclear Medicine Physician (S.M.).

7.6   Supplementary materials

Table 7.6: Post-test diagnosis grouped by amyloid PET visual assessment (negative + positive).

| Center | NA | Diagnosis subtype | |
		MCI / MCI-AD / AD dem.	FTD / VCI / CBS / MSA
FPA-BS	9+0	12+0/ 0+0 / 0+19	3+3 / 4+2 / 0+2 /1+0
HUG-GE	11+2	11+2/ 0+6 / 0+6	2+0 / 0+0/ 0+0/ 0+0
ICSM-PV	5+0	2+2 / 0+0 / 0+9	0+1 / 0+0 / 0+0 / 0+0
HSM-GE	8+1	2+2 / 0+2 / 0+14	0+0 / 0+0 / 0+0 / 0+0

Legend: NA, Normal Aging; MCI, Mild Cognitive Impairment; MCI-AD, MCI due to Alzheimer's Disease; AD dem, dementia due to Alzheimer's Disease; FTD, Frontotemporal Dementia; VCI, Vascular Cognitive Impairment; CBS, Cortico-basal Syndrome; MSA, Multisystem atrophy.
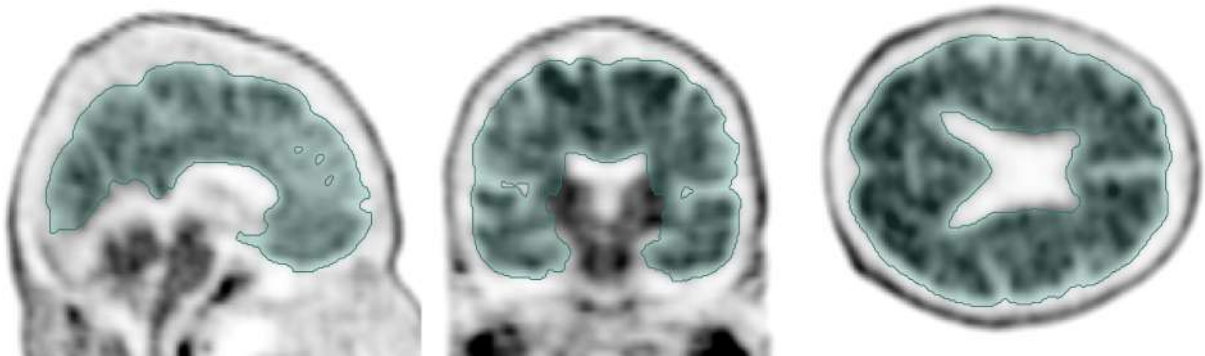
Figure 7.4: An example of the confidential volume C (coronal, sagittal and axial views). From the brain parenchyma the cerebellum, the ventricles, the brainstem and the basal ganglia are excluded.
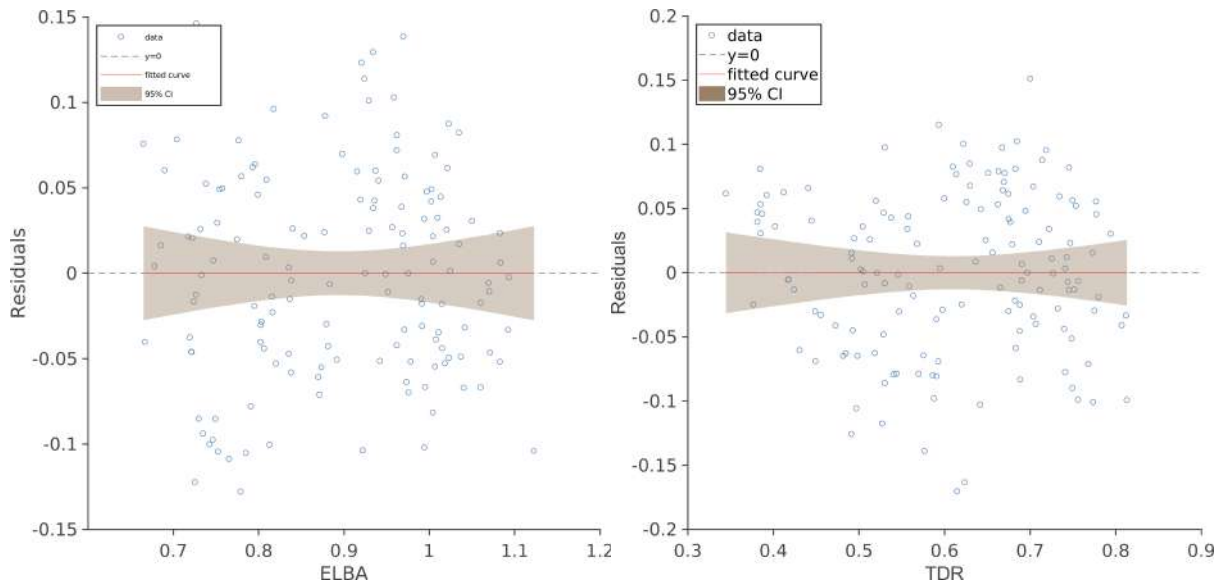
Figure 7.5: Residuals of the linear regression TDr~ELBA versus ELBA (left). Residuals of the regression ELBA~TDr versus TDr (right). The red line represents the fitting curve, the brown area represents the 95% confidence interval. The dashed line represents the equation y = 0.
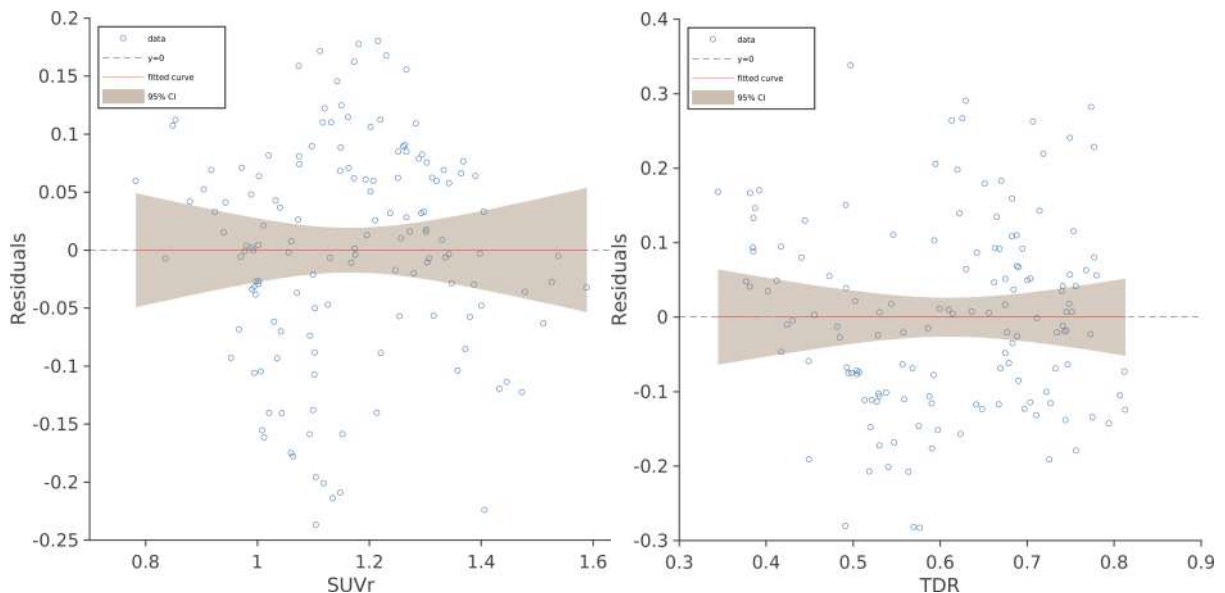
Figure 7.6: Residuals of the linear regression TDr~SUVr versus SUVr (left). Residuals of the regression SUVr~TDr versus TDr (right). The red line represents the fitting curve, the brown area represents the 95% confidence interval. The dashed line represents the equation y = 0.
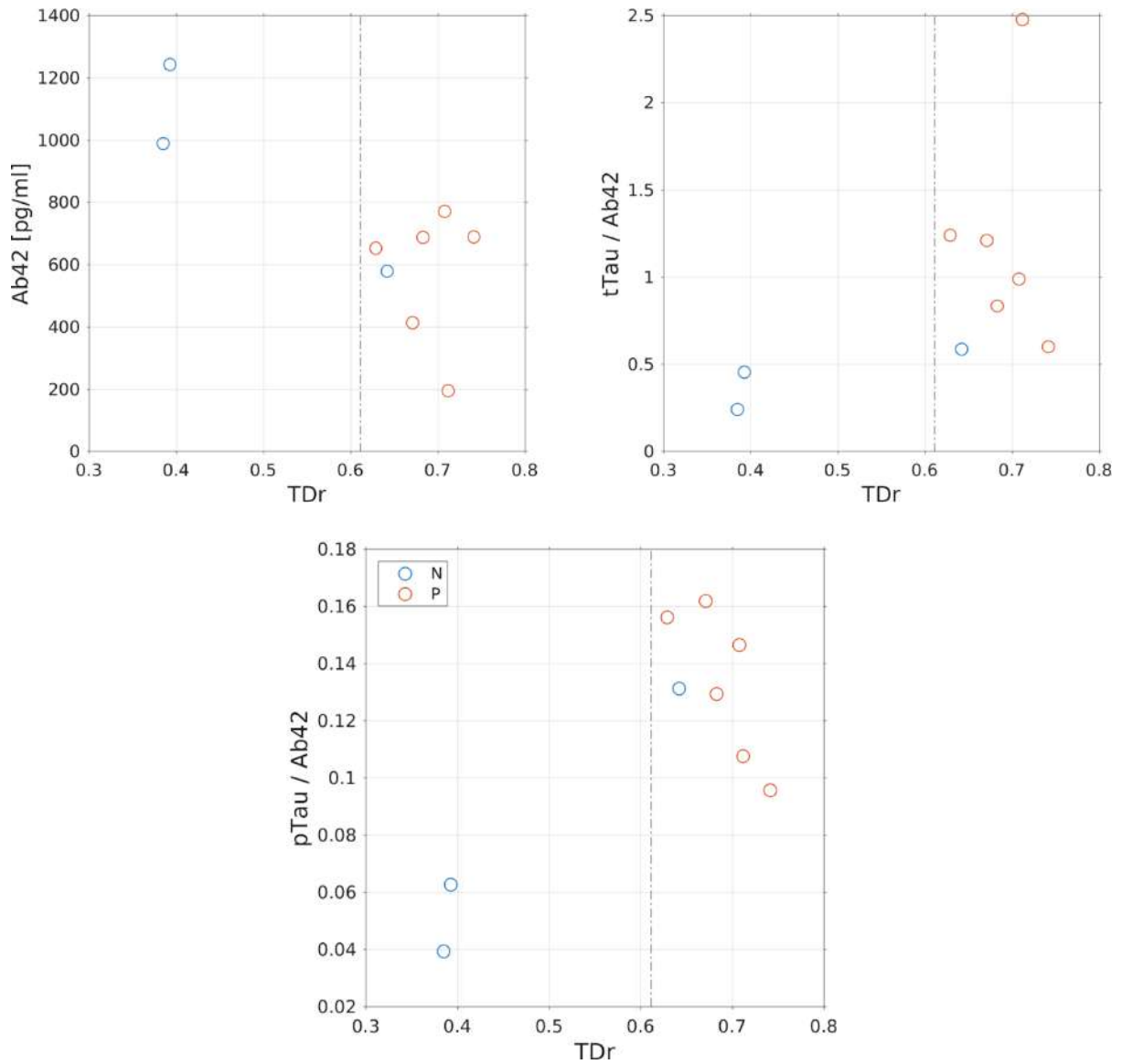
Figure 7.7: CSF protein concentration versus TDr grouped by visual assessment (negative, positive). Amyloid beta 1-42 ($A\beta_{1-42}$), total Tau (tTau) and phosphorilated Tau (pTau). The dotted vertical line shows the cut-off on the TDr values.

7.6.1   Appendix A: threshold computation

We detail here the basics of the threshold calculation (I_E^0 and I_L^0). The average ROI thickness was computed on all early scans and for different threshold values (quantiles), so we have one average thickness per patient.

In figure 7.8 we show the average thicknesses versus the quantile. We see that setting $I_E^0 = 0.85$ appears reasonable, as the dispersion is low and it encompasses the thickness range found in literature ([2.5 - 3.74] mm). Conversely, we also looked at the I_E^0 value that corresponds to an average thickness of 3 mm.

Figure 7.9 shows the distribution of I_E^0 due to a fixed average 3 mm thickness. The quantiles distribution mean is $\mu = 0.847 \pm 0.036$.

A threshold based on quantile value (therefore a relative value) instead of an absolute cutoff is a more robust approach with respect to inter-individual variabilities. A percentile-based threshold depends on the single scan's intensity distribution which is not affected by normalization. According to the manufacturer's information for the tracer (Eli Lilly and Company. *Amyvid^{TM} (florbetapir [18F] injection*) for intravenous use prescribing information, December 2013. http://pi.lilly.com/us/amyvid-uspi.pdf.), the normalization on the maximum intensity is recommended for a correct assessment. Thus, the threshold on I_L^0 was set to delineate a non-negligible volume D_L on each scan ($\mu = 13.47 \pm 1.2$ ml) which is less susceptible to intensity fluctuations but, at the same time, contains the maximum intensity of each scan.

Figure 7.8: Average thicknesses varying I_E^0 in a range from 0.75 up to 0.95. The dark area represents twice the standard deviation of the average thickness with $I_E^0 = 0.85$ ($2\sigma = 0.317$).
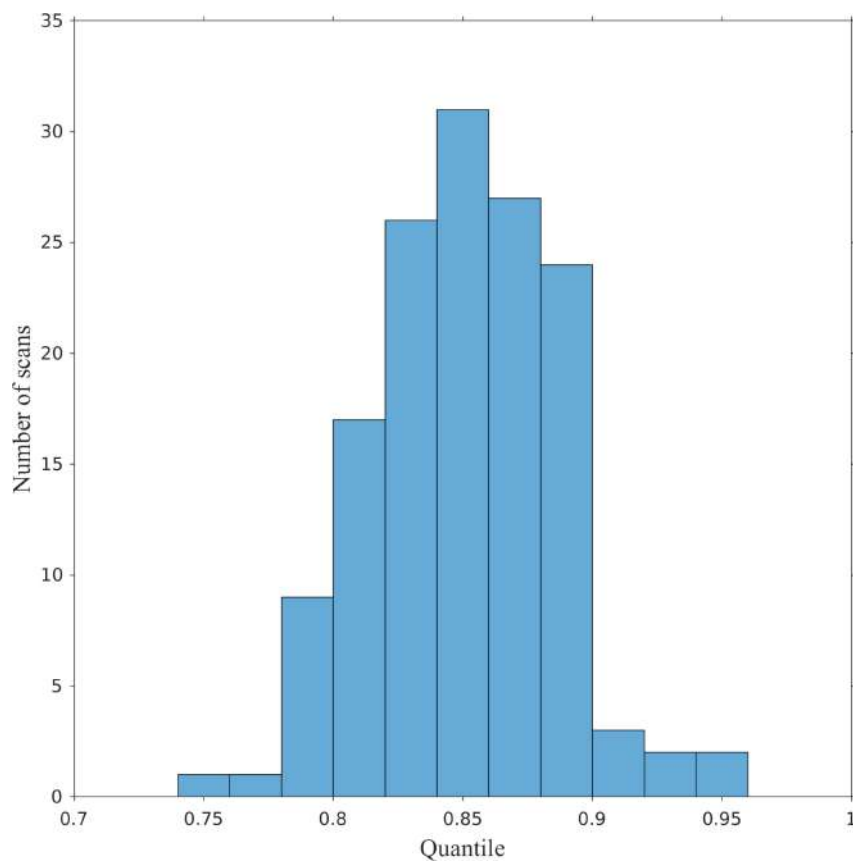
Figure 7.9: Distribution of quantiles I_E^0 used to outlines a domain D_E whose average thickness is 3 mm.

Chapter 8

Probing the role of a regional quantitative assessment of amyloid PET

8.1 Introduction

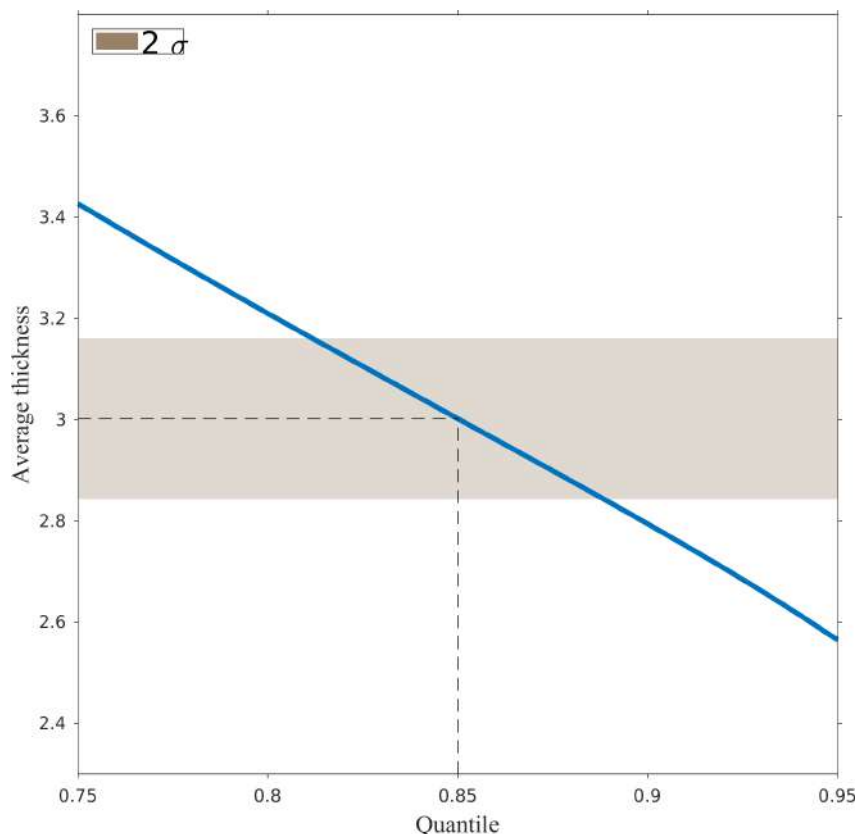Amyloid PET (amy-PET) allows to evaluate the presence of increased brain amyloid-β (Aβ) deposition, the hallmark of Alzheimer pathology. This occurs in virtually all patients with Alzheimer's disease (AD) [125], in other neurodegenerative diseases (such as dementia with Lewy bodies, DLB [240], as well as in otherwise healthy elderly subjects [286, 145, 132].

In AD, according to the biomarker-based model, the Aβ accumulation starts many years before symptoms onset: thus, patients are expected to have already reached the plateau of Aβ deposition at the time of the diagnosis [127].

In clinical practice, the amy-PET is visually inspected to provide a binary positive/negative outcome; it has a high negative predictive value, representing a robust tool to reject AD diagnosis in case of a negative scan [136]. The positive predictive value is milder and strongly relies on subject age and on pre-test probability level of having AD, due to the high prevalence of isolated brain amyloidosis in the elderly [136].

Borderline amy-PET results have been reported not only in the general population where they can be expected during the accumulation stage, but even in patients with cognitive symptoms and suspected to be affected with AD or another dementia [214]. Indeed, Aβ accumulation represents a dynamic process and thus a dichotomic reading may not be adequate with respect to the underlying biological phenomenon.

Semi-quantitative methods are available to help visual reading, among those the standardized uptake value ratio (SUVr) based methods are the most used [139]. Compared to visual readings, semi-quantitative methods can also be used to characterize the regional differences in amyloid-β deposition.

To date, local Aβ burden has not been associated with specific clinical symptoms. However, recent studies have shown that exaggerated accumulation in basal ganglia is a marker of a more severe AD clinical course [105, 46], but other regions might contribute [212, 177]. Indeed, the spreading patterns of Aβ and whether different trajectories of regional accumulation exist among patients are not well understood yet.

With the aim of investigating the role of regional amyloid-β burden and its implication on clinical-neuropsychological features, we performed a regional analysis of Aβ load

in a naturalistic cohort of patients undergoing amy-PET for a suspect of AD.

Our a priori hypothesis is that the distribution of amyloid is not homogeneous across brain regions, but different regions are characterized by a different degree of amyloid deposition [22].

This hypothesis is in line with the known progression of amyloid deposition in AD brain from neuropathological studies, however it has not been previously used to guide our approach to amy-PET imaging interpretation. Indeed, to date only the whole brain amyloid-β load is used in the majority of amy-PET studies, while the presence of regional differences in the Aβ burden is often neglected. This limited focus on whole brain metrics is unusual in the application of imaging metrics to study the physiopathology of neurological diseases, as shown for example by the development of regional metrics of damage as aids in the diagnostic processes in other conditions such as multiple sclerosis [164], or by the focus on regional patterns of hypometabolism in FDG-PET studies of neurodegenerative conditions [55].

8.2   Material and methods

8.2.1   Patient selection

We retrospectively enrolled 109 consecutive patients (aged 54-87, $\mu = 72.2 \pm 5.8$) who underwent amy-PET for a clinical suspicion of AD. Patients were evaluated for a first assessment of cognitive complaints with standard clinical evaluation, including screening blood and urine exams, neurological and neuropsychological evaluation, structural neuroimaging (Magnetic Resonance Imaging, in most cases) by the memory clinic of University Hospital in Genoa.

In the case the caring physician was still unconfident with the diagnosis, at the end of the diagnostic procedure, the patient was asked to undergo amy-PET.

The 109 patients were selected from a naturalistic dataset following these criteria: they were symptomatic subjects with suspicion of AD, but whose diagnosis could not be confirmed in the absence of amyloid status. Those who underwent amy-PET shared this background: i) a cognitive complaint with objectively confirmed impairment; ii) AD as a possible diagnosis, but when the diagnosis is uncertain after a comprehensive evaluation by a dementia expert; and iii) when the awareness of the presence or absence of amyloid-beta pathology is expected to increase diagnostic certainty and alter management.

The amy-PET examination observed the appropriate use criteria [136], that is: i) patients suffered from persistent or progressive unexplained mild cognitive impairment, ii) patients satisfied core clinical criteria for possible AD because of unclear clinical presentation, either atypical clinical course or etiologically mixed presentation and iii) patients showed progressive dementia and atypically early age of onset (usually defined as 65 years or less in age). Thus, the diagnoses were defined after the information on amyloid status determined by the amy-PET.

The neuropsychological examination included: (1) test of semantic and phonological verbal fluency to assess language; (2) Trail-Making Test (TMT) A and Stroop color-word test to assess attention and working memory; (3) TMT B, Stroop color test and symbol-digit for executive functions; (4) Rey Auditory Verbal Memory Test (immediate and delayed recall) to investigate verbal memory; (5) figure copying of the mental deterioration battery (simple copy) to assess visuoconstruction abilities. Mini-mental state examination (MMSE) was used as a measure of global cognitive function. The 15-item

geriatric depression scale (GDS) was administered to rule out depression. Moreover, patients underwent baseline clinical evaluation, including clinical interview and questionnaires for ADLs, IADLs and Clinical Dementia Rating (CDR) in order to assess the presence of dementia.

Raw scores were converted into z-scores, computed using normative population reference data as previously reported [200].

Further information on neuropsychological assessment, demographics and final diagnostic hypotheses are reported in table 8.1. ApoE genotypes were available for 51 patients (details are provided in the supplementary material, Appendix A).

Table 8.1: Demographics, final diagnostic hypotheses, and neuropsychological assessment for the overall dataset and grouped by low, mid, and high global Aβ levels. Apart from the MMSE, all the neuropsychological tests are reported as z-scored values.

		Overall	Low	Mid	High
Demographics	Sample size	109	36	36	37
	Age [y]	72.2±5.8	73.6±4.8	73.2±5	69.9±6.7
	Sex (M%)	50.4%	55.4%	52.7%	43.2%
	Education [y]	10.2±4.3	9.7±4.4	10.1±4.4	10.8±4.3
Final diagnostic hypotheses	MCIAD	51	6	22	23
	PseudoD/SCI	15	11	4	-
	MCI undetermined origin	6	6	-	-
	probAD	27	4	9	14
	probFTD	10	9	1	-
Neuropsychological tests	MMSE score	26.2 [13 30]	25.7 [13 30]	26.6 [21 30]	26.3 [18 30]
	RAVLT Immediate	-3.1±1.6	-3.1±1.5	-3.2±1.9	-3.1±1.5
	RAVLT Delayed	-2.5±1.4	-2.4±1.3	-2.4±1.4	-2.7±1.1
	Semantic Verbal Fluency	-1.5±1.2	-1.4±1.3	-1.5±1.3	-1.5±1.1
	Visuoconstruction	-0.7±0.9	-0.7±0.9	-0.5±1.0	-0.8±0.9
	TMT-A	-1.6±1.5	-1.5±1.5	-1.8±1.5	-1.4±1.5
	TMT-B	-2.0±2.0	-2.0±2.4	-2.1±2.0	-2.0±1.5
	Symbol Digit	-0.5±1.5	-0.7±1.3	-0.1±1.5	-0.7±1.8
	Stroop Colour	-1.0±0.9	-1.0±1.1	-1.2±0.9	-0.7±07
	Stroop Colour and Word	-1.0±0.8	-0.8±0.9	-1.1±0.8	-1.0±0.5

MMSE, Mini-Mental State Examination; MCIAD, Mild cognitive impairment due to AD; PseudoD, Pseudodementia (Depression-related cognitive dysfunction); SCI, subjective cognitive impairment; probAD, probable AD dementia; probFTD, probable frontotemporal dementia; RAVLT, Rey Auditory Verbal Learning Test; TMT, Trail making test.

8.2.2   Amyloid PET acquisition

Amy-PET were acquired with a PET/CT system (Siemens BioGraph 16) following the recommendations of tracer manufacturers and the guidelines provided by the European Association of Nuclear Medicine and the Society of Nuclear Medicine [184]. Scans were acquired with all the fluorinated tracers available at the time of the examination, (i.e.: ^{18}F-Flutemetamol, 36 subjects; ^{18}F-Florbetapir, 59 subjects and ^{18}F-Florbetaben, 14 subjects) and reconstructed on a 256×256 matrix with a voxel size of 1.33×1.33×2.00

mm. Injected doses ranged between 185 MBq and 370 MBq in compliance to the dosage suggested by the tracer manufacturer [66, 219, 90].

Each scan was visually assessed by 2 independent trained nuclear medicine physicians with a binary output (31 negative, 78 positive), discrepancies were resolved by consensus. No statistically significant differences were observed in neuropsychological assessment between the amyloid-positive and negative patients (t-test, p>0.05). This is in line with the naturalistic quality of the dataset as all subjects underwent an amyloid PET scan in order to clarify the diagnosis of an already established cognitive deficit, although of various etiologies.

This study was approved by the local Ethics Committee; all subjects gave written informed consent to undergo amyloid PET in accordance with the Declaration of Helsinki as well as to have their anonymized data used for retrospective research.

8.2.3 Image processing

In addition to the binary reading, all the amyloid PET scans were analysed with two independent semi-quantitative approaches or quantifiers: SUVr and ELBA.

The SUVr [139] is defined as the ratio of counts between a target region of interest (ROI) and a reference one. The whole cerebellum was used as reference as it is demonstrated to provide measures less prone to segmentation error than other choices (i.e: cerebellum gray matter, brain stem) [244].

ELBA is a SUVr-independent approach designed to capture intensity distribution patterns that are global properties of the whole brain and do not require a reference ROI [43].

The PickAtlas toolbox [169], was used to divide the supra-tentorial gray matter into 11 ROIs for each hemisphere, as detailed in table 8.2. ROIs in the left hemisphere were progressively numbered, from anterior to posterior, from 1 to 11. The same numbering order was applied in the right hemisphere so that the ROI 1 and 12 were homologous as well as the 2 and the 13 and so on. The brain parcellation is shown in the supplementary figure 8.6.

Regional SUVr and ELBA were calculated on these 22 ROIs that were maintained large enough to be less susceptible to intensity fluctuations (average volume: $\mu = 54.8 \pm 28.8$ ml). In order to compare measures obtained from scans acquired with different tracers we mapped the results of the two quantifiers with a reference model of uptake conversion into the same tracer (^{18}F-Florbetapir, which is the most common in the dataset) [42].

The inter-independence of ELBA and SUVr enabled us to combine them in a single, more robust score. Thus, the geometric mean of the two quantifiers provided a regional quantification for each ROI.

The two quantifiers were applied onto the spatially-normalized image [42]. Each scan was mapped onto the MNI space (isotropic spacing, voxel dimension $1.00 \times 1.00 \times 1.00$ mm) with a multi-step registration procedure consististing in global intensity re-scaling, rigid registration and affine registration. Then, the 22 ROIs atlas and the cerebellar ROI were mapped from the MNI space to the affine-transformed PET with a deformable registration.

The ANTs registration toolkit [9] was used with the mutual information metric.

Table 8.2: List of the 22 ROIs. In the Composition column each ROI is defined and the corresponding name is listed in the Label columns. Since the atlas is symetrical, the ROIs were progressively numbered from 1 to 22 (columns #). The ROIs were numbered according to their position, from anterior to posterior: in the left hemisphere the ROIs were numbered from 1 to 11, whereas in the right one they were numbered from 12 to 22.

Composition	#	Label (L)	#	Label (R)
Insula, Rolandic operculum	1	Insular cortex	12	Insular cortex
Superior, middle and inferior occipital gyrus, lingual gyrus, cuneus, calcarine sulcus	2	Occipital cortex	13	Occipital cortex
Hippocampus, parahippocampal cortex, amygdala, fusiform gyrus	3	Mesial temporal lobe	14	Mesial temporal lobe
Caudate, putamen, pallidum, thalamus	4	Subcortical gray matter	15	Subcortical gray matter
Precentral, postcentral and paracentral lobule,supplementary motor area	5	Primary motor and sensorimotor cortex	16	Primary motor and sensorimotor cortex
Precuneus, posterior cingulate cortex	6	Precuneus and posterior cingulate cortex	17	Precuneus and posterior cingulate cortex
Parietal cortex without postcentral cortex	7	Parietal cortex	18	Parietal cortex
Superior, middle and inferior temporal gyrus, temporal pole, Heschl gyrus	8	Temporal cortex	19	Temporal cortex
Dorsolateral prefrontal cortex	9	Dorsolateral prefrontal cortex	20	Dorsolateral prefrontal cortex
Rectus gyrus, olfactory cortex, orbitofrontal cortex	10	Orbitofrontal cortex	21	Orbitofrontal cortex
Medial frontal cortex, anterior cingulate cortex	11	Mesial frontal cortex	22	Mesial frontal cortex

(L) = left hemisphere; (R) = right hemisphere;

8.2.4 Methods overview

In order to evaluate the possible additional value of a regional assessment of amyloid PET we first checked if the association of the $A\beta$ deposition among different regions varied along with the global burden. Patients were grouped according to their overall $A\beta$ load and the regional correlation maps from each group were compared to the overall correlation map. Subsequently, the correlation was used as a measure of similarity between the different regions and a hierarchical clustering merged together the ROIs into a number of meta-ROIs. Finally, a regression analysis between neuropsychological assessment and the ratio of $A\beta$ load between different meta-ROIs was carried out looking for clinical implication on different $A\beta$ spreading across the meta-ROIs.

A graphical representation of the whole process is provided in figure 8.1.
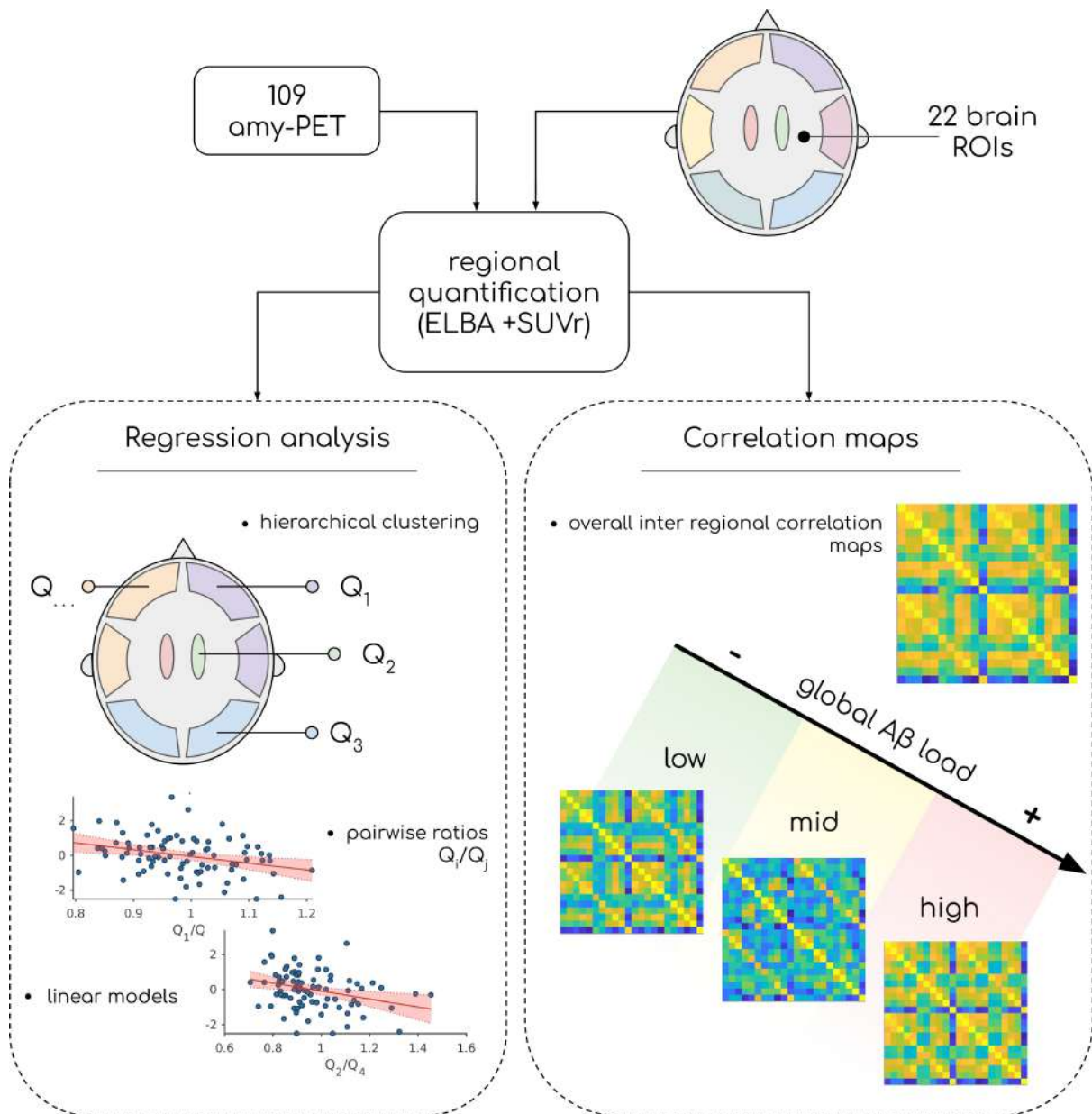
Figure 8.1: A graphical representation of the analyses summarized in the subsection 8.2.4.

Correlation maps

The image processing delivered for each scan a set of 22 regional scores, one for each ROI, used to calculate the inter-region correlation matrix of Pearson coefficient for the whole dataset (C_D).

To evaluate whether the association of the Aβ deposition in different brain regions varies with the global burden, the dataset was splitted into three subsets of low, medium and high global amyloid-β levels. These are defined as tertiles on the first principal component scores of the quantification estimated by the principal component analysis (PCA). The PCA was performed on the SUVr and ELBA scores extracted from each ROIs. In PCA, the first principal component accounts for the greatest variance in the input data. In this case, the first principal component (PC) is the one that better captures the variability of the Aβ load estimated by the two quantifiers. Moreover, this approach allows to take advantage of the independence of the SUVr and ELBA providing a robust

ranking value.

Afterwards, the dataset was splitted into tertiles of the first PC, providing the three subsets described in table 8.1. Similarly, to C_D, an inter-region correlation matrix of Pearson coefficient was calculated for each subset: one for the low-amyloid group (C_L), one for the medium-amyloid group (C_M) and one for the high-amyloid group (C_H).

Finally, in order to check whether C_L, C_M and C_H significantly differed from C_D, a bootstrap analysis was performed, and the four correlation matrices were compared.

ROIs aggregation and regression analysis

To mitigate the collinearity of the regional uptake, the target ROIs were merged together according to the pairwise similarity measured with C_D. This operation was carried out by applying a correlation-based hierarchical clustering to C_D. The conventional UPGMA was used as linkage criteria. The output clusters are referred to as meta-ROIs.

Subsequently, a score Q_i was associated with each meta-ROI (i=1, .. , N where N is the total number of meta-ROIs) representing the Aβ deposition in each meta-ROI. Each Qi score was calculated by averaging the regional scores from the generating merged ROIs. To investigate the different distribution of the amyloid-β deposition between meta-ROIs, the pairwise ratios of the Qi scores were calculated (Q_i/Q_j, where i, j=1, .. , N and i≠j).

Linear regression was used to examine the direct association between the Aβ deposition (both whole-brain deposition and regional Q_i scores) and all the z-scored neuropsychological tests listed in table 8.11. Similarly, we tested regression with the pairwise ratios Q_i/Q_j. All models were adjusted for age, education and sex.

For each significant regression, the Cook's distance was calculated. This metric is commonly used to spot the highly influential points of a model, providing, for each observation, a distance proportional to the effect of deleting such observation. In this study the Cook's distance was used to assess whether patients with low, medium and high amyloid-β burden differently contributed to each model and therefore, whether the information linked to the cognitive decline was uniformly distributed over the range of global Aβ.

Validation and confirmatory tests

To test the robustness and validate our analyses we computed several variations and cross-checks over the whole procedure.

To probe whether the results of the correlation analysis were independent of the choice of the axis over which the patients were ordered, the same analysis was performed with MMSE and age as ranking variables (details in the supplementary material, Appendix B).

To test the consistency of our results with respect to the quantification approaches, we repeated the analyses using only the SUVr. Thus, the global SUVr was used as a ranking value and the regional SUVr as a representation of the regional load. For added robustness, the analysis of the correlation maps was also replicated using the centiloid as ranking value [143] (further information in the supplementary material, Appendix C).

The robustness of the regression analysis to clustering variations was tested by varying the cut-off (see the supplementary material, Appendix D).

Finally, to assess whether possible differences in the ^{18}F-Florbetapir regional reten-
tion might affected results, we replicated the analyses in the subgroup acquired only
with this radiotracer (see supplementary material, Appendix E for more details).

8.3   Results

8.3.1   Correlation maps

The correlation matrix C_D for the whole dataset is shown in figure 8.2. Pearson
correlation coefficients (ρ) of C_D range from 0.21 to 0.98 and the average ρ is equal to
0.73. It can be observed that the subcortical gray matter ROIs (the number 11 and 22,
according to table 8.2) exhibit the smallest correlations with other brain regions (average
ρ=0.47 and ρ=0.39 respectively, [0.21 0.74]).

Conversely, strong correlation was noticed between homologous ROIs in the two hemi-
spheres (average ρ=0.95, [0.89 0.98]).
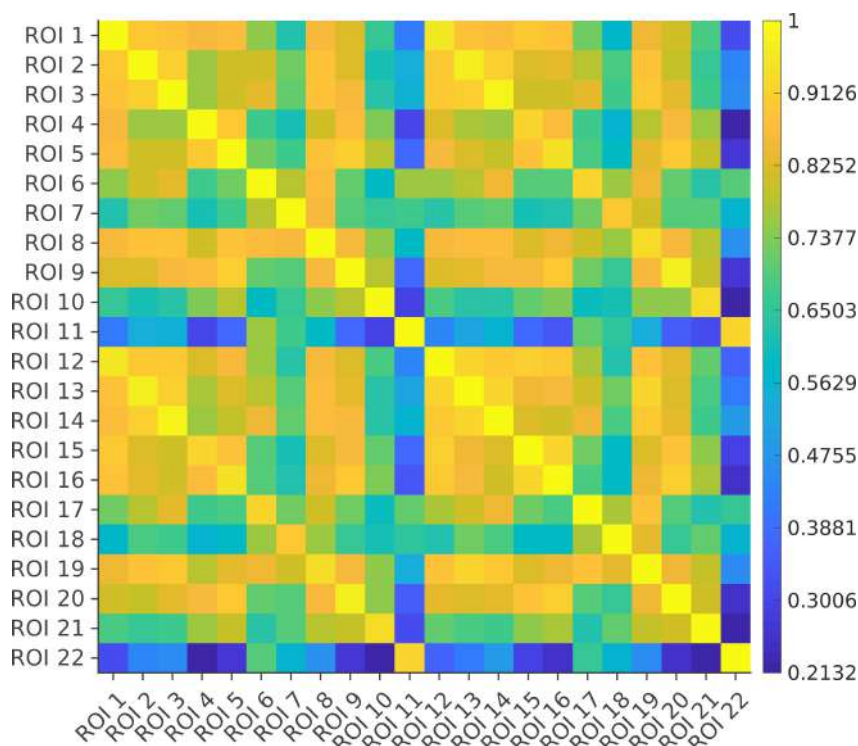
Figure 8.2: Inter-regional correlation matrix C_D of Pearson coefficient calculated for the whole
dataset. Details on the ROIs composition are provided in table 8.2.

Figure 8.3 displays the correlation matrices C_L, C_M and C_H of the three groups of
patients with low, medium and high levels of brain amyloidosis, respectively.

As figure 8.3 (c) suggests, the matrix C_H of the group with high levels of Aβ exhibited
the strongest average correlation (ρ=0.51 [-0.31 0.97]), whereas C_M, corresponding to the
medium group, showed the weakest average correlation (ρ=0.23 [-0.46 0.94]), figure 8.3
(b). The average correlation for C_L is ρ=0.38 [-0.41 0.94], figure 8.3 (a).

Similarly to what observed in C_D, the subcortical gray matter ROIs exhibited the
smallest average ρ with other ROIs in C_L, C_M and C_H. Specifically, the smallest cor-
relations for the subcortical gray matter ROIs were observed in C_L where the average

ρ for the ROI 11 and for the ROI 22 were ρ=-0.04 [-0.37 0.42] and ρ=-0.10 [-0.41 0.49] respectively. In C_M and C_H the average coefficients for the ROI 11 were ρ=0.01 [-0.45 0.75] and ρ=0.07 [-0.24 0.56] respectively. The average coefficients for the ROI 22 were ρ=0.01 [-0.46 0.69] in C_M, and ρ=0.00 [-0.31 0.51] in C_H.

Similarly to what observed for the entire cohort, the average correlation between homologous ROIs is strong not only for the low but also for the medium and the high amyloid group: ρ=0.84 [0.68 0.94], ρ=0.77 [0.49 0.94] and ρ=0.90 [0.78 0.97] respectively.

The bootstrap analysis evidenced that the correlation matrices from the low (C_L), medium (C_M) and high (C_H) subsets significantly differed from the overall matrix C_D respectively at 90.1%, 93.8% and 75.2% of the total number of matrix elements. Statistical significance was quantified by the 95% bootstrap confidence interval.

The bootstrap was also applied to compare the connectivity matrices C_L, C_M and C_H. C_M differs from C_L and CH at 83% and 81.4% respectively. Whereas C_L and C_H differed at 71.1% of the total number of elements. Thus, C_M is the correlation matrix that mostly differed from the other two.

8.3.2   ROIs aggregation and regression analyses

The dendrogram of the hierarchical clustering of C_D was cut to 0.2, thus providing 5 meta-ROIs whose composition is described in table 8.3. This result is robust to small variations of the cut-off (supplementary material, Appendix D).

Aside from the meta-ROI 5, which is the largest composite cluster of highly correlated neocortical regions (average correlation ρ=0.86 [0.75 0.98]), the other meta-ROIs included only a single region and its contralateral homologous one.

Table 8.3: The meta-ROI composition is explained: the names of the ROIs in the Composition column correspond to the labels listed in table 8.2 and an incremental ID (#) is used to uniquely identify each meta-ROI. All ROIs in the Composition column are intended as right and left.

meta-ROI (#)	Composition
1	Insular cortex
2	Occipital cortex
3	Orbitofrontal cortex
4	Subcortical gray matter
5	Medial temporal lobe, Primary motor and sensorimotor cortex,Precuneus and posterior cingulate cortex, Parietal cortex, Temporal cortex, Dorsolateral prefrontal cortex and Medial frontal cortex

The ANOVA excluded statistically significant differences of the neuropsychological tests between patients with low, mid and high levels of global amyloid. The regression analysis tested the association between the Aβ load and the cognitive impairment.

No significant relationship was observed between the amyloid-β burden in each meta-ROI (Q_i) nor in the whole-brain, and the neuropsychological test scores. Conversely, weak but still significant associations were observed between the pairwise ratios Q_i/Q_j and the semantic verbal fluency test (p<0.05). The p-values of the regression models were corrected with the Benjamini-Yekutieli procedure for multiple testing.

Interestingly, all the significant ratios involved the Q_4 that represents the subcortical gray matter meta-ROI. In figure 8.4 all the significant models are shown. No other ratios
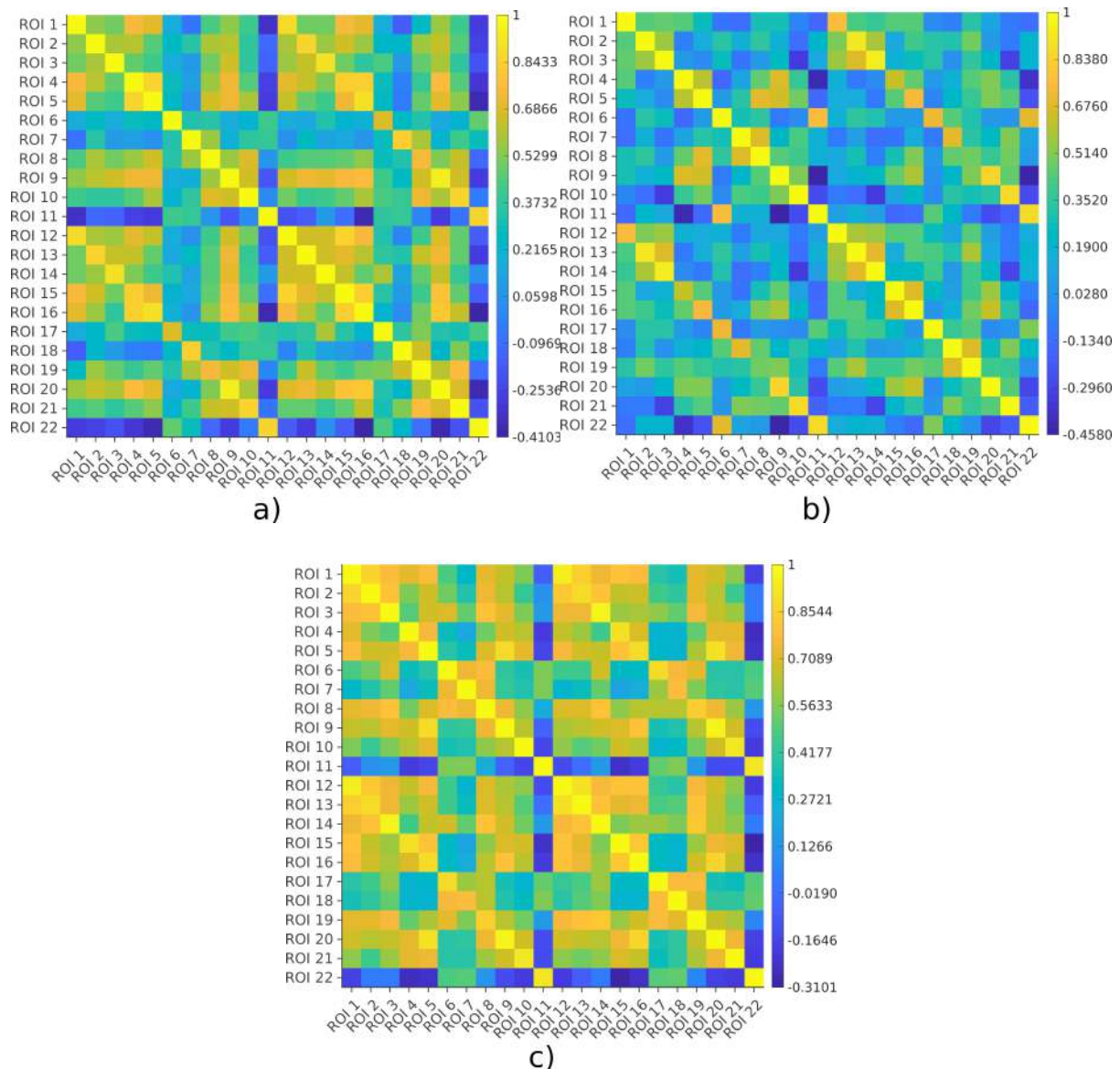
Figure 8.3: Inter-regional correlation matrix of Pearson coefficient (C_L, C_M, C_H) calculated for a) the low, b) medium and c) high amyloid group respectively. Details on the ROIs composition are provided in table 8.2.

besides those listed in figure 8.4 showed significant relationship with the neuropsychological variables.

For each model in figure 8.4, the Cook's distances were calculated. Then, given that the Cook's distance is characteristic of each observation, and therefore of each patient, they were grouped according to the low, medium and high level of amyloid. Results are illustrated in figure 8.5: the boxplots display the distribution of the Cook's distances grouping patients by global Aβ levels and provide a representation of the influence on the models of each group of patients. The p-values below 0.05 refer to the models where the Cook's distance of the low-amyloid patients is significantly greater than that of the high-amyloid. Although the significance is not reached for each model, the Cook's distances mostly trended downward with the amyloid load.
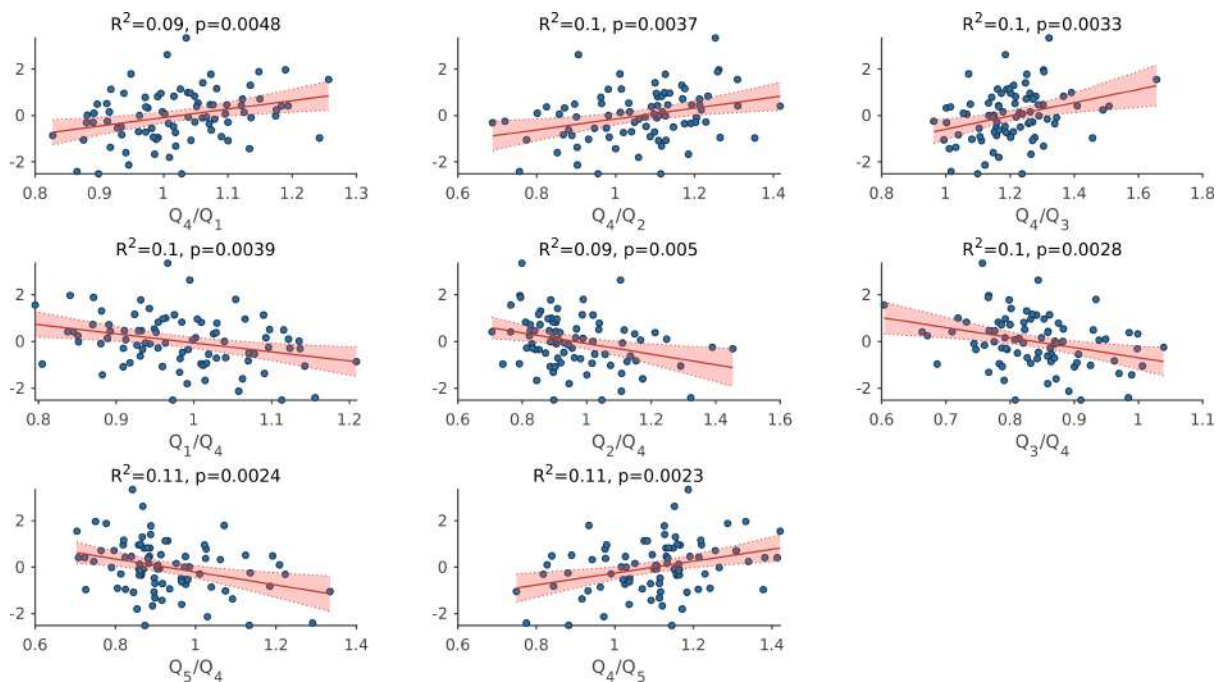
Figure 8.4: Associations of pairwise ratios (x-axis) and semantic fluency (y-axis). In each scatter plot the patients are denoted with dots, the red line is the linear regression and the pale red area represents the 95% confidence interval. The significance and the strength of the association are indicated with the relative p-value and the R^2 respectively. The Q_i/Q_j are dimensionless as they represent the ratios of Aβ deposition in each meta-ROI calculated by averaging regional SUVr and ELBA. Q_1: Insular cortex, Q_2: Occipital cortex, Q_3: Orbitofrontal cortex, Q_4: Subcortical gray matter, Q_5: Highly correlated neocortical regions.
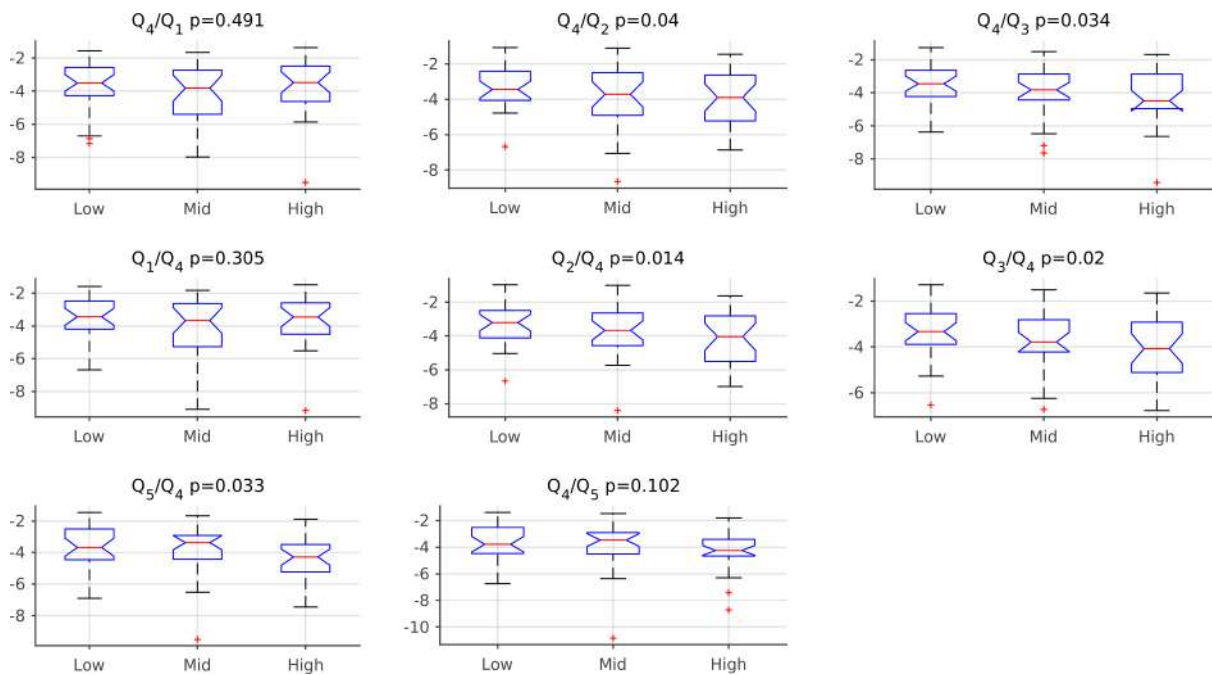
Figure 8.5: A Cook's distance for each linear regression model depicted in figure 8.4. The distances were grouped according to the level of amyloid of each observation (i.e. low, medium and high). The p-values refers to the significance of a one-tailed t-test between the low and the high groups. The Q_i/Q_j are dimensionless as they represent the ratios of Aβ deposition in each meta-ROI calculated by averaging regional SUVr and ELBA. Q_1: Insular cortex, Q_2: Occipital cortex, Q_3: Orbitofrontal cortex, Q_4: Subcortical gray matter, Q_5: Highly correlated neocortical regions.

8.4 Discussion

The overall purpose of this study was to explore the role of regional Aβ deposition in a cohort of subjects affected by cognitive decline.

While the majority of imaging studies focused on whole brain Aβ load to date, the possible inter-regional differences in Aβ accumulation and its clinical correlates are less well characterized. Indeed, while the presence of differences in Aβ regional accumulation has been described in several neuropathological studies [259, 233] its impact on symptomatic subjects is still unclear. Thus, to interpret the results of this study one should consider that our cohort is composed by symptomatic outpatients affected by different disorders (either AD or not-AD related), leading to impaired cognition. These subjects, all initially suspected having AD, could not be effectively distinguished into the proper diagnosis without information on amyloid status.

The first result is that Aβ accumulation affects the brain regions differently. Indeed, the variability in the covariance observed among any two brain regions reflects the differences in the levels of Aβ accumulation. If the amyloid-β spreaded linearly within brain regions we would not have observed any differences between the correlation maps of patients at increasing levels of Aβ and the overall dataset. The correlation map analysis with MMSE and age as ranking variables found significantly less differences (< 13% for age and < 2% for MMSE, p<0.05), suggesting that that global Aβ is a privileged information (supplementary material, Appendix B).

In line with recent literature [104, 46, 177, 98], this observation confirms that brain regions show different vulnerability to amyloid-β deposition, emphasizing the value of topographical information provided by the amy-PET. Studies in patients with AD suggest that differences in regional vulnerability may be explained by distinct regional molecular properties and related biochemical pathways [99] or by structural characteristics and connectivity of brain regions [212, 207] as well as by regional differences in genetic expression [247].

From this perspective it is reasonable that contralateral homologous regions, sharing the same cytoarchitecture and being strictly functionally interconnected, present similar susceptibility to Aβ deposition. Indeed, a strong correlation in regional tracer retention was observed across homologous regions, for all amounts of global Aβ deposition.

The presence of a substantial inter-regional correlation in the lower tertile of global Aβ burden, i.e., the most heterogeneous group from the diagnostic point of view, suggests that regional- (and not only merely disease-) specific factors impact the regional distribution of Aβ [249, 250].

The observation of a consistent inter-regional correlation in Aβ levels in symptomatic subjects without AD represents a distinguishing feature of this study. Indeed, these patients may share the early involvement of some more vulnerable areas to Aβ accumulation, regardless of the underlying neurodegenerative disease. As one can expect the patients in the medium and high tertiles of global Aβ burden are predominantly amyloid positive in the AD spectrum (90.4%). Interestingly, we noticed that the covariances among brain regions evolved with the global Aβ levels resulting in an increased inter-regional correlation with the increase of global amyloid-β burden. This is in line with observations of Villain et al. [273] and Pereira et al. [216] that the dynamics of Aβ accumulation is not constant nor related to baseline clinical status, but it is associated with the global neocortical amyloid-β burden. The heterogeneity in Aβ deposition was more pronounced in patients with intermediate load possibly due to different accumulation

path or rate between brain regions [124].

Independently of the global Aβ burden, we observed poor or no correlation between the subcortical gray matter ROIs and other brain regions. Among the regions considered in this study, the subcortical gray matter is the one with the most independent uptake. This observation is in line with neuropathological data showing that amyloid-β accumulation in the subcortical gray matter, particularly in the striatum, is at least partially independent of cortical accumulation [105, 46, 259, 15].

Actually, autopsy studies suggest that the striatal Aβ plaques may be mainly restricted to higher Braak NFT stages in AD subjects, predicting NFT stage and the presence of more severe cognitive decline at the time of death. The role of genetics may also be relevant on striatal Aβ spreading; two familial AD studies showed early striatal PET-Aβ signal, and early striatal Aβ was also observed in Down syndrome (DS) [103]. Regional differences in amyloid-β accumulation are not limited to the subcortical gray matter as shown by the hierarchical clustering based on the correlation map (i.e. the 5 meta-ROIs, see table 8.3) as well as by available literature. Among the cortical regions, for example, the orbitofrontal cortex and the insula are considered as early accumulators, whereas the occipital cortex is one of the latest [212, 177].

The overall brain Aβ load is in itself not strictly associated with clinical symptoms [286, 145, 132] and this was observed also in our data. The lack of association observed between regional Aβ load and cognitive performance is consistent with the recognized notion that amyloid-β, unlike tau pathology, is not directly related to clinical symptoms [290, 203].

However, the relationship with the relative regional burden has not been studied in depth. The role of subcortical gray matter Aβ involvement on cognition has been investigated with different results. Striatal involvement has been suggested to be able to predict cognitive decline better than cortical Aβ. It has also been found that striatum involvement may be able to identify patients with more rapid cognitive deterioration [105, 46, 15]. Whether the expansion of amyloid-β into striatum leads directly to cognitive decline or whether it indicates disease duration or higher cortical Aβ burden or merely represents a proxy of tau pathology [259], remains to be determined. An association of cognition (and more in details of semantic verbal fluency) to the ratio between regional cortical and subcortical Aβ deposition was observed, rather than to the cortical or subcortical Aβ per se.

The semantic fluency is known to be affected early on in AD [241, 29]. Moreover, it may be impaired in FTD (typically in semantic dementia but in other variants as well [226]), in SCI [199], in DS with dementia [114] and in Lewy-body diseases [172]. A more evident impairment of semantic fluency seems mainly related to a more aggressive neurodegeneration, but the entity of amyloidosis might play a role. For instance, in a large neuropathological series of non-demented people, semantic memory was associated with number of neurofibrillary tangles but with Aβ load as well [21]. Our results hint to a possible role of regional Aβ in cognitive decline irrespective of the underlying diagnosis, as shown by Cook's distance analysis. Indeed, the semantic fluency was mostly driven by the patients with lower global amyloid-β, predominantly negative scans and with heterogeneous diagnosis classes.

Several studies [39, 279, 123] pointed out a biological impact of Aβ load already before the quantitative threshold required for amyloid-scan positivity is reached. These data highlight the role of regional Aβ assessment, suggesting that the amy-PET is an available resource that has not yet been fully explored. Regional approaches to amy-PET

analysis could be instrumental to understand the spatial pattern of amyloid deposition over time thus allowing to understand the possible role of local anatomical factor on the amyloid cascade. Even if this work won't impact the clinical practice directly in its current form, we believe it represents a step in the direction of more complex pattern-like analyses, to be used in research settings only that may lead to new insight with possibly prognostic implication. Future studies are needed to explore the relationship between regional Aβ, the onset of neurodegeneration, and cognition.

The results of this study should be replicated on a larger, multicentric dataset. However, the monocentric nature of this cohort likely prevented possible biases in center and/or method inhomogeneities. Moreover, our cohort included only cross-sectional data so further analysis on longitudinal data should be undertaken to deepen the relative dynamic of the regional Aβ deposition and the possible relationship with the clinical status.

The dataset is biased towards amyloid positive cases (71.5%). However, this condition is related to the naturalistic quality of the data and the analyses were all based on the estimation of Aβ on a continuous scale.

The use of different tracers should be further investigated: although it is known that no marked differences in the diagnostic accuracy of the fluorinated Aβ tracers are presented for both global quantitative and visual approaches [42], it is still unclear whether combining regional quantitative information is equivalent across different tracers. However, to mitigate this possible effect, a mapping model was applied [42]. Overall, there was no material difference in the observed results using only patients acquired with ^{18}F-Florbetapir (supplementary material, Appendix E).

Both the reference and the target ROIs size and definition impaired the quantification and the derived analyses [244, 264, 254]. Precautionarily, large regions were chosen to make the quantification less susceptible to fluctuations. Moreover, the use of two combined independent methods with independent weaknesses (i.e.: SUVr and ELBA) should mitigate, at least partially, these issues. However, our observations were reasonably independent of the quantification approach and to the representation of the global Aβ deposition (supplementary material, Appendix C).

8.4.1 Conclusions

This study focused on the potential added value derived by the regional information provided by the amyloid PET. Its results should be interpreted considering the naturalistic quality of the dataset of symptomatic outpatients.

As stated by staging works based on anatomopathological and imaging findings, the Aβ spreading proceeds differently between cortical and subcortical regions as well as between patients. Different susceptibility to Aβ accumulation was observed among brain regions, however homologous regions share the same trajectory in a symmetrical manner with the contralateral ones. The Aβ uptake of the subcortical gray matter was independent from the cortical one, resulting poorly correlated to the other brain regions independently of the global amyloid-β burden.

The overall brain Aβ load as well as the regional Aβ was not directly related to cognitive performance, but a significant association of semantic verbal fluency was observed with a coarse measure of differences in regional distribution of Aβ, always involving the subcortical gray matter.

Regional Aβ assessment represents an available resource on amy-PET scan with possibly clinical and prognostic implications, but it is poorly examined yet.
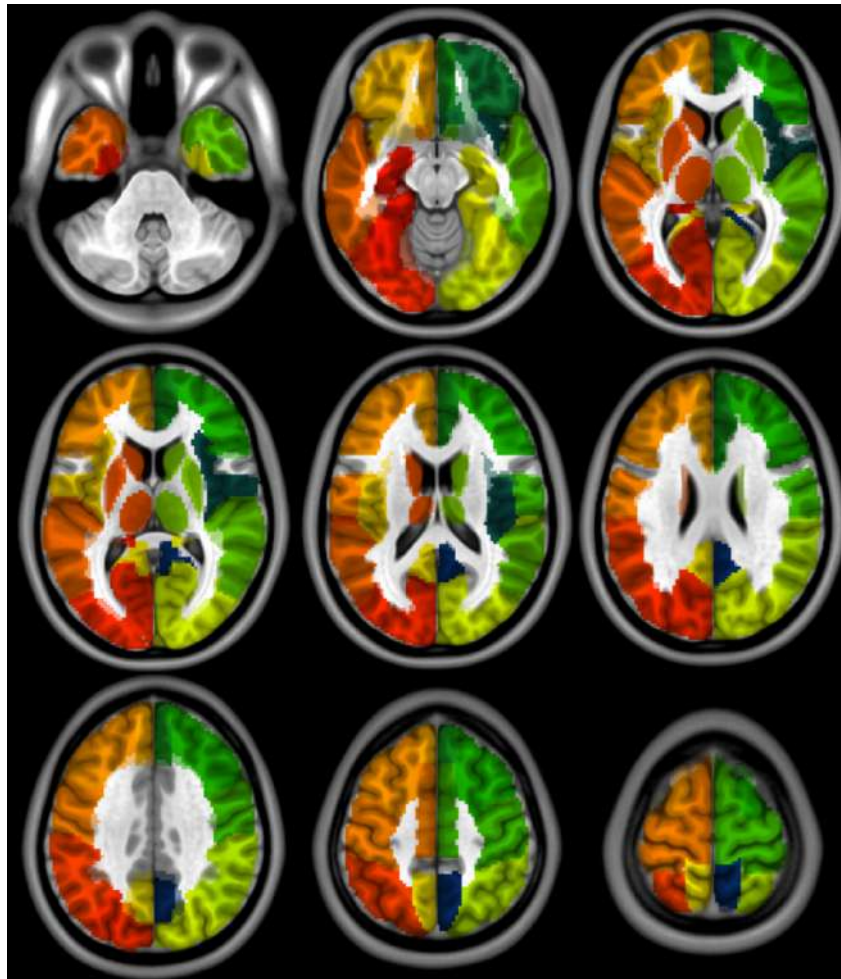
8.5   Supplementary materials

Figure 8.6: Brain parcellation adopted for this study. Each hemisphere was divided into 11 ROIs. A more detailed description of each ROI is provided in table 8.2.

8.5.1   Appendix A: apolipoprotein E genotype

Data on apolipoprotein E (ApoE) genotype status are resumed in the supplementary table 8.4. They were available for 51 patients: 14, 19 and 18 from the low, medium and high amyloid group respectively. As expected, the prevalence of the e4 allele is linked with high amyloid burden.

Table 8.4: ApoE genotype for the overall dataset and grouped by low, mid and high global $A\beta$ levels.

		Overall	Low	Mid	High
Genotype	e2e3	2	1	1	-
	e3e3	26	11	9	6
	e3e4	19	2	7	10
	e4e4	4	-	2	2

8.5.2   Appendix B: alternative partitioning

To prove that global amyloid load was a privileged information, the dataset was splitted into tertiles on MMSE and age. For each subgroup the inter-regional correlation matrix was calculated and a bootstrap analysis was repeated to compare each matrix with C_D.

The bootstrap analysis evidenced that the correlation matrices from the low, medium and high subsets, derived from MMSE-based splitting, differed from C_D only at 1.2%, 1.6% and 1.2% of the total number of elements respectively.

The bootstrap on the subsets derived from the age-based splitting showed that the correlation matrices from the low, medium and high subsets differed at 8.2%, 10.3% and 12.4% of the total number of elements. These results suggest that the information of global amyloid burden is privileged to spot the differences in global amyloid deposition.

8.5.3   Appendix C: centiloid scale

To test the consistency of our results we repeated the analyses using only the regional SUVr. The analysis of the correlation matrices showed that C_D differed from C_L, C_M and C_H at 95%, 87.6% and 71.2% respectively. The hierarchical clustering provided the same meta-ROI aggregation and significant associations were still observed between the pairwise ratios involving the subcortical gray matter meta-ROI and the semantic verbal fluency test (p<0.05 after Benjamini-Yekutieli procedure for multiple testing, supplementary figure 8.7). The linear models were alla adjusted for age, education and sex.

These results are similar to those observed using both ELBA and SUVr in terms of R^2 and significance. Interestingly, significant associations of the stroop color and word test with pairwise ratios were observed (p<0.05 after Benjamini-Yekutieli procedure for multiple testing). As the supplementary figure 8.8 shows, the meta-ROIs involved in those ratios are: number 5, 4 and 1. Unlike what was observed for the verbal fluency, there are two significant ratios (Q_5/Q_1 and its reciprocal) that do not involve the striatal meta-ROI, but rather the insular and the largest neocortical meta-ROI. However, the associations of the pairwise ratios with the stroop color and word test vanished with even small variations in the clustering making them unreliable (see supplementary material,
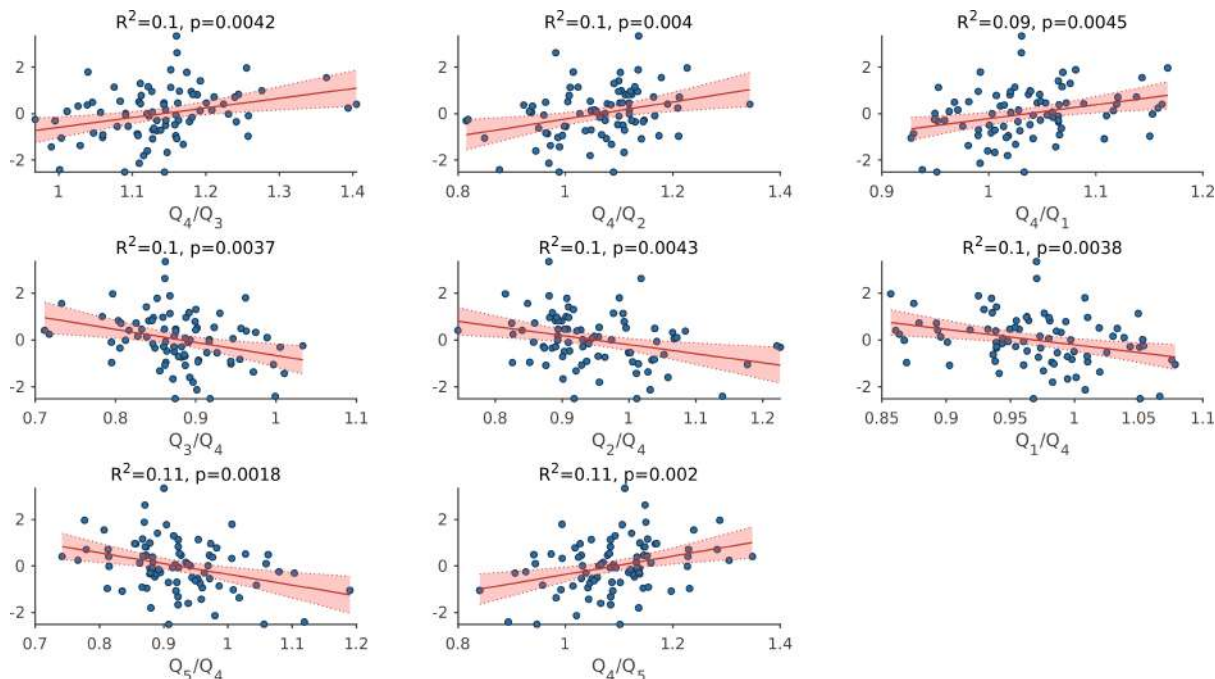
Figure 8.7: Associations of pairwise ratios (x-axis) and semantic fluency (y-axis). In each scatter plot the patients are denoted with dots, the red line is the regression model and the pale red area represents the 95% confidence interval. The significance and the strength of the association are indicated with the relative p-value and the R^2 respectively.

Appendix D). These observations suggest that our results are reasonably independent of the choice of the quantification approach.

We also tested the use of a uniform scale of global Aβ load (i.e. the centiloid) as a ranking value in the analysis of the correlation maps. According to Klunk and colleagues [143], the cortico-cerebellar SUVr of each amy-PET were scaled to a 0 to 100 scale where 0 represents a definitively Aβ-negative brain and 100 reflects the average signal observed in patients with typical mild-to-moderate AD dementia. For each tracer, the 0 of the scale was derived by averaging the cortico-cerebellar SUVr of negative scans (22 subjects for the ^{18}F-Florbetapir, 25 for the ^{18}F-Florbetaben and 26 for the ^{18}FFlutemetamol). Similarly, the 100 for each tracer was computed as the average of cortico-cerebellar SUVr of positive scan of patients with mild-to-moderate AD dementia (27 subjects for the ^{18}F-Florbetapir, 29 for the ^{18}F-Florbetaben and 30 for the ^{18}F-Flutemetamol). These scans come from independent studies conducted in our center and their clinical status was confirmed after 2 years of follow-up. The dataset was splitted into three subsets defined as tertiles of the centiloid values: the thresholds between the low, medium and high subsets were 34.5 and 49.7 respectively (centiloid values are detailed in the supplementary table 8.4).

Table 8.5: SUVr, ELBA and centiloid scores for the overall dataset and grouped by low, mid and high global Aβ levels.

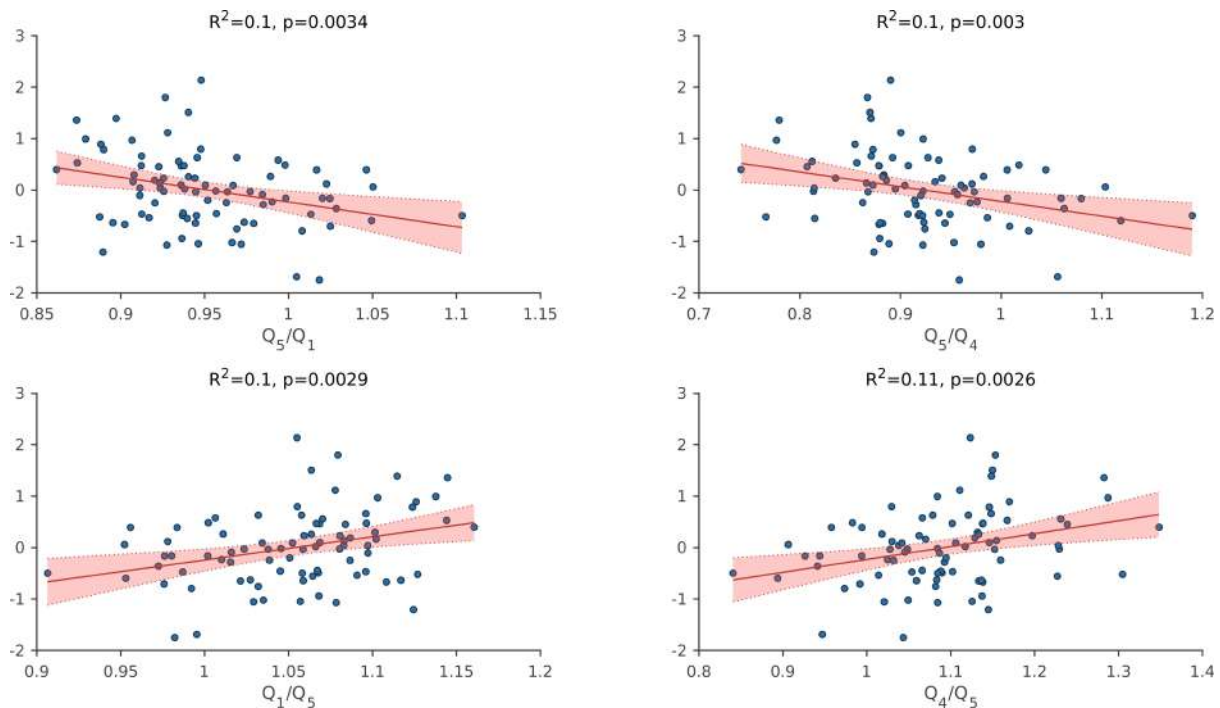|	Overall	Low	Mid	High
SUVr	1.24±0.12	1.12±0.05	1.2±0.06	1.37±0.09
ELBA	0.93±0.12	0.83±0.09	0.92±0.06	1.04±0.10
Centiloid	44.6±19.6	23.6±6.3	42.9±4.2	66.7±12.2

Figure 8.8: Associations of pairwise ratios (x-axis) and stroop color and word (y-axis). In each scatter plot the patients are denoted with dots, the red line is the regression model and the pale red area represents the 95% confidence interval. The significance and the strength of the association are indicated with the relative p-value and the R^2 respectively.

For each subgroup an inter-regional correlation matrix was calculated and a bootstrap analysis compared each matrix with C_D. The correlation matrices of the low, mid and high subsets differed from C_D at 91.3%, 90.5% and 70.2% of the total number of elements respectively. These results suggest that the variability observed in the covariance among any two regions reflects the differences in the level of Aβ accumulation independently of the approach used to represent the amount of global amyloid-β deposition.

8.5.4 Appendix D: clustering variations

The results of the hierarchical clustering were tested by varying the cut point originally set to 0.2. The cut was first set to 0.28 providing 4 meta-ROIs described in the supplementary table 8.6.

Compared to previous results, the clustering merged the orbitofrontal cortex into the neocortical meta-ROI. The linear regression analysis confirmed that the semantic verbal fluency was significantly associated only with the pairwise ratios of brain meta-ROIs involving the subcortical gray matter (p<0.05 after Benjamini-Yekutieli procedure for multiple testing, see the supplementary figure 8.9). All models were adjusted for age, education and sex.

To increase the number of clusters to 6, the cut applied to the dendrogram was set to 0.15. The resulting parcellation is described in the supplementary table 8.6: the new meta-ROI came from the splitting of the largest neocortical region into two meta-ROIs. Again, significant associations (models adjusted for age, education and sex) were observed between semantic verbal fluency with the pairwise ratios of brain meta-ROIs involving the striatal meta-ROI (p<0.05 after Benjamini-Yekutieli procedure for multiple

Table 8.6: The meta-ROI composition varying the number of clusters. The names of the ROIs in the Composition column corresponds to the Label listed in table 2 and an incremental ID (#) is used to uniquely identify each ROI. All ROIs in the Composition column are intended as right and left.

cut=0.28; 4 clusters		cut=0.15; 6 clusters	
meta-ROI (#)	Composition	meta-ROI (#)	Composition
1	Insular cortex	1	Insular cortex
2	Occipital cortex	2	Occipital cortex
3	Medial temporal lobe, Primary motor and sensorimotor cortex, Precuneus and posterior cingulate cortex, Parietal cortex, Temporal cortex, Dorsolateral prefrontal cortex, Medial frontal cortex and Orbitofrontal cortex	3	Orbitofrontal cortex
4	Subcortical gray matter	4	Subcortical gray matter
-	-	5	Medial temporal lobe, Precuneus and posterior cingulate cortex, Medial frontal cortex
-	-	6	Primary motor and sensorimotor cortex, Parietal cortex, Temporal cortex, Dorsolateral prefrontal cortex
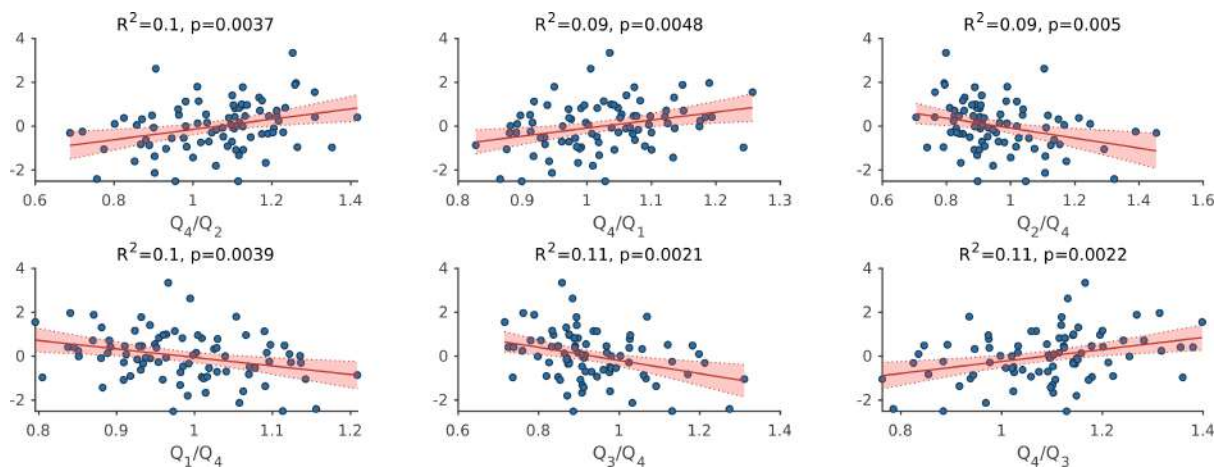
Figure 8.9: Associations of pairwise ratios (x-axis) and semantic verbal fluency (y-axis) with a 4 meta-ROI clustering (see supplementary table 8.6 for further details). In each scatter plot the patients are denoted with dots, the red line is the regression model and the pale red area represents the 95% confidence interval. The significance and the strength of the association are indicated with the relative p-value and the R^2 respectively.

testing, see the supplementary figure 8.10).

Moreover, significant associations (p<0.05, Benjamini-Yekutieli procedure for multiple testing) of the stroop color and word test were also observed with the ratios: Q_1/Q_6, Q_4/Q_6 and their reciprocals (see supplementary figure 8.11).

However, the significance of the models involving the stroop color and word test de-
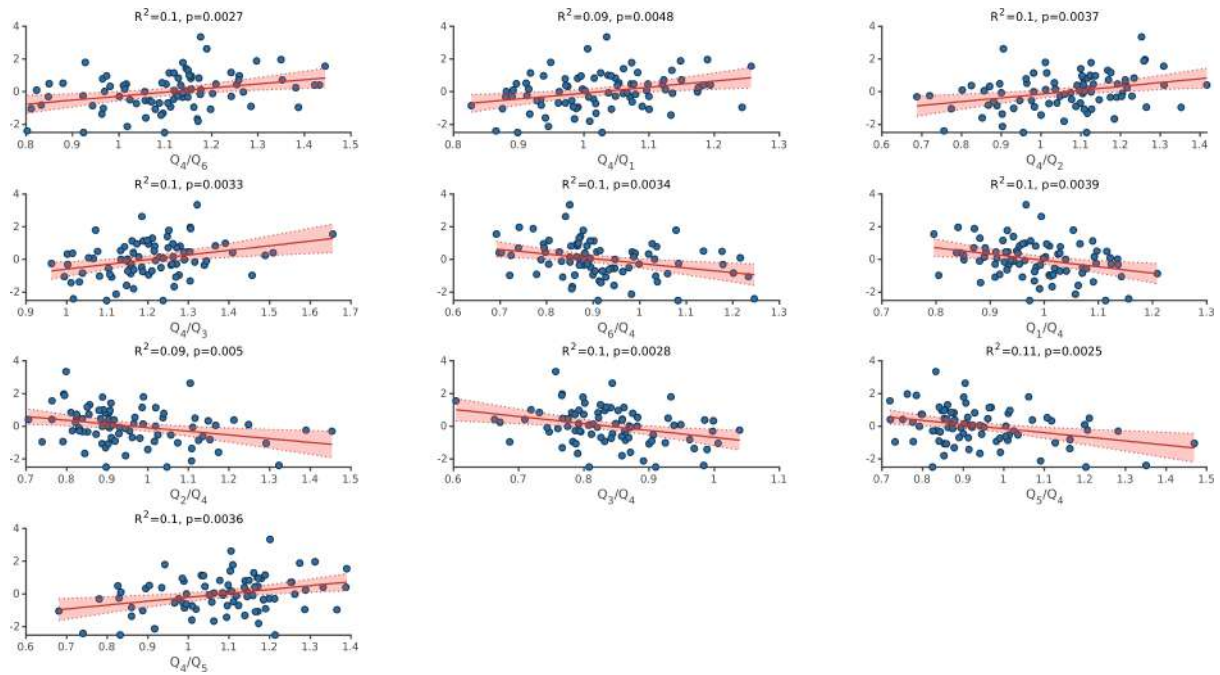
Figure 8.10: Associations of pairwise ratios (x-axis) and semantic verbal fluency (y-axis) with a 6 meta-ROI clustering (see supplementary table 8.6 for further details). In each scatter plot the patients are denoted with dots, the red line is the regression model and the pale red area represents the 95% confidence interval. The significance and the strength of the association are indicated with the relative p-value and the R^2 respectively.
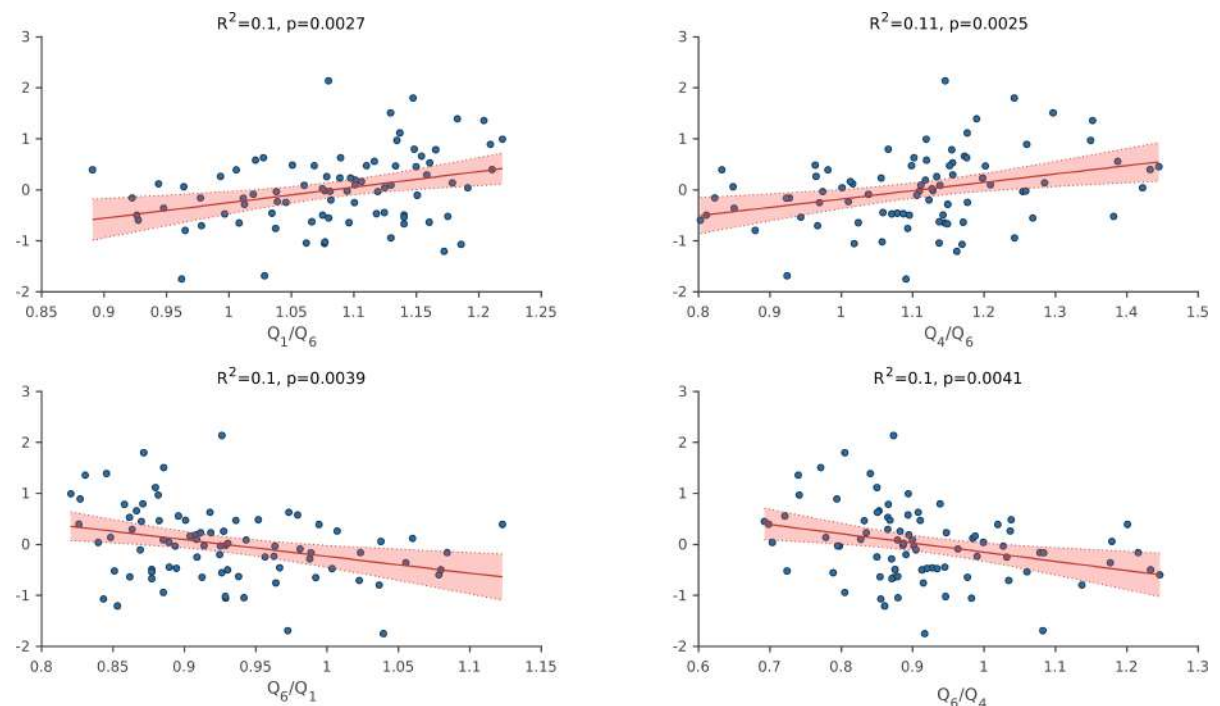
Figure 8.11: Associations of pairwise ratios (x-axis) and stroop color and word (y-axis) with a 6 meta-ROI clustering (see supplementary table 8.6 for further details). In each scatter plot the patients are denoted with dots, the red line is the regression model and the pale red area represents the 95% confidence interval. The significance and the strength of the association are indicated with the relative p-value and the R^2 respectively.

pends even on small variation of the clustering, suggesting that these results are due to statistical fluctuations. Conversely, varying the number of clusters, the associations of semantic verbal fluency to the ratios involving the subcortical gray matter were still significant.

8.5.5   Appendix E: tracer-related differences

To assess whether possible differences in the regional retention of the ^{18}F-Florbetapir may affect results, the analyses were replicated only in the subset acquired with this radiotracer (59 patients).

The dataset was splitted into three subgroups of low, mid and high levels of global amyloid, and, for each subgroup, an inter-region correlation matrix of Pearson coefficient was calculated. The correlation matrices from the low (C_L), medium (C_M) and high (C_H) subsets significantly differed from the overall matrix C_D respectively at 70.2%, 87.1% and 74.4% of the total number of matrix elements. These results are consistent with what observed taking into account all the radiotracers confirming that regional Aβ accumulation varies with levels of global Aβ burden.

The hierarchical clustering provided the same 5-metaROI parcellation described in table 8.3.

The results of the linear regressions (adjusted for age, sex and education) are similar to those obtained with all the fluorinated tracers: the only significant associations (p<0.05 after Benjamini-Yekutieli procedure for multiple testing) were those with the semantic verbal fluency and pairwise ratios involving the subcortical gray matter.

As the supplementary figure 8.12 depicts, both the significance and the R^2 slightly increased. These observations hint that the characteristics of the ^{18}F-Florbetapir binding did not affect the overall results, particularly those pointing to the subcortical structures. However, these results should be carefully taken into account due to the relatively small sample available.

Figure 8.12: Associations of pairwise ratios (x-axis) and semantic verbal fluency (y-axis) of the ^{18}F-Florbetapir subgroup. In each scatter plot the patients are denoted with dots, the red line is the regression model and the pale red area represents the 95% confidence interval. The significance and the strength of the association are indicated with the relative p-value and the R^2 respectively.
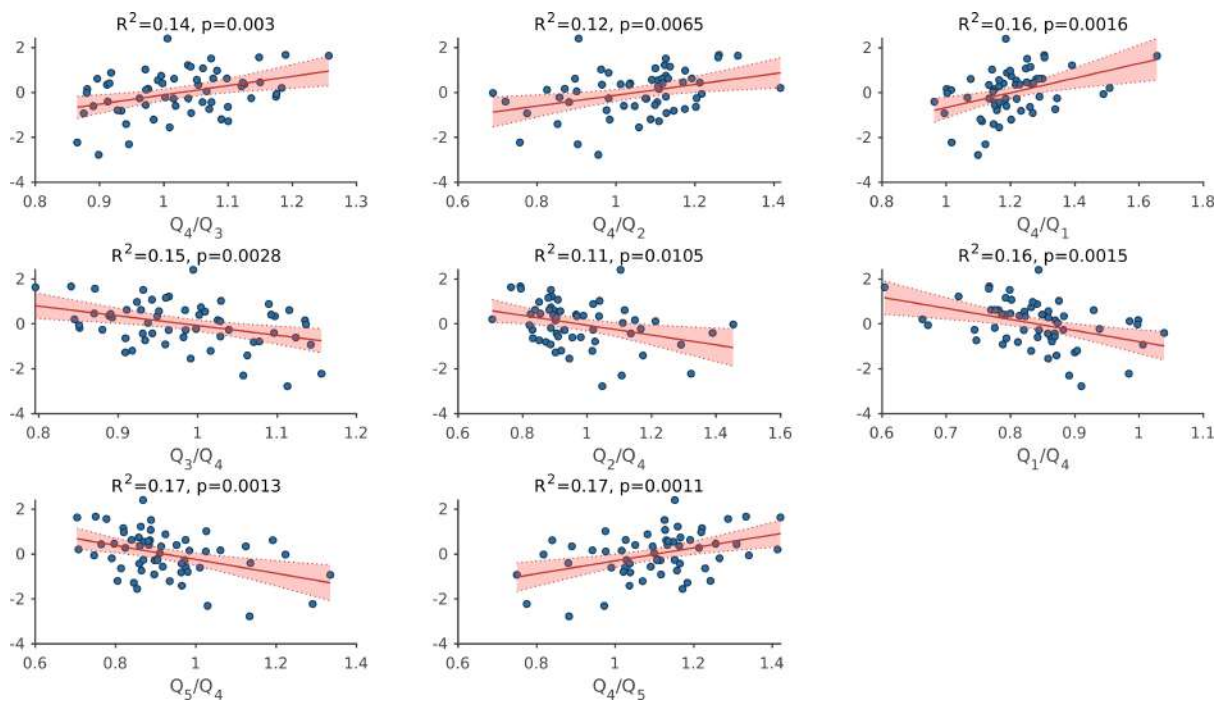
Chapter 9

A comparison of advanced semi-quantitative amyloid PET analysis methods

9.1 Introduction

Amyloid PET (amy-PET) is an imaging technique that enables highly accurate, in-vivo detection of amyloid-β (Aβ) plaques, considered a pathological hallmark of Alzheimer's disease (AD) [125]. Over the years, amy-PET has provided useful support to clinicians by increasing diagnostic confidence and helping them refine management plans [12, 72].

In clinical practice, amy-PET is mainly inspected qualitatively with the aid of structural imaging (i.e., CT or MRI), with results classified as positive or negative. The negative predictive value of the test is very high, whereas the implications of a positive result are more complex and depend also on the prevalence of brain amyloidosis in the elderly.

Several studies have reported Aβ deposition, both global and regional, to be common in cognitively healthy subjects in late adulthood, and to increase with age [134, 130, 228, 92].

Semi-quantitative or quantitative approaches are increasingly being used to complement qualitative assessments. These measures are essential to much of the research on neurodegeneration as they improve agreement between raters [195, 49, 42], are part of the inclusion criteria (and outcome biomarkers) in anti-amyloid clinical trials [248, 65, 239, 113, 268] and provide valuable information on Aβ distribution that may be useful in staging the progress of an individual's Aβ pathology [98, 177, 237].

To date, there is no established consensus on how to semi-quantitatively assess amy-PET. Besides SUVr, the most widely used [139] method, various alternatives using different sources of information are available. Analysis can be based on standard late acquisition alone, as with methods like ELBA or Aβ_L [43, 285], or can include tracer kinetic information obtained by adding early acquisition, as with TDr [41]. Our group proposed a more sophisticated procedure, called the Slope Index (SI), which also takes into consideration atrophy and spillover by including MRI data [37].

In this study, we compare various semi-quantitative approaches with increasing degrees of refinement at both the global and regional levels: SUVr, ELBA, TDr, WMR and SI. In the absence of absolute quantification, we selected SI - the most complete approach - as the reference measure of Aβ load. The choice of a reliable measure as reference allowed us to assess the efficacy of the quantifiers and the feasibility of using them in

clinical and research settings.

Although kinetic modeling is optimal for accurate therapy monitoring and longitudinal studies [244] (in this case, a valuable compromise is made between accuracy and simplicity [26]), advanced semi-quantitative approaches (especially using dual-time-window protocols) might be an option if a larger error is acceptable. The results of the present study are potentially of great importance in view of anti-amyloid treatments in patients with AD. While it can be argued that amyloid plaque load, as measured by amy-PET with standard late acquisition, is a valid surrogate endpoint for drug approval and could demonstrate a clinical benefit in AD, it should also be noted that advanced semi-quantitative methods (such as those discussed in this paper) that also include blood flow analysis (using early phase) are able to detect not only amyloid load [87] but also neurodegeneration (as ^{18}F-FDG does), and therefore represent a more robust end point for monitoring disease-modifying drugs targeting amyloid load deposition.

9.2   Material and methods

9.2.1   Dataset

In this study, we used a single-center dataset to test different semi-quantitative approaches including dual-time-window protocols. The data were obtained from 85 patients (aged 44-87, μ=70.9±10.1; 45.8% women) at the University Hospital of Leipzig, Germany. The subjects are described in detail in [37], and their clinical diagnoses are listed in Supplementary Table 9.3.

In accordance with the Declaration of Helsinki, all subjects gave written informed consent to undergoing brain PET/MRI and to having their anonymized data used for retrospective research.

9.2.2   PET/MRI acquisition

Each patient received an intravenous injection of ~300 MBq ^{18}F-Florbetaben in an integrated 3T PET/MRI system (Biograph mMR; Siemens), then underwent PET/MRI with scans performed at 0 to 10 minutes (early) and at 90 to 110 minutes (late) after injection. Late acquisition was in accordance with the recommendations of the tracer manufacturer [219] and the guidelines of the European Association of Nuclear Medicine and the Society of Nuclear Medicine [184].

Anatomical data were also obtained via 3DT1 1-mm isotropic MRI in parallel with the PET scan. Further details on the 3DT1 MRI acquisition, and the amyloid PET reconstructions and correction are provided elsewhere [37].

The 85 late scans were visually inspected by two independent nuclear medicine experts and classified as either amyloid-negative (54 subjects, aged 44-87, μ=69.9±10.6) or amyloid-positive (31 subjects, aged 48-83, μ=72.3±9.1). Discrepancies were resolved by consensus discussion with a third independent reviewer.

9.2.3   Image processing

Each amyloid PET was semi-quantitatively assessed by means of five independent approaches (hereinafter referred to as *quantifiers*): SUVr [139], ELBA [43], TDr [41],

WMR [37] and SI [37]. Details of each quantifier can be found in their respective papers. A brief summary of their underlying methodologies is given here:

The SUVr is defined as the ratio of counts between a target region of interest (ROI) and a reference one [139]. In this work, it was normalized (as is frequently the case in the literature) using the whole cerebellum [244]. ELBA is a radiomic-based, SUVr-independent approach designed to capture intensity distribution patterns that are global properties of the whole brain and do not require a reference ROI [43]. TDr is defined in [41] and is the ratio of counts exploiting the information on tracer kinetics provided by dual-time-point acquisition in order to adapt both the target and the reference ROIs of each individual. The SI and WMR indices are obtained from an analytical method that requires dual-time-point amyloid PET acquisition and a co-registered MR, allowing for blood flow and partial volume effect corrections (PVEC) [37]. Each quantifier is designed to capture specific characteristics of the image that are directly or indirectly related to the expected amyloid load and are shown in the amyloid PET. These methods make use of different types of information, details of which are shown in Table 9.4 along with the minimum requirements to perform the analysis.

Subcortical volumes, segmentation of the subcortical white matter (WM), and cortical thickness and surface area were estimated from the 3DT1 MRI using FreeSurfer 5.3[1] [77]. This processing included motion correction, skull stripping, registration to Talairach space, segmentation, intensity normalization, and parcellation mapping according to the Desikan-Killiany cortical labelling protocol.

In this study, we compared the quantifiers at both the global and regional levels. Five lobar ROIs for each hemisphere were obtained from the FreeSurfer parcellation (i.e., the frontal, parietal, temporal, occipital, and central structures); see Supplementary Figure 9.6. The global ROI was obtained by merging the 10 lobar ROIs. The global and lobar ROIs were used as target regions in the analyses.

For the SI and WMR quantifiers, image registration to the MNI space was guided by individual patient's 3DT1, which resulted in the atlas ROIs accurately overlapping with those of the patients. For SUVr, ELBA and TDr - since an MRI is not required - image registration was guided only by a generic amyloid template in the MNI space (see [43]), resulting in a coarser alignment between the atlas and the patients' PET.

The results from each quantifier were z-scored to enable better comparison of the different methods with possibly different scales.

Table 9.1: Minimum requirements for each quantifier.

	Acquisition			Processing	
	PET late	PET early	MRI T13D	reference ROI	target ROI
SUVr	•			•	•
ELBA	•				
TDr	•	•			
WMR	•	•	•	•	•
SI	•	•	•	•	•

---

[1]https://httsp://surfer.nmr.mgh.harvard.edu

9.2.4   Overview of the methods

Due to the lack of an absolute quantification (full kinetic acquisition was not available in our dataset), the SI quantifier - the most comprehensive and sophisticated approach - was used as the reference measure for amyloid burden. SI includes correction for atrophy, spillover and blood flow dependence, and is therefore the quantifier that takes the most error sources into consideration. Selecting a robust measure as the reference allowed us to assess the efficacy of the other quantifiers and the feasibility of their use in clinical and research settings.

To compare both the global and lobar SUVr, ELBA, TDr and WMR with SI, we first determined the correlations and quantified the dispersion with a Bland-Altman analysis. The discriminating power of the different approaches compared with the visual assessment was then measured by the area under the receiver operating characteristic curve (AUC-ROC).

Assuming SUVr, ELBA, TDr and WMR to be proxy measures of the true amyloid load (estimated from the SI), we linearly combined them to obtain more robust indices, and compared these combinations with SI.

Finally, we assessed the sensitivity of each semi-quantification method to amyloid plaque accumulation in patients classified qualitatively as amyloid-negative, with the idea that a more sensitive method could better identify an amyloid load that was physiologically increasing with age.

9.2.5   Assessment of the differences between the quantifiers and SI

The agreement between SUVr, ELBA, TDr and WMR and SI was assessed with a Bland-Altman analysis. The divergences were quantified by the σ of the difference between the global and the lobar SI and the corresponding values of the other quantifiers. The confidence intervals for the σ were obtained from a 1,000 iteration bootstrap procedure.

We linearly combined SUVr, ELBA, TDr and WMR into three scores: AVG1, AVG2 and AVG3. The inverse of the global divergences from SI ($1/\sigma$) were used as weights for the average mean of the quantifiers of concern. Thus, the quantifier having a better agreement with SI contributed more to each combination. Specifically, AVG1 is the weighted mean of SUVr and ELBA, AVG2 is the weighted mean of SUVr, ELBA, TDr, and AVG3 is the weighted mean of SUVr, ELBA, TDr and WMR. The linear correlation between the global and regional SUVr, ELBA, TDr, WMR, AVG1, AVG2 and AVG3 and the corresponding SI was measured by the Pearson correlation coefficient.

To verify SUVr, ELBA, TDr and WMR as independent measures of amyloid load, we looked at the residuals of all possible linear models including these measures (i.e.: SUVr~ELBA, SUVr~TDr, SUVr~WMR, ELBA~TDr, ELBA~WMR and TDr~WMR). The Pearson correlation coefficient between the residuals and the predictors was estimated for each model.

9.2.6   Agreement of quantifiers with visual classification

The discriminating power of the quantifiers and of their combinations were measured by AUC for negative- vs. positive-labeled scans. This assessment was repeated for both

the global and lobar scores. The generalized performance of each score was estimated using a 1,000 iteration bootstrap procedure.

9.2.7 Comparisons in amyloid-negative patients

Linear regression was used to test for possible associations between each quantifier (global and lobar scores), age and cortical thickness in amyloid-negative patients. Before running the regressions, the variance inflation factor (VIF) was computed to verify the possible collinearity between age and cortical thickness (global and lobar).

9.3 Results

9.3.1 Analysis of the differences between the quantifiers and SI

The average divergences of each quantifier from SI are summarized in Figure 9.1 (the corresponding 95% confidence intervals are reported in Supplementary Table 9.4). In each Bland-Altman plot examined, the regression lines and the zero bias line fell within the 95% confidence interval, thus excluding bias changes over the measuring interval. Examples of the Bland-Altman plots and the divergences from SI are given in Figure 9.5.

Among the quantifiers, SUVr and TDr exhibited lower dispersion from SI both globally (whole brain; σ_{SUVr} = 0.31, σ_{TDr} = 0.32) and regionally (average over lobes; σ_{SUVr} = 0.42, σ_{TDr} = 0.43). The highest dispersion from SI at the global level was exhibited by WMR (whole brain σ = 0.57), and at the regional level by ELBA (average lobar σ = 0.55). The lowest variances (σ = 0.31), were observed in TDr (frontal right lobe) and WMR (parietal right lobe). This is in line with the results that showed the frontal and parietal to be the lobes with the lowest dispersion (averages over quantifiers; $\sigma_{frontal}$ = 0.35, $\sigma_{parietal}$ = 0.35). On the other hand, ELBA in the right subcortical ROI exhibited the highest dispersion (σ = 1.06); the highest variances with SI were also observed in this region (average over quantifiers; $\sigma_{central}$ = 0.78).

As expected, the σ of the three linear combinations (i.e., AVG1, AVG2 and AVG3) was lower than those of the quantifiers included in each combination (whole brain; σ_{AVG1} = 0.25, σ_{AVG2} = 0.24, σ_{AVG3} = 0.25; see Figure 9.5). Moreover, the regional average σ of the linear combinations decreased as another quantifier was added.

As evidenced by the correlation coefficients (ρ) summarized in Figure 9.2, each quantifier correlated strongly with SI both globally and regionally, although with some exceptions. In line with the dispersion analysis, there was only a moderate correlation in the subcortical regions(average $\rho_{central}$ = 0.67). Moderate correlations were also observed between SI and WMR (right subcortical ρ = 0.69; left temporal ρ = 0.67), and between SI and ELBA (central ROI; ρ_{right} = 0.43, ρ_{left} = 0.46). The strongest correlations were found in the frontal and parietal lobes (average over quantifiers; $\rho_{frontal}$ = 0.94, $\rho_{parietal}$ = 0.94). Consistent with the dispersion analysis, SUVr and TDr exhibited the strongest correlations with SI both globally (whole brain; ρ_{SUVr} = 0.95, ρ_{TDr} = 0.95) and regionally (average over lobes; ρ_{SUVr} = 0.9, ρ_{TDr} = 0.9). Nonetheless, the lowest correlations were with WMR at the whole-brain level (ρ = 0.83), and with ELBA at the regional level (average over lobes; ρ = 0.81). Also consistent with the dispersions, the coefficients ρ of the three linear combinations were higher than those of the single quantifiers included in each combination (at both the regional and global levels).

The residuals and the predictor variables of the linear models - SUVr~ELBA, SUVr~TDr, SUVr~WMR, ELBA~TDr, ELBA~WMR and TDr~WMR - were found to be uncorrelated, while the linear regressions of the residuals of each model against the respective predictor were all found to be compatible with the null model.
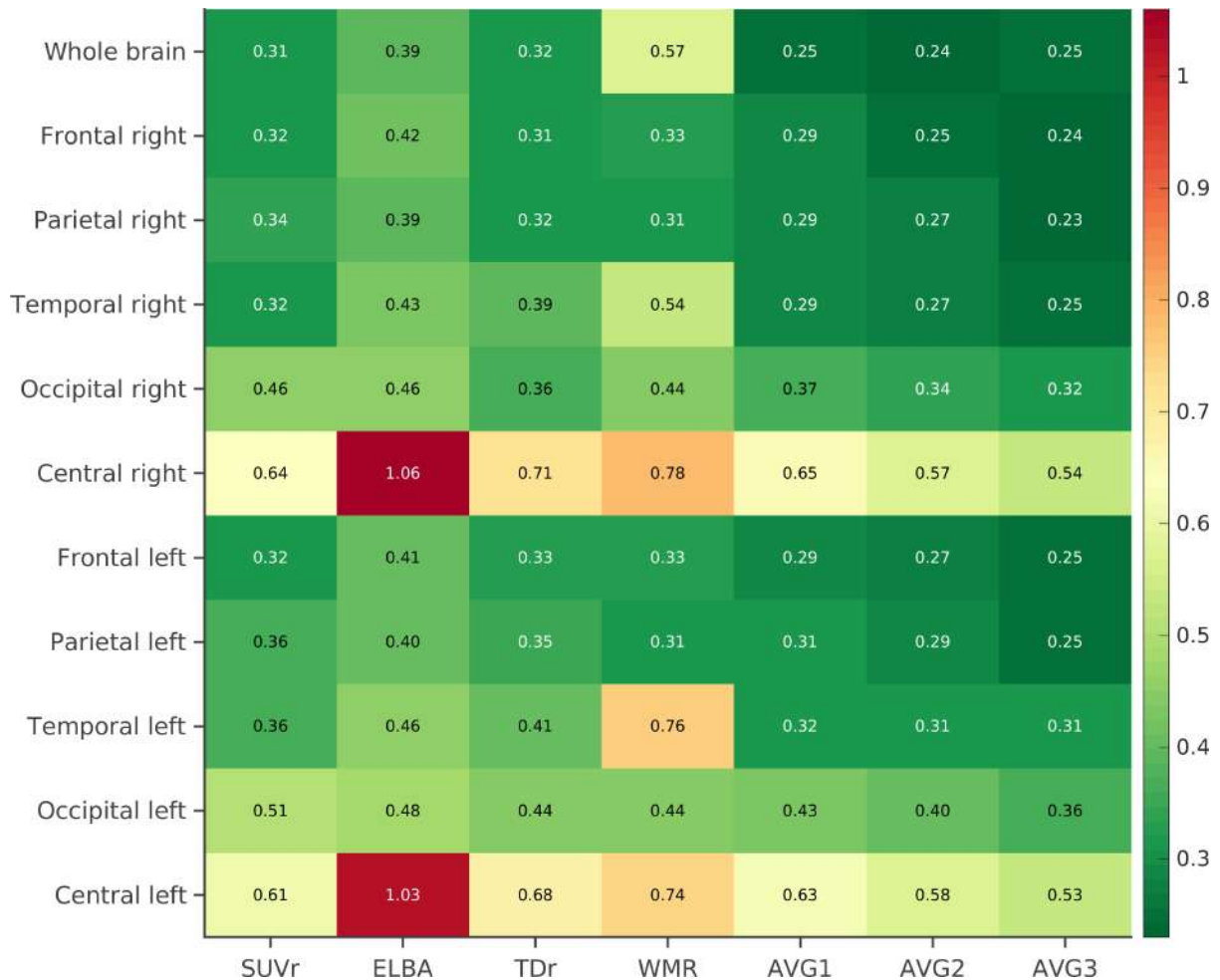
Figure 9.1: Dispersion of quantifiers (and their linear combinations) with SI at brain and lobar level. The values reported correspond to the bootstrapped discrepancies with SI and are expressed as the average σ from the Bland-Altman analysis.
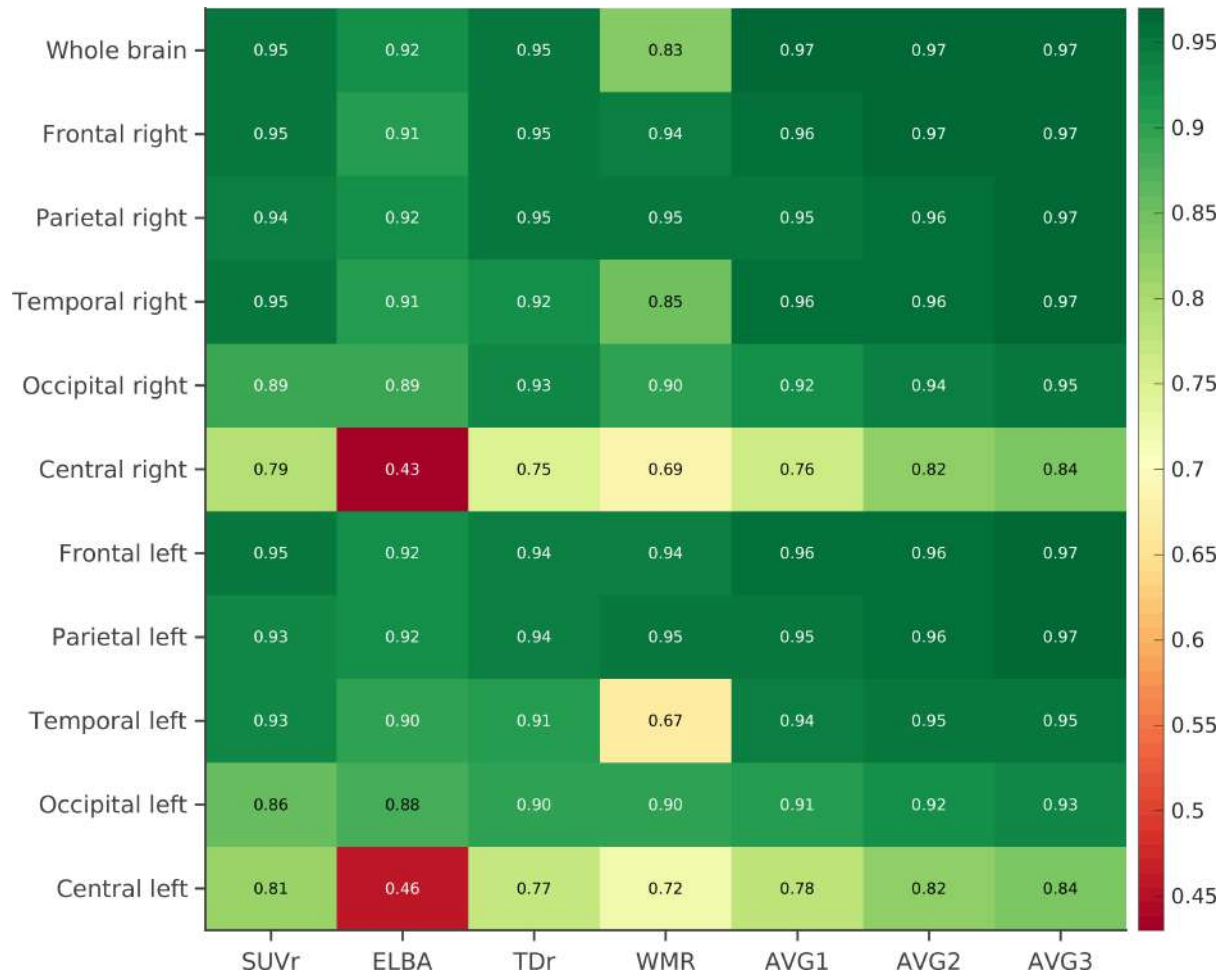
Figure 9.2: Correlations between the quantifiers (and their linear combinations) and SI at the whole-brain and lobar levels (significant at p <0.05).
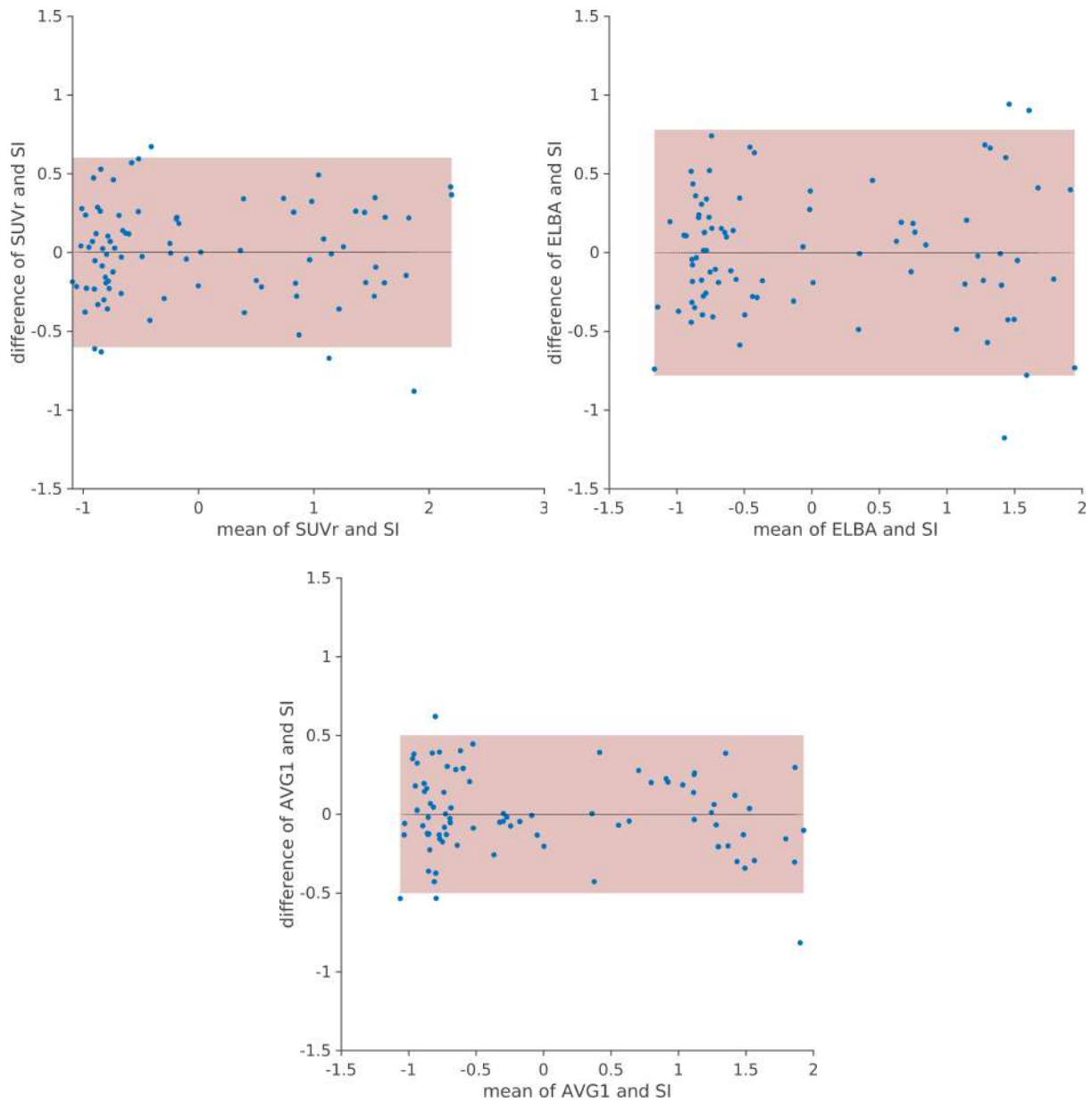
Figure 9.3: Bland-Altman plots of SUVr vs. SI (top left), ELBA vs. SI (top right) and AVG1 (weighted mean of SUVr and ELBA) vs. SI (bottom). In these plots the quantifiers are compared at the whole brain level. As expected, the combination of two methods (AVG1) lowers the dispersion (red area) of the Bland-Altman plot as compared to single methods.

9.3.2   Agreement with the visual classification

The bootstrapped generalized performance vs. the consensus binary visual assessment is summarized in Figure 9.4 and in Supplementary Table 9.5. The results were excellent for all the approaches (whole brain average AUC = 0.99), and for their weighted averages (whole brain average AUC = 1).

The lowest AUCs were observed in the subcortical lobes with ELBA (AUC_{left} = 0.79, AUC_{right} = 0.71), whereas regional AUC = 1 was observed for different quantifiers in different regions (e.g., parietal, frontal, temporal). The central was the lobe with the lowest AUC (average AUC over the quantifiers = 0.9), whereas the parietal and frontal had the highest (average AUC over the quantifiers = 0.99). With a global value of 0.98, WMR had a slightly lower AUC than the other quantifiers.

However, in interpreting these results it should be borne in mind that the slight differences in the average AUCs are not relevant if the confidence intervals overlap.

Figure 9.4: Regional and whole-brain bootstrapped performances (expressed as average AUC) of the quantifiers and their linear combinations vs. visual assessment.

9.3.3   Comparisons in amyloid-negative patients

A moderate correlation between age and cortical thickness was observed in amyloid-negative patients ($|\rho|$<0.48, p<0.05). However, the VIF excluded collinearity of these

variables (<1.29 for all covariates).

The results from the linear models are given in Table 9.2. Below, we describe the significant associations that survived a Benjamini-Hochberg correction for multiple comparisons.

At the global level, TDr, WMR and SI were significantly associated with age (adjusted p <0.05). Similarly, in each brain lobe (both right and left hemispheres) significant associations were observed between TDr, WMR and SI and age (adjusted p <0.05). The only exception was WMR in the right occipital lobe, which was not related to age (p >0.05).

Linear relationships between SUVr, ELBA and age were observed only in the right temporal lobes (adjusted p <0.05). No associations between cortical thickness and the quantifiers survived at both the global and lobar levels. The regression slopes of each significant association were positive. Figure 9.5 shows the positive associations between the quantifiers including early acquisitions and age at the whole brain level.
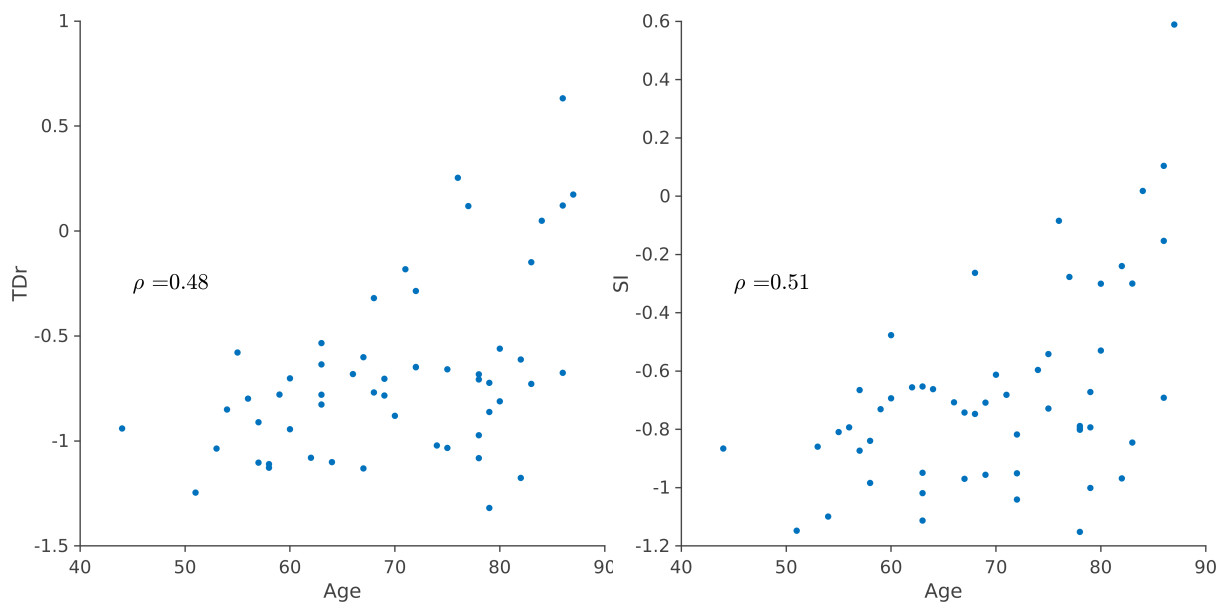

Figure 9.5: Scatter plot of age vs. whole-brain SI (right) and TDr (left) in the amyloid-negative subset. Both SI and TDr significantly correlate with age (ρ=0.51 and ρ=0.48 respectively) in subjects qualitatively evaluated as negative, demonstrating the potential to identify subtle changes in amyloid load.

Table 9.2: Associations between the quantifier scores, age, and cortical thickness at the global and lobar levels in qualitatively-assessed amyloid-negative patients.

Region	Quantifier	Age		Thickness	
		β	p	β	p
Whole brain	SUVr		n.s.		n.s.
	ELBA		n.s.		n.s.
	TDr	0.021	** a		n.s.
	WMR	0.022	* a		n.s.
	SI	0.02	** a	0.724	*
Frontal right / left	SUVr		n.s. / n.s.		n.s. / n.s.
	ELBA		n.s. / n.s.		n.s. / n.s.
	TDr	0.019 / 0.020	** a / ** a		n.s. / n.s.
	WMR	0.017 / 0.016	* a / * a		n.s. / n.s.
	SI	0.018 / 0.019	** a / ** a	- / 0.698	n.s. / *
Parietal right / left	SUVr		n.s. / n.s.		n.s. / n.s.
	ELBA		n.s. / n.s.		n.s. / n.s.
	TDr	0.018 / 0.020	* a / ** a		n.s. / n.s.
	WMR	0.014 / 0.013	* a / * a		n.s. / n.s.
	SI	0.019 / 0.019	** a / ** a		n.s. / n.s.
Temporal right / left	SUVr	0.017 / -	* a / n.s.	0.859 / -	* / n.s.
	ELBA	0.013 / -	* a / n.s.	1.010 / -	* / n.s.
	TDr	0.023 / 0.021	** a / ** a		n.s. / n.s.
	WMR	0.028 / 0.028	* a / * a	1.130 / 1.901	* / *
	SI	0.023 / 0.020	** a / ** a	0.885 / 0.574	* / *
Occipital right / left	SUVr		n.s. / n.s.		n.s. / n.s.
	ELBA		n.s. / n.s.		n.s. / n.s.
	TDr	0.019 / 0.019	** a / * a		n.s. / n.s.
	WMR	- / 0.018	n.s. / * a		n.s. / n.s.
	SI	0.021 / 0.026	** a / ** a		n.s. / n.s.

**p < 0.001, *p < 0.05, n.s. p > 0.05
a Still significant (p<0.05) after the p-values correction for multiple comparison with the Benjamini-Hochberg procedure for multiple testing

9.4   Discussion

The overall purpose of this study was to compare approaches for semi-quantitative analysis of amy-PET imaging using different sources of information and with increasing levels of refinement. Among the methods considered in this comparison, SI is the most comprehensive and the most complex as it takes into account the widest range of potentially confounding factors, and, like WMR, it requires dual-time-point PET/MRI acquisition (or a PET/CT and a 3DT1 MPRAGE, 1-mm isotropic acquisition) and the construction of a patient-specific atlas [37]. SI was therefore kept as the reference measure of Aβ against which the performances of SUVr [139], TDr [41], ELBA [43] and WMR [37] were calculated.

At the whole-brain level, each quantifier showed excellent agreement with the visual assessment, so in terms of the binary classification there was substantial equivalence between the methods. Visual assessment showed that our dataset mainly comprised two

distinct clusters: amyloid-negative (SI; μ=0.01±0.12) and amyloid-positive patients (SI; μ=0.65±0.19). A much larger dataset including patients with clinically mild cognitive impairment could better elucidate the "gray zone" between positivity and negativity, and possibly heighten the differences among the methods.

The correlation analysis showed that there were strong associations between SI and every quantifier considered in this study, at both the regional and global levels.

At the global level, WMR (although derived from early and late acquisitions and a PET/MR scan) was the approach that most diverged from SI (confirmed by the dispersion analysis) as it considers the kinetics in a given cortical region compared with the kinetics in the WM in the same subject. Other quantifiers, however, use WM information, although only partially: ELBA measures the contrast between white and gray matter, and TDr uses WM to normalize the counts on the hot spot. Only SUVr (at least the implementation with critical-cerebellar ROIs) focuses mainly on pure cortical distribution, without considering WM distribution. The fact that WMR correlates with the visual binary classification and with age in cases classified as qualitatively negative shows it to be a good metric, albeit based on different assumptions.

At the regional level, the differences between the quantifiers seem to be related to specific characteristics of the approaches. For example, a lack of agreement between ELBA and SI was found in the basal ganglia (central ROI). This may be explained by several factors: first, image registration does not rely on the accompanying MRI, and second, ELBA is based on the WM/GM contrast, which is harder to identify in deep structures. SI, on the other hand, constructs a patient-specific atlas (based on the patient's MR), which allows for a much more precise alignment of the basal ganglia, deep nuclei, and insula.

As seen in the results section, SUVr, ELBA, TDr and WMR all come close to SI despite differing in their nature and characteristics. By linearly combining these techniques we obtained scores (i.e., AVG1, AVG2, AVG3) closer to SI. Moreover, by repeating the analysis with AVG1, AVG2 and AVG3 calculated as unweighted averages, these combinations were found to be even closer to SI than the single approaches (see Supplementary Table 9.6). This suggests that the weights, calculated with respect to SI, only introduce an improvement factor and confirms the suitability of SI as the reference. If this were not the case, then combining different independent methods blind to the reference would not achieve greater closeness, and might even move away from it.

In this study, we found that a combination of independent quantifiers provided better results than the individual quantifiers both in terms of correlation and distance from the chosen reference method. This suggests that using different sources of information and/or independent techniques can provide a better estimation of amyloid load. The analysis of the independence of SUVr, ELBA and TDr confirms the observations of our group [41] using a different radiotracer.

In patients qualitatively classified as amyloid negative, the methods that included a correction for blood flow (SI, WMR and TDr) were able to identify the physiologic accumulation of amyloid with age, showing that a metric that includes the early phase is more accurate (i.e., that includes information on blood flow and hence on neurodegeneration).

9.5 Conclusions

The quantifiers we evaluated (SUVr, ELBA, TDr and WMR), came close to SI, chosen as the reference method, even though they are different in nature and in their characteristics. If we were to single out one method, it would be TDr (accepting some imprecision in the deep structures), which appears to be accurate (deriving information from dual time points) and easier to implement than SI (no CT or MR needed). However, this study suggests that a combination of independent quantifiers yields better results than the individual approaches, both in terms of correlation and distance from the chosen reference method. Efforts should therefore be made towards developing multi-classifier systems to measure surrogate endpoints for therapy evaluation. Moreover, the ability of some quantifiers (TDr, WMR and SI) to depict variations in brain amyloid load with age in subjects assessed qualitatively as amyloid-negative demonstrates the goodness of the estimate and their potential for identifying subtle variations in amyloid load compared with standard methods (such as SUVr).

9.6   Supplementary materials

Table 9.3: Diagnoses of the patients grouped by visual classification. MCI: mild cognitive impairment; LBD: Lewy body dementia; bvFTD: behavioral variant frontotemporal degeneration; probADD: probable AD dementia; possADD: possible AD dementia; atypAD: atypical AD; mixDem: mixed-type dementia.

diagnosis	Visual classification	
	negative	positive
MCI	23	10
LBD	1	-
bvFTD	4	1
probADD	8	9
possADD	14	7
atypAD	2	3
mixDem	2	1

Table 9.4: Dispersion of quantifiers (and their linear combinations) with SI at brain and lobar level: results of Bland-Altman analysis. The bootstrapped discrepancies with SI are expressed as average σ and its 95% confidence interval.

|	SUVr	ELBA	TDr	WMR	AVG1	AVG2	AVG3
Whole brain	.31 [.3 - .31]	.39 [.39 - .4]	.32 [.32 - .33]	.57 [.56 - .58]	.25 [.25 - .25]	.24 [.24 - .25]	.25 [.25 - .26]
Frontal right	.32 [.32 - 32]	.42 [.42 - 43]	.31 [.31 - .31]	.33 [.33 - .33]	.29 [.29 - .3]	.25 [.25 - .26]	.24 [.23 - .24]
Parietal right	.34 [.34 - .35]	.39 [.39 - .4]	.32 [.32 - .32]	.31 [.30 - .31]	.29 [.29 - .29]	.27 [.26 - .27]	.23 [.23 - .24]
Temporal right	.32 [.32 - .32]	.43 [.42 - .43]	.39 [.39 - .39]	.54 [.54 - .55]	.29 [.28 - .29]	.27 [.27 - .27]	.25 [.25 - .25]
Occipital right	.46 [.46 - .47]	.46 [.45 - .46]	.36 [.36 - .37]	.44 [.44 - .45]	.37 [.37 - .37]	.34 [.34 - .34]	.32 [.32 - .33]
Central right	.64 [.63 - .64]	1.06 [1.05 - 1.07]	.71 [.71 - .72]	.78 [.77 - .79]	.65 [.64 - .65]	.57 [.57 - .58]	.54 [.54 - .55]
Frontal left	.32 [.32 - .32]	.41 [.41 - .41]	.33 [.33 - .34]	.33 [.33 - .33]	.29 [.29 - .29]	.27 [.27 - .27]	.25 [.25 - .25]
Parietal left	.36 [.36 - .36]	.4 [.4 - .4]	.35 [.35 - .35]	.31 [.31 - .31]	.31 [.31 - .31]	.29 [.29 - .29]	.25 [.25 - .25]
Temporal left	.36 [.36 - .36]	.46 [.45 - .46]	.41 [.41 - .41]	.76 [.75 - .78]	.32 [.32 - .33]	.31 [.3 - .31]	.31 [.31 - .32]
Occipital left	.51 [.51 - .51]	.48 [.48 - .49]	.44 [.44 - .44]	.44 [.44 - .44]	.43 [.42 - .43]	.40 [.40 - .40]	.36 [.35 - .36]
Central left	.61 [.61 - .62]	1.03 [1.02 - 1.04]	.68 [.67 - .68]	.74 [.74 - .75]	.63 [.63 - .64]	.58 [.57 - .58]	.53 [.53 - .54]
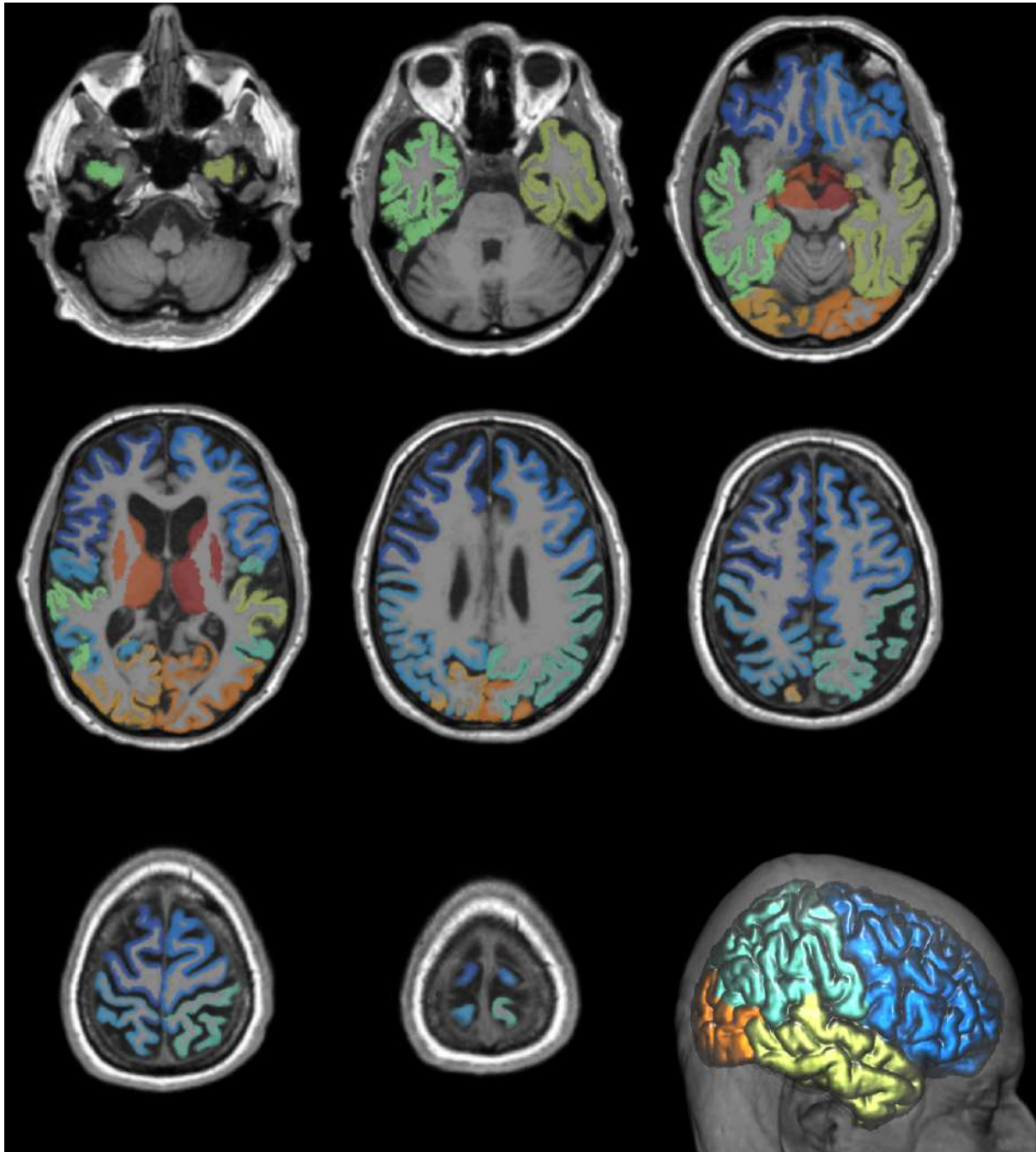
Figure 9.6: The lobular parcellation of the brain adopted for this study. Each hemisphere (the right shown here) was divided into 5 ROIs: frontal (blue), parietal (turquoise), temporal (yellow), occipital (orange), central structures (dark red).

Table 9.5: Regional and whole-brain bootstrapped performance (expressed as average AUC and CI 95%) of the quantifiers and their linear combinations versus visual assessment.

	SUVr	ELBA	TDr	WMR	AVG1	AVG2	AVG3	SI
Whole brain	.99 [.9 - 1]	1 [1 - 1]	1 [.98 - 1]	.98 [.93 - .99]	1 [.98 - 1]	1 [.99 - 1]	1 [.99 - 1]	1 [.98 - 1]
Frontal right	.98 [.91 - 1]	.99 [.97 - 1]	.99 [.97 - 1]	.99 [.96 - 1]	.99 [.95 - 1]	.99 [.97 - 1]	.99 [.97 - 1]	.99 [.96 - 1]
Parietal right	.99 [.94 - 1]	1 [.99 - 1]	.99 [.97 - 1]	.99 [.95 - 1]	1 [.98 - 1]	1 [.97 - 1]	.99 [.97 - 1]	.99 [.97 - 1]
Temporal right	.97 [.87 - 1]	.99 [.97 - 1]	.99 [.96 - 1]	.95 [.83 - .99]	.99 [.95 - 1]	.99 [.97 - 1]	.99 [.97 - 1]	.99 [.96 - 1]
Occipital right	.98 [.94 - 1]	.98 [.93 - 1]	.99 [.96 - 1]	.93 [.84 - .98]	.99 [.96 - 1]	.99 [.97 - 1]	.99 [.96 - 1]	.97 [.92 - 99]
Central right	.96 [.83 - .99]	.71 [.58 - .82]	.94 [.88 - .97]	.9 [.77 - .96]	.95 [.87 - .98]	.97 [.91 - .99]	.97 [.91 - .99]	.97 [.91 - .99]
Frontal left	.99 [.93 - 1]	1 [1 - 1]	1 [.99 - 1]	1 [.97 - 1]	1 [.96 - 1]	1 [.99 - 1]	1 [.99 - 1]	1 [.97 - 1]
Parietal left	.99 [.96 - 1]	1 [1 - 1]	.99 [.97 - 1]	.99 [.96 - 1]	1 [.99 - 1]	1 [.99 - 1]	1 [.99 - 1]	1 [.96 - 1]
Temporal left	.99 [.95 - 1]	1 [1 - 1]	.99 [.98 - 1]	.96 [.89 - .99]	1 [.99 - 1]	1 [1 - 1]	1 [1 - 1]	.99 [.97 - 1]
Occipital left	.98 [.92 - 1]	.96 [.88 - .99]	.97 [.91 - .99]	.91 [.81 - .96]	.98 [.94 - 1]	.98 [.95 - 1]	.97 [.93 - .99]	.93 [.85 - .98]
Central left	.96 [.85 - .99]	.79 [.68 - .87]	.98 [.95 - 1]	.94 [.86 - .98]	.95 [.85 - .99]	.98 [.93 - 1]	.99 [.97 - 1]	.96 [.89 - .98]

Table 9.6: Bootstrapped dispersions, Pearson correlation coefficients and bootstrapped performance of the three combinations AVG1, AVG2 and AVG3 calculated as unweighted, arithmetic means of the quantifiers.

	Dispersion (σ)			Correlation (ρ)			AUC		
	AVG1	AVG2	AVG3	AVG1	AVG2	AVG3	AVG1	AVG2	AVG3
Whole brain	.26 [.26 - .26]	.25 [.25 - .25]	.28 [.27 - .28]	0.96	0.97	0.96	1 [.97 - 1]	1 [.98 - 1]	1 [.99 - 1]
Frontal right	.30 [.30 - .30]	.26 [.26 - .26]	.24 [.24 - .24]	0.95	0.96	0.97	.99 [.93 - 1]	.99 [.97 - 1]	.99 [.97 - 1]
Parietal right	.29 [.29 - .30]	.27 [.27 - .27]	.24 [.23 - .24]	0.95	0.96	0.97	.1 [.98 - 1]	.1 [.98 - 1]	.99 [.97 - 1]
Temporal right	.29 [.29 - .30]	.28 [.27 - .28]	.26 [.26 - .26]	0.95	0.96	0.96	.99 [.95 - 1]	.99 [.96 - 1]	.99 [.97 - 1]
Occipital right	.37 [.37 - .37]	.34 [.34 - .35]	.33 [.33 - .33	0.93	0.94	0.94	.99 [.98 - 1]	.99 [.96 - 1]	.99 [.96 - .99]
Central right	.70 [.70 - .71]	.60 [.60 - .71]	.56 [.56 - .57]	0.72	0.79	0.82	.92 [.83 - .97]	.95 [.87 - .99]	.96 [.90 - .99]
Frontal left	.29 [.29 - .30]	.28 [.27 - .28]	.26 [.26 - .26]	0.95	0.96	0.97	1 [.97 - 1]	1 [.99 - 1]	1 [.99 - 1]
Parietal left	.31 [.31 - .31]	.29 [.29 - .29]	.25 [.25 - .25]	0.95	0.96	0.97	1 [.99 - 1]	1 [.99 - 1]	1 [.99 - 1]
Temporal left	.33 [.33 - .33]	.31 [.31 - .32]	.35 [.34 - .35]	0.94	0.95	0.94	1 [.99 - 1]	1 [1 - 1]	1 [1 - 1]
Occipital left	.42 [.42 - .42]	.40 [.40 - .40]	.36 [.35 - .36]	0.9	0.92	0.93	.98 [.94 - 1]	.98 [.94 - 1]	.98 [.92 - .99]
Central left	.68 [.68 - .69]	.61 [.60 - .61]	.56 [.55 - .56]	0.73	0.79	0.82	.94 [.84 - .98]	.97 [.91 - .99]	.99 [.97 - 1]

Chapter 10

An attempt to model the relationship between amyloid and tau at the regional level

10.1 Introduction

The combination of Aβ deposits and NTFs has characterised the Alzheimer's disease since the first diagnostic criteria [179]. Despite the introduction of radioligands for the in-vivo assessment of these key events has resulted in substantial progress in understanding the AD pathology, the underlying mechanisms that link tau and amyloid are still not fully understood.

In a recent study, Jack and colleagues [128] address this question using data of a large multicenter cohort (1343 participants) including cognitively unimpaired, MCI, DLB, FTD and AD patients. They all underwent amyloid and tau PET examinations that were analysed with a standard SUVr approach. Based on previously established abnormality cut points of SUVr, each subject was classified as having either normal or abnormal levels of amyloid and tau into four groups (A-/T-, A+/T-, A-/T+ and A+/T+). The subsequent analyses aimed to determine relationships between the bivariate distribution of Aβ and tau at whole brain level and the frequency with which patients fell into the four groups. In figure 10.1 the bivariate amyloid and tau levels of the entire population, at whole brain level, are represented.
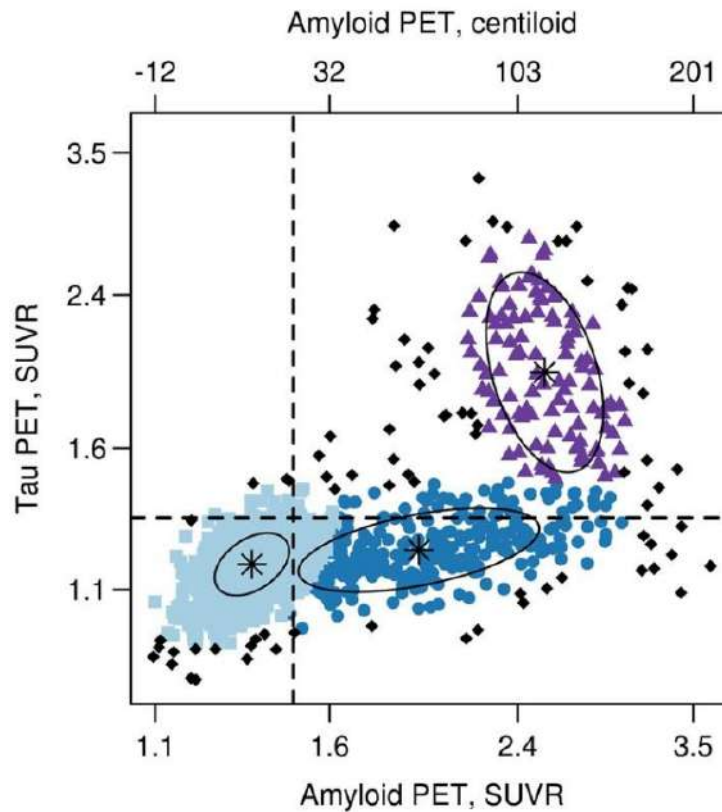
Figure 10.1: Scatterplot of global tau PET SUVr versus global amyloid PET SUVr with points coloured according to the three-cluster classification from a bivariate mixture model. The vertical and horizontal lines represent the cut points of 1.48 SUVr for amyloid PET and 1.33 SUVr for tau PET. It can be observed that the most frequent pathway to A+/T- requires moving from state A-/T- to state A+/T-. Courtesy of Jack and colleagues [128].

The results of this study are in line with the view that increasing tau burden is generally associated with abnormal amyloid levels. Interestingly, the authors showed that the proportion of amyloid-positive patients increases with age, before a gradual increase in tau-positive proportion. In figure 10.2 the Aβ and tau levels for different ages among cognitively unimpaired, MCI and AD.
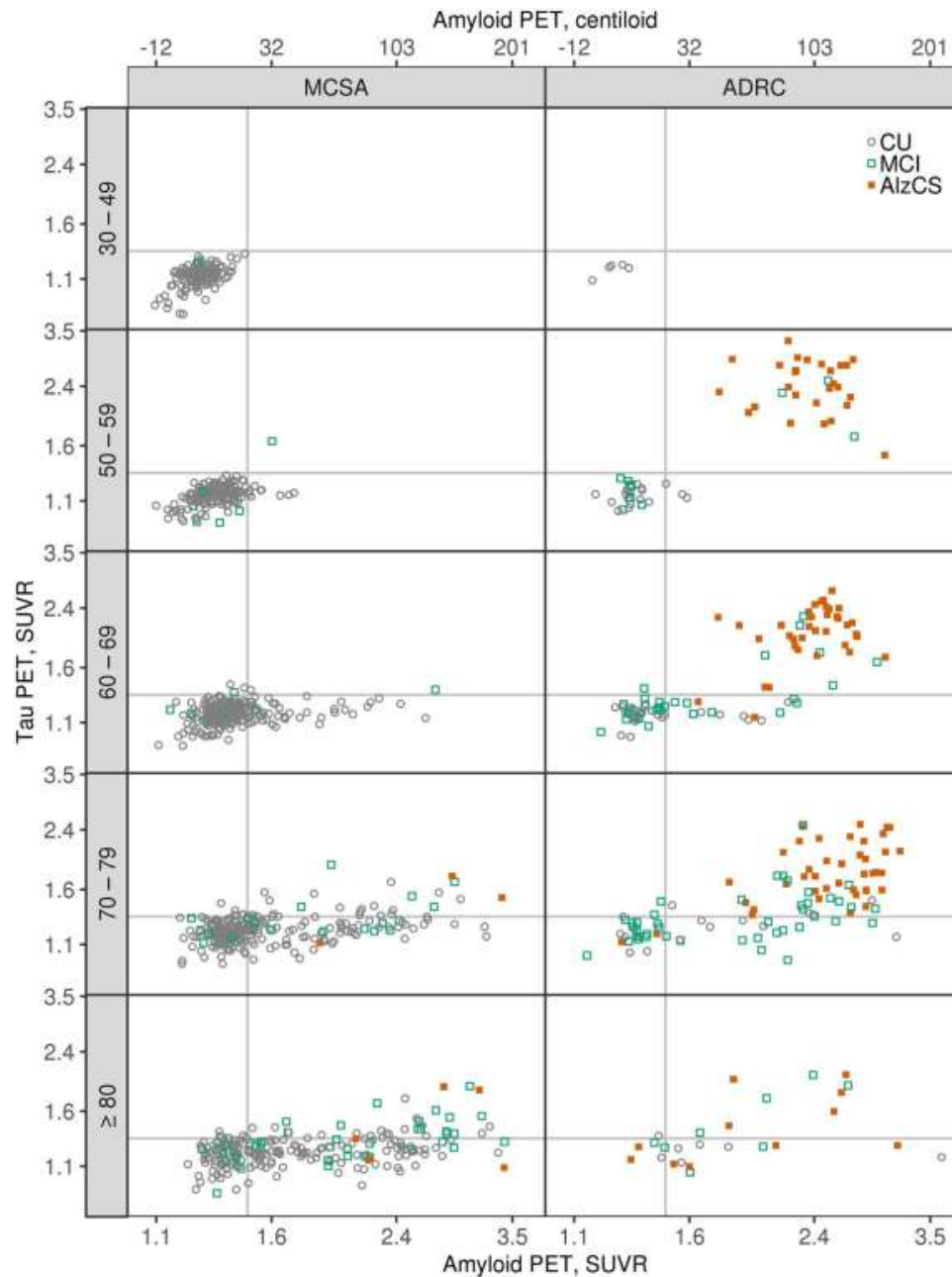
Figure 10.2: Scatter plots of tau PET SUVr versus amyloid PET SUVR by age groups among cognitively unimpaired (CU), MCI, and AD individuals. The vertical and horizontal lines represent the cut points of 1.48 SUVr for amyloid PET and 1.33 SUVr for tau PET. Points are coloured by clinical diagnosis. Tau PET and amyloid PET values are in SUVr units but the data is plotted on a log scale, which accounts for the uneven spacing. Axis labels on the top of the columns represent amyloid PET values on a centiloid scale. Courtesy of Jack and colleagues [128].

In aggregate these data led to the conclusion that progression in the AD continuum likely involves transactions from A-/T- to A+/T- to A+/T+. This suggests that high levels of brain Aβ may not directly cause the tau pathology, but rather seems to be a prerequisite. On this basis, we aim to assess the relationship between Aβ and tau at the regional level.

10.2 Material and methods

This study is based on a single center dataset of 153 patients (aged 33-89, μ = 72.4 ± 8.1; 50.3% male) with cognitive complaints recruited and evaluated at the Geneva Memory Clinic. These patients underwent a diagnostic workup, in the framework of a prospective study, including neuropsychological assessment (MMSE; μ = 25.54 ± 4.2), structural neuroimaging (MRI T13D), amyloid and tau PET within a 6 months timeframe. Etiological diagnoses were made by physicians using conventional criteria: 84 were classified as non-AD and 69 as AD. A Siemens Biograph mCT PET scanner was used to perform the PET examinations. The amyloid PET were acquired with two radioligands (75 with ^{18}F-Flutemetamol and 78 with ^{18}F-Florbetapir), whereas all the tau PET were acquired with the same radiotracer (^{18}F-Flortaucipir). The scans were acquired according to the recommendations of the tracer manufacturers [66, 90, 219, 159] and to the guidelines of the EANM and of the SNMMI [136]. For each patient, an anatomical mask was delineated on the T13D according to the AAL3 parcellation [229], with the statistical parametric mapping package. The obtained masks provided an anatomical atlas whose regions were used as target ROIs to calculate the SUVr on both amyloid and tau PET. The cerebellar gray matter and the cerebellar crus were used as reference regions respectively for amyloid and tau. To make the quantification less susceptible to fluctuations, the anatomical regions delineated on each T13D were merged together into 10 larger ROIs (details are provided in table 10.1). To compare measures obtained from scans acquired with different tracers we mapped the SUVr results from ^{18}F-Flutemetamol scans onto ^{18}F-Flutorbetapir with a reference model of uptake conversion [42].

Table 10.1: The ROI composition is explained: the names in the "Composition" column correspond to the labels of the AAL3 parcellation [229].

Composition	ROI name
ACC_pre, ACC_sub, ACC_sup	ACC
OFCmed, OFCpost, Olfactory, OFCant, OFClat	Olfactory
Cuneus, Precuneus	Cuneus and Precuneus
Cingulate_Ant, Cingulate_Mid, Cingulate_Post	Cingulate
Frontal_Inf_Oper, Frontal_Inf_Orb, Frontal_Inf_Tri, Frontal_Med_Orb, Frontal_Mid, Frontal_Sup, Frontal_Sup_Medial	Frontal
Occipital_Inf, Occipital_Mid, Occipital_Sup, Calcarine	Occipital
Putamen, Pallidum	Putamen and Pallidum
Paracentral_Lobule, Postcentral, Precentral	Para Pre Postcentral
Parietal_Inf, Parietal_Sup	Parietal
ParaHippocampal, Temporal_Inf, Temporal_Mid, Temporal_Sup, Temporal_Pole_Mid, Temporal_Pole_Sup	Temporal

A simple model has been developed to coarsely describe the amyloid and tau relationship between each pair of brain regions. This model is based on some following

assumptions:

- The dynamics of tau and amyloid accumulation are comparable and can be described by the same curve.

- The data used to develop the model provide a complete representation of the full positivity and negativity spectrum of both amyloid and tau.

- Regional tau and amyloid levels increase solely and, over a period of tim, each patient is assumed to move from a negative to a positive state for each biomarker.

Since it has been shown to properly describe the accumulation dynamics of the two biomarkers [31, 210], a sigmoid function was chosen to describe both the amyloid and tau behaviors. This simple model is designed to fit the regional distribution of amyloid and tau so that, for each pair of brain regions, a single parameter coarsely describes the local amyloid/tau relationship. The parameter (w) expresses the difference of the two sigmoids (see figure 10.3), and it is calculated as follows:

$$w = log(\frac{x - xy}{y - xy}) \qquad (10.1)$$

Where x and y are the regional amyloid and tau burden respectively.
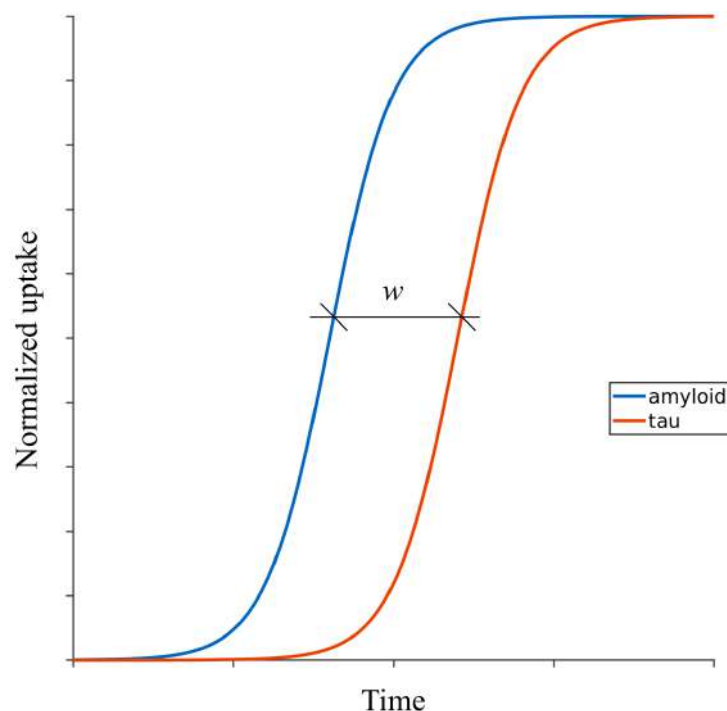
Figure 10.3: The sigmoids represent the regional deposition of amyloid and tau, the parameter w is the delay between the two curves.

For each pair of brain regions, the model provides a distribution of w representing the possible trajectories of amyloid and tau accumulation of each patient (see figure 10.4).
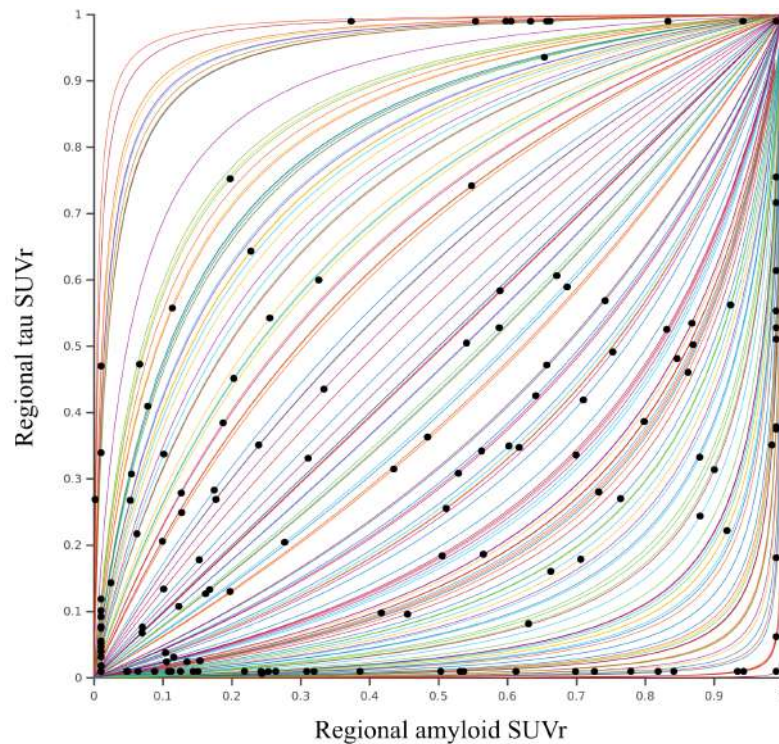
Figure 10.4: Each curve represents the possible trajectory of tau/amyloid accumulation of an individual patient (black dots) for a given pair of brain regions.

Given all simplifying assumptions, w should be interpreted as a coarse representation of the regional amyloid/tau relationship rather than an actual delay. In detail:

- $w > 0$; tau is delayed with respect to amyloid, as w increases the trajectories become more convex.

- $w = 0$; tau and amyloid deposition occurs approximately at the same rate.

- $w < 0$; amyloid is delayed with respect to tau, as w increases the trajectories become more concave.

The w distributions from each pair of ROIs were compared with the global distribution, which made it possible to identify regions with abnormal behaviour. Subsequently, the symmetry of the w distributions across left and right hemispheres in the global population in AD and non-AD patients was assessed. Finally, the relationship between the regional distributions of w and markers of neurodegeneration in both AD and non-AD patients was assessed.

10.3   Results

The average of the w distributions were used to represent the amyloid/tau population trend for each pair of brain regions, a matrix representation of the output of the model is provided in figure 10.5.
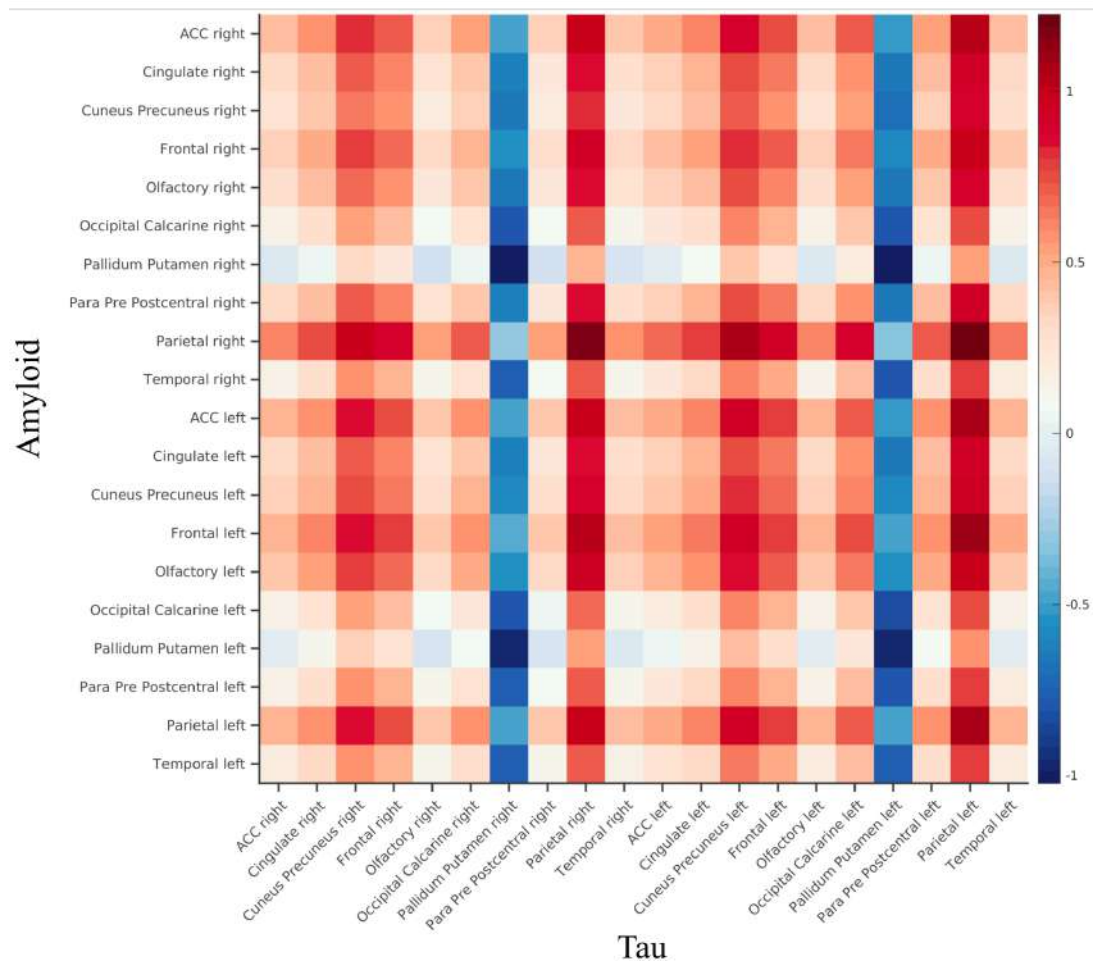
Figure 10.5: Matrix representation of the average w for any possible combination of brain ROIs.

Each local distribution was compared to the global one with a t-test. We observed that the pairs of regions in which the average w was significantly different ($p<0.05$) from the global distribution were those involving pallidum, putamen, cuneus, precuneus and parietal. Specifically, tau accumulation seemed to anticipate ($w<0$, blue cells in figure 10.5) amyloid in the pallidum and putamen (right or left indifferently). This may be due to the off-target binding of ^{18}F-Flortaucipir in these regions [10]. Conversely, the greatest delay of tau compared to amyloid ($w>0$, red cells in figure 10.5) was observed in parietal, cuneus and precuneus. These regions are Aβ accumulation sites in the early stages of AD [212].

In both AD and non-AD populations the symmetry of the amyloid/tau relationship across brain hemispheres was assessed. The average w of each pair of brain regions was compared to its contralateral homologous one with a t-test. In the AD subgroup, no differences were observed between the two hemispheres. Conversely, in non-AD patients, significant differences ($p<0.05$) were observed in cuneus and precuneus, frontal, olfactory, occipital and calcarine ROIs.

To assess whether significant associations between the model output and neurodegeneration existed, the regional distributions of w (averaged across brain hemispheres) were regressed against MMSE and hippocampal volume. All models were adjusted for age, sex and education. This regression analysis was carried out on both the AD and non-AD population and the p-values of the models were all corrected with the Benjamini-

Yekutieli procedure for multiple testing. As table 10.2 shows, in non-AD patients, the only significant association was observed between MMSE and the w distribution from occipital and calcarine ROI (p<0.05). Conversely, in AD patients (see table 10.3), significant associations were observed with MMSE in all brain ROIs (p<0.05). This suggested a relationship between the shape of the amyloid/tau accumulation profile (coarsely described by w) and the cognitive decline: shorter delay between tau and amyloid corresponded to lower MMSE values. Conversely, when tau was delayed with respect to Aβ load, higher MMSE scores occurred. Similarly, hippocampal volume was related to the w distributions in a majority of regions (p<0.05) in AD patients (see table 10.3). This result is in line with what has been observed for the MMSE: a loss in total hippocampal volume was linked to to a more linear trend in the tau amyloid relationship. As one may notice, in both table 10.2 and 10.3, the age is significant (p<0.05) in almost every model both for non-AD and AD subgroups suggesting that the tau deposition is slower with respect to the amyloid in the elderly.

Table 10.2: Associations between the regional w distributions, age, education, MMSE and hippocampal volume in non-AD patients. In each cell the β coefficient of the significant regressors.

ROI	$w \sim$ Age + Education+ Sex + MMSE				$w \sim$ Age + Education + Sex + Hip. Vol.			
	Age	Education	Sex	MMSE	Age	Education	Sex	Hip. Vol.
ACC	0.02 *	n.s.	n.s.	n.s.	n.s.	n.s.	n.s.	n.s.
Olfactory	0.01 *	n.s.	n.s.	n.s.	n.s.	n.s.	n.s.	n.s.
Cuneus and Precuneus	0.02 *	n.s.	n.s.	n.s.	0.02 *	n.s.	n.s.	n.s.
Cingulate	10^{-3} *	n.s.	n.s.	n.s.	10^{-3} *	n.s.	n.s.	n.s.
Frontal	10^{-3} *	n.s.	n.s.	n.s.	10^{-3} *	n.s.	n.s.	n.s.
Occipital	0.02 *	n.s.	n.s.	0.01 *	0.02 *	n.s.	n.s.	n.s.
Putamen and Pallidum	0.01 *	n.s.	n.s.	n.s.	0.04 *	n.s.	n.s.	n.s.
Para Pre Postcentral	10^{-3} *	n.s.	n.s.	n.s.	10^{-3} *	n.s.	n.s.	n.s.
Parietal	10^{-3} *	n.s.	n.s.	n.s.	10^{-3} *	n.s.	n.s.	n.s.
Temporal	10^{-3} *	n.s.	n.s.	n.s.	10^{-3} *	n.s.	n.s.	n.s.

* p < 0.05; n.s. not significant;

Table 10.3: Associations between the regional w distributions, age, education, MMSE and hippocampal volume in AD patients. In each cell the β coefficient of the significant regressors.

ROI	$w \sim$ Age + Education+ Sex + MMSE				$w \sim$ Age + Education + Sex + Hip. Vol.			
	Age	Education	Sex	MMSE	Age	Education	Sex	Hip. Vol.
ACC	n.s.	n.s.	n.s.	10^{-3} *	0.02 *	n.s.	n.s.	0.01 *
Olfactory	0.02 *	n.s.	n.s.	10^{-3} *	10^{-3} *	n.s.	n.s.	0.04 *
Cuneus and Precuneus	0.01 *	n.s.	n.s.	10^{-3} *	0.01 *	n.s.	n.s.	n.s.
Cingulate	10^{-3} *	n.s.	n.s.	10^{-3} *	10^{-3} *	n.s.	n.s.	10-3 *
Frontal	0.01 *	n.s.	n.s.	10^{-3} *	10^{-3} *	n.s.	n.s.	n.s.
Occipital	10^{-3} *	n.s.	n.s.	0.01 *	10^{-3} *	n.s.	n.s.	n.s.
Putamen and Pallidum	10^{-3} *	n.s.	n.s.	0.01 *	10^{-3} *	n.s.	n.s.	0.01 *
Para Pre Postcentral	10^{-3} *	n.s.	n.s.	10^{-3} *	10^{-3} *	n.s.	n.s.	n.s.
Parietal	10^{-3} *	n.s.	n.s.	10^{-3} *	10^{-3} *	n.s.	n.s.	0.04 *
Temporal	10^{-3} *	n.s.	n.s.	10^{-3} *	10^{-3} *	n.s.	n.s.	0.01 *

* p < 0.05; n.s. not significant;

10.4   Further developments

These very preliminary results need to be confirmed by further analysis. To perform a first validation of our model, we are planning to compare the estimated accumulation profile with the model with the actual trajectories that can be derived with the analysis of longitudinal data. Moreover, to check the consistency of the results obtained with the linear models we are planning to test different markers of neurodegeneration (such as MTA and FDG uptake) and risk factors of AD such as the APOE.

Chapter 11

Remarks & conclusions

Amyloid PET allow for low-invasive in-vivo detection of amyloid plaques; it significantly contributes to both early and differential diagnosis of AD in the framework of the amyloid cascade hypothesis. The implications of this, relatively new, imaging examination are not obvious and still being assessed; large multicentre initiatives are trying to determine the impact of amyloid PET on diagnostic confidence, on patient management, on caregivers and on clinical outcome both in patients who strictly meet the AUCr and in those who do not [84, 225].

Among the main drawbacks of this investigation approach, compared to others such as CSF assessment, the cost needs to be taken in consideration as it will easily reach 3000$ per scan [89]. In this regard, the above mentioned initiatives will also play a role in the debate on the cost-effectiveness of amyloid PET, which is still open. However, the amyloid PET: I) has potential to detect change over time related to normal aging, disease course or therapy effects [149, 40, 255, 244], II) variability of its measurements across the centers is relatively low (on condition that standardized protocols and appropriate analysis pipeline are applied) [170], III) provides additional information on neurodegeneration or neuronal injury with an early acquisition [54, 205, 231, 40] and IV) provides regional information on amyloid pathology which, although still rather unexplored, have shown to be beneficial for staging [98, 177, 105, 237].

In this context, with the possible near introduction of anti-amyloid treatment and relative shift towards early diagnosis, a surge in the demand of amyloid PET and a more refined use of this imaging data is conceivable. Foreseeable consequential challenges include the development and diffusion of more complete approaches to analysis that will likely require, for clinicians handling amyloid imaging, specific training also including the interpretation of more elaborate information that goes beyond the classical dichotomy.

Unlike many other diseases (e.g.: the infectious ones), the moment at which the AD is triggered has not yet exactly determined. Rather, the progression seems a long, dynamic process with a gradual shifting of biomarker to abnormal levels that leads to worsening cognition. The dynamic nature of biomarker changes and its consequences are the reason why efforts are being made to study borderline subjects: several studies pointed out a possible biological role of $A\beta$ in individuals with cortical sub-threshold levels [39, 279, 123, 150, 73]. Some of the results that we discussed in our study on the role of regional analysis of amyloid PET also point in this direction [215]. Certainly, these considerations are made possible by quantitative or semi-quantitative approaches that allow for a subtle interpretation of the imaging data by giving a representation of

the accumulation dynamic. The early (asymptomatic) stage of AD is believed to be the optimal target for therapeutic interventions and is not yet clear how to define the correct "gray zone" to identify at-risk individuals. As we discussed, these patients are also those in whom even experienced readers struggle to give coherent readings, and it is precisely in this condition that the quantitative and semi-quantitative analysis are most supportive [42]. Defining at-risk individuals is one of the critical issues in anti-amyloid trials. Many posit that the failure of some of these trials (for example those of bapinezumab or gantenerumab) could be also linked to suboptimal selection of patient inclusion criteria. One possible criticism is that the selected patients might were too advanced in terms of the disease process, and this would have resulted in too little or too late drug administration [181]. The ranking values provided by quantitative and semi-quantitative approaches, in synergy with more articulated visual scales [209], represent a valuable solution by allowing to better define target patients. Besides a better and more homogeneous cohort selection, a robust and accurate analysis of the imaging data would provide a more sensitive factor in response to therapy and possibly lower the time and number of subjects needed to evaluate the endpoints.

In any case, in spite of recent developments, especially in drug treatment, the conceptualization of AD and the role of amyloid deposition are still a matter of debate. According to the current amyloid cascade hypothesis, Aβ accumulation is followed by a deterministic chain of events including tau deposition, neurodegeneration and cognitive impairment. This model fits well some types of AD (such as the autosomal dominant), but seems less suitable to describe sporadic AD. An alternative probabilistic model has been proposed suggesting a decrease in the weight of the amyloid cascade with respect to genetic risk factors and other stochastic factors [83]. Moreover, the IWG has recently suggested caution in the interpretation and clinical use of the purely biological biomarker-based definition of AD [63]. According to these new reccomendations, the main limitations of the A/T/N model include: I) risk of confusion between the presence of Alzheimer's brain lesions and AD, II) low predictive accuracy of this model, III) interpretation of the diagnosis in presence of other pathologies, IV) uncertainty about the pathogenesis model of AD, V) difficulty in classifying cognitively unimpaired biomarker-positive individuals, VI) lack of harmonization in biomarker thresholds, VII) generalisability and accessibility of biomarker in clinical practice and VIII) ethical concerns arising from informing a cognitively unimpaired individual of having an irreversible and degenerative disease on the basis of biomarker profiling alone.

Currently, there is no consensus on which is the best way (and the most feasible in clinical practice) to perform a quantitative assessment of amyloid PET. The full kinetic modeling, relying on fewer assumptions than typical semi-quantitative methods such as the SUVr, is more accurate and not biased, for example, by changes in rCBF or tracer clearance. However, these method are complex, invasive and require a full dynamic acquisition with additional discomfort for the patients. Thus, research is shifting towards the development of semi-quantitative methods that take into accounts acquisitions from specific time frames enabling integration of blood flow information. This results in: I) error reduction due to the blood flow correction, II) a more patient-friendly image acquisition protocol and III) allow the clinical site to manage the tomograph timeslot more efficiently. The TDr [41] was proposed bearing that in mind, and comparisons with very sophisticated approaches [37] stressed the accuracy of this method, which is accompanied by a remarkable ease of implementation. These factors would make the TDr an ideal candidate for adoption in clinical practice.

Having different, independent, techniques at our disposal to estimate the same biological phenomenon allow to exploit their strengths and mitigate their weaknesses. Indeed, the benefit of independent methods is that they are differently sensitive to both acquisition and pathophysiological characteristics (i.e.: image reconstruction parameters, presence of noise or atrophy). Thus, as evidenced by our results, it is possible to integrate different metrics into a single, more robust, score. This observation, although obvious, might deserves to be deepened as it would suggest a way to increase the reliability of the semi-quantitative assesment with no need for additional data. Further efforts could help to define the best strategy for integrate independent measures, to identify those that make the most significant contribution and to test the impact of these combinations on longitudinal assessments, which is a major test bench for the next methodological developments.

Methodological improvements in the analysis of amyloid imaging, that are supporting the study of AD, may also further our understanding of other diseases such as the multiple sclerosis (MS). MS presents with a wide variety of symptoms including motor disabilities, cognitive deficits, fatigue and is characterised by destruction of normal myelin and axonal loss [152]. Because of the structural similarities between $A\beta$ fibrils and myelin basic protein, amyloid tracers also bind to these proteins causing the distinctive, non-specific uptake of WM. Due to these similarities, it has been suggested that amyloid tracer fixation may be used as a marker of demyelination and remyelination in the central nervous system, which is an unsolved matter in the treatment of MS [178, 187, 222]. According to these observations, a reduction in the uptake of observed MS lesions is associated with reduced remyelination and vice-versa. Although the promising results, many issues still need to be addressed: optimized acquisition protocols to investigate demyelination/remyelination are lacking, and the size of the lesions (which is comparable to PET resolution) can make to reliably estimate these biological processes difficult when using standard approaches [187].

Finally, it is interesting to note that imaging analysis methods, such as those for amyloid, are becoming both increasingly informative and complex, requiring specialised hardware and personnel that are often not available in clinical centres other than those of excellence and research. Furthermore, the analysis for individual patient classification typically includes a comparison with normative population, adding difficulties related to data storage and maintenance. To bridge these gaps and facilitate the diffusion of the imaging biomarkers, optimized technical solutions (both based on cloud or on local computing) are gaining momentum by providing automated, reproducible, standardized image processing. However, this transition still requires the achievement of other important objectives such as the harmonization of image acquisition and analysis or the definition of widely accepted standards for quality assurance and control processes.

Appendix A

Scientific contributions

- Chincarini A., Peira E., Morbelli S., Pardini M., Bauckneht M., Arbizu J., Castelo-Branco M., Büsing K., de Mendonça A., Didic M., Dottorini M., Engelborghs S., Ferrarese C., Frisoni G.B., Garibotto V., Guedj E., Hausner L., Hugon J., Verhaeghe J., Mecocci P., Musarra M., Queneau M., Riverol M., Santana I., Guerra U.P. and Nobili F.M. *"Semi-quantification and grading of amyloid PET: A project of the European Alzheimer's Disease Consortium (EADC)"*. Neuroimage: Clinical. ;23:101846. doi: 10.1016/j.nicl.2019.101846. Epub 2019 May 4.

- Morbelli S., Chincarini A., Brendel M., Rominger A., Bruffaerts R., Vandenberghe R., Kramberger M.G., Trost M., Garibotto V., Nicastro N., Frisoni G.B., Lemstra A.W., van der Zande J., Pilotto A., Padovani A., Garcia-Ptacek S., Savitcheva I., Ochoa-Figueroa M.A., Davidsson A., Camacho V., Peira E., Arnaldi D., Bauckneht M., Pardini M., Sambuceti G., Aarsland D. and Nobili F.M. *"Metabolic Patterns across Core Features in Dementia with Lewy Bodies"*. Annals of Neurology. 2019 May;85(5):715-725. doi: 10.1002/ana.25453. Epub 2019 Mar 22.

- Huber M., Beyer L., Prix C., Schönecker S., Palleis C., Rauchmann B.S., Morbelli S., Chincarini A., Bruffaerts R., Vandenberghe R., Van Laere K., Kramberger M.G., Trost M., Grmek M., Garibotto V., Nicastro N., Frisoni G.B., Lemstra A.W., van der Zande J., Pilotto A., Padovani A., Garcia-Ptacek S., Savitcheva I., Ochoa-Figueroa M.A., Davidsson A., Camacho V., Peira E., Arnaldi D., Bauckneht M., Pardini M., Sambuceti G., Vöglein J., Schnabel J., Unterrainer M., Perneczky R., Pogarell O., Buerger K., Catak C., Bartenstein P., Cumming P., Ewers M., Danek A., Levin J., Aarsland D., Nobili F.M., Rominger A. and Brendel M. *"Metabolic Correlates of Dopaminergic Loss in Dementia with Lewy Bodies"*. Movement Disorders. 2020 Apr;35(4):595-605. doi: 10.1002/mds.27945. Epub 2019 Dec 16.

- Chincarini A., Peira E., Corosu M., Morbelli S., Bauckneht M., Capitanio S., Pardini M., Arnaldi D., Vellani C., D'Ambrosio D., Garibotto V., Assal F., Paghera B., Savelli G., Stefanelli A., Guerra U.P. and Nobili F.M. *"A kinetics-based approach to amyloid PET semi-quantification"*. European Journal of Nuclear Medicine and Molecular Imaging. 2020 Aug;47(9):2175-2185. doi: 10.1007/s00259-020-04689-y. Epub 2020 Jan 25.

- Orso B., Arnaldi D., Famà F., Girtler N., Brugnolo A., Doglione E., Filippi L., Massa F., Peira E., Bauckneht M., Morbelli S., Nobili F.M. and Pardini M. *"Anatomical*

and neurochemical bases of theory of mind in de novo Parkinson's Disease". Cortex. 2020 Sep;130:401-412. doi: 10.1016/j.cortex.2020.06.012. Epub 2020 Jul 10.

- Massa F., Bauckneht M., Peira E., Lapucci C., Picco A., Capitanio S., Arnaldi D., Roccatagliata L., Chincarini A. and Nobili F.M (2020). *"Neuroimaging Findings in Mild Cognitive Impairment"*. In Dierckx R. A. J. O., Otte A., de Vries E. F. J., van Waarde A., Leenders K.L. *"PET and SPECT in Neurology"*. Springer. ISBN: 978-3-030-53168-3.

- Peira E., Grazzini M., Bauckneht M., Sensi F., Bosco P., Arnaldi D., Morbelli S., Chincarini A., Pardini M. and Nobili F.M. *"Probing the Role of a Regional Quantitative Assessment of Amyloid PET"*. Journal of Alzheimer's Disease. 2021;80(1):383-396. doi: 10.3233/JAD-201156.

- Bauckneht M., Chincarini A., Brendel M., Rominger A., Beyer L., Bruffaerts R., Vandenberghe R., Kramberger M.G., Trost M., Garibotto V., Nicastro N., Frisoni G.B., Lemstra A.W., van Berckel B.N.M., Pilotto A., Padovani A., Ochoa-Figueroa M.A., Davidsson A., Camacho V., Peira E., Arnaldi D., Pardini M., Donegani M.I., Raffa S., Miceli A., Sambuceti G., Aarsland D., Nobili F.M. and Morbelli S. *"Associations among education, age, and the dementia with Lewy bodies (DLB) metabolic pattern: A European-DLB consortium project"*. Alzheimer's & Dementia. 2021 Aug;17(8):1277-1286. doi: 10.1002/alz.12294. Epub 2021 Feb 2.

- Massa F., Chincarini A., Bauckneht M., Raffa S., Peira E., Arnaldi D., Pardini M., Pagani M., Orso B., Donegani M.I., Brugnolo A., Biassoni E., Mattioli P., Girtler N., Guerra U.P., Morbelli S. and Nobili F.M. *"Added value of semiquantitative analysis of brain FDG-PET for the differentiation between MCI-Lewy bodies and MCI due to Alzheimer's disease"*. European Journal of Nuclear Medicine and Molecular Imaging. 2021 Oct 15. doi: 10.1007/s00259-021-05568-w.

- Orso B., Famà F., Giorgetti L., Mattioli P., Donniaquio A., Girtler N., Brugnolo A., Massa F., Peira E., Pardini M., Morbelli S., Nobili F.M. and Arnaldi D. *"Polysomnographic correlates of sleep disturbances in de novo, drug naïve Parkinson's Disease"*. Neurological Sciences. 2021 Sep 29. doi: 10.1007/s10072-021-05622-3.

- Massa F., Arnaldi D., Balma M., Bauckneht M., Chincarini A., Ferraro P.M., Grazzini M., Lapucci C., Meli R., Morbelli S., Pardini M., Peira E., Raffa S., Roccatagliata L. and Nobili F.M. (2021). *"Sex differences in neuroimaging biomarkers"*. In Ferretti M.T., Schumacher-Dimech A, Santuccione-Chadha A. *"Sex and Gender Differences in Alzheimer's Disease"*. Elsevier. ISBN: 978-0-12-819344-0.

- Orso B., Lorenzini L., Arnaldi D., Girtler N., Brugnolo A., Doglione E., Mattioli P., Biassoni E., Massa F., Peira E., Bauckneht M., Donegani M.I., Morbelli S., Nobili F.M., Pardini M. *"The role of hub and spoke regions in Theory of Mind in early Alzheimer's Disease and Frontotemporal Dementia"*. Biomedicines. 2022 Feb 24;10(3):544. doi: 10.3390/biomedicines10030544

- Girtler N., Chincarini A., Brugnolo A., Doglione E., Orso B., Morbelli S., Massa F., Peira E., Biassoni E., Donniaquio A., Grisanti S., Pardini M., Arnaldi D., Nobili F. *"The Free and Cued Selective Reminding Test: Discriminative Values in a Naturalistic Cohort"*. Journal of Alzheimer's Disease. 2022 Apr 6. doi: 10.3233/JAD-215043.

- Orso B., Arnaldi D., Peira E., Famà F., Giorgetti L., Girtler N., Brugnolo A., Mattioli P., Biassoni E., Donniaquio A., Massa F., Bauckneht M., Miceli A., Morbelli S., Nobili F., Pardini M. *"The role of monoaminergic tones and brain metabolism in cognition in de novo Parkinson's Disease"*. submitted to Journal of Parkinson's Disease.

- Peira E., Poggiali D., Pardini M., Barthel H., Sabri O., Morbelli S., Cagnis A., Chincarini A. and Cecchin D. *"A comparison of advanced semi-quantitative amyloid PET analysis methods."*. submitted to European Journal of Nuclear Medicine and Molecular Imaging.

- Peira E., Sensi F., Rei L., Gianeri R., Tortora D., Piccardo A, Bottoni G., Morana G. and Chincarini A. *"Towards an automated approach to the semi-quantification of 18F-DOPA PET in pediatric diffuse astrocytic tumors"*. Oral presentation at the European Congress of Medical Physics (ECMP) 2020.

- Peira E., Grazzini M., Sensi F., Rei L., Morbelli S., Nobili F.M., Pardini M. and Chincarini A. *"Amyloid PET: is there room for regional analysis?"*. Poster presentation at the European Congress of Medical Physics (ECMP) 2020.

Appendix B

List of abbreviations

AA	*Alzheimer's Association*
Aβ	*Amyloid Beta*
AD	*Alzheimer's Disease*
ADI	*Alzheimer's Disease International*
ADNI	*Alzheimer's Disease Neuroimaging Initiative*
ADRDA-NINCDS	*National Institute of Neurological and Communicative Disorders and Stroke's Alzheimer's Disease and Related Disorders Association*
AIF	*Arterial Input Function*
AMYPAD	*Amyloid Imaging to Prevent Alzheimer's Disease*
amyPET	*amyloid PET*
APP	*Amyloid Precursor Protein*
APOE	*Apolipoprotein E*
AUC	*Area Under Curve*
AUCr	*Appropriate Use Criteria*
BBB	*Blood Brain Barrier*
CAA	*Cerebral Amyloid Angiopathy*
CDR	*Clinical Dementia Rating*
CSF	*Cerebro-spinal Fluid*

CT   *Computerized Tomography*

DAT-SPECT   *Dopamine Transporter Scan-SPECT*

DLB   *Lewy Body Dementia*

DS   *Down Syndrome*

EADC   *European Alzheimer's Disease Consortium*

ELBA   *Evaluation of Brain Amyloidosis*

EMA   *European Medicines Agency*

FBP   *Filtered Back Projection*

FDA   *Food and Drug Administration*

FDG   *Fluorodeoxyglucose*

FOV   *Field of View*

FTD   *Frontotemporal Dementia*

FWHM   *Full Width at Half Maximum*

GM   *Gray Matter*

ICC   *Intra-Class Correlation Coefficient*

IDE   *Insulin Degrading Enzyme*

IDEAS   *Imaging Dementia-Evidence for Amyloid Scanning*

IWG   *International Working Group*

LOR   *Line of Response*

MCI   *Mild Cognitive Impairment*

MLEM   *Maximum-Likelihood Expectation Maximization*

MNI   *Montreal Neurological Institute*

MRI   *Magnetic Resonance Imaging*

MS   *Multiple Sclerosis*

MTL   *Medial Temporal Lobe*

NIA   *National Institute of Aging*

NEP   *Neutral Endopeptidase*

NFTs   *Neurofibrillary Tangles*

OSEM   *Ordered Subset Expectation Maximization*

PCA   *Principal Component Analysis*

PET   *Positron Emission Tomography*

PiB   *Pittsburgh Compound B*

PSF   *Point Spread Function*

PVE   *Partial Volume Effect*

rCBF   *Regional Cerebral Blood Flow*

ROI   *Region Of Interest*

SCI   *Subjective Cognitive Impairment*

SI   *Slope Index*

SPECT   *Single-Photon Emission Computed Tomography*

SUV   *Standardized Uptake Value*

SUVr   *Standardized Uptake Value ratio*

TDr   *Time Delayed Ratio*

ThT   *Thioflavin-T*

TOF   *Time of Flight*

VaD   *Vascular Dementia*

WM   *White Matter*

WMR   *White Matter Ratio*

Bibliography

[1] P. D. ACTON, H. ZHUANG, AND A. ALAVI, *Quantification in pet*, Radiologic Clinics of North America, 42 (2004). ↱ 4.1.1

[2] M. Y. AKSENOV, M. V. AKSENOVA, M. E. HARRIS, K. HENSLEY, D. A. BUTTER-FIELD, AND J. M. CARNEY, *Enhancement of β-amyloid peptide aβ(1-40)-mediated neurotoxicity by glutamine synthetase*, Journal of Neurochemistry, 65 (2002). ↱ 1.1

[3] A. ALESSIO, C. STEARNS, S. TONG, S. ROSS, S. KOHLMYER, A. GANIN, AND P. KINAHAN, *Application and evaluation of a measured spatially variant system model for pet image reconstruction*, IEEE Transactions on Medical Imaging, 29 (2010). ↱ 2.2

[4] A. ALTMANN, L. TIAN, V. W. HENDERSON, AND M. D. GREICIUS, *Sex modifies the apoe -related risk of developing alzheimer disease*, Annals of Neurology, 75 (2014). ↱ 3.4

[5] D. ALTOMARE, C. FERRARI, C. FESTARI, U. P. GUERRA, C. MUSCIO, A. PADOVANI, G. B. FRISONI, AND M. BOCCARDI, *Quantitative appraisal of the amyloid imaging taskforce appropriate use criteria for amyloid-pet*, Alzheimer's & Dementia, 14 (2018). ↱ 3.2

[6] H. K. ANANDATHEERTHAVARADA, G. BISWAS, M.-A. ROBIN, AND N. G. AVADH-ANI, *Mitochondrial targeting and a novel transmembrane arrest of alzheimer's amyloid precursor protein impairs mitochondrial function in neuronal cells*, Journal of Cell Biology, 161 (2003). ↱ 1.1

[7] L. G. APOSTOLOVA, J. M. HAIDER, N. GOUKASIAN, G. D. RABINOVICI, G. CHÉTELAT, J. M. RINGMAN, S. KREMEN, J. D. GRILL, L. RESTREPO, M. F. MENDEZ, AND D. H. SILVERMAN, *Critical review of the appropriate use criteria for amyloid imaging: Effect on diagnosis and patient care*, Alzheimer's & Dementia: Diagnosis, Assessment & Disease Monitoring, 5 (2016). ↱ 3.2

[8] I. ASLLANI, A. BOROGOVAC, AND T. R. BROWN, *Regression algorithm correcting for partial volume effects in arterial spin labeling mri*, Magnetic Resonance in Medicine, 60 (2008). ↱ 7.2.2

[9] B. B. AVANTS, N. J. TUSTISON, G. SONG, P. A. COOK, A. KLEIN, AND J. C. GEE, *A reproducible evaluation of ants similarity metric performance in brain image registration*, NeuroImage, 54 (2011). ↱ 4.2.1, 6.2.5, and 8.2.3

[10] S. L. Baker, T. M. Harrison, A. Maass, R. L. Joie, and W. J. Jagust, *Effect of off-target binding on ¹⁸ f-flortaucipir variability in healthy controls across the life span*, Journal of Nuclear Medicine, 60 (2019), pp. 1444–1451. ↱ 10.3

[11] L. L. Barnes, R. S. Wilson, J. L. Bienias, J. A. Schneider, D. A. Evans, and D. A. Bennett, *Sex differences in the clinical manifestations of alzheimer disease pathology*, Archives of General Psychiatry, 62 (2005). ↱ 3.4

[12] H. Barthel and O. Sabri, *Clinical use and utility of amyloid imaging*, Journal of Nuclear Medicine, 58 (2017). ↱ 9.1

[13] R. J. Bateman, C. Xiong, T. L. Benzinger, A. M. Fagan, A. Goate, N. C. Fox, D. S. Marcus, N. J. Cairns, X. Xie, T. M. Blazey, D. M. Holtzman, A. Santacruz, V. Buckles, A. Oliver, K. Moulder, P. S. Aisen, B. Ghetti, W. E. Klunk, E. McDade, R. N. Martins, C. L. Masters, R. Mayeux, J. M. Ringman, M. N. Rossor, P. R. Schofield, R. A. Sperling, S. Salloway, and J. C. Morris, *Clinical and biomarker changes in dominantly inherited alzheimer's disease*, New England Journal of Medicine, 367 (2012). ↱ 1.3 and 3.3

[14] T. G. Beach, S. E. Monsell, L. E. Phillips, and W. Kukull, *Accuracy of the clinical diagnosis of alzheimer disease at national institute on aging alzheimer disease centers, 2005–2010*, Journal of Neuropathology & Experimental Neurology, 71 (2012). ↱ 3.2 and 5.3

[15] T. G. Beach, D. R. Thal, M. Zanette, A. Smith, and C. Buckley, *Detection of striatal amyloid plaques with [18f]flutemetamol: Validation with postmortem histopathology*, Journal of Alzheimer's Disease, 52 (2016). ↱ 8.4

[16] G. A. Becker, M. Ichise, H. Barthel, J. Luthardt, M. Patt, A. Seese, M. Schultze-Mosgau, B. Rohde, H.-J. Gertz, C. Reininger, and O. Sabri, *Pet quantification of 18f-florbetaben binding to β-amyloid deposits in human brains*, Journal of Nuclear Medicine, 54 (2013). ↱ 5.2

[17] D. Bergeron, M. L. Gorno-Tempini, G. D. Rabinovici, M. A. Santos-Santos, W. Seeley, B. L. Miller, Y. Pijnenburg, M. A. Keulen, C. Groot, B. N. M. van Berckel, W. M. van der Flier, P. Scheltens, J. D. Rohrer, J. D. Warren, J. M. Schott, N. C. Fox, R. Sanchez-Valle, O. Grau-Rivera, E. Gelpi, H. Seelaar, J. M. Papma, J. C. van Swieten, J. R. Hodges, C. E. Leyton, O. Piguet, E. J. Rogalski, M. M. Mesulam, L. Koric, K. Nora, J. Pariente, B. Dickerson, I. R. Mackenzie, G. R. Hsiung, S. Belliard, D. J. Irwin, D. A. Wolk, M. Grossman, M. Jones, J. Harris, D. Mann, J. S. Snowden, P. Chrem-Mendez, I. L. Calandri, A. A. Amengual, C. Miguet-Alfonsi, E. Magnin, G. Magnani, R. Santangelo, V. Deramecourt, F. Pasquier, N. Mattsson, C. Nilsson, O. Hansson, J. Keith, M. Masellis, S. E. Black, J. A. Matías-Guiu, M. Cabrera-Martin, C. Paquet, J. Dumurgier, M. Teichmann, M. Sarazin, M. Bottlaender, B. Dubois, C. C. Rowe, V. L. Villemagne, R. Vandenberghe, E. Granadillo, E. Teng, M. Mendez, P. T. Meyer, L. Frings, A. Lleó, R. Blesa, J. Fortea, S. W. Seo, J. Diehl-Schmid, T. Grimmer, K. S. Frederiksen, P. Sánchez-Juan,

G. CHÉTELAT, W. JANSEN, R. W. BOUCHARD, R. J. LAFORCE, P. J. VISSER, AND R. OSSENKOPPELE, *Prevalence of amyloid-β pathology in distinct variants of primary progressive aphasia*, Annals of Neurology, 84 (2018). ↰ 3 and 4.2

[18] J. BLAUTZIK, M. BRENDEL, J. SAUERBECK, S. KOTZ, F. SCHEIWEIN, P. BARTENSTEIN, J. SEIBYL, AND A. ROMINGER, *Reference region selection and the association between the rate of amyloid accumulation over time and the baseline amyloid burden*, European Journal of Nuclear Medicine and Molecular Imaging, 44 (2017). ↰ 4.2

[19] R. BOELLAARD, *Standards for pet image acquisition and quantitative data analysis*, Journal of Nuclear Medicine, 50 (2009). ↰ 4.2

[20] J. BOWSHER, V. JOHNSON, T. TURKINGTON, R. JASZCZAK, C. FLOYD, AND R. COLEMAN, *Bayesian reconstruction and use of anatomical a priori information for emission tomography*, IEEE Transactions on Medical Imaging, 15 (1996). ↰ 2.2

[21] P. A. BOYLE, L. YU, R. S. WILSON, J. A. SCHNEIDER, AND D. A. BENNETT, *Relation of neuropathology with cognitive decline among older persons without dementia*, Frontiers in Aging Neuroscience, 5 (2013). ↰ 8.4

[22] H. BRAAK AND E. BRAAK, *Neuropathological stageing of alzheimer-related changes*, Acta Neuropathologica, 82 (1991). ↰ 4.2, 5.3, and 8.1

[23] M. BRENDEL, M. HÖGENAUER, A. DELKER, J. SAUERBECK, P. BARTENSTEIN, J. SEIBYL, AND A. ROMINGER, *Improved longitudinal [18f]-av45 amyloid pet by white matter reference and voi-based partial volume effect correction*, NeuroImage, 108 (2015). ↰ 7.2.3

[24] R. F. BUCKLEY, E. C. MORMINO, R. E. AMARIGLIO, M. J. PROPERZI, J. S. RABIN, Y. Y. LIM, K. V. PAPP, H. I. JACOBS, S. BURNHAM, B. J. HANSEEUW, V. DORÉ, A. DOBSON, C. L. MASTERS, M. WALLER, C. C. ROWE, P. MARUFF, M. C. DONOHUE, D. M. RENTZ, D. KIRN, T. HEDDEN, J. CHHATWAL, A. P. SCHULTZ, K. A. JOHNSON, V. L. VILLEMAGNE, AND R. A. SPERLING, *Sex, amyloid, and apoe epsilon4 and risk of cognitive decline in preclinical alzheimer's disease: Findings from three well-characterized cohorts*, Alzheimer's & Dementia, 14 (2018). ↰ 3.4

[25] R. F. BUCKLEY, E. C. MORMINO, J. S. RABIN, T. J. HOHMAN, S. LANDAU, B. J. HANSEEUW, H. I. L. JACOBS, K. V. PAPP, R. E. AMARIGLIO, M. J. PROPERZI, A. P. SCHULTZ, D. KIRN, M. R. SCOTT, T. HEDDEN, M. FARRELL, J. PRICE, J. CHHATWAL, D. M. RENTZ, V. L. VILLEMAGNE, K. A. JOHNSON, AND R. A. SPERLING, *Sex differences in the association of global amyloid and regional tau deposition measured by positron emission tomography in clinically normal older adults*, JAMA Neurology, 76 (2019). ↰ 3.4

[26] S. BULLICH, H. BARTHEL, N. KOGLIN, G. A. BECKER, S. D. SANTI, A. JOVALEKIC, A. W. STEPHENS, AND O. SABRI, *Validation of noninvasive tracer kinetic analysis of ¹⁸ f-florbetaben pet using a dual–time-window acquisition protocol*, Journal of Nuclear Medicine, 59 (2018). ↰ 5.2 and 9.1

[27] S. Bullich, N. Roé-Vellvé, M. Marquié, S. M. Landau, H. Barthel, V. L. Villemagne, Ángela Sanabria, J. P. Tartari, O. Sotolongo-Grau, V. Doré, N. Koglin, A. Müller, A. Perrotin, A. Jovalekic, S. D. Santi, L. Tárraga, A. W. Stephens, C. C. Rowe, O. Sabri, J. P. Seibyl, and M. Boada, *Early detection of amyloid load using 18f-florbetaben pet*, Alzheimer's Research & Therapy, 13 (2021). ↪ 4.2

[28] S. Bullich, V. L. Villemagne, A. M. Catafau, A. Jovalekic, N. Koglin, C. C. Rowe, and S. D. Santi, *Optimal reference region to measure longitudinal amyloid-β change with ¹⁸ f-florbetaben pet*, Journal of Nuclear Medicine, 58 (2017). ↪ 4.2

[29] L. Bäckman, S. Jones, A.-K. Berger, E. J. Laukka, and B. J. Small, *Cognitive impairment in preclinical alzheimer's disease: A meta-analysis.*, Neuropsychology, 19 (2005). ↪ 5.3 and 8.4

[30] D. L. Campbell, H. Kang, and S. Shokouhi, *Application of haralick texture features in brain [¹⁸f]-florbetapir positron emission tomography without reference region normalization*, Clinical Interventions in Aging, Volume 12 (2017). ↪ 4.3

[31] A. Caroli and G. Frisoni, *The dynamics of alzheimer's disease biomarkers in the alzheimer's disease neuroimaging initiative cohort*, Neurobiology of Aging, 31 (2010), pp. 1263–1274. ↪ 10.2

[32] M. Carome and S. Wolfe, *Florbetapir-pet imaging and postmortem β-amyloid pathology*, JAMA, 305 (2011). ↪ 3.1

[33] A. M. Catafau and S. Bullich, *Amyloid pet imaging: applications beyond alzheimer's disease*, Clinical and Translational Imaging, 3 (2015). ↪ 2

[34] A. M. Catafau, S. Bullich, J. P. Seibyl, H. Barthel, B. Ghetti, J. Leverenz, J. W. Ironside, W. J. Schulz-Schaeffer, A. Hoffmann, and O. Sabri, *Cerebellar amyloid-β plaques: How frequent are they, and do they influence ¹⁸ f-florbetaben suv ratios?*, Journal of Nuclear Medicine, 57 (2016). ↪ 4.2

[35] C. Catana, *Attenuation correction for human pet/mri studies*, Physics in Medicine & Biology, 65 (2020). ↪ 2.1.1

[36] E. Cavedo, P. A. Chiesa, M. Houot, M. T. Ferretti, M. J. Grothe, S. J. Teipel, S. Lista, M.-O. Habert, M.-C. Potier, B. Dubois, and H. Hampel, *Sex differences in functional and molecular neuroimaging biomarkers of alzheimer's disease in cognitively normal older adults with subjective memory complaints*, Alzheimer's & Dementia, 14 (2018). ↪ 3.4

[37] D. Cecchin, H. Barthel, D. Poggiali, A. Cagnin, S. Tiepolt, P. Zucchetta, P. Turco, P. Gallo, A. C. Frigo, O. Sabri, and F. Bui, *A new integrated dual time-point amyloid pet/mri data analysis method*, European Journal of Nuclear Medicine and Molecular Imaging, 44 (2017). ↪ 4.3, 5.2, 5.4, 7.1, 9.1, 9.2.1, 9.2.2, 9.2.3, 9.4, and 11

[38] A. CHARIDIMOU, K. FARID, AND J.-C. BARON, *Amyloid-pet in sporadic cerebral amyloid angiopathy*, Neurology, 89 (2017). ↰ 1.2

[39] G. CHATELAT, V. L. VILLEMAGNE, P. BOURGEAT, K. E. PIKE, G. JONES, D. AMES, K. A. ELLIS, C. SZOEKE, R. N. MARTINS, G. J. O'KEEFE, O. SALVADO, C. L. MASTERS, AND C. C. ROWE, *Relationship between atrophy and β-amyloid deposition in alzheimer's disease*, Annals of Neurology, (2009). ↰ 5.3, 8.4, and 11

[40] K. CHEN, A. ROONTIVA, P. THIYYAGURA, W. LEE, X. LIU, N. AYUTYANONT, H. PROTAS, J. LUO, R. BAUER, C. RESCHKE, D. BANDY, R. A. KOEPPE, A. S. FLEISHER, R. J. CASELLI, S. LANDAU, W. J. JAGUST, M. W. WEINER, AND E. M. REIMAN, *Improved power for characterizing longitudinal amyloid-β pet changes and evaluating amyloid-modifying treatments with a cerebral white matter reference region*, Journal of Nuclear Medicine, 56 (2015). ↰ 4.2, 7.2.3, 7.4, and 11

[41] A. CHINCARINI, E. PEIRA, M. COROSU, S. MORBELLI, M. BAUCKNEHT, S. CAPITANIO, M. PARDINI, D. ARNALDI, C. VELLANI, D. D'AMBROSIO, V. GARIBOTTO, F. ASSAL, B. PAGHERA, G. SAVELLI, A. STEFANELLI, U. P. GUERRA, AND F. NOBILI, *A kinetics-based approach to amyloid pet semi-quantification*, European Journal of Nuclear Medicine and Molecular Imaging, 47 (2020). ↰ 5.2, 5.4, 9.1, 9.2.3, 9.4, and 11

[42] A. CHINCARINI, E. PEIRA, S. MORBELLI, M. PARDINI, M. BAUCKNEHT, J. ARBIZU, M. CASTELO-BRANCO, K. BÜSING, A. DE MENDONÇA, M. DIDIC, M. DOTTORINI, S. ENGELBORGHS, C. FERRARESE, G. FRISONI, V. GARIBOTTO, E. GUEDJ, L. HAUSNER, J. HUGON, J. VERHAEGHE, P. MECOCCI, M. MUSARRA, M. QUENEAU, M. RIVEROL, I. SANTANA, U. GUERRA, AND F. NOBILI, *Semi-quantification and grading of amyloid pet: A project of the european alzheimer's disease consortium (eadc)*, NeuroImage: Clinical, 23 (2019). ↰ 5.1, 7.4, 7.4.1, 8.2.3, 8.4, 9.1, 10.2, and 11

[43] A. CHINCARINI, F. SENSI, L. REI, I. BOSSERT, S. MORBELLI, U. P. GUERRA, G. FRISONI, A. PADOVANI, AND F. NOBILI, *Standardized uptake value ratio-independent evaluation of brain amyloidosis*, Journal of Alzheimer's Disease, 54 (2016). ↰ 4.3, 4.3.1, 4.5, 5.4, 6.2.4, 6.2.5, 7.1, 7.2.5, 8.2.3, 9.1, 9.2.3, and 9.4

[44] K. CHIOTIS, L. SAINT-AUBERT, M. BOCCARDI, A. GIETL, A. PICCO, A. VARRONE, V. GARIBOTTO, K. HERHOLZ, F. NOBILI, A. NORDBERG, G. B. FRISONI, B. WINBLAD, AND C. R. JACK, *Clinical validity of increased cortical uptake of amyloid ligands on pet as a biomarker for alzheimer's disease in the context of a structured 5-phase development framework*, Neurobiology of Aging, 52 (2017). ↰ 6.4

[45] S. H. CHO, Y. S. CHOE, S. PARK, Y. J. KIM, H. J. KIM, H. JANG, S. J. KIM, J. P. KIM, Y. H. JUNG, B. C. KIM, D. L. NA, S. H. MOON, AND S. W. SEO, *Appropriate reference region selection of 18f-florbetaben and 18f-flutemetamol beta-amyloid pet expressed in centiloid*, Scientific Reports, 10 (2020). ↰ 4.2

[46] S. H. CHO, J.-H. SHIN, H. JANG, S. PARK, H. J. KIM, S. E. KIM, S. J. KIM, Y. KIM, J. S. LEE, D. L. NA, S. N. LOCKHART, G. D. RABINOVICI, J.-K. SEONG, AND S. W. SEO, *Amyloid involvement in subcortical regions predicts cognitive decline*, European Journal of Nuclear Medicine and Molecular Imaging, 45 (2018). ↰ 6.4.1, 8.1, and 8.4

[47] C. M. CLARK, *Use of florbetapir-pet for imaging β-amyloid pathology*, JAMA, 305 (2011). ↱ 4.2.1

[48] C. M. CLARK, M. J. PONTECORVO, T. G. BEACH, B. J. BEDELL, R. E. COLEMAN, P. M. DORAISWAMY, A. S. FLEISHER, E. M. REIMAN, M. N. SABBAGH, C. H. SADOWSKY, J. A. SCHNEIDER, A. ARORA, A. P. CARPENTER, M. L. FLITTER, A. D. JOSHI, M. J. KRAUTKRAMER, M. LU, M. A. MINTUN, AND D. M. SKOV-RONSKY, *Cerebral pet with florbetapir compared with neuropathology at autopsy for detection of neuritic amyloid-β plaques: a prospective cohort study*, The Lancet Neurology, 11 (2012). ↱ 3, 3.1, 4.2, 7.1, and 7.2.3

[49] L. E. COLLIJ, E. KONIJNENBERG, J. REIMAND, M. TEN KATE, A. DEN BRABER, I. L. ALVES, M. ZWAN, M. YAQUB, D. M. VAN ASSEMA, A. M. WINK, A. A. LAMMERTSMA, P. SCHELTENS, P. J. VISSER, F. BARKHOF, AND B. N. VAN BERCKEL, *Assessing amyloid pathology in cognitively normal subjects using ¹⁸ f-flutemetamol pet: Comparing visual reads and quantitative methods*, Journal of Nuclear Medicine, 60 (2019). ↱ 6.4 and 9.1

[50] C. COMTAT, P. E. KINAHAN, J. A. FESSLER, T. BEYER, D. W. TOWNSEND, M. DE-FRISE, AND C. MICHEL, *Clinically feasible reconstruction of 3d whole-body pet/ct data using blurred anatomical labels*, Physics in Medicine and Biology, 47 (2002). ↱ 2.2

[51] K. B. CONTRACTOR, L. M. KENNY, C. R. COOMBES, F. E. TURKHEIMER, E. O. ABOAGYE, AND L. ROSSO, *Evaluation of limited blood sampling population input approaches for kinetic quantification of [18f]fluorothymidine pet data*, EJNMMI Research, 2 (2012). ↱ 7.2.2

[52] K. D. COON, A. J. MYERS, D. W. CRAIG, J. A. WEBSTER, J. V. PEARSON, D. H. LINCE, V. L. ZISMANN, T. G. BEACH, D. LEUNG, L. BRYDEN, R. F. HALPERIN, L. MARLOWE, M. KALEEM, D. G. WALKER, R. RAVID, C. B. HEWARD, J. RO-GERS, A. PAPASSOTIROPOULOS, E. M. REIMAN, J. HARDY, AND D. A. STEPHAN, *A high-density whole-genome association study reveals that apoe is the major susceptibility gene for sporadic late-onset alzheimer's disease*, The Journal of Clinical Psychiatry, 68 (2007). ↱ 1.3

[53] C. CURTIS, J. E. GAMEZ, U. SINGH, C. H. SADOWSKY, T. VILLENA, M. N. SAB-BAGH, T. G. BEACH, R. DUARA, A. S. FLEISHER, K. A. FREY, Z. WALKER, A. HUNJAN, C. HOLMES, Y. M. ESCOVAR, C. X. VERA, M. E. AGRONIN, J. ROSS, A. BOZOKI, M. AKINOLA, J. SHI, R. VANDENBERGHE, M. D. IKONOMOVIC, P. F. SHERWIN, I. D. GRACHEV, G. FARRAR, A. P. L. SMITH, C. J. BUCKLEY, R. MCLAIN, AND S. SALLOWAY, *Phase 3 trial of flutemetamol labeled with radioactive fluorine 18 imaging and neuritic plaque density*, JAMA Neurology, 72 (2015). ↱ 6.4 and 6.4.1

[54] S. DAERR, M. BRENDEL, C. ZACH, E. MILLE, D. SCHILLING, M. J. ZACHERL, K. BÜRGER, A. DANEK, O. POGARELL, A. SCHILDAN, M. PATT, H. BARTHEL, O. SABRI, P. BARTENSTEIN, AND A. ROMINGER, *Evaluation of early-phase [18 f]-florbetaben pet acquisition in clinical routine cases*, NeuroImage: Clinical, 14 (2017). ↱ 7.4 and 11

[55] P. Daniela, S. Orazio, P. Alessandro, N. F. Mariano, I. Leonardo, D. R. P. Anthony, F. Giovanni, and C. Carlo, *A survey of fdg- and amyloid-pet imaging in dementia and grade analysis*, BioMed Research International, 2014 (2014). ⌐ 8.1

[56] A. de Wilde, R. Ossenkoppele, W. Pelkmans, F. Bouwman, C. Groot, I. van Maurik, M. Zwan, M. Yaqub, F. Barkhof, A. A. Lammertsma, G. J. Biessels, P. Scheltens, B. N. van Berckel, and W. M. van der Flier, *Assessment of the appropriate use criteria for amyloid pet in an unselected memory clinic cohort: The abide project*, Alzheimer's & Dementia, 15 (2019). ⌐ 3.2

[57] B. C. Dickerson, S. M. McGinnis, C. Xia, B. H. Price, A. Atri, M. E. Murray, M. F. Mendez, and D. A. Wolk, *Approach to atypical alzheimer's disease and case studies of the major subtypes*, CNS Spectrums, 22 (2017). ⌐ 3 and 4.2

[58] B. D.L., T. D.W., V. P.E., and M. M.N., *Positron Emission Tomography*, Springer-Verlag, 2005. ⌐ 2.1, 2.1.1, and 2.2

[59] A. Drzezga, T. Grimmer, G. Henriksen, M. Muhlau, R. Perneczky, I. Miederer, C. Praus, C. Sorg, A. Wohlschlager, M. Riemenschneider, H. J. Wester, H. Foerstl, M. Schwaiger, and A. Kurz, *Effect of apoe genotype on amyloid plaque load and gray matter volume in alzheimer disease*, Neurology, 72 (2009). ⌐ 6.1

[60] B. Dubois, H. H. Feldman, C. Jacova, J. L. Cummings, S. T. DeKosky, P. Barberger-Gateau, A. Delacourte, G. Frisoni, N. C. Fox, D. Galasko, S. Gauthier, H. Hampel, G. A. Jicha, K. Meguro, J. O'Brien, F. Pasquier, P. Robert, M. Rossor, S. Salloway, M. Sarazin, L. C. de Souza, Y. Stern, P. J. Visser, and P. Scheltens, *Revising the definition of alzheimer's disease: a new lexicon*, The Lancet Neurology, 9 (2010). ⌐ 1.3

[61] B. Dubois, H. H. Feldman, C. Jacova, S. T. DeKosky, P. Barberger-Gateau, J. Cummings, A. Delacourte, D. Galasko, S. Gauthier, G. Jicha, K. Meguro, J. O'Brien, F. Pasquier, P. Robert, M. Rossor, S. Salloway, Y. Stern, P. J. Visser, and P. Scheltens, *Research criteria for the diagnosis of alzheimer's disease: revising the nincds–adrda criteria*, The Lancet Neurology, 6 (2007). ⌐ 1.3

[62] B. Dubois, H. H. Feldman, C. Jacova, H. Hampel, J. L. Molinuevo, K. Blennow, S. T. DeKosky, S. Gauthier, D. Selkoe, R. Bateman, S. Cappa, S. Crutch, S. Engelborghs, G. B. Frisoni, N. C. Fox, D. Galasko, M.-O. Habert, G. A. Jicha, A. Nordberg, F. Pasquier, G. Rabinovici, P. Robert, C. Rowe, S. Salloway, M. Sarazin, S. Epelbaum, L. C. de Souza, B. Vellas, P. J. Visser, L. Schneider, Y. Stern, P. Scheltens, and J. L. Cummings, *Advancing research diagnostic criteria for alzheimer's disease: the iwg-2 criteria*, The Lancet Neurology, 13 (2014). ⌐ 1.3, 6.1, and 7.1

[63] B. Dubois, N. Villain, G. B. Frisoni, G. D. Rabinovici, M. Sabbagh, S. Cappa, A. Bejanin, S. Bombois, S. Epelbaum, M. Teichmann, M.-O. Habert, A. Nordberg, K. Blennow, D. Galasko, Y. Stern, C. C. Rowe, S. Salloway, L. S. Schneider, J. L. Cummings, and H. H. Feldman, *Clinical diagnosis of alzheimer's disease: recommendations of the international working group*, The Lancet Neurology, 20 (2021), pp. 484–496. ⌐ 11

[64] J. G. Dubroff and I. M. Nasrallah, *Will pet amyloid imaging lead to overdiagnosis of alzheimer dementia?*, Academic Radiology, 22 (2015). ↱ 3.2

[65] M. F. Egan, J. Kost, T. Voss, Y. Mukai, P. S. Aisen, J. L. Cummings, P. N. Tariot, B. Vellas, C. H. van Dyck, M. Boada, Y. Zhang, W. Li, C. Furtek, E. Mahoney, L. H. Mozley, Y. Mo, C. Sur, and D. Michelson, *Randomized trial of verubecestat for prodromal alzheimer's disease*, New England Journal of Medicine, 380 (2019). ↱ 1.3 and 9.1

[66] Ely-Lilly and Company, *Amyvid™ (florbetapir f18 injection) for intravenous use prescribing information*, 2012. ↱ 3.1, 3.3, 8.2.2, and 10.2

[67] M. Ezeani and M. Omabe, *A new perspective of lysosomal cation channel-dependent homeostasis in alzheimer's disease*, Molecular Neurobiology, 53 (2016). ↱ 1.1

[68] A. M. Fagan, C. M. Roe, C. Xiong, M. A. Mintun, J. C. Morris, and D. M. Holtzman, *Cerebrospinal fluid tau/β-amyloid42 ratio as a prediction of cognitive decline in nondemented older adults*, Archives of Neurology, 64 (2007). ↱ 1.3 and 3.3

[69] A. M. Fagan, C. Xiong, M. S. Jasielec, R. J. Bateman, A. M. Goate, T. L. S. Benzinger, B. Ghetti, R. N. Martins, C. L. Masters, R. Mayeux, J. M. Ringman, M. N. Rossor, S. Salloway, P. R. Schofield, R. A. Sperling, D. Marcus, N. J. Cairns, V. D. Buckles, J. H. Ladenson, J. C. Morris, and D. M. Holtzman, *Longitudinal change in csf biomarkers in autosomal-dominant alzheimer's disease*, Science Translational Medicine, 6 (2014). ↱ 1.3 and 3.3

[70] A. P. Fan, H. An, F. Moradi, J. Rosenberg, Y. Ishii, T. Nariai, H. Okazawa, and G. Zaharchuk, *Quantification of brain oxygen extraction and metabolism with [15o]-gas pet: A technical review in the era of pet/mri*, NeuroImage, 220 (2020). ↱ 4.1

[71] G. fang Chen, T. hai Xu, Y. Yan, Y. ren Zhou, Y. Jiang, K. Melcher, and H. E. Xu, *Amyloid beta: structure, biology and structure-based therapeutic development*, Acta Pharmacologica Sinica, 38 (2017). ↱ 1.1 and 1.1

[72] E. R. Fantoni, A. Chalkidou, J. T. O. Brien, G. Farrar, and A. Hammers, *A systematic review and aggregated analysis on the impact of amyloid pet brain imaging on the diagnosis, diagnostic confidence, and management of patients being evaluated for alzheimer's disease*, Journal of Alzheimer's Disease, 63 (2018). ↱ 9.1

[73] M. E. Farrell, X. Chen, M. M. Rundle, M. Y. Chan, G. S. Wig, and D. C. Park, *Regional amyloid accumulation and cognitive decline in initially amyloid-negative adults*, Neurology, 91 (2018), pp. e1809–e1821. ↱ 5.3 and 11

[74] M. E. Farrell, K. M. Kennedy, K. M. Rodrigue, G. Wig, G. N. Bischof, J. R. Rieck, X. Chen, S. B. Festini, M. D. Devous, and D. C. Park, *Association of longitudinal cognitive decline with amyloid burden in middle-aged and older adults*, JAMA Neurology, 74 (2017). ↱ 6.1

[75] M. T. Ferretti, M. F. Iulita, E. Cavedo, P. A. Chiesa, A. S. Dimech, A. S. Chadha, F. Baracchi, H. Girouard, S. Misoch, E. Giacobini, H. Depypere, and H. Hampel, *Sex differences in alzheimer disease — the gateway to precision medicine*, Nature Reviews Neurology, 14 (2018). ↰ 3.4

[76] M. T. Ferretti, A. Schumacher-Dimech, and A. Santuccione-Chadha, *Sex and Gender Differences in Alzheimer's Disease: The Women's Brain Project*, Springer, 1 ed., 2021. ↰ 3.4

[77] B. Fischl, *Freesurfer*, NeuroImage, 62 (2012). ↰ 9.2.3

[78] B. Fischl and A. M. Dale, *Measuring the thickness of the human cerebral cortex from magnetic resonance images*, Proceedings of the National Academy of Sciences, 97 (2000). ↰ 7.2.4

[79] D. W. Fisher, D. A. Bennett, and H. Dong, *Sexual dimorphism in predisposition to alzheimer's disease*, Neurobiology of Aging, 70 (2018). ↰ 3.4

[80] A. S. Fleisher, *Using positron emission tomography and florbetapir f 18 to image cortical amyloid in patients with mild cognitive impairment or dementia due to alzheimer disease*, Archives of Neurology, 68 (2011). ↰ 6.1

[81] A. S. Fleisher, K. Chen, X. Liu, N. Ayutyanont, A. Roontiva, P. Thiyyagura, H. Protas, A. D. Joshi, M. Sabbagh, C. H. Sadowsky, R. A. Sperling, C. M. Clark, M. A. Mintun, M. J. Pontecorvo, R. E. Coleman, P. Doraiswamy, K. A. Johnson, A. P. Carpenter, D. M. Skovronsky, and E. M. Reiman, *Apolipoprotein e ϵ4 and age effects on florbetapir positron emission tomography in healthy aging and alzheimer disease*, Neurobiology of Aging, 34 (2013). ↰ 4.2.1

[82] A. S. Fleisher, A. D. Joshi, K. L. Sundell, Y.-F. Chen, S. Kollack-Walker, M. Lu, S. Chen, M. D. Devous, J. Seibyl, K. Marek, E. R. Siemers, and M. A. Mintun, *Use of white matter reference regions for detection of change in florbetapir positron emission tomography from completed phase 3 solanezumab trials*, Alzheimer's & Dementia, 13 (2017). ↰ 7.2.3

[83] G. B. Frisoni, D. Altomare, D. R. Thal, F. Ribaldi, R. van der Kant, R. Ossenkoppele, K. Blennow, J. Cummings, C. van Duijn, P. M. Nilsson, P.-Y. Dietrich, P. Scheltens, and B. Dubois, *The probabilistic model of alzheimer disease: the amyloid hypothesis revised*, Nature Reviews Neuroscience, 23 (2022), pp. 53–66. ↰ 11

[84] G. B. Frisoni, F. Barkhof, D. Altomare, J. Berkhof, M. Boccardi, E. Canzoneri, L. Collij, A. Drzezga, G. Farrar, V. Garibotto, R. Gismondi, J.-D. Gispert, F. Jessen, M. Kivipelto, I. L. Alves, J. L. Molinuevo, A. Nordberg, P. Payoux, C. Ritchie, I. Savicheva, P. Scheltens, M. E. Schmidt, J. M. Schott, A. Stephens, B. van Berckel, B. Vellas, Z. Walker, and N. Raffa, *Amypad diagnostic and patient management study: Rationale and design*, Alzheimer's & Dementia, 15 (2019). ↰ 3 and 11

[85] G. B. Frisoni, M. Boccardi, F. Barkhof, K. Blennow, S. Cappa, K. Chiotis, J.-F. Démonet, V. Garibotto, P. Giannakopoulos, A. Gietl, O. Hansson, K. Herholz, C. R. Jack, F. Nobili, A. Nordberg, H. M. Snyder, M. T. Kate, A. Varrone, E. Albanese, S. Becker, P. Bossuyt, M. C. Carrillo, C. Cerami, B. Dubois, V. Gallo, E. Giacobini, G. Gold, S. Hurst, A. Lönneborg, K.-O. Lovblad, N. Mattsson, J.-L. Molinuevo, A. U. Monsch, U. Mosimann, A. Padovani, A. Picco, C. Porteri, O. Ratib, L. Saint-Aubert, C. Scerri, P. Scheltens, J. M. Schott, I. Sonni, S. Teipel, P. Vineis, P. J. Visser, Y. Yasui, and B. Winblad, *Strategic roadmap for an early diagnosis of alzheimer's disease based on biomarkers*, The Lancet Neurology, 16 (2017). ↰ 6.4

[86] G. Gagno, F. Ferro, A. L. Fluca, M. Janjusevic, M. Rossi, G. Sinagra, A. P. Beltrami, R. Moretti, and A. Aleksova, *From brain to heart: Possible role of amyloid-β in ischemic heart disease and ischemia-reperfusion injury*, International Journal of Molecular Sciences, 21 (2020). ↰ 1.2

[87] V. Garibotto, N. L. Albert, H. Barthel, B. van Berckel, R. Boellaard, M. Brendel, D. Cecchin, O. Ekmekcioglu, E. van de Giessen, E. Guedj, A. A. Lammerstma, F. Semah, T. Traub-Weidinger, D. V. Weehaeghe, and S. Morbelli, *The approval of a disease-modifying treatment for alzheimer's disease: impact and consequences for the nuclear medicine community*, European Journal of Nuclear Medicine and Molecular Imaging, 48 (2021). ↰ 5.4 and 9.1

[88] J. Gaugler, B. James, T. Johnson, A. Marin, and J. Weuve, *Alzheimer's disease facts and figures 2020*, Alzheimer's & Dementia, (2020). ↰ 1.3 and 1.3

[89] S. Gauthier, P. Rosa-Neto, J. Morais, and C. Webster, *World alzheimer report 2021*, 2021. ↰ 11

[90] GE-Healthcare, *Vizamyl™ (flutemetamol f18) injection prescribing information*, 2013. ↰ 3.1, 3.3, 8.2.2, and 10.2

[91] S. S. Golla, S. C. Verfaillie, R. Boellaard, S. M. Adriaanse, M. D. Zwan, R. C. Schuit, T. Timmers, C. Groot, P. Schober, P. Scheltens, W. M. van der Flier, A. D. Windhorst, B. N. van Berckel, and A. A. Lammertsma, *Quantification of [¹⁸ f]florbetapir: A test–retest tracer kinetic modelling study*, Journal of Cerebral Blood Flow & Metabolism, 39 (2019). ↰ 4.2.1

[92] J. Gonneaud, E. M. Arenaza-Urquijo, F. Mézenge, B. Landeau, M. Gaubert, A. Bejanin, R. de Flores, M. Wirth, C. Tomadesso, G. Poisnel, A. Abbas, B. Desgranges, and G. Chételat, *Increased florbetapir binding in the temporal neocortex from age 20 to 60 years*, Neurology, 89 (2017). ↰ 9.1

[93] B. A. Gordon, T. Blazey, Y. Su, A. M. Fagan, D. M. Holtzman, J. C. Morris, and T. L. S. Benzinger, *Longitudinal β-amyloid deposition and hippocampal volume in preclinical alzheimer disease and suspected non–alzheimer disease pathophysiology*, JAMA Neurology, 73 (2016). ↰ 1.3 and 3.3

[94] B. A. GORDON, T. M. BLAZEY, Y. SU, A. HARI-RAJ, A. DINCER, S. FLORES, J. CHRISTENSEN, E. MCDADE, G. WANG, C. XIONG, N. J. CAIRNS, J. HASSENSTAB, D. S. MARCUS, A. M. FAGAN, C. R. JACK, R. C. HORNBECK, K. L. PAUMIER, B. M. ANCES, S. B. BERMAN, A. M. BRICKMAN, D. M. CASH, J. P. CHHATWAL, S. CORREIA, S. FÖRSTER, N. C. FOX, N. R. GRAFF-RADFORD, C. LA FOUGÈRE, J. LEVIN, C. L. MASTERS, M. N. ROSSOR, S. SALLOWAY, A. J. SAYKIN, P. R. SCHOFIELD, P. M. THOMPSON, M. M. WEINER, D. M. HOLTZMAN, M. E. RAICHLE, J. C. MORRIS, R. J. BATEMAN, AND T. L. S. BENZINGER, *Spatial patterns of neuroimaging biomarker change in individuals from families with autosomal dominant alzheimer's disease: a longitudinal study*, The Lancet Neurology, 17 (2018). ↱ 1.3 and 3.3

[95] M. L. GORNO-TEMPINI, S. M. BRAMBATI, V. GINEX, J. OGAR, N. F. DRONKERS, A. MARCONE, D. PERANI, V. GARIBOTTO, S. F. CAPPA, AND B. L. MILLER, *The logopenic/phonological variant of primary progressive aphasia*, Neurology, 71 (2008). ↱ 1.3

[96] R. F. GOTTESMAN, A. L. SCHNEIDER, Y. ZHOU, X. CHEN, E. GREEN, N. GUPTA, D. S. KNOPMAN, A. MINTZ, A. RAHMIM, A. R. SHARRETT, L. E. WAGENKNECHT, D. F. WONG, AND T. H. MOSLEY, *The aric-pet amyloid imaging study*, Neurology, 87 (2016). ↱ 3.4

[97] T. GRIMMER, O. GOLDHARDT, L.-H. GUO, B. H. YOUSEFI, S. FÖRSTER, A. DRZEZGA, C. SORG, P. ALEXOPOULOS, H. FÖRSTL, A. KURZ, AND R. PERNECZKY, *Lrp-1 polymorphism is associated with global and regional amyloid load in alzheimer's disease in humans in-vivo*, NeuroImage: Clinical, 4 (2014). ↱ 6.4

[98] M. J. GROTHE, H. BARTHEL, J. SEPULCRE, M. DYRBA, O. SABRI, AND S. J. TEIPEL, *In vivo staging of regional amyloid deposition*, Neurology, 89 (2017). ↱ 6.4.1, 8.4, 9.1, and 11

[99] M. J. GROTHE, J. SEPULCRE, G. GONZALEZ-ESCAMILLA, I. JELISTRATOVA, M. SCHÖLL, O. HANSSON, AND S. J. TEIPEL, *Molecular properties underlying regional vulnerability to alzheimer's disease pathology*, Brain, (2018). ↱ 8.4

[100] U. P. GUERRA, F. M. NOBILI, A. PADOVANI, D. PERANI, A. PUPI, S. SORBI, AND M. TRABUCCHI, *Recommendations from the italian interdisciplinary working group (aimn, aip, sindem) for the utilization of amyloid imaging in clinical practice*, Neurological Sciences, 36 (2015). ↱ 3.2 and 3.3.1

[101] T. GUO, S. M. LANDAU, AND W. J. JAGUST, *Detecting earlier stages of amyloid deposition using pet in cognitively normal elderly adults*, Neurology, 94 (2020). ↱ 4.2 and 5.3

[102] S. Y. GUÉNETTE, *Mechanisms of aβ clearance and catabolism*, NeuroMolecular Medicine, 4 (2003). ↱ 1.1

[103] B. L. HANDEN, A. D. COHEN, U. CHANNAMALAPPA, P. BULOVA, S. A. CANNON, W. I. COHEN, C. A. MATHIS, J. C. PRICE, AND W. E. KLUNK, *Imaging brain amyloid in nondemented young adults with down syndrome using pittsburgh compound b*, Alzheimer's & Dementia, 8 (2012). ↱ 8.4

[104] B. J. Hanseeuw, R. A. Betensky, H. I. L. Jacobs, A. P. Schultz, J. Sepulcre, J. A. Becker, D. M. O. Cosio, M. Farrell, Y. T. Quiroz, E. C. Mormino, R. F. Buckley, K. V. Papp, R. A. Amariglio, I. Dewachter, A. Ivanoiu, W. Huijbers, T. Hedden, G. A. Marshall, J. P. Chhatwal, D. M. Rentz, R. A. Sperling, and K. Johnson, *Association of amyloid and tau with cognition in preclinical alzheimer disease*, JAMA Neurology, 76 (2019). ⌐ 1.3, 3.3, 5.5, and 8.4

[105] B. J. Hanseeuw, R. A. Betensky, E. C. Mormino, A. P. Schultz, J. Sepulcre, J. A. Becker, H. I. Jacobs, R. F. Buckley, M. R. LaPoint, P. Vannini, N. J. Donovan, J. P. Chhatwal, G. A. Marshall, K. V. Papp, R. E. Amariglio, D. M. Rentz, R. A. Sperling, and K. A. Johnson, *Pet staging of amyloidosis using striatum*, Alzheimer's & Dementia, 14 (2018). ⌐ 8.1, 8.4, and 11

[106] O. Hansson, J. Seibyl, E. Stomrud, H. Zetterberg, J. Q. Trojanowski, T. Bittner, V. Lifke, V. Corradini, U. Eichenlaub, R. Batrla, K. Buck, K. Zink, C. Rabe, K. Blennow, and L. M. Shaw, *Csf biomarkers of alzheimer's disease concord with amyloid-β pet and predict clinical progression: A study of fully automated immunoassays in biofinder and adni cohorts*, Alzheimer's & Dementia, 14 (2018). ⌐ 6.1

[107] J. Hardy and G. Higgins, *Alzheimer's disease: the amyloid cascade hypothesis*, Science, 256 (1992). ⌐ 1.3

[108] E. Head and I. T. Lott, *Down syndrome and beta-amyloid deposition*, Current Opinion in Neurology, 17 (2004). ⌐ 1.2

[109] D. Henley, N. Raghavan, R. Sperling, P. Aisen, R. Raman, and G. Romano, *Preliminary results of a trial of atabecestat in preclinical alzheimer's disease*, New England Journal of Medicine, 380 (2019). ⌐ 1.3

[110] K. Herholz and W. Heiss, *Positron emission tomography in clinical neurology*, Molecular Imaging & Biology, 6 (2004). ⌐ 2 and 2.1.1

[111] T. J. Hohman, L. Dumitrescu, L. L. Barnes, M. Thambisetty, G. Beecham, B. Kunkle, K. A. Gifford, W. S. Bush, L. B. Chibnik, S. Mukherjee, P. L. D. Jager, W. Kukull, P. K. Crane, S. M. Resnick, C. D. Keene, T. J. Montine, G. D. Schellenberg, J. L. Haines, H. Zetterberg, K. Blennow, E. B. Larson, S. C. Johnson, M. Albert, D. A. Bennett, J. A. Schneider, and A. L. Jefferson, *Sex-specific association of apolipoprotein e with cerebrospinal fluid levels of tau*, JAMA Neurology, 75 (2018). ⌐ 3.4

[112] D. Holland, R. Desikan, A. Dale, and L. McEvoy, *Higher rates of decline for women and apolipoprotein e ε4 carriers*, American Journal of Neuroradiology, 34 (2013). ⌐ 3.4

[113] L. S. Honig, B. Vellas, M. Woodward, M. Boada, R. Bullock, M. Borrie, K. Hager, N. Andreasen, E. Scarpini, H. Liu-Seifert, M. Case, R. A. Dean, A. Hake, K. Sundell, V. P. Hoffmann, C. Carlson, R. Khanna, M. Mintun, R. DeMattos, K. J. Selzler, and E. Siemers, *Trial of solanezumab for mild dementia due to alzheimer's disease*, New England Journal of Medicine, 378 (2018). ⌐ 1.3 and 9.1

[114] L. D. Hoyo, L. Xicota, G. Sánchez-Benavides, A. Cuenca-Royo, S. de Sola, K. Langohr, A. B. Fagundo, M. Farré, M. Dierssen, and R. de la Torre, *Semantic verbal fluency pattern, dementia rating scores and adaptive behavior correlate with plasma aβ42 concentrations in down syndrome young adults*, Frontiers in Behavioral Neuroscience, 9 (2015). ↪ 8.4

[115] E. Hudry, J. Dashkoff, A. D. Roe, S. Takeda, R. M. Koffie, T. Hashimoto, M. Scheel, T. Spires-Jones, M. Arbel-Ornath, R. Betensky, B. L. Davidson, and B. T. Hyman, *Gene transfer of human apoe isoforms results in differential modulation of amyloid deposition and neurotoxicity in mouse brain*, Science Translational Medicine, 5 (2013). ↪ 1.1

[116] H. Hudson and R. Larkin, *Accelerated image reconstruction using ordered subsets of projection data*, IEEE Transactions on Medical Imaging, 13 (1994). ↪ 2.2

[117] C. Hutton, E. D. Vita, J. Ashburner, R. Deichmann, and R. Turner, *Voxel-based cortical thickness measurements in mri*, NeuroImage, 40 (2008). ↪ 7.2.4

[118] I. Häggströmi, *Quantitative Methods for Tumor Imaging with Dynamic PET*, 2014. ↪ 2.3, 2.4, 2.2, 4.2, and 4.2

[119] Y. Ikoma, H. Watabe, M. Shidahara, M. Naganawa, and Y. Kimura, *Pet kinetic analysis: error consideration of quantitative analysis in dynamic studies*, Annals of Nuclear Medicine, 22 (2008). ↪ 4.1.1

[120] M. D. Ikonomovic, C. J. Buckley, K. Heurling, P. Sherwin, P. A. Jones, M. Zanette, C. A. Mathis, W. E. Klunk, A. Chakrabarty, J. Ironside, A. Ismail, C. Smith, D. R. Thal, T. G. Beach, G. Farrar, and A. P. L. Smith, *Post-mortem histopathology underlying β-amyloid pet imaging following flutemetamol f 18 injection*, Acta Neuropathologica Communications, 4 (2016). ↪ 4.2.1

[121] M. D. Ikonomovic, W. E. Klunk, E. E. Abrahamson, C. A. Mathis, J. C. Price, N. D. Tsopelas, B. J. Lopresti, S. Ziolko, W. Bi, W. R. Paljug, M. L. Debnath, C. E. Hope, B. A. Isanski, R. L. Hamilton, and S. T. DeKosky, *Post-mortem correlates of in vivo pib-pet amyloid imaging in a typical case of alzheimer's disease*, Brain, 131 (2008). ↪ 3 and 7.1

[122] R. B. Innis, V. J. Cunningham, J. Delforge, M. Fujita, A. Gjedde, R. N. Gunn, J. Holden, S. Houle, S.-C. Huang, M. Ichise, H. Iida, H. Ito, Y. Kimura, R. A. Koeppe, G. M. Knudsen, J. Knuuti, A. A. Lammertsma, M. Laruelle, J. Logan, R. P. Maguire, M. A. Mintun, E. D. Morris, R. Parsey, J. C. Price, M. Slifstein, V. Sossi, T. Suhara, J. R. Votaw, D. F. Wong, and R. E. Carson, *Consensus nomenclature for <i>in vivo</i> imaging of reversibly binding radioligands*, Journal of Cerebral Blood Flow & Metabolism, 27 (2007). ↪ 4.1

[123] P. S. Insel, N. Mattsson, R. S. Mackin, M. Schöll, R. L. Nosheny, D. Tosun, M. C. Donohue, P. S. Aisen, W. J. Jagust, and M. W. Weiner, *Accelerating rates of cognitive decline and imaging markers associated with β-amyloid pathology*, Neurology, 86 (2016). ↪ 5.3, 8.4, and 11

[124] P. S. INSEL, E. C. MORMINO, P. S. AISEN, W. K. THOMPSON, AND M. C. DONO-HUE, *Neuroanatomical spread of amyloid β and tau in alzheimer's disease: implications for primary prevention*, Brain Communications, 2 (2020). ↱ 8.4

[125] C. R. JACK, D. A. BENNETT, K. BLENNOW, M. C. CARRILLO, B. DUNN, S. B. HAEBERLEIN, D. M. HOLTZMAN, W. JAGUST, F. JESSEN, J. KARLAWISH, E. LIU, J. L. MOLINUEVO, T. MONTINE, C. PHELPS, K. P. RANKIN, C. C. ROWE, P. SCHELTENS, E. SIEMERS, H. M. SNYDER, R. SPERLING, C. ELLIOTT, E. MASLIAH, L. RYAN, AND N. SILVERBERG, *Nia-aa research framework: Toward a biological definition of alzheimer's disease*, Alzheimer's & Dementia, 14 (2018). ↱ 1.3, 1.4, 5.5, 6.1, 7.1, 8.1, and 9.1

[126] C. R. JACK, D. A. BENNETT, K. BLENNOW, M. C. CARRILLO, H. H. FELDMAN, G. B. FRISONI, H. HAMPEL, W. J. JAGUST, K. A. JOHNSON, D. S. KNOPMAN, R. C. PETERSEN, P. SCHELTENS, R. A. SPERLING, AND B. DUBOIS, *A/t/n: An unbiased descriptive classification scheme for alzheimer disease biomarkers*, Neurology, 87 (2016). ↱ 1.3

[127] C. R. JACK, D. S. KNOPMAN, W. J. JAGUST, R. C. PETERSEN, M. W. WEINER, P. S. AISEN, L. M. SHAW, P. VEMURI, H. J. WISTE, S. D. WEIGAND, T. G. LESNICK, V. S. PANKRATZ, M. C. DONOHUE, AND J. Q. TROJANOWSKI, *Tracking pathophysiological processes in alzheimer's disease: an updated hypothetical model of dynamic biomarkers*, The Lancet Neurology, 12 (2013). ↱ 8.1

[128] C. R. JACK, H. J. WISTE, H. BOTHA, S. D. WEIGAND, T. M. THERNEAU, D. S. KNOPMAN, J. GRAFF-RADFORD, D. T. JONES, T. J. FERMAN, B. F. BOEVE, K. KANTARCI, V. J. LOWE, P. VEMURI, M. M. MIELKE, J. A. FIELDS, M. M. MACHULDA, C. G. SCHWARZ, M. L. SENJEM, J. L. GUNTER, AND R. C. PETERSEN, *The bivariate distribution of amyloid-β and tau: relationship with established neurocognitive clinical syndromes*, Brain, 142 (2019), pp. 3230–3242. ↱ 5.5, 10.1, 10.1, and 10.2

[129] C. R. JACK, H. J. WISTE, S. D. WEIGAND, D. S. KNOPMAN, P. VEMURI, M. M. MIELKE, V. LOWE, M. L. SENJEM, J. L. GUNTER, M. M. MACHULDA, B. E. GREGG, V. S. PANKRATZ, W. A. ROCCA, AND R. C. PETERSEN, *Age, sex, and <i>apoe</i> epsilon4 effects on memory, brain structure, and β-amyloid across the adult life span*, JAMA Neurology, 72 (2015). ↱ 3.4

[130] C. R. JACK, H. J. WISTE, S. D. WEIGAND, W. A. ROCCA, D. S. KNOPMAN, M. M. MIELKE, V. J. LOWE, M. L. SENJEM, J. L. GUNTER, G. M. PREBOSKE, V. S. PANKRATZ, P. VEMURI, AND R. C. PETERSEN, *Age-specific population frequencies of cerebral β-amyloidosis and neurodegeneration among people with normal cognitive function aged 50–89 years: a cross-sectional study*, The Lancet Neurology, 13 (2014). ↱ 9.1

[131] C. R. JACK, H. J. WISTE, S. D. WEIGAND, T. M. THERNEAU, D. S. KNOPMAN, V. LOWE, P. VEMURI, M. M. MIELKE, R. O. ROBERTS, M. M. MACHULDA, M. L. SENJEM, J. L. GUNTER, W. A. ROCCA, AND R. C. PETERSEN, *Age-specific and sex-specific prevalence of cerebral β-amyloidosis, tauopathy, and neurodegeneration in cognitively unimpaired individuals aged 50–95 years: a cross-sectional study*, The Lancet Neurology, 16 (2017). ↱ 3.4

[132] W. J. JAGUST AND S. M. LANDAU, *Apolipoprotein e, not fibrillar -amyloid, reduces cerebral glucose metabolism in normal aging*, Journal of Neuroscience, 32 (2012). ↱ 8.1 and 8.4

[133] W. J. JAGUST, S. M. LANDAU, R. A. KOEPPE, E. M. REIMAN, K. CHEN, C. A. MATHIS, J. C. PRICE, N. L. FOSTER, AND A. Y. WANG, *The alzheimer's disease neuroimaging initiative 2 pet core: 2015*, Alzheimer's & Dementia, 11 (2015). ↱ 7.1

[134] W. J. JANSEN, R. OSSENKOPPELE, D. L. KNOL, B. M. TIJMS, P. SCHELTENS, F. R. J. VERHEY, P. J. VISSER, P. AALTEN, D. AARSLAND, D. ALCOLEA, M. ALEXANDER, I. S. ALMDAHL, S. E. ARNOLD, I. BALDEIRAS, H. BARTHEL, B. N. M. VAN BERCKEL, K. BIBEAU, K. BLENNOW, D. J. BROOKS, M. A. VAN BUCHEM, V. CAMUS, E. CAVEDO, K. CHEN, G. CHETELAT, A. D. COHEN, A. DRZEZGA, S. ENGELBORGHS, A. M. FAGAN, T. FLADBY, A. S. FLEISHER, W. M. VAN DER FLIER, L. FORD, S. FÖRSTER, J. FORTEA, N. FOSKETT, K. S. FREDERIKSEN, Y. FREUND-LEVI, G. B. FRISONI, L. FROELICH, T. GABRYELEWICZ, K. D. GILL, O. GKATZIMA, E. GÓMEZ-TORTOSA, M. F. GORDON, T. GRIMMER, H. HAMPEL, L. HAUSNER, S. HELLWIG, S.-K. HERUKKA, H. HILDEBRANDT, L. ISHIHARA, A. IVANOIU, W. J. JAGUST, P. JOHANNSEN, R. KANDIMALLA, E. KAPAKI, A. KLIMKOWICZ-MROWIEC, W. E. KLUNK, S. KÖHLER, N. KOGLIN, J. KORNHUBER, M. G. KRAMBERGER, K. V. LAERE, S. M. LANDAU, D. Y. LEE, M. DE LEON, V. LISETTI, A. LLEÓ, K. MADSEN, W. MAIER, J. MARCUSSON, N. MATTSSON, A. DE MENDONÇA, O. MEULENBROEK, P. T. MEYER, M. A. MINTUN, V. MOK, J. L. MOLINUEVO, H. M. MØLLERGÅRD, J. C. MORRIS, B. MROCZKO, S. V. DER MUSSELE, D. L. NA, A. NEWBERG, A. NORDBERG, A. NORDLUND, G. P. NOVAK, G. P. PARASKEVAS, L. PARNETTI, G. PERERA, O. PETERS, J. POPP, S. PRABHAKAR, G. D. RABINOVICI, I. H. G. B. RAMAKERS, L. RAMI, C. R. DE OLIVEIRA, J. O. RINNE, K. M. RODRIGUE, E. RODRÍGUEZ-RODRÍGUEZ, C. M. ROE, U. ROT, C. C. ROWE, E. RÜTHER, O. SABRI, P. SANCHEZ-JUAN, I. SANTANA, M. SARAZIN, J. SCHRÖDER, C. SCHÜTTE, S. W. SEO, F. SOETEWEY, H. SOININEN, L. SPIRU, H. STRUYFS, C. E. TEUNISSEN, M. TSOLAKI, R. VANDENBERGHE, M. M. VERBEEK, V. L. VILLEMAGNE, S. J. B. VOS, L. J. C. VAN WAALWIJK VAN DOORN, G. WALDEMAR, A. WALLIN, ÅSA K. WALLIN, J. WILTFANG, D. A. WOLK, M. ZBOCH, AND H. ZETTERBERG, *Prevalence of cerebral amyloid pathology in persons without dementia*, JAMA, 313 (2015). ↱ 3, 3.4, and 9.1

[135] W.-S. JIN, X.-L. BU, Y.-H. LIU, L.-L. SHEN, Z.-Q. ZHUANG, S.-S. JIAO, C. ZHU, Q.-H. WANG, H.-D. ZHOU, T. ZHANG, AND Y.-J. WANG, *Plasma amyloid-beta levels in patients with different types of cancer*, Neurotoxicity Research, 31 (2017). ↱ 1.2

[136] K. A. JOHNSON, S. MINOSHIMA, N. I. BOHNEN, K. J. DONOHOE, N. L. FOSTER, P. HERSCOVITCH, J. H. KARLAWISH, C. C. ROWE, M. C. CARRILLO, D. M. HARTLEY, S. HEDRICK, V. PAPPAS, AND W. H. THIES, *Appropriate use criteria for amyloid pet: A report of the amyloid imaging task force, the society of nuclear medicine and molecular imaging, and the alzheimer's association*, Alzheimer's & Dementia, 9 (2013). ↱ 3, 3.1, 3.2, 7.2.1, 8.1, 8.2.1, and 10.2

[137] S. E. JONES, B. R. BUCHBINDER, AND I. AHARON, *Three-dimensional mapping of cortical thickness using laplace's equation*, Human Brain Mapping, 11 (2000). ↱ 7.2.4

[138] J. S. KARP, S. SURTI, M. E. DAUBE-WITHERSPOON, AND G. MUEHLLEHNER, *Benefit of time-of-flight in pet: Experimental and clinical results*, Journal of Nuclear Medicine, 49 (2008). ↱ 2.1.1

[139] P. E. KINAHAN AND J. W. FLETCHER, *Positron emission tomography-computed tomography standardized uptake values in clinical practice and assessing response to therapy*, Seminars in Ultrasound, CT and MRI, 31 (2010). ↱ 5.4, 6.2.5, 7.1, 8.1, 8.2.3, 9.1, 9.2.3, and 9.4

[140] A. KLEIN, J. ANDERSSON, B. A. ARDEKANI, J. ASHBURNER, B. AVANTS, M.-C. CHIANG, G. E. CHRISTENSEN, D. L. COLLINS, J. GEE, P. HELLIER, J. H. SONG, M. JENKINSON, C. LEPAGE, D. RUECKERT, P. THOMPSON, T. VERCAUTEREN, R. P. WOODS, J. J. MANN, AND R. V. PARSEY, *Evaluation of 14 nonlinear deformation algorithms applied to human brain mri registration*, NeuroImage, 46 (2009). ↱ 4.2.1

[141] W. KLEIN, W. STINE, AND D. TEPLOW, *Small assemblies of unmodified amyloid β-protein are the proximate neurotoxin in alzheimer's disease*, Neurobiology of Aging, 25 (2004). ↱ 1.1

[142] W. E. KLUNK, H. ENGLER, A. NORDBERG, Y. WANG, G. BLOMQVIST, D. P. HOLT, M. BERGSTRÖM, I. SAVITCHEVA, G.-F. HUANG, S. ESTRADA, B. AUSÉN, M. L. DEBNATH, J. BARLETTA, J. C. PRICE, J. SANDELL, B. J. LOPRESTI, A. WALL, P. KOIVISTO, G. ANTONI, C. A. MATHIS, AND B. LÅNGSTRÖM, *Imaging brain amyloid in alzheimer's disease with pittsburgh compound-b*, Annals of Neurology, 55 (2004). ↱ 3, 3.1, and 4.2

[143] W. E. KLUNK, R. A. KOEPPE, J. C. PRICE, T. L. BENZINGER, M. D. DEVOUS, W. J. JAGUST, K. A. JOHNSON, C. A. MATHIS, D. MINHAS, M. J. PONTECORVO, C. C. ROWE, D. M. SKOVRONSKY, AND M. A. MINTUN, *The centiloid project: Standardizing quantitative amyloid plaque estimation by pet*, Alzheimer's & Dementia, 11 (2015). ↱ 3, 4.2, 4.2, 4.2.1, 6.1, 6.2.5, 7.1, 7.2.3, 7.2.5, 8.2.4, and 8.5.3

[144] W. D. KNIGHT, A. A. OKELLO, N. S. RYAN, F. E. TURKHEIMER, S. R. M. DE LLANO, P. EDISON, J. DOUGLAS, N. C. FOX, D. J. BROOKS, AND M. N. ROSSOR, *Carbon-11-pittsburgh compound b positron emission tomography imaging of amyloid deposition in presenilin 1 mutation carriers*, Brain, 134 (2011). ↱ 4.2

[145] D. S. KNOPMAN, C. R. JACK, H. J. WISTE, S. D. WEIGAND, P. VEMURI, V. J. LOWE, K. KANTARCI, J. L. GUNTER, M. L. SENJEM, M. M. MIELKE, R. O. ROBERTS, B. F. BOEVE, AND R. C. PETERSEN, *Brain injury biomarkers are not dependent on β-amyloid in normal elderly*, Annals of Neurology, 73 (2013). ↱ 8.1 and 8.4

[146] L. H. KULLER AND O. L. LOPEZ, *Engage and emerge: Truth and consequences?*, Alzheimer's & Dementia, 17 (2021). ↱ 1.3 and 4

[147] R. Laforce, J.-P. Soucy, L. Sellami, C. Dallaire-Théroux, F. Brunet, D. Bergeron, B. L. Miller, and R. Ossenkoppele, *Molecular imaging in dementia: Past, present, and future*, Alzheimer's & Dementia, 14 (2018). ↱ 3

[148] S. M. Landau, C. Breault, A. D. Joshi, M. Pontecorvo, C. A. Mathis, W. J. Jagust, and M. A. Mintun, *Amyloid-β imaging with pittsburgh compound b and florbetapir: Comparing radiotracers and quantification methods*, Journal of Nuclear Medicine, 54 (2013). ↱ 4.2.1 and 7.2.3

[149] S. M. Landau, A. Fero, S. L. Baker, R. Koeppe, M. Mintun, K. Chen, E. M. Reiman, and W. J. Jagust, *Measurement of longitudinal β-amyloid change with ¹⁸ f-florbetapir pet and standardized uptake value ratios*, Journal of Nuclear Medicine, 56 (2015). ↱ 4.2, 7.2.3, and 11

[150] S. M. Landau, A. Horng, and W. J. Jagust, *Memory decline accompanies sub-threshold amyloid accumulation*, Neurology, 90 (2018), pp. e1452–e1460. ↱ 5.3 and 11

[151] S. M. Landau, B. A. Thomas, L. Thurfjell, M. Schmidt, R. Margolin, M. Mintun, M. Pontecorvo, S. L. Baker, and W. J. Jagust, *Amyloid pet imaging in alzheimer's disease: a comparison of three radiotracers*, European Journal of Nuclear Medicine and Molecular Imaging, 41 (2014). ↱ 4.2.1 and 7.1

[152] H. Lassmann, W. Brück, and C. F. Lucchinetti, *The immunopathology of multiple sclerosis: An overview*, Brain Pathology, 17 (2007), pp. 210–218. ↱ 11

[153] I. Law, H. Iida, S. Holm, S. Nour, E. Rostrup, C. Svarer, and O. B. Paulson, *Quantitation of regional cerebral blood flow corrected for partial volume effect using o-15 water and pet: Ii. normal values and gray matter blood flow response to visual activation*, Journal of Cerebral Blood Flow & Metabolism, 20 (2000). ↱ 7.2.2

[154] R. M. Leahy and J. Qi, *Statistical approaches in quantitative positron emission-tomography*, Statistics and Computing, 10 (2000). ↱ 2.2

[155] V. Leinonen, J. O. Rinne, D. F. Wong, D. A. Wolk, J. Q. Trojanowski, P. F. Sherwin, A. Smith, K. Heurling, M. Su, and I. D. Grachev, *Diagnostic effectiveness of quantitative [18f]flutemetamol pet imaging for detection of fibrillar amyloid β using cortical biopsy histopathology as the standard of truth in subjects with idiopathic normal pressure hydrocephalus*, Acta Neuropathologica Communications, 2 (2014). ↱ 4.2.1 and 7.2.3

[156] J. P. Lerch, J. C. Pruessner, A. Zijdenbos, H. Hampel, S. J. Teipel, and A. C. Evans, *Focal decline of cortical thickness in alzheimer's disease identified by computational neuroanatomy*, Cerebral Cortex, 15 (2005). ↱ 7.2.4

[157] S. E. Lesné, M. A. Sherman, M. Grant, M. Kuskowski, J. A. Schneider, D. A. Bennett, and K. H. Ashe, *Brain amyloid-β oligomers in ageing and alzheimer's disease*, Brain, 136 (2013). ↱ 1.1

[158] R. Lewitt and S. Matej, *Overview of methods for image reconstruction from projections in emission computed tomography*, Proceedings of the IEEE, 91 (2003). ↱ 2.2

[159] E. Lilly and Company, *Tauvid™ (flortaucipir f 18 injection), for intravenous use initial u.s. approval: 2020*, 2020. ↱ 10.2

[160] S. Lim, B. K. Yoo, H.-S. Kim, H. L. Gilmore, Y. Lee, H. pil Lee, S.-J. Kim, J. Letterio, and H. gon Lee, *Amyloid-β precursor protein promotes cell proliferation and motility of advanced breast cancer*, BMC Cancer, 14 (2014). ↱ 1.2

[161] H. Liu, Y.-H. Nai, F. Saridin, T. Tanaka, J. O. Doherty, S. Hilal, B. Gyanwali, C. P. Chen, E. G. Robins, and A. Reilhac, *Improved amyloid burden quantification with nonspecific estimates using deep learning*, European Journal of Nuclear Medicine and Molecular Imaging, 48 (2021). ↱ 4.3

[162] J. M. Long and D. M. Holtzman, *Alzheimer disease: An update on pathobiology and treatment strategies*, Cell, 179 (2019). ↱ 1.3

[163] M. N. Lonsdale and T. Beyer, *Dual-modality pet/ct instrumentation—today and tomorrow*, European Journal of Radiology, 73 (2010). ↱ 2.1.1

[164] C. Louapre, B. Bodini, C. Lubetzki, L. Freeman, and B. Stankoff, *Imaging markers of multiple sclerosis prognosis*, Current Opinion in Neurology, 30 (2017). ↱ 8.1

[165] V. J. Lowe, E. S. Lundt, M. L. Senjem, C. G. Schwarz, H.-K. Min, S. A. Przybelski, K. Kantarci, D. Knopman, R. C. Petersen, and C. R. Jack, *White matter reference region in pet studies of ¹¹ c-pittsburgh compound b uptake: Effects of age and amyloid-β deposition*, Journal of Nuclear Medicine, 59 (2018). ↱ 4.2

[166] G. Lucignani, G. Paganelli, and E. Bombardieri, *The use of standardized uptake values for assessing fdg uptake with pet in oncology: a clinical perspective*, Nuclear Medicine Communications, 25 (2004). ↱ 4.2

[167] T. F. Lundeen, J. P. Seibyl, M. F. Covington, N. Eshghi, and P. H. Kuo, *Signs and artifacts in amyloid pet*, RadioGraphics, 38 (2018). ↱ 3.2, 3.3, and 3.4

[168] R. Lundqvist, J. Lilja, B. A. Thomas, J. Lötjönen, V. L. Villemagne, C. C. Rowe, and L. Thurfjell, *Implementation and validation of an adaptive template registration method for ¹⁸ f-flutemetamol imaging data*, Journal of Nuclear Medicine, 54 (2013). ↱ 4.2.1

[169] J. A. Maldjian, P. J. Laurienti, R. A. Kraft, and J. H. Burdette, *An automated method for neuroanatomic and cytoarchitectonic atlas-based interrogation of fmri data sets*, NeuroImage, 19 (2003). ↱ 8.2.3

[170] A. Mallik, A. Drzezga, and S. Minoshima, *Clinical amyloid imaging*, Seminars in Nuclear Medicine, 47 (2017), pp. 31–43. ↱ 11

[171] K. G. Malmos, L. M. Blancas-Mejia, B. Weber, J. Buchner, M. Ramirez-Alvarado, H. Naiki, and D. Otzen, *Tht 101: a primer on the use of thioflavin t to investigate amyloid formation*, Amyloid, 24 (2017). ↱ 3.1

[172] D. G. MARCHAND, R. B. POSTUMA, F. ESCUDIER, J. D. ROY, A. PELLETIER, J. MONTPLAISIR, AND J.-F. GAGNON, *How does dementia with lewy bodies start? prodromal cognitive changes in rem sleep behavior disorder*, Annals of Neurology, 83 (2018). ↱ 8.4

[173] K. MATSUBARA, M. IBARAKI, H. SHIMADA, Y. IKOMA, T. SUHARA, T. KINOSHITA, AND H. ITCO, *Impact of spillover from white matter by partial volume effect on quantification of amyloid deposition with [11c]pib pet*, NeuroImage, 143 (2016). ↱ 2.2 and 5.2

[174] M. P. MATTSON, *Pathways towards and away from alzheimer's disease*, Nature, 430 (2004). ↱ 1.1

[175] N. MATTSSON, P. S. INSEL, S. LANDAU, W. JAGUST, M. DONOHUE, L. M. SHAW, J. Q. TROJANOWSKI, H. ZETTERBERG, K. BLENNOW, AND M. WEINER, *Diagnostic accuracy of csf ab42 and florbetapir pet for alzheimer's disease*, Annals of Clinical and Translational Neurology, 1 (2014). ↱ 7.1

[176] N. MATTSSON, A. LÖNNEBORG, M. BOCCARDI, K. BLENNOW, AND O. HANSSON, *Clinical validity of cerebrospinal fluid aβ42, tau, and phospho-tau as biomarkers for alzheimer's disease in the context of a structured 5-phase development framework*, Neurobiology of Aging, 52 (2017). ↱ 3.4

[177] N. MATTSSON, S. PALMQVIST, E. STOMRUD, J. VOGEL, AND O. HANSSON, *Staging β-amyloid pathology with amyloid positron emission tomography*, JAMA Neurology, 76 (2019). ↱ 5.3, 8.1, 8.4, 9.1, and 11

[178] J. A. MATÍAS-GUIU, M. N. CABRERA-MARTÍN, J. MATÍAS-GUIU, C. OREJA-GUEVARA, C. RIOLA-PARADA, T. MORENO-RAMOS, J. ARRAZOLA, AND J. L. CARRERAS, *Amyloid pet imaging in multiple sclerosis: an 18f-florbetaben study*, BMC Neurology, 15 (2015), p. 243. ↱ 11

[179] G. MCKHANN, D. DRACHMAN, M. FOLSTEIN, R. KATZMAN, D. PRICE, AND E. M. STADLAN, *Clinical diagnosis of alzheimer's disease: Report of the nincds-adrda work group* under the auspices of department of health and human services task force on alzheimer's disease*, Neurology, 34 (1984). ↱ 1.3 and 10.1

[180] G. M. MCKHANN, D. S. KNOPMAN, H. CHERTKOW, B. T. HYMAN, C. R. JACK, C. H. KAWAS, W. E. KLUNK, W. J. KOROSHETZ, J. J. MANLY, R. MAYEUX, R. C. MOHS, J. C. MORRIS, M. N. ROSSOR, P. SCHELTENS, M. C. CARRILLO, B. THIES, S. WEINTRAUB, AND C. H. PHELPS, *The diagnosis of dementia due to alzheimer's disease: Recommendations from the national institute on aging-alzheimer's association workgroups on diagnostic guidelines for alzheimer's disease*, Alzheimer's & Dementia, 7 (2011). ↱ 1.3, 1.3, 1.3, 6.1, and 6.2.1

[181] D. MEHTA, R. JACKSON, G. PAUL, J. SHI, AND M. SABBAGH, *Why do trials for alzheimer's disease drugs keep failing? a discontinued drug perspective for 2010-2015*, Expert Opinion on Investigational Drugs, 26 (2017). ↱ 1.3 and 11

[182] P. T. MEYER, S. HELLWIG, F. AMTAGE, C. ROTTENBURGER, U. SAHM, P. REULAND, W. A. WEBER, AND M. HÜLL, *Dual-biomarker imaging of regional cerebral*

amyloid load and neuronal activity in dementia with pet and ¹¹ c-labeled pittsburgh compound b, Journal of Nuclear Medicine, 52 (2011). ↱ 7.2.2

[183] M. M. MIELKE, H. J. WISTE, S. D. WEIGAND, D. S. KNOPMAN, V. J. LOWE, R. O. ROBERTS, Y. E. GEDA, D. M. SWENSON-DRAVIS, B. F. BOEVE, M. L. SENJEM, P. VEMURI, R. C. PETERSEN, AND C. R. JACK, *Indicators of amyloid burden in a population-based study of cognitively normal elderly*, Neurology, 79 (2012). ↱ 3.4

[184] S. MINOSHIMA, A. E. DRZEZGA, H. BARTHEL, N. BOHNEN, M. DJEKIDEL, D. H. LEWIS, C. A. MATHIS, J. MCCONATHY, A. NORDBERG, O. SABRI, J. P. SEIBYL, M. K. STOKES, AND K. V. LAERE, *Snmmi procedure standard/eanm practice guideline for amyloid pet imaging of the brain 1.0*, Journal of Nuclear Medicine, 57 (2016). ↱ 3.2, 6.2.2, 8.2.2, and 9.2.2

[185] J. L. MOLINUEVO, K. BLENNOW, B. DUBOIS, S. ENGELBORGHS, P. LEW-CZUK, A. PERRET-LIAUDET, C. E. TEUNISSEN, AND L. PARNETTI, *The clinical use of cerebrospinal fluid biomarker testing for alzheimer's disease diagnosis: A consensus paper from the alzheimer's biomarkers standardization initiative*, Alzheimer's & Dementia, 10 (2014). ↱ 6.1

[186] S. MOMJIAN, B. K. OWLER, Z. CZOSNYKA, M. CZOSNYKA, A. PENA, AND J. D. PICKARD, *Pattern of white matter regional cerebral blood flow and autoregulation in normal pressure hydrocephalus*, Brain, 127 (2004). ↱ 7.2.2

[187] S. MORBELLI, M. BAUCKNEHT, S. CAPITANIO, M. PARDINI, L. ROCCATAGLIATA, AND F. NOBILI, *A new frontier for amyloid pet imaging: multiple sclerosis*, European Journal of Nuclear Medicine and Molecular Imaging, 46 (2019), pp. 276–279. ↱ 11

[188] E. C. MORMINO, J. T. KLUTH, C. M. MADISON, G. D. RABINOVICI, S. L. BAKER, B. L. MILLER, R. A. KOEPPE, C. A. MATHIS, M. W. WEINER, AND W. J. JAGUST, *Episodic memory loss is related to hippocampal-mediated -amyloid deposition in elderly subjects*, Brain, 132 (2009). ↱ 4.2.1

[189] J. C. MORRIS, *The clinical dementia rating (cdr)*, Neurology, 43 (1993). ↱ 1.3

[190] L. MOSCONI, V. BERTI, C. QUINN, P. MCHUGH, G. PETRONGOLO, I. VARSAVSKY, R. S. OSORIO, A. PUPI, S. VALLABHAJOSULA, R. S. ISAACSON, M. J. DE LEON, AND R. D. BRINTON, *Sex differences in alzheimer risk*, Neurology, 89 (2017). ↱ 3.4

[191] S. MUKHOPADHYAY AND D. BANERJEE, *A primer on the evolution of aducanumab: The first antibody approved for treatment of alzheimer's disease*, Journal of Alzheimer's Disease, (2021). ↱ 1.3 and 5.4

[192] K. R. MURPHY, S. M. LANDAU, K. R. CHOUDHURY, C. A. HOSTAGE, K. S. SHPANSKAYA, H. I. SAIR, J. R. PETRELLA, T. Z. WONG, AND P. M. DORAISWAMY, *Mapping the effects of apoe4, age and cognitive status on 18f-florbetapir pet measured regional cortical patterns of beta-amyloid density and growth*, NeuroImage, 78 (2013). ↱ 3.4

[193] E. S. MUSIEK AND D. M. HOLTZMAN, *Three dimensions of the amyloid hypothesis: time, space and 'wingmen'*, Nature Neuroscience, 18 (2015). ↱ 1.3

[194] M. Naganawa, J.-D. Gallezot, V. Shah, T. Mulnix, C. Young, M. Dias, M.-K. Chen, A. M. Smith, and R. E. Carson, *Assessment of population-based input functions for patlak imaging of whole body dynamic 18f-fdg pet*, EJNMMI Physics, 7 (2020). ↪ 4.1

[195] A. P. Nayate, J. G. Dubroff, J. E. Schmitt, I. Nasrallah, R. Kishore, D. Mankoff, and D. A. Pryma, *Use of standardized uptake value ratios decreases interreader variability of [18f] florbetapir pet brain scan interpretation*, American Journal of Neuroradiology, 36 (2015). ↪ 6.4 and 9.1

[196] N. Nelissen, K. V. Laere, L. Thurfjell, R. Owenius, M. Vandenbulcke, M. Koole, G. Bormans, D. J. Brooks, and R. Vandenberghe, *Phase 1 study of the pittsburgh compound b derivative ¹⁸ f-flutemetamol in healthy volunteers and patients with probable alzheimer disease*, Journal of Nuclear Medicine, 50 (2009). ↪ 4.2.1

[197] U. Neniskyte, J. J. Neher, and G. C. Brown, *Neuronal death induced by nanomolar amyloid β is mediated by primary phagocytosis of neurons by microglia*, Journal of Biological Chemistry, 286 (2011). ↪ 1.1

[198] E. Niemantsverdriet, J. Ottoy, C. Somers, E. D. Roeck, H. Struyfs, F. Soetewey, J. Verhaeghe, T. V. den Bossche, S. V. Mosseivelde, J. Goeman, P. P. D. Deyn, P. Mariën, J. Versijpt, K. Sleegers, C. V. Broeckhoven, L. Wyffels, A. Albert, S. Ceyssens, S. Stroobants, S. Staelens, M. Bjerke, and S. Engelborghs, *The cerebrospinal fluid aβ1–42/aβ1–40 ratio improves concordance with amyloid-pet for diagnosing alzheimer's disease in a clinical setting*, Journal of Alzheimer's Disease, 60 (2017). ↪ 6.1

[199] T. Nikolai, O. Bezdicek, H. Markova, H. Stepankova, J. Michalec, M. Kopecek, M. Dokoupilova, J. Hort, and M. Vyhnalek, *Semantic verbal fluency impairment is detectable in patients with subjective cognitive decline*, Applied Neuropsychology: Adult, 25 (2018). ↪ 8.4

[200] F. Nobili, D. Mazzei, B. Dessi, S. Morbelli, A. Brugnolo, P. Barbieri, N. Girtler, G. Sambuceti, G. Rodriguez, and M. Pagani, *Unawareness of memory deficit in amnestic mci: Fdg-pet findings*, Journal of Alzheimer's Disease, 22 (2010). ↪ 8.2.1

[201] R. Ossenkoppele, Y. A. L. Pijnenburg, D. C. Perry, B. I. Cohn-Sheehy, N. M. E. Scheltens, J. W. Vogel, J. H. Kramer, A. E. van der Vlies, R. L. Joie, H. J. Rosen, W. M. van der Flier, L. T. Grinberg, A. J. Rozemuller, E. J. Huang, B. N. M. van Berckel, B. L. Miller, F. Barkhof, W. J. Jagust, P. Scheltens, W. W. Seeley, and G. D. Rabinovici, *The behavioural/dysexecutive variant of alzheimer's disease: clinical, neuroimaging and pathological features*, Brain, 138 (2015). ↪ 1.3

[202] R. Ossenkoppele, G. D. Rabinovici, R. Smith, H. Cho, M. Schöll, O. Strandberg, S. Palmqvist, N. Mattsson, S. Janelidze, A. Santillo, T. Ohlsson, J. Jögi, R. Tsai, R. L. Joie, J. Kramer, A. L. Boxer, M. L. Gorno-Tempini, B. L. Miller, J. Y. Choi, Y. H. Ryu, C. H. Lyoo, and O. Hansson, *Discriminative accuracy of [¹⁸ f]flortaucipir positron*

emission tomography for alzheimer disease vs other neurodegenerative disorders, JAMA, 320 (2018), p. 1151. ↱ 5.5

[203] R. OSSENKOPPELE, D. R. SCHONHAUT, M. SCHÖLL, S. N. LOCKHART, N. AYAKTA, S. L. BAKER, J. P. O'NEIL, M. JANABI, A. LAZARIS, A. CANTWELL, J. VOGEL, M. SANTOS, Z. A. MILLER, B. M. BETTCHER, K. A. VOSSEL, J. H. KRAMER, M. L. GORNO-TEMPINI, B. L. MILLER, W. J. JAGUST, AND G. D. RABINOVICI, *Tau pet patterns mirror clinical and neuroanatomical variability in alzheimer's disease*, Brain, 139 (2016). ↱ 5.5 and 8.4

[204] S. OSTROWITZKI, R. A. LASSER, E. DORFLINGER, P. SCHELTENS, F. BARKHOF, T. NIKOLCHEVA, E. ASHFORD, S. RETOUT, C. HOFMANN, P. DELMAR, G. KLEIN, M. ANDJELKOVIC, B. DUBOIS, M. BOADA, K. BLENNOW, L. SANTARELLI, AND P. FONTOURA, *A phase iii randomized trial of gantenerumab in prodromal alzheimer's disease*, Alzheimer's Research & Therapy, 9 (2017). ↱ 1.3

[205] J. OTTOY, M. MIEDEMA, C. D. PUYDT, J. VERHAEGHE, S. DELEYE, S. ENGELBORGHS, S. STROOBANTS, AND S. STAELENS, *[p2-363]: Early frame 18f-av45 and 18f-fdg-pet as proxies of cbf: Comparison to 15o-h2o pet data*, Alzheimer's & Dementia, 13 (2017). ↱ 7.4 and 11

[206] S. OVEISGHARAN, Z. ARVANITAKIS, L. YU, J. FARFEL, J. A. SCHNEIDER, AND D. A. BENNETT, *Sex differences in alzheimer's disease and common neuropathologies of aging*, Acta Neuropathologica, 136 (2018). ↱ 3.4

[207] S. V. OVSEPIAN AND V. B. O'LEARY, *Neuronal activity and amyloid plaque pathology: An update*, Journal of Alzheimer's Disease, 49 (2015). ↱ 8.4

[208] B. K. OWLER, S. MOMJIAN, Z. CZOSNYKA, M. CZOSNYKA, A. PÉNA, N. G. HARRIS, P. SMIELEWSKI, T. FRYER, T. DONOVAN, J. COLES, A. CARPENTER, AND J. D. PICKARD, *Normal pressure hydrocephalus and cerebral blood flow: A pet study of baseline values*, Journal of Cerebral Blood Flow & Metabolism, 24 (2004). ↱ 7.2.2

[209] B. PAGHERA, D. ALTOMARE, A. PELI, S. MORBELLI, A. BUSCHIAZZO, M. BAUCKNEHT, R. GIUBBINI, C. RODELLA, L. CAMONI, M. BOCCARDI, C. FESTARI, C. MUSCIO, A. PADOVANI, G. B. FRISONI, AND U. P. GUERRA, *Comparison of visual criteria for amyloid-pet reading: could criteria merging reduce inter-rater variability?*, The Quarterly Journal of Nuclear Medicine and Molecular Imaging, 64 (2020). ↱ 3 and 11

[210] S. PALMQVIST, P. S. INSEL, E. STOMRUD, S. JANELIDZE, H. ZETTERBERG, B. BRIX, U. EICHENLAUB, J. L. DAGE, X. CHAI, K. BLENNOW, N. MATTSSON, AND O. HANSSON, *Cerebrospinal fluid and plasma biomarker trajectories with increasing amyloid deposition in alzheimer's disease*, EMBO Molecular Medicine, 11 (2019). ↱ 10.2

[211] S. PALMQVIST, N. MATTSSON, AND O. HANSSON, *Cerebrospinal fluid analysis detects cerebral amyloid-β accumulation earlier than positron emission tomography*, Brain, 139 (2016). ↱ 6.1

[212] S. Palmqvist, M. Schöll, O. Strandberg, N. Mattsson, E. Stomrud, H. Zetterberg, K. Blennow, S. Landau, W. Jagust, and O. Hansson, *Earliest accumulation of β-amyloid occurs within the default-mode network and concurrently affects brain connectivity*, Nature Communications, 8 (2017). ↑ 5.3, 8.1, 8.4, and 10.3

[213] S. Palmqvist, H. Zetterberg, K. Blennow, S. Vestberg, U. Andreasson, D. J. Brooks, R. Owenius, D. Hägerström, P. Wollmer, L. Minthon, and O. Hansson, *Accuracy of brain amyloid detection in clinical practice using cerebrospinal fluid β-amyloid 42*, JAMA Neurology, 71 (2014). ↑ 4.2.1

[214] P. Payoux, J. Delrieu, A. Gallini, D. Adel, A. S. Salabert, A. Hitzel, C. Cantet, M. Tafani, D. D. Verbizier, J. Darcourt, P. Fernandez, J. Monteil, I. Carrié, T. Voisin, S. Gillette-Guyonnet, M. Pontecorvo, B. Vellas, and S. Andrieu, *Cognitive and functional patterns of nondemented subjects with equivocal visual amyloid pet findings*, European Journal of Nuclear Medicine and Molecular Imaging, 42 (2015). ↑ 6.1 and 8.1

[215] E. Peira, M. Grazzini, M. Bauckneht, F. Sensi, P. Bosco, D. Arnaldi, S. Morbelli, A. Chincarini, M. Pardini, and F. Nobili, *Probing the role of a regional quantitative assessment of amyloid pet*, Journal of Alzheimer's Disease, 80 (2021). ↑ 5.3 and 11

[216] J. B. Pereira, T. O. Strandberg, S. Palmqvist, G. Volpe, D. van Westen, E. Westman, and O. Hansson, *Amyloid network topology characterizes the progression of alzheimer's disease during the predementia stages*, Cerebral Cortex, 28 (2018). ↑ 8.4

[217] K. E. Pike, K. A. Ellis, V. L. Villemagne, N. Good, G. Chételat, D. Ames, C. Szoeke, S. M. Laws, G. Verdile, R. N. Martins, C. L. Masters, and C. C. Rowe, *Cognition and beta-amyloid in preclinical alzheimer's disease: Data from the aibl study*, Neuropsychologia, 49 (2011). ↑ 3.4

[218] K. E. Pike, G. Savage, V. L. Villemagne, S. Ng, S. A. Moss, P. Maruff, C. A. Mathis, W. E. Klunk, C. L. Masters, and C. C. Rowe, *β-amyloid imaging and memory in non-demented individuals: evidence for preclinical alzheimer's disease*, Brain, 130 (2007). ↑ 1.3

[219] Piramal-Imaging, *Neuraceq™ (florbetaben f18) injection prescribing information*, 2014. ↑ 3.1, 3.3, 8.2.2, 9.2.2, and 10.2

[220] M. J. Pontecorvo, M. D. Devous, M. Navitsky, M. Lu, S. Salloway, F. W. Schaerf, D. Jennings, A. K. Arora, A. McGeehan, N. C. Lim, H. Xiong, A. D. Joshi, A. Siderowf, and M. A. Mintun, *Relationships between flortaucipir pet tau binding and amyloid burden, clinical diagnosis, age and cognition*, Brain, (2017). ↑ 4.2 and 5.5

[221] J. C. Price, W. E. Klunk, B. J. Lopresti, X. Lu, J. A. Hoge, S. K. Ziolko, D. P. Holt, C. C. Meltzer, S. T. DeKosky, and C. A. Mathis, *Kinetic modeling of amyloid binding in humans using pet imaging and pittsburgh compound-b*, Journal of Cerebral Blood Flow & Metabolism, 25 (2005). ↑ 7.2.2 and 7.4

[222] V. PYTEL, J. A. MATIAS-GUIU, J. MATÍAS-GUIU, A. CORTÉS-MARTÍNEZ, P. MONTERO, T. MORENO-RAMOS, J. ARRAZOLA, J. L. CARRERAS, AND M. N. CABRERA-MARTÍN, *Amyloid pet findings in multiple sclerosis are associated with cognitive decline at 18 months*, Multiple Sclerosis and Related Disorders, 39 (2020), p. 101926. ↱ 11

[223] F. QIAO, J. W. CLARK, T. PAN, AND O. MAWLAWI, *Joint model of motion and anatomy for pet image reconstruction*, Medical Physics, 34 (2007). ↱ 2.2

[224] Y. T. QUIROZ, R. A. SPERLING, D. J. NORTON, A. BAENA, J. F. ARBOLEDA-VELASQUEZ, D. COSIO, A. SCHULTZ, M. LAPOINT, E. GUZMAN-VELEZ, J. B. MILLER, L. A. KIM, K. CHEN, P. N. TARIOT, F. LOPERA, E. M. REIMAN, AND K. A. JOHNSON, *Association between amyloid and tau accumulation in young adults with autosomal dominant alzheimer disease*, JAMA Neurology, 75 (2018). ↱ 1.3

[225] G. D. RABINOVICI, C. GATSONIS, C. APGAR, K. CHAUDHARY, I. GAREEN, L. HANNA, J. HENDRIX, B. E. HILLNER, C. OLSON, O. H. LESMAN-SEGEV, J. ROMANOFF, B. A. SIEGEL, R. A. WHITMER, AND M. C. CARRILLO, *Association of amyloid positron emission tomography with subsequent change in clinical management among medicare beneficiaries with mild cognitive impairment or dementia*, JAMA, 321 (2019). ↱ 3, 3.2, and 11

[226] K. G. RANASINGHE, K. P. RANKIN, I. V. LOBACH, J. H. KRAMER, V. E. STURM, B. M. BETTCHER, K. POSSIN, S. C. YOU, A. K. LAMARRE, T. SHANY-UR, M. L. STEPHENS, D. C. PERRY, S. E. LEE, Z. A. MILLER, M. L. GORNO-TEMPINI, H. J. ROSEN, A. BOXER, W. W. SEELEY, G. D. RABINOVICI, K. A. VOSSEL, AND B. L. MILLER, *Cognition and neuropsychiatry in behavioral variant frontotemporal dementia by disease stage*, Neurology, 86 (2016). ↱ 8.4

[227] D. A. ROBERTS, J. A. DETRE, L. BOLINGER, E. K. INSKO, AND J. S. LEIGH, *Quantitative magnetic resonance imaging of human brain perfusion at 1.5 t using steady-state inversion of arterial water.*, Proceedings of the National Academy of Sciences, 91 (1994). ↱ 7.2.2

[228] K. M. RODRIGUE, K. M. KENNEDY, M. D. DEVOUS, J. R. RIECK, A. C. HEBRANK, R. DIAZ-ARRASTIA, D. MATHEWS, AND D. C. PARK, *-amyloid burden in healthy aging: Regional distribution and cognitive consequences*, Neurology, 78 (2012). ↱ 4.2 and 9.1

[229] E. T. ROLLS, C.-C. HUANG, C.-P. LIN, J. FENG, AND M. JOLIOT, *Automated anatomical labelling atlas 3*, NeuroImage, 206 (2020), p. 116189. ↱ 10.2 and 10.1

[230] A. D. ROSES, *Genetic testing for alzheimer disease*, Archives of Neurology, 54 (1997). ↱ 1.3

[231] A. H. ROSTOMIAN, C. MADISON, G. D. RABINOVICI, AND W. J. JAGUST, *Early ¹¹ c-pib frames and ¹⁸ f-fdg pet measures are comparable: A study validated in a cohort of ad and ftld patients*, Journal of Nuclear Medicine, 52 (2011). ↱ 7.4 and 11

[232] C. C. ROWE, U. ACKERMAN, W. BROWNE, R. MULLIGAN, K. L. PIKE, G. O'KEEFE, H. TOCHON-DANGUY, G. CHAN, S. U. BERLANGIERI, G. JONES, K. L. DICKINSON-ROWE, H. P. KUNG, W. ZHANG, M. P. KUNG, D. SKOVRONSKY, T. DYRKS, G. HOLL, S. KRAUSE, M. FRIEBE, L. LEHMAN, S. LINDEMANN, L. M. DINKELBORG, C. L. MASTERS, AND V. L. VILLEMAGNE, *Imaging of amyloid β in alzheimer's disease with 18f-bay94-9172, a novel pet tracer: proof of mechanism*, The Lancet Neurology, 7 (2008). ↱ 3.3

[233] C. C. ROWE, S. NG, U. ACKERMANN, S. J. GONG, K. PIKE, G. SAVAGE, T. F. COWIE, K. L. DICKINSON, P. MARUFF, D. DARBY, C. SMITH, M. WOODWARD, J. MERORY, H. TOCHON-DANGUY, G. O'KEEFE, W. E. KLUNK, C. A. MATHIS, J. C. PRICE, C. L. MASTERS, AND V. L. VILLEMAGNE, *Imaging beta-amyloid burden in aging and dementia*, Neurology, 68 (2007). ↱ 8.4

[234] M. N. SABBAGH AND J. CUMMINGS, *Open peer commentary to "failure to demonstrate efficacy of aducanumab: An analysis of the emerge and engage trials as reported by biogen december 2019"*, Alzheimer's & Dementia, 17 (2021). ↱ 1.3

[235] O. SABRI, M. N. SABBAGH, J. SEIBYL, H. BARTHEL, H. AKATSU, Y. OUCHI, K. SENDA, S. MURAYAMA, K. ISHII, M. TAKAO, T. G. BEACH, C. C. ROWE, J. B. LEVERENZ, B. GHETTI, J. W. IRONSIDE, A. M. CATAFAU, A. W. STEPHENS, A. MUELLER, N. KOGLIN, A. HOFFMANN, K. ROTH, C. REININGER, AND W. J. SCHULZ-SCHAEFFER, *Florbetaben pet imaging to detect amyloid beta plaques in alzheimer's disease: Phase 3 study*, Alzheimer's & Dementia, 11 (2015). ↱ 3, 3.1, and 3.1

[236] G. B. SAHA, *Basics of PET Imaging*, Springer New York, 2010. ↱ 2.1 and 2.1.1

[237] F. A. SAKR, M. J. GROTHE, E. CAVEDO, I. JELISTRATOVA, M.-O. HABERT, M. DYRBA, G. GONZALEZ-ESCAMILLA, H. BERTIN, M. LOCATELLI, S. LEHERICY, S. TEIPEL, B. DUBOIS, AND H. HAMPEL, *Applicability of in vivo staging of regional amyloid burden in a cognitively normal cohort with subjective memory complaints: the insight-pread study*, Alzheimer's Research & Therapy, 11 (2019). ↱ 9.1 and 11

[238] S. SALLOWAY, J. E. GAMEZ, U. SINGH, C. H. SADOWSKY, T. VILLENA, M. N. SABBAGH, T. G. BEACH, R. DUARA, A. S. FLEISHER, K. A. FREY, Z. WALKER, A. HUNJAN, Y. M. ESCOVAR, M. E. AGRONIN, J. ROSS, A. BOZOKI, M. AKINOLA, J. SHI, R. VANDENBERGHE, M. D. IKONOMOVIC, P. F. SHERWIN, G. FARRAR, A. P. SMITH, C. J. BUCKLEY, D. R. THAL, M. ZANETTE, AND C. CURTIS, *Performance of [¹⁸ f]flutemetamol amyloid imaging against the neuritic plaque component of cerad and the current (2012) nia-aa recommendations for the neuropathologic diagnosis of alzheimer's disease*, Alzheimer's & Dementia: Diagnosis, Assessment & Disease Monitoring, 9 (2017). ↱ 3, 3.1, and 3.1

[239] S. SALLOWAY, R. SPERLING, N. C. FOX, K. BLENNOW, W. KLUNK, M. RASKIND, M. SABBAGH, L. S. HONIG, A. P. PORSTEINSSON, S. FERRIS, M. REICHERT, N. KETTER, B. NEJADNIK, V. GUENZLER, M. MILOSLAVSKY, D. WANG, Y. LU, J. LULL, I. C. TUDOR, E. LIU, M. GRUNDMAN, E. YUEN, R. BLACK, AND H. R. BRASHEAR, *Two phase 3 trials of bapineuzumab in mild-to-moderate alzheimer's disease*, New England Journal of Medicine, 370 (2014). ↱ 1.3 and 9.1

[240] L. SARRO, M. L. SENJEM, E. S. LUNDT, S. A. PRZYBELSKI, T. G. LESNICK, J. GRAFF-RADFORD, B. F. BOEVE, V. J. LOWE, T. J. FERMAN, D. S. KNOPMAN, G. COMI, M. FILIPPI, R. C. PETERSEN, C. R. JACK, AND K. KANTARCI, *Amyloid-β deposition and regional grey matter atrophy rates in dementia with lewy bodies*, Brain, 139 (2016). ↱ 1.2 and 8.1

[241] J. SAXTON, O. L. LOPEZ, G. RATCLIFF, C. DULBERG, L. P. FRIED, M. C. CARLSON, A. B. NEWMAN, AND L. KULLER, *Preclinical alzheimer disease: Neuropsychological test performance 1.5 to 8 years prior to onset*, Neurology, 63 (2004). ↱ 5.3 and 8.4

[242] N. M. SCHEININ, K. WIKMAN, A. JULA, M. PEROLA, T. VAHLBERG, J. ROKKA, K. NÅGREN, M. VIITANEN, AND J. O. RINNE, *Cortical 11c-pib uptake is associated with age, apoe genotype, and gender in "healthy aging"*, Journal of Alzheimer's Disease, 41 (2014). ↱ 3.4

[243] P. SCHELTENS, D. LEYS, F. BARKHOF, D. HUGLO, H. C. WEINSTEIN, P. VERMERSCH, M. KUIPER, M. STEINLING, E. C. WOLTERS, AND J. VALK, *Atrophy of medial temporal lobes on mri in "probable" alzheimer's disease and normal ageing: diagnostic value and neuropsychological correlates.*, Journal of Neurology, Neurosurgery & Psychiatry, 55 (1992). ↱ 6.4

[244] M. E. SCHMIDT, P. CHIAO, G. KLEIN, D. MATTHEWS, L. THURFJELL, P. E. COLE, R. MARGOLIN, S. LANDAU, N. L. FOSTER, N. S. MASON, S. D. SANTI, J. SUHY, R. A. KOEPPE, AND W. JAGUST, *The influence of biological and technical factors on quantitative analysis of amyloid pet: Points to consider and recommendations for controlling variability in longitudinal data*, Alzheimer's & Dementia, 11 (2015). ↱ 3.3.1, 4.1, 4.2, 4.2.1, 6.2.5, 6.4, 7.1, 8.2.3, 8.4, 9.1, 9.2.3, and 11

[245] M. SCHÖLL, R. OSSENKOPPELE, O. STRANDBERG, S. PALMQVIST, J. JÖGI, T. OHLSSON, R. SMITH, AND O. HANSSON, *Distinct 18f-av-1451 tau pet retention patterns in early- and late-onset alzheimer's disease*, Brain, 140 (2017). ↱ 1.3

[246] D. J. SELKOE AND J. HARDY, *The amyloid hypothesis of alzheimer's disease at 25 years*, EMBO Molecular Medicine, 8 (2016). ↱ 1.3

[247] J. SEPULCRE, M. J. GROTHE, F. D'OLEIRE UQUILLAS, L. ORTIZ-TERÁN, I. DIEZ, H.-S. YANG, H. I. L. JACOBS, B. J. HANSEEUW, Q. LI, G. EL-FAKHRI, R. A. SPERLING, AND K. A. JOHNSON, *Neurogenetic contributions to amyloid beta and tau spreading in the human cortex*, Nature Medicine, 24 (2018). ↱ 8.4

[248] J. SEVIGNY, P. CHIAO, T. BUSSIÈRE, P. H. WEINREB, L. WILLIAMS, M. MAIER, R. DUNSTAN, S. SALLOWAY, T. CHEN, Y. LING, J. O'GORMAN, F. QIAN, M. ARASTU, M. LI, S. CHOLLATE, M. S. BRENNAN, O. QUINTERO-MONZON, R. H. SCANNEVIN, H. M. ARNOLD, T. ENGBER, K. RHODES, J. FERRERO, Y. HANG, A. MIKULSKIS, J. GRIMM, C. HOCK, R. M. NITSCH, AND A. SANDROCK, *The antibody aducanumab reduces aβ plaques in alzheimer's disease*, Nature, 537 (2016). ↱ 9.1

[249] M. SHINOHARA, S. FUJIOKA, M. E. MURRAY, A. WOJTAS, M. BAKER, A. ROVELET-LECRUX, R. RADEMAKERS, P. DAS, J. E. PARISI, N. R. GRAFF-RADFORD, R. C. PETERSEN, D. W. DICKSON, AND G. BU, *Regional distribution*

of synaptic markers and app correlate with distinct clinicopathological features in sporadic and familial alzheimer's disease, Brain, 137 (2014). ⌐ 8.4

[250] M. SHINOHARA, R. C. PETERSEN, D. W. DICKSON, AND G. BU, *Brain regional correlation of amyloid-β with synapses and apolipoprotein e in non-demented individuals: potential mechanisms underlying regional vulnerability to amyloid-β accumulation*, Acta Neuropathologica, 125 (2013). ⌐ 8.4

[251] M. SORET, S. L. BACHARACH, AND I. BUVAT, *Partial-volume effect in pet tumor imaging*, Journal of Nuclear Medicine, 48 (2007). ⌐ 2.2, 2.5, 2.2, 2.2, and 2.6

[252] D. STRUL, R. B. SLATES, M. DAHLBOM, S. R. CHERRY, AND P. K. MARSDEN, *An improved analytical detector response function model for multilayer small-diameter pet scanners*, Physics in Medicine and Biology, 48 (2003). ⌐ 2.2

[253] Y. SU, T. M. BLAZEY, C. J. OWEN, J. J. CHRISTENSEN, K. FRIEDRICHSEN, N. JOSEPH-MATHURIN, Q. WANG, R. C. HORNBECK, B. M. ANCES, A. Z. SNYDER, L. A. CASH, R. A. KOEPPE, W. E. KLUNK, D. GALASKO, A. M. BRICKMAN, E. MCDADE, J. M. RINGMAN, P. M. THOMPSON, A. J. SAYKIN, B. GHETTI, R. A. SPERLING, K. A. JOHNSON, S. P. SALLOWAY, P. R. SCHOFIELD, C. L. MASTERS, V. L. VILLEMAGNE, N. C. FOX, S. FÖRSTER, K. CHEN, E. M. REIMAN, C. XIONG, D. S. MARCUS, M. W. WEINER, J. C. MORRIS, R. J. BATEMAN, AND T. L. S. BENZINGER, *Quantitative amyloid imaging in autosomal dominant alzheimer's disease: Results from the dian study group*, PLOS ONE, 11 (2016). ⌐ 7.2.3

[254] Y. SU, T. M. BLAZEY, A. Z. SNYDER, M. E. RAICHLE, D. S. MARCUS, B. M. ANCES, R. J. BATEMAN, N. J. CAIRNS, P. ALDEA, L. CASH, J. J. CHRISTENSEN, K. FRIEDRICHSEN, R. C. HORNBECK, A. M. FARRAR, C. J. OWEN, R. MAYEUX, A. M. BRICKMAN, W. KLUNK, J. C. PRICE, P. M. THOMPSON, B. GHETTI, A. J. SAYKIN, R. A. SPERLING, K. A. JOHNSON, P. R. SCHOFIELD, V. BUCKLES, J. C. MORRIS, AND T. L. BENZINGER, *Partial volume correction in quantitative amyloid imaging*, NeuroImage, 107 (2015). ⌐ 7.1 and 8.4

[255] Y. SU, S. FLORES, R. C. HORNBECK, B. SPEIDEL, A. G. VLASSENKO, B. A. GORDON, R. A. KOEPPE, W. E. KLUNK, C. XIONG, J. C. MORRIS, AND T. L. BENZINGER, *Utilizing the centiloid scale in cross-sectional and longitudinal pib pet studies*, NeuroImage: Clinical, 19 (2018). ⌐ 4.2.1 and 11

[256] L. K. SUNDAR, O. MUZIK, L. RISCHKA, A. HAHN, I. RAUSCH, R. LANZENBERGER, M. HIENERT, E.-M. KLEBERMASS, F.-G. FÜCHSEL, M. HACKER, M. PILZ, E. PATARAIA, T. TRAUB-WEIDINGER, AND T. BEYER, *Towards quantitative [18f]fdg-pet/mri of the brain: Automated mr-driven calculation of an image-derived input function for the non-invasive determination of cerebral glucose metabolic rates*, Journal of Cerebral Blood Flow & Metabolism, 39 (2019). ⌐ 4.1

[257] D. F. TANG-WAI, N. R. GRAFF-RADFORD, B. F. BOEVE, D. W. DICKSON, J. E. PARISI, R. CROOK, R. J. CASELLI, D. S. KNOPMAN, AND R. C. PETERSEN, *Clinical, genetic, and neuropathologic characteristics of posterior cortical atrophy*, Neurology, 63 (2004). ⌐ 1.3

[258] D. R. THAL, T. G. BEACH, M. ZANETTE, K. HEURLING, A. CHAKRABARTY, A. IS-MAIL, A. P. SMITH, AND C. BUCKLEY, *[^{18} f]flutemetamol amyloid positron emission tomography in preclinical and symptomatic alzheimer's disease: Specific detection of advanced phases of amyloid-β pathology*, Alzheimer's & Dementia, 11 (2015). ↱ 5.3 and 7.1

[259] D. R. THAL, U. RÜB, M. ORANTES, AND H. BRAAK, *Phases of aβ-deposition in the human brain and its relevance for the development of ad*, Neurology, 58 (2002). ↱ 4.2, 4.2, 5.3, and 8.4

[260] L. THURFJELL, J. LILJA, R. LUNDQVIST, C. BUCKLEY, A. SMITH, R. VANDEN-BERGHE, AND P. SHERWIN, *Automated quantification of ^{18} f-flutemetamol pet activity for categorizing scans as negative or positive for brain amyloid: Concordance with visual image reads*, Journal of Nuclear Medicine, 55 (2014). ↱ 4.2, 4.2.1, and 7.1

[261] M. TOLAR, S. ABUSHAKRA, J. A. HEY, A. PORSTEINSSON, AND M. SABBAGH, *Aducanumab, gantenerumab, ban2401, and alz-801—the first wave of amyloid-targeting drugs for alzheimer's disease with potential for near term approval*, Alzheimer's Research & Therapy, 12 (2020). ↱ 1.3 and 4

[262] S. TONG, A. M. ALESSIO, AND P. E. KINAHAN, *Image reconstruction for pet/ct scanners: past achievements and future challenges*, Imaging in Medicine, 2 (2010). ↱ 2.2 and 2.2

[263] L. TREMBATH, M. NEWELL, AND M. D. DEVOUS, *Technical considerations in brain amyloid pet imaging with ^{18} f-florbetapir*, Journal of Nuclear Medicine Technology, 43 (2015). ↱ 3.3.1

[264] V. TRYPUTSEN, A. DIBERNARDO, M. SAMTANI, G. P. NOVAK, V. A. NARAYAN, AND N. RAGHAVAN, *Optimizing regions-of-interest composites for capturing treatment effects on brain amyloid in clinical trials*, Journal of Alzheimer's Disease, 43 (2014). ↱ 7.1 and 8.4

[265] B. N. VAN BERCKEL, R. OSSENKOPPELE, N. TOLBOOM, M. YAQUB, J. C. FOSTER-DINGLEY, A. D. WINDHORST, P. SCHELTENS, A. A. LAMMERTSMA, AND R. BOELLAARD, *Longitudinal amyloid imaging using ^{11} c-pib: Methodologic considerations*, Journal of Nuclear Medicine, 54 (2013). ↱ 4.2, 4.2.1, and 5.2

[266] M. J. VAN OSCH, W. M. TEEUWISSE, M. A. VAN WALDERVEEN, J. HENDRIKSE, D. A. KIES, AND M. A. VAN BUCHEM, *Can arterial spin labeling detect white matter perfusion signal?*, Magnetic Resonance in Medicine, 62 (2009). ↱ 7.2.2

[267] R. VANDENBERGHE, K. V. LAERE, A. IVANOIU, E. SALMON, C. BASTIN, E. TRIAU, S. HASSELBALCH, I. LAW, A. ANDERSEN, A. KORNER, L. MINTHON, G. GARRAUX, N. NELISSEN, G. BORMANS, C. BUCKLEY, R. OWENIUS, L. THURFJELL, G. FARRAR, AND D. J. BROOKS, *^{18} f-flutemetamol amyloid imaging in alzheimer disease and mild cognitive impairment: A phase 2 trial*, Annals of Neurology, 68 (2010). ↱ 3.1

[268] S. VANDENBERGHE, E. MIKHAYLOVA, E. D'HOE, P. MOLLET, AND J. S. KARP, *Recent developments in time-of-flight pet*, EJNMMI Physics, 3 (2016). ↱ 2.1.1 and 9.1

[269] S. Varadarajan, S. Yatin, M. Aksenova, and D. Butterfield, *Review: Alzheimer's amyloid β-peptide-associated free radical oxidative stress and neurotoxicity*, Journal of Structural Biology, 130 (2000). ↱ 1.1

[270] P. Vemuri, D. S. Knopman, T. G. Lesnick, S. A. Przybelski, M. M. Mielke, J. Graff-Radford, M. E. Murray, R. O. Roberts, M. Vassilaki, V. J. Lowe, M. M. Machulda, D. T. Jones, R. C. Petersen, and C. R. Jack, *Evaluation of amyloid protective factors and alzheimer disease neurodegeneration protective factors in elderly individuals*, JAMA Neurology, 74 (2017). ↱ 3.4

[271] L. Vermunt, S. A. Sikkes, A. Hout, R. Handels, I. Bos, W. M. Flier, S. Kern, P. Ousset, P. Maruff, I. Skoog, F. R. Verhey, Y. Freund-Levi, M. Tsolaki, Åsa K. Wallin, M. O. Rikkert, H. Soininen, L. Spiru, H. Zetterberg, K. Blennow, P. Scheltens, G. Muniz-Terrera, and P. J. Visser, *Duration of preclinical, prodromal, and dementia stages of alzheimer's disease in relation to age, sex, and <i>apoe</i> genotype*, Alzheimer's & Dementia, 15 (2019). ↱ 1.3, 1.3, and 3.3

[272] R. S. Vest and C. J. Pike, *Gender, sex steroid hormones, and alzheimer's disease*, Hormones and Behavior, 63 (2013). ↱ 3.4

[273] N. Villain, G. Chételat, B. Grassiot, P. Bourgeat, G. Jones, K. A. Ellis, D. Ames, R. N. Martins, F. Eustache, O. Salvado, C. L. Masters, C. C. Rowe, and V. L. Villemagne, *Regional dynamics of amyloid-β deposition in healthy elderly, mild cognitive impairment and alzheimer's disease: a voxelwise pib–pet longitudinal study*, Brain, 135 (2012). ↱ 8.4

[274] V. L. Villemagne, S. Burnham, P. Bourgeat, B. Brown, K. A. Ellis, O. Salvado, C. Szoeke, S. L. Macaulay, R. Martins, P. Maruff, D. Ames, C. C. Rowe, and C. L. Masters, *Amyloid β deposition, neurodegeneration, and cognitive decline in sporadic alzheimer's disease: a prospective cohort study*, The Lancet Neurology, 12 (2013). ↱ 4.2.1 and 5.2

[275] V. L. Villemagne, V. Doré, P. Bourgeat, S. C. Burnham, S. Laws, O. Salvado, C. L. Masters, and C. C. Rowe, *Aβ-amyloid and tau imaging in dementia*, Seminars in Nuclear Medicine, 47 (2017). ↱ 3

[276] V. L. Villemagne, M. T. Fodero-Tavoletti, C. L. Masters, and C. C. Rowe, *Tau imaging: early progress and future directions*, The Lancet Neurology, 14 (2015), pp. 114–124. ↱ 5.5

[277] V. L. Villemagne, K. Ong, R. S. Mulligan, G. Holl, S. Pejoska, G. Jones, G. O'Keefe, U. Ackerman, H. Tochon-Danguy, J. G. Chan, C. B. Reininger, L. Fels, B. Putz, B. Rohde, C. L. Masters, and C. C. Rowe, *Amyloid imaging with ¹⁸ f-florbetaben in alzheimer disease and other dementias*, Journal of Nuclear Medicine, 52 (2011). ↱ 7.1

[278] V. L. Villemagne and C. C. Rowe, *Long night's journey into the day: Amyloid-β imaging in alzheimer's disease*, Journal of Alzheimer's Disease, 33 (2012). ↱ 6.4

[279] S. VILLENEUVE, G. D. RABINOVICI, B. I. COHN-SHEEHY, C. MADISON, N. AYAKTA, P. M. GHOSH, R. L. JOIE, S. K. ARTHUR-BENTIL, J. W. VOGEL, S. M. MARKS, M. LEHMANN, H. J. ROSEN, B. REED, J. OLICHNEY, A. L. BOXER, B. L. MILLER, E. BORYS, L.-W. JIN, E. J. HUANG, L. T. GRINBERG, C. DECARLI, W. W. SEELEY, AND W. JAGUST, *Existing pittsburgh compound-b positron emission tomography thresholds are too high: statistical and pathological evaluation*, Brain, 138 (2015). ↱ 5.3, 8.4, and 11

[280] S. VILLENEUVE, J. W. VOGEL, J. GONNEAUD, A. P. BINETTE, P. ROSA-NETO, S. GAUTHIER, R. J. BATEMAN, A. M. FAGAN, J. C. MORRIS, T. L. S. BENZINGER, S. C. JOHNSON, J. C. S. BREITNER, AND J. POIRIER, *Proximity to parental symptom onset and amyloid-β burden in sporadic alzheimer disease*, JAMA Neurology, 75 (2018). ↱ 3.4

[281] S. J. VOS, C. XIONG, P. J. VISSER, M. S. JASIELEC, J. HASSENSTAB, E. A. GRANT, N. J. CAIRNS, J. C. MORRIS, D. M. HOLTZMAN, AND A. M. FAGAN, *Preclinical alzheimer's disease and its outcome: a longitudinal cohort study*, The Lancet Neurology, 12 (2013). ↱ 1.3 and 3.3

[282] J. WANG, S. XING, Y. HUANG, P. FAN, J. FU, G. YANG, L. YANG, AND P. LV, *Highly stable gasified straw slag as a novel solid base catalyst for the effective synthesis of biodiesel: Characteristics and performance*, Applied Energy, 190 (2017). ↱ 6.1

[283] H. WATABE, Y. IKOMA, Y. KIMURA, M. NAGANAWA, AND M. SHIDAHARA, *Pet kinetic analysis—compartmental model*, Annals of Nuclear Medicine, 20 (2006). ↱ 4.1

[284] A. M. WESSELS, P. N. TARIOT, J. A. ZIMMER, K. J. SELZLER, S. M. BRAGG, S. W. ANDERSEN, J. LANDRY, J. H. KRULL, A. M. DOWNING, B. A. WILLIS, S. SHCHERBININ, J. MULLEN, P. BARKER, J. SCHUMI, C. SHERING, B. R. MATTHEWS, R. A. STERN, B. VELLAS, S. COHEN, E. MACSWEENEY, M. BOADA, AND J. R. SIMS, *Efficacy and safety of lanabecestat for treatment of early and mild alzheimer disease*, JAMA Neurology, 77 (2020). ↱ 1.3

[285] A. WHITTINGTON AND R. N. GUNN, *Amyloid load: A more sensitive biomarker for amyloid imaging*, Journal of Nuclear Medicine, 60 (2019). ↱ 4.3, 5.4, and 9.1

[286] M. WIRTH, S. VILLENEUVE, C. M. HAASE, C. M. MADISON, H. OH, S. M. LANDAU, G. D. RABINOVICI, AND W. J. JAGUST, *Associations between alzheimer disease biomarkers, neurodegeneration, and cognition in cognitively normal older people*, JAMA Neurology, (2013). ↱ 8.1 and 8.4

[287] K. E. WISNIEWSKI, H. M. WISNIEWSKI, AND G. Y. WEN, *Occurrence of neuropathological changes and dementia of alzheimer's disease in down's syndrome*, Annals of Neurology, 17 (1985). ↱ 1.2

[288] R. WOLZ, A. J. SCHWARZ, K. R. GRAY, P. YU, AND D. L. HILL, *Enrichment of clinical trials in mci due to ad using markers of amyloid and neurodegeneration*, Neurology, 87 (2016). ↱ 7.1

[289] D. F. WONG, P. B. ROSENBERG, Y. ZHOU, A. KUMAR, V. RAYMONT, H. T. RAVERT, R. F. DANNALS, A. NANDI, J. R. BRAŠIĆ, W. YE, J. HILTON, C. LYKETSOS, H. F. KUNG, A. D. JOSHI, D. M. SKOVRONSKY, AND M. J. PONTECORVO, *In vivo imaging of amyloid deposition in alzheimer disease using the radioligand ¹⁸ f-av-45 (flobetapir f 18)*, Journal of Nuclear Medicine, 51 (2010). ↱ 4.2, 4.2.1, and 7.2.2

[290] C. XIA, S. J. MAKARETZ, C. CASO, S. MCGINNIS, S. N. GOMPERTS, J. SEPUL-CRE, T. GOMEZ-ISLA, B. T. HYMAN, A. SCHULTZ, N. VASDEV, K. A. JOHNSON, AND B. C. DICKERSON, *Association of in vivo [¹⁸ f]av-1451 tau pet imaging results with cortical atrophy and symptoms in typical and atypical alzheimer disease*, JAMA Neurology, 74 (2017). ↱ 8.4

[291] M. YAMADA, *Cerebral amyloid angiopathy: Emerging concepts*, Journal of Stroke, 17 (2015). ↱ 1.2

[292] J. YANG, C. HU, N. GUO, J. DUTTA, L. M. VAINA, K. A. JOHNSON, J. SEPULCRE, G. E. FAKHRI, AND Q. LI, *Partial volume correction for pet quantification and its impact on brain network in alzheimer's disease*, Scientific Reports, 7 (2017). ↱ 4.2

[293] S. M. YATIN, M. YATIN, T. AULICK, K. B. AIN, AND D. BUTTERFIELD, *Alzheimer's amyloid β-peptide associated free radicals increase rat embryonic neuronal polyamine uptake and ornithine decarboxylase activity: protective effect of vitamin e*, Neuroscience Letters, 263 (1999). ↱ 1.1

[294] F. Q. YE, K. F. BERMAN, T. ELLMORE, G. ESPOSITO, J. D. VAN HORN, Y. YANG, J. DUYN, A. M. SMITH, J. A. FRANK, D. R. WEINBERGER, AND A. C. MCLAUGHLIN, *H215o pet validation of steady-state arterial spin tagging cerebral blood flow measurements in humans*, Magnetic Resonance in Medicine, 44 (2000). ↱ 7.2.2

[295] D. YORK, N. M. EVENSEN, M. L. MARTINEZ, AND J. D. B. DELGADO, *Unified equations for the slope, intercept, and standard errors of the best straight line*, American Journal of Physics, 72 (2004). ↱ 6.2.6

[296] K. ZHANG, H. HERZOG, J. MAULER, C. FILSS, T. W. OKELL, E. R. KOPS, L. TELLMANN, T. FISCHER, B. BROCKE, W. STURM, H. H. COENEN, AND N. J. SHAH, *Comparison of cerebral blood flow acquired by simultaneous [¹⁵ o]water positron emission tomography and arterial spin labeling magnetic resonance imaging*, Journal of Cerebral Blood Flow & Metabolism, 34 (2014). ↱ 4.2.1 and 5.2

[297] S. K. ZIOLKO, L. A. WEISSFELD, W. E. KLUNK, C. A. MATHIS, J. A. HOGE, B. J. LOPRESTI, S. T. DEKOSKY, AND J. C. PRICE, *Evaluation of voxel-based methods for the statistical analysis of pib pet amyloid imaging studies in alzheimer's disease*, NeuroImage, 33 (2006). ↱ 4.2

[298] B. V. ZLOKOVIC, *Clearing amyloid through the blood-brain barrier*, Journal of Neurochemistry, 89 (2004). ↱ 1.1